








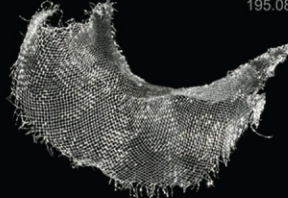

# Конденсированные среды и межфазные границы

РЕЦЕНЗИРУЕМЫЙ НАУЧНЫЙ ЖУРНАЛ

# Condensed Matter and Interphases

Kondensirovannyye Sredy i Mezhfaznyye Granitsy  
PEER-REVIEWED SCIENTIFIC JOURNAL

Том 23, № 1  
Vol. 23, No. 1  
2021

<p>Co 27 58.933</p>  <p>Cobalt</p>	<p>Ni 28 58.693</p>  <p>Nickel</p>	<p>Cu 29 63.546</p>  <p>Copper</p>
<p>Rh 45 102.91</p>  <p>Rhodium</p>	<p>Pd 46 106.42</p>  <p>Palladium</p>	<p>Ag 47 107.87</p>  <p>Silver</p>
<p>Ir 77 192.22</p>  <p>Iridium</p>	<p>Pt 78 195.08</p>  <p>Platinum</p>	<p>Au 79 196.97</p>  <p>Gold</p>

# Condensed Matter and Interphases

## Kondensirovannye sredy i mezhfaznye granitsy

Peer-reviewed scientific journal

Published since January 1999

Periodicity: Quarterly

Volume 23, No. 1, 2021

Full-text version is available in the Russian language on the website: <https://journals.vsu.ru/kcmf>

**Condensed Matter and Interphases** (Kondensirovannye Sredy i Mezhfaznye Granitsy) publishes articles in Russian and English dedicated to key issues of condensed matter and physicochemical processes at interfaces and in volumes.

**The mission of the journal** is to provide open access to the results of original research (theoretical and experimental) at the intersection of contemporary condensed matter physics and chemistry, material science and nanoindustry, solid state chemistry, inorganic chemistry, and physical chemistry, and to share scientific data in the **following sections**: atomic, electron, and cluster structure of solids, liquids, and interphase boundaries; phase equilibria and defect formation processes; structure and physical and chemical properties of interphases; laser thermochemistry and photostimulated processes on solid surfaces; physics and chemistry of surface, thin films and heterostructures; kinetics and mechanism of formation of film structures; electrophysical processes in interphase boundaries; chemistry of surface phenomena in sorbents; devices and new research methods.

**The journal accepts for publication**: reviews, original articles, short communications by leading Russian scientists, foreign researchers, lecturers, postgraduate and undergraduate students.

### FOUNDER AND PUBLISHER:

Voronezh State University

The journal is registered by the Russian Federal Service for Supervision of Communications, Information Technology and Mass Media, Certificate of Registration ПИ № ФС77-78771 date 20.07.2020

The journal is included in the List of peer reviewed scientific journals published by the Higher Attestation Commission in which major research results from the dissertations of Candidates of Sciences (PhD) and Doctor of Science (DSc) degrees are to be published.

Scientific specialties of dissertations and their respective branches of science are as follows: 02.00.01 – Inorganic Chemistry, 02.00.04 – Physical Chemistry, 02.00.05 – Electrochemistry, 02.00.21 – Solid State Chemistry (Chemical sciences); 01.04.07 – Condensed Matter Physics (Physical Sciences)

The journal is indexed and archived in: Russian Scientific Index Citations, Scopus, Chemical Abstract, EBSCO, DOAJ, CrossRef

Editorial Board and Publisher Office:

1 Universitetskaya pl., Voronezh 394018

Phone: +7 (432) 2208445

<https://journals.vsu.ru/kcmf/about>

E-mail: [kcmf@main.vsu.ru](mailto:kcmf@main.vsu.ru)

Signed for printing 30.03.2021

Price – not fixed

Subscription is available using the unified catalogue “Russian Press”, subscription index 80568

When reprinting the materials, a reference to the Condensed Matter and Interphases must be cited

The journal’s materials are available under the Creative Commons “Attribution” 4.0 Global License



© Voronezh State University, 2021

### EDITOR-IN-CHIEF:

V. N. Semenov, DSc in Chemistry, Professor (Voronezh)

### VICE EDITORS-IN-CHIEF:

E. P. Domashevskaya, DSc in Physics and Mathematics, Professor (Voronezh)

P. Volovitch, DSc, Professor (Paris, France)

### EDITORIAL BOARD:

N. N. Afonin, DSc in Chemistry, Professor (Voronezh)

V. I. Vasil'eva, DSc in Chemistry, Professor (Voronezh)

A. V. Vvedenskii, DSc in Chemistry, Professor (Voronezh)

V. V. Gusarov, DSc in Chemistry, Associate Member of the RAS (St. Petersburg)

V. E. Guterman, DSc in Chemistry, Professor (Rostov-on-Don)

B. M. Darinskii, DSc in Physics and Mathematics, Professor (Voronezh)

V. P. Zlomanov, DSc in Chemistry, Professor (Moscow)

V. M. Ievlev, DSc in Physics and Mathematics, Full Member of the RAS (Moscow)

A. D. Izotov, DSc in Chemistry, Associate Member of the RAS (Moscow)

O. A. Kozaderov, DSc in Chemistry (Voronezh)

A. I. Marchakov, DSc in Chemistry, Professor (Moscow)

I. Ya. Mittova, DSc in Chemistry, Professor (Voronezh)

V. V. Nikonenko, DSc in Chemistry, Professor (Krasnodar)

O. V. Ovchinnikov, DSc in Physics and Mathematics, Professor (Voronezh)

S. N. Saltykov, DSc in Chemistry (Lipetsk)

V. F. Selemenev, DSc in Chemistry, Professor (Voronezh)

V. A. Terekhov, DSc in Physics and Mathematics, Professor (Voronezh)

E. A. Tutov, DSc in Chemistry (Voronezh)

P. P. Fedorov, DSc in Chemistry, Professor (Moscow)

V. A. Khonik, DSc in Physics and Mathematics, Professor (Voronezh)

V. A. Shaposhnik, DSc in Chemistry, Professor (Voronezh)

A. B. Yaroslavtsev, DSc in Chemistry, Associate Member of the RAS (Moscow)

### INTERNATIONAL MEMBERS OF THE EDITORIAL BOARD:

M. B. Babanly, DSc in Chemistry, Associate Member of the ANAS (Baku, Azerbaijan)

T. Bellezze, DSc (Ancona, Italy)

R. M. Mane, DSc (Kolhapur, India)

Nguyen Anh Tien, PhD in Chemistry, Associate Professor (Ho Chi Minh City, Vietnam)

V. V. Pan'kov, DSc in Chemistry, Professor (Minsk, Belarus)

F. Scholz, DSc, Professor (Greifswald, Germany)

M. S. Wickleder, DSc, Professor (Cologne, Germany)

V. Sivakov, DSc (Jena, Germany)

### EXECUTIVE SECRETARY:

V. A. Logacheva, PhD in Chemistry (Voronezh)

## CONTENTS

## REVIEW

*Burliaev D. V., Kozaderov O. A., Volovitch P.*  
Zinc-nickel alloy coatings: electrodeposition kinetics, corrosion, and selective dissolution.  
A review

## ORIGINAL ARTICLES

*Bakhtiyarly I. B., Kurbanova R. J., Abdullaeva Sh. S., Mukhtarova Z. M., Mammadova F. M.*  
Liquidus surface of the quasi-ternary system  $\text{Cu}_2\text{S}-\text{In}_2\text{S}_3-\text{FeS}$

*Grevtseva I. G., Chevychelova T. A., Derepko V. N., Ovchinnikov O. V., Smirnov M. S., Perepelitsa A. S., Parshina A. S.*  
Spectral manifestations of the exciton-plasmon interaction of  $\text{Ag}_2\text{S}$  quantum dots with silver and gold nanoparticles

*Imamaliyeva S. Z., Alakbarzade G. I., Babanly D. M., Bulanova M. V., Gasymov V. A., Babanly M. B.*  
Phase relations in the  $\text{Tl}_2\text{Te}-\text{TlBiTe}_2-\text{TlTbTe}_2$  system

*Lenshin A. S., Lukin A. N., Peshkov Ya. A., Kannykin S. V., Agapov B. L., Seredin P. V., Domashevskaya E. P.*  
Features of the two-stage formation of macroporous and mesoporous silicon structures

*Ovchinnikov O. V., Smirnov M. S., Grevtseva I. G., Derepko V. N., Chevychelova T. A., Leonova L. Yu., Perepelitsa A. S., Kondratenko T. S.*  
Luminescent properties of colloidal mixtures of  $\text{Zn}_{0.5}\text{Cd}_{0.5}\text{S}$  quantum dots and gold nanoparticles

*Ryabtsev S. V., Ghareeb D. A. A., Sinelnikov A. A., Turishchev S. Yu., Obvintseva L. A., Shaposhnik A. V.*  
Ozone detection by means of semiconductor gas sensors based on palladium (II) oxide

3 *Samoylov A. M., Pelipenko D. I., Kuralenko N. S.*  
Calculation of the nonstoichiometry area of nanocrystalline palladium (II) oxide films

16 *Spiridonova T. S., Savina A. A., Kadyrova Yu. M., Belykh E. P., Khaikina E. G.*  
New compounds  $\text{Li}_3\text{Ba}_2\text{Bi}_3(\text{XO}_4)_8$  ( $X = \text{Mo}, \text{W}$ ): synthesis and properties

25 *Suntsov Yu. K., Suntsova N. S.*  
Vapour-liquid phase equilibria and thermodynamic properties of solutions of the ethylbenzene and n-alkylbenzenes binary systems

32 *Tomina E. V., Pavlenko A. A., Kurkin N. A.*  
Synthesis of bismuth ferrite nanopowder doped with erbium ions

41 *Ushakov S. N., Uslamina M. A., Pynenkov A. A., Mishkin V. P., Nishchev K. N., Kuznetsov S. V., Chernova E. V., Fedorov P. P.*  
Growth and physical properties of  $\text{CaSrBaF}_6$  single crystals

49 *Shalaev P. V., Bondina E. V., Sankova N. N., Parkhomchuk E. V., Dolgushin S. A.*  
Synthesis and experimental study of liquid dispersions of magnetic fluorescent polystyrene microspheres

49 *Shchukin A. E., Kaul A. R., Vasiliev A. L., Rudnev I. A.*  
Synthesis, structure and superconducting properties of laminated thin film composites of  $\text{YBa}_2\text{Cu}_3\text{O}_{7-d}/\text{Y}_2\text{O}_3$  as components of 2G HTS wires

Guide for Authors – 2021

56

62

73

81

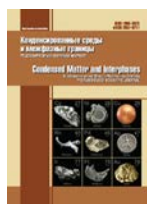
93

101

108

122

140



# Condensed Matter and Interphases

Kondensirovannye Sredy i Mezhfaznye Granitsy  
<https://journals.vsu.ru/kcmf/>

## Review

Review article

<https://doi.org/10.17308/kcmf.2021.23/3292>

## Zinc-nickel alloy coatings: electrodeposition kinetics, corrosion, and selective dissolution. A review

D. V. Burliaev, O. A. Kozaderov<sup>✉</sup>, P. Volovitch<sup>2</sup>

<sup>1</sup>Voronezh State University,  
1 Universitetskaya pl., Voronezh 394018, Russian Federation

<sup>2</sup>PSL University, CNRS-Chimie ParisTech, Institut de Recherche de Chimie Paris,  
11 rue Pierre et Marie Curie, Paris, France

### Abstract

A review of the literature is devoted to the patterns of the electrodeposition of zinc-nickel alloys including the kinetics of cathodic reduction of zinc, nickel, and zinc-nickel alloys in ammonium chloride, sulphate, and glycinate deposition electrolytes. We studied the data on the effectiveness of the corrosion resistance of zinc-nickel coatings and summarised the principal patterns of selective dissolution of the Zn-Ni alloys. The role of the addition of glycine to an ammonium chloride deposition electrolyte was determined in the modification of the morphological and anticorrosive properties of the coatings.

**Keywords:** electrodeposition, kinetics, zinc-nickel coatings, ammonium chloride electrolyte, glycine, current efficiency, corrosion, selective dissolution, voltammetry, chronoamperometry

**For citation:** Burliaev D. V., Kozaderov O. A., Volovitch P. Zinc-nickel alloy coatings: electrodeposition kinetics, corrosion, and selective dissolution. A review. *Kondensirovannye sredy i mezhfaznye granitsy = Condensed Matter and Interphases*. 2021;23(1): 3–15. <https://doi.org/10.17308/kcmf.2021.23/3292>

**Для цитирования:** Бурляев Д. В., Козадеров О. А., Волович П. Цинк-никелевые сплавные покрытия: кинетика электроосаждения, коррозия и селективное растворение. Обзор. *Конденсированные среды и межфазные границы*. 2021;23(1): 3–15. <https://doi.org/10.17308/kcmf.2021.23/3292>

### 1. Introduction

Zinc-nickel coatings considerably exceed pure zinc coatings in terms of their anticorrosive properties and also possess excellent physical properties [1], and, as a result, they are widely used in the aviation [2, 3], aerospace [4], and automotive industries [1–5]. Zinc-based coatings with a Ni content of 10–18 at. % show the best mechanical characteristics and protective properties in relation to steel [6–11], as they mainly consist of a zinc-enriched  $\gamma$ -phase which has high corrosion resistance, hardness, and strength [1–14]. The principal method of synthesis of Zn–Ni coatings is the cathodic electrodeposition [15–24], therefore it is very important to study the kinetic patterns of the

electrochemical synthesis of these coatings as well as the specific features of the formation of their anticorrosive properties and the increase of electrocatalytic activity.

### 2. Zinc-nickel alloys: general description and production

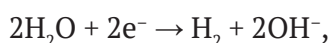
The analysis of the phase diagram of the Zn–Ni system [6] is indicative of the complex nature of the interaction between the components which is typical for Zn – transition metal systems. The  $\gamma$  phase, which forms the basis of most corrosion-resistant Zn–Ni coatings, corresponds to the homogeneity region of 74–85 at. % Zn. It crystallises from the alloy at 881 °C and can be described by different formulas, for example,  $\text{NiZn}_3$ ,  $\text{Ni}_2\text{Zn}_{11}$ ,  $\text{Ni}_3\text{Zn}_{10}$ ,  $\text{Ni}_4\text{Zn}_{22}$ , or  $\text{Ni}_5\text{Zn}_{21}$  [7, 8]. The mechanical strength of the alloy reaches its maximum and stabilises with a

✉ Oleg A. Kozaderov, e-mail: [ok@chem.vsu.ru](mailto:ok@chem.vsu.ru)  
© Burliaev D. V., Kozaderov O. A., Volovitch P., 2021



nickel content of more than 20 at. %, which also improves the thermal stability of the alloys [9, 10]. Anticorrosive and mechanical properties of zinc-nickel alloy coatings depend heavily on the phase composition. Homogeneous coatings consisting of  $\gamma$ -phase of the  $\text{Ni}_2\text{Zn}_{11}$  (or  $\text{Ni}_5\text{Zn}_{21}$ ) composition and corresponding to the nickel content of 10–18 % (wt) are most corrosion-resistant [2, 4, 11, 12].

Electrodeposition is the main method for the production of zinc-nickel alloy coatings [1–15]. A specific feature of this process for Zn-Ni systems is that it follows the mechanism of anomalous codeposition when a more electronegative component (zinc) is deposited first despite the presence of nickel, which is a more electropositive component. The mechanism of this process has been studied well in chloride and sulphate solutions [16–18]. Anomalous codeposition can be explained by the hydroxide suppression mechanism. As it happens, a secondary process of hydrogen evolution takes place at the same time with the electrodeposition based on the reaction:



during which the medium is alkalisied. The increased pH of the electrolyte solution contributes to the formation of the adsorptive zinc hydroxide  $\text{Zn}(\text{OH})_2(\text{ads})$ . Therefore, metal zinc is reduced at the cathode from the adsorbed hydroxide film blocking the transportation of nickel to the surface of the electrode. As a result, the reduction of nickel and hydrogen is suppressed [19, 20]. Along with the hydroxide suppression mechanism, a hypothesis of underpotential deposition of zinc is also suggested as an explanation of the anomalous codeposition [20, 21].

The quality of the synthesised Zn–Ni coating greatly depends on a number of factors: the composition and pH of the deposition electrolyte, the hydrodynamic regime, current density or electrode potential of the deposition, the temperature, and the material used as a substrate for the deposition [21, 22]. A variation in the factors leads to changes not only in the chemical and phase compositions of the coatings, but also in current efficiency, morphology, and visual and anticorrosive characteristics [21–24]. For instance, when studying the influence of the substrate material on the process of electrodeposition of zinc-nickel alloys, it was shown that a coating

deposited on a copper substrate has a more homogeneous chemical composition as compared to the coating deposited on a steel substrate. The nature of the substrate can also influence the phase composition of the coatings and its mechanical properties [23].

Zinc-nickel alloy coatings are deposited from electrolytes of various compositions, including oxalate [25], citrate [26], sulphate [27], chloride [28], sulphate-chloride [29], ethylenediamine [30], ammine, and ammonia-chloride [29, 31] solutions. Currently, cyanide, sulphamate, and pyrophosphate electrolytes are less popular due to ecological reasons as well as their low performance and high cost [29].

Deposition electrolytes often contain different additives that significantly influence the properties of the synthesised alloys. Complexation additives are widely used that ensure a more compact morphology of the coatings, their fineness, smoothness, and typical gloss. Among them are sodium acetate in weakly alkaline electrolytes [32], amines and 5,5'-dimethyl hydantoin [24] in strongly alkaline (pH = 9–10) electrolytes [24], saccharin (pH = 13–14) [33], polyethylene glycol, coumarin, piperonal, and vanillin (pH = 14) [34], gelatine in acid electrolytes [35], boric acid, glycerol, mannitol, sorbitol (pH = 1–3) [36, 37], and many others.

It was shown, based on the example of an alkaline solution of the electrolyte with the addition of 5,5'-dimethyl hydantoin, that the increased content of nickel in an electrolyte solution increases its atomic fraction in the coating. However, at the same time, the current efficiency of the electrodeposition of the alloy significantly decreases. It probably occurs due to the acceleration of a side process, e.g. hydrogen evolution. An increasing of cathodic current density also has a similar influence. The influence of temperature is ambiguous. Indeed, the dependence of nickel content in the coating on the temperature has an extreme character, as an increase in temperature contributed to the rise of the current efficiency of the target process. It was assumed that it was generated by cathodic depolarisation and the increase in overpotential of the hydrogen evolution. Most likely an increased stirring rate of the electrolyte accelerates the diffusion-controlled formation of

zinc hydroxide, thus increasing the rate of zinc deposition and, as a result, reducing the nickel content in the coating. This, in its turn, increases the current efficiency due to the reduction of the contribution of the hydrogen evolution reaction to the overall rate of the cathodic process [24, 31, 38, 40–42].

The above-mentioned factors can considerably influence the morphology of the deposited coatings. For example, an increased content of nickel in the electrolyte leads to a rougher and more inhomogeneous surface [24].

An advantage of acid electrolytes is the slightly greater content of nickel in the deposited alloy, which improves the anticorrosive characteristics of the coatings. On the other hand, the coatings synthesised from alkaline electrolytes can have a more compact morphology of the surface due to the slower electrodeposition and reduced rate of the side process of hydrogen evolution. However, in most cases acid electrolytes are more available and environmentally-friendly [43]. Among acid solutions, an ammonium chloride deposition electrolyte is the most optimal from the point of view of its environmental safety, cheap and available components, easy production, ability to use at room temperature, and chemical and phase compositions of the synthesised Zn-Ni coatings. Polyligand ammonia-chloride-glycinate solutions with  $\text{pH} < 7$  are promising electrolytes for the deposition of alloys of the Zn-Ni system [4, 11, 14]. The addition of an aminoacetic acid improves the morphology of the coatings, reducing the rate of the hydrogen evolution reaction, thus increasing the current efficiency of the electrodeposition.

### 1.1. Kinetics of cathodic deposition of zinc, nickel, and zinc-nickel alloys

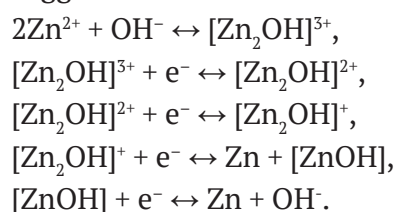
According to multiple studies, the kinetics of the cathodic reduction of zinc depends heavily on the electrolyte composition. Indeed, as for simple electrolytes (sulphate, chloride, and cyanide) without any additives, the process of electrodeposition is mainly determined by concentration polarisation, while adsorption processes become more important when organic substances are added to the electrolyte [44, 45].

In [46] it is shown that the limiting stage of the process changes over time in an ammonium chloride electrolyte. The analysis of deposition

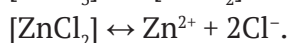
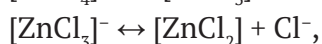
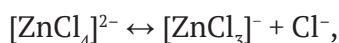
in the Cottrell coordinates criterion for diffusion control  $i-t^{-1/2}$ , shows that at the beginning the curves are not extrapolated to the origin of the coordinates. This is most likely indicative of a certain kinetic stage at the interphase boundary, for instance, a heterogeneous chemical reaction. This reaction may be due to the adsorption of discharging hydrated zinc or zinc hydroxide ions. The likelihood of this process increases with the time of electrodeposition as the pH of the near-electrode layer rises.

With an increase in the duration of the process, the dependence  $i-t^{-1/2}$  is extrapolated to the origin of the coordinates, which is indicative of the establishment of the diffusion control over the process of zinc electroreduction. At the same time, the calculated value of the diffusion coefficient shows that the process of diffusion mass transfer of discharging particles probably occurs in the solid phase, particularly in the film which forms on the electrode surface from the adsorbed and discharging particles. The reaction order for zinc is close to one with a potential of  $-1.05$  V and equals 1.5 with a potential of  $-1.1$  V. This indicates the accelerated electroreduction of zinc with the shift of the deposition potential towards the negative region. Over time, a new heterogeneous process takes place – crystallisation with the formation of two-dimensional nuclei. It is proved by the linearization of chronoamperograms in the criteria coordinates  $\lg(i/t) - t^2$  [46].

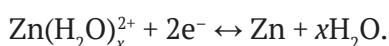
According to [47], electrochemical stages in the cathodic process of zinc deposition with  $\text{pH} > 2$  were preceded by a quick chemical reaction of the formation of a binuclear zinc hydroxocomplex. Therefore, the following mechanism for the electrochemical process was suggested:



At the same time, the reduction of zinc in chloride electrolytes is preceded by the dissociation reaction of an instable complex  $[\text{ZnCl}_4]^{2-}$ :



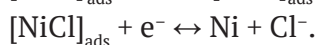
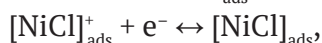
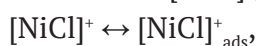
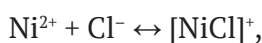
The discharge of zinc ions in this case occurs from the hydrated ions [47,48]:



Nucleation during the electrodeposition of zinc from sulphate solutions occurs instantly with pH ~ 2. When the pH of the solution increases up to 4, continuous nucleation begins prevailing over instantaneous nucleation. Presumably, this is related to the acceleration of the formation of the adsorbed particle  $\text{ZnOH}_{(\text{ads})}$  which blocks the active deposition centres on the substrate surface [49].

It was established [50] that 3D zinc nucleation is typical for the chloride electrolyte. Nucleation occurs continuously with low concentrations of  $\text{ZnCl}_2$  (from 0.01 to 0.1 M) and instantly when the salt concentration increases up to 0.6 M. Zinc is mainly found in the complex form  $[\text{ZnCl}_4]^{2-}$ .

During the electrodeposition of nickel, the reaction of hydrogen evolution contributes more to the overall rate of the cathodic process as compared to zinc [51]. According to the distribution diagram [52], nickel is mainly in the form of  $[\text{NiCl}]^+$  in chloride electrolytes, therefore, the presumable mechanism of the cathodic nickel deposition can be presented in the following way [51, 52]:



In this case, under conditions of a small overpotential, the penultimate charge transfer reaction is presumably considered to be limiting, while the diffusion of nickel ions towards the electrode surface becomes the limiting stage in case of a further shift of the deposition potential towards the negative region [51, 52].

Linear sweep voltammetry is widely used to establish the principal patterns of electrodeposition for the film alloys of the zinc-nickel system. The analysis of the dependence of the cathode current density at the peak of a voltammogram on the square root of the scan rate proves that the stage of diffusion mass transfer

is at least one of the limiting stages [50, 53–60]. The maximum peak potential on cathodic voltammograms shifts with the increase of the scan rate and linearly depends on the scan rate logarithm. Therefore, the charge transfer stage irreversibly continues.

Peak current ( $i_p$ ) also rises with the increase of the potential scan rate in proportion to  $V^{1/2}$  in the presence of amino acids in the deposition electrolyte [62–64], which is typical for reversible processes controlled both by diffusion and the charge transfer stage. At the same time, the values of the Semerano  $X_c$  criterion for the solutions with glycine, alanine, and serine are 0.35, 0.35, and 0.38 respectively, which is indicative of the irreversibility of the process of reduction of nickel ions in these solutions [62, 65]. The control of the process by the charge transfer stage is proved by the shift of the peak potential in the studied electrolytes towards negative values with the increase of the potential scan rate and its linear dependence on  $\lg V$ . It is interesting that the  $i_p - V^{1/2}$  dependencies are not extrapolated to zero, which indicates the contribution of the side reaction of hydrogen evolution to the process of nickel deposition [62]. Linear dependence  $i_p$  from the square root of the rotation rate of the disc electrode  $w^{1/2}$  in the studied solutions in the range of values of  $w$  from 2 to 17 rps is indicative of the presence of diffusion limitations. With the rotation rates of the disk electrode  $w = 17 \div 25$  rps, current is essentially independent of the rotation rate of the electrode, which shows that the process already occurs in the kinetic mode [62, 65]. The values of the concentration criterion Semerano  $X_c < 1$ , in their turn, indicate the presence of adsorption complications in the process. Thus, based on the above-mentioned analysis we can assume that the process of the reduction of nickel ions from the solutions with glycine, alanine, and serine is irreversible and occurs in the mixed kinetics mode complicated by adsorption [62]. Similar patterns are also valid for succinate and asparaginate nickelling electrolytes [66].

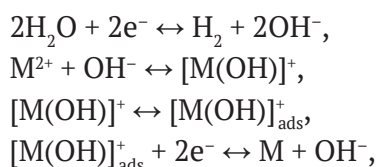
The nucleation mechanism during the deposition of a zinc-nickel alloy is studied using chronoamperometry. Thus, the analysis of chronoamperograms of the electrodeposition of Zn-Ni alloy from an acid sulphate deposition electrolyte without additives showed that nucleation occurs in a

continuous mode of activation of potential nucleation centres [67]. The addition of an aminoacetic acid to a sulphate nickelling solution accelerates the cathodic electrodeposition of nickel [68], and in this case, the nucleation stage proceeds according to the mechanism of instantaneous nucleation [69]. As for an acid sulphate nickel plating electrolyte with the addition of boric acid, saccharin, and coumarin [70], electrodeposition proceeds in mixed diffusion-kinetic mode, and the activation of potential 3D nucleation centres also occurs instantly.

To take into account the contribution of the hydrogen evolution reaction to the total value of cathode current in [69], authors used an approach which allows obtaining partial curves of nickel deposition and hydrogen evolution using non-linear approximation [53]. It was established that the contribution of the hydrogen reaction to the total rate of the cathodic process increased from 2 % with a potential of  $-1.23$  V to 18 % with a potential of  $-1.43$  V (SCE), which naturally reduces the current efficiency of nickel electrodeposition [69].

In an acid chloride deposition electrolyte containing the product of condensation of vanillin and hexamine (VH) crystallisation is controlled by diffusion: cathodic current reaches its maximum ( $I_{\max}$ ) at  $t = t_{\max}$ , then a smooth decrease of current was observed. To determine the kinetics of the process, the obtained current transients were plotted in the coordinates  $(I/I_{\max})^2 - (t/t_{\max})$  and compared to the theoretical curves calculated using the Scharifker-Hills model for instantaneous and continuous 3D nucleation [53].

According to the commonly acknowledged method of electrode deposition of iron sub-group metals [71, 72], the cathodic process in such systems occurs in the following way:



where  $\text{M} = \text{Fe}, \text{Co}, \text{Ni}$ . Obviously, the electrodeposition mechanism greatly depends on the stability of the  $[\text{M}(\text{OH})]_{\text{ads}}^+$  and  $[\text{M}(\text{OH})]^+$  particles. As for the zinc-nickel system, the  $[\text{Ni}(\text{OH})]^+$  complex has greater thermodynamic stability than  $[\text{Zn}(\text{OH})]^+$  [71]. The  $[\text{Ni}(\text{OH})]^+$  concentration near

the cathodes remains approximately constant, although the cathode process is complicated by the parallel hydrogen evolution, therefore the currents on the theoretical curves must have higher values. Nevertheless, if the activation of 3D nucleation centres proceeds instantly in the absence of the VH additive along the entire length of the curve, then in the presence of the additive (but only with more positive deposition potentials) the initial sections of the curves correspond more to the mechanism of continuous nucleation. However, with greater periods of time there are almost no differences between the two solutions.

A similar kinetic situation is observed in acid sulphate electrolytes for the deposition of alloys of the zinc-nickel system with and without the addition of the condensation product of vanillin and serine (VS). The adding of an organic additive results in a change in the mechanism of 3D nucleation from instant to continuous, and it occurs in the entire range of deposition potentials [73].

In [74] it was established that instantaneous 3D nucleation is also typical for chloride-citrate electrolytes for the deposition of Zn-Ni alloys regardless of the deposition potential, temperature, or pH of the solution. However, if the solution is enriched with nickel ( $[\text{Ni}^{2+}]/[\text{Zn}^{2+}] = 4$ ), the nucleation mechanism is characterised by the continuous activation of nucleation centres. The effect is accounted for by the fact that citrate ions block some part of the active centres of the cathode surface, which are available for the reduction of  $\text{Ni}^{2+}$  ions, and at the same time inhibit the hydrogen evolution [74,75].

### 1.2. The corrosion resistance of zinc-nickel alloys

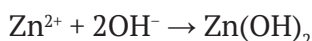
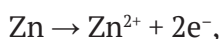
Zn-Ni coatings with a composition of 10-18 at. % Ni ensure optimal corrosion protection as compared to cadmium and its alloys as well as pure zinc [76–78]. In [9, 78, 79] it was established that the phase composition considerably influences the corrosion resistance of coatings in addition to the chemical composition and surface morphology. The  $\gamma$ -phase of  $\text{Ni}_5\text{Zn}_{21}$  has the greatest corrosion resistance, and the enrichment of the surface layer with nickel has an additional influence on the corrosion process. This layer probably stabilises zinc hydroxide  $\text{Zn}(\text{OH})_2$  on the surface of the alloy as the main product of corrosion, which prevents further alloy dissolution, providing a barrier effect that is more effective than that of zinc oxide ZnO



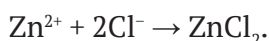
[9, 79]. The high corrosion resistance of these coatings correlates to the homogeneous surface morphology. Indeed, the presence of cracks, grooves, and structural inhomogeneities has a negative effect on the corrosion resistance of the alloys [9].

Electrochemical corrosion of a zinc-nickel alloy coating in aqueous chloride solutions can proceed in accordance with the following mechanism [80]:

- Anodic dissolution of zinc:

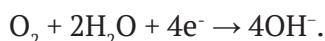


and/or:

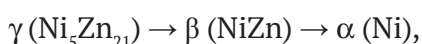


The formation of other products of zinc and, less likely, nickel oxidation is also possible [79]. As for the initial stage of the dissolution of Zn-Ni coatings in chloride solutions, the main products are simonkolleite  $\text{Zn}_5(\text{OH})_8\text{Cl}_2 \cdot \text{H}_2\text{O}$ , zinc oxide ZnO and hydrozincite  $\text{Zn}_5(\text{CO}_3)_2(\text{OH})_6$  [81].

- Cathodic process, reduction of molecular oxygen present in the electrolyte solution:



In addition, the corrosion process is often complicated by the phase transformation



resulting from a gradual change in the chemical composition of the alloy during the dissolution in accordance with the phase diagram of the Zn-Ni system [82].

Corrosion of the Zn-Ni alloy often leads to significant morphological changes in the surface of the alloy coating: a large number of cracks are formed on its surface during the dissolution. The process occurs mainly selectively, as dezincification of the surface is observed, and the surface is also covered with sparingly soluble products of the corrosion process [82].

The analysis of the transients of the corrosion potential of zinc-nickel coatings with various compositions, as compared to similar data obtained with iron and zinc, showed that Zn-Ni-coatings with a nickel content less than 18 at. % remain sacrificial in relation to the protected metal and are characterised by a higher corrosion potential as compared to pure zinc [17,

83]. If the corrosion potential of zinc remains relatively constant, practically not changing over time, the corrosion potential of any Zn-Ni coating gradually increases and stabilises. Primarily, this can be related to the partial dezincification of the surface of zinc-nickel alloys, which leads to the increased surface concentration of a more electropositive component, nickel. The increased concentration of nickel in the coatings during its dezincification leads to a shift in the corrosion potential towards the positive region. A similar dependence is also usually observed for the corrosion rate  $i_{\text{corr}}$ : the increased concentration of nickel in the alloy contributes to a decrease in the value  $i_{\text{corr}}$  [84–87].

The introduction of the complexing agent  $\text{NH}_4\text{Cl}$  into the chloride deposition electrolyte significantly reduces the current density of the corrosion in case of the dissolution of the zinc-nickel coating [88]. This may be related to an improvement in the morphology of the coatings due to the complexation of metal ions, a decrease in their deposition rates, and the formation of fine-crystalline dense coatings.

In [89] authors studied the influence of the temperature (from 25 to 70 °C) on the electrodeposition and effectiveness of corrosion resistance of zinc-nickel coatings synthesised from an ammonia-chloride electrolyte, and it showed that the best morphology and the lowest corrosion current density is typical for the coating obtained at 25 °C.

Fine-grained nanocrystalline zinc-nickel coatings with an increased corrosion resistance can also be obtained by deposition from an alkaline electrolyte with the addition of 2,2-bipyridine and 5,5'-dimethylhydantoin [90].

### 1.3. Selective dissolution of zinc-nickel alloys

Under specific conditions, selective dissolution is typical for the electrodeposited zinc-nickel alloys, that is the oxidation of the electronegative component, zinc, with further enrichment of the surface layer with an electropositive component, nickel, which is usually accompanied by the development of the surface [91–93].

A region of low currents which is practically independent of potential is observed on the anodic polarisation curves obtained on zinc and zinc-nickel coatings in sulphate, chloride, and carbonate solutions. A sharp increase in the

current density is observed when reaching the critical potential of the selective dissolution of the alloy  $E_{cr}$ . Determination of the composition of the solution after selective dissolution allows determining the selectivity factor ( $SF$ ) characterising the process:

$$SF = \frac{n_{Zn}^{2+} \cdot n_{Ni}}{n_{Ni}^{2+} \cdot n_{Zn}}$$

Here  $n_{Ni}^{2+}$  and  $n_{Zn}^{2+}$  are the total amount of nickel and zinc in the solution after selective dissolution, while  $n_{Ni}$  and  $n_{Zn}$  are the total amount of nickel and zinc in the alloy. The highest selectivity factor is observed in the alloy  $(NH_4)_2SO_4$  ( $SF = 74.3 \div 77.1$ ), and the lowest in the alloy  $NaHCO_3$  ( $SF = 3.54 \div 5.24$ ), while the NaCl solution is characterised by an intermediate value  $SF = 19.1 \div 31.2$  [92].

A study of the selective dissolution of the alloys of the Zn-Ni system in a chloride solution, particularly at increased temperatures, conducted in [94], showed that the anodic process has three stages. Active dissolution of the alloy begins at a potential of  $\approx -1.2$  V (SCE) and is accompanied by the formation of a layer of corrosion products, mainly zincates, on the alloy surface:



The dissolution of the alloy slows down in a potential region that is more positive than  $-0.9$  V (SCE), and zinc oxide ZnO and zinc hydroxide  $Zn(OH)_2$ , as well as, less likely,  $NiCl_2$  and/or  $NiClOH_{(ads)}$  are formed. Thus, a porous passivating layer, which includes a number of different corrosion products, is formed on the surface of the alloy. According to previous studies [12, 94, 95], the presence of nickel stabilises the  $Zn(OH)_2$  layer on the surface which can inhibit the adsorption of  $Cl^-$  more effectively as compared to ZnO. As a result, the likelihood of pitting decreases, which significantly increases the corrosion resistance of the coating in chloride environments [94].

Surface chemical and morphological modifications of electrodeposited and chromium(III)-passivated monophasic zinc-nickel coatings induced by selective dissolution and corrosion in chloride solutions are demonstrated in [96]. The passivated samples showed slower anodic dissolution, less significant de-alloying, smaller surface dezincification and lower coating cracking.

The selective dissolution (SD) of Zn-Ni alloys is used to obtain nanoporous nickel, which is a catalyst for various reactions, for example, oxidation of CO or methanol or a reduction of hydrogen or oxygen [97–100]. Thus, in [97], using selective dissolution of a heterophase zinc-nickel alloy consisting of NiZn and  $NiZn_3$ , they obtained finely dispersed nickel with the size of particles in the surface phase being 40–60 nm in a 2 M solution of NaOH.

In addition to the selective dissolution of zinc-nickel alloys, mostly in alkali solutions [101], other methods are also used to synthesise nanoporous nickel, for example, cathodic treatment of the nickel surface in a saturated solution  $ZnCl_2 - NaCl$  [102]; selective dissolution of pyrometallurgical alloys of the  $Ni_{30}Mn_{70}$  type in an ammonium sulphate solution [103]; SD of the alloys similar to  $Mg_{90-x}Ni_xY_{10}$  ( $x = 10, 15, 20, 25$  at. %) in citric acid [104], SD of the alloys of the Cu-Ni system in acid solutions [105], the SD of the alloys of the Ni-Al system alkaline solutions [98], etc.

According to previous studies [104, 106], the SD of binary alloys (including the zinc-nickel system) has 4 stages:

1. Quick dissolution of a more electronegative component.
2. Regrouping of the atoms of more electro-positive components into clusters.
3. Fusion and growth of neighbouring clusters of the electropositive component with the formation of ligaments between clusters.
4. Enlargement of ligaments between clusters.

The cyclic voltammogram of a smooth nickel electrode and zinc-nickel alloy after alkaline treatment (practically nanoporous nickel) shows the presence of anodic peaks at 0.38 V for a smooth nickel surface and at 0.49 V for a nanoporous nickel surface [107]. In this case, the average values of the current density on the dezincified surface are significantly greater than the corresponding values for smooth nickel. It is related to a change in morphology, and, therefore, a more developed surface of nanoporous nickel can be successfully used in sorption, catalysis, and electrocatalysis processes [107, 108].

Anodic oxidation of methanol in an alkaline solution with nanoporous nickel proceeds almost 12 times faster than with smooth nickel. This indicates the significant effectiveness of the use

of nanoporous nickel in the process of methanol oxidation, for example, in fuel cells based on this process.

Cathodic processes in an alkaline solution on nanoporous nickel obtained by the selective dissolution of Zn-Ni alloys are also more effective as compared to smooth nickel. Thus, nanoporous nickel has greater electrocatalytic activity in the hydrogen evolution reaction [108], which can be used in the industry to intensify the process of hydrogen production [107–111].

## 2. Conclusions

Zinc-nickel alloy coatings with a nickel content of 18 at. % have optimal corrosion resistance and mechanical characteristics among binary zinc-based alloys, which makes them a promising material for the corrosion protection of various types of steel. The  $\gamma$ -phase, which can be described by different formulas ( $\text{NiZn}_3$ ,  $\text{Ni}_2\text{Zn}_{11}$ ,  $\text{Ni}_3\text{Zn}_{10}$ ,  $\text{Ni}_4\text{Zn}_{22}$ ,  $\text{Ni}_5\text{Zn}_{21}$ ), forms the basis of most corrosion-resistant zinc-nickel alloys. In addition to the corrosion protection of various types of steel, zinc-nickel alloys can be used as the initial material for the electrochemical synthesis of porous (as well as nanoporous) nickel, which is a promising electrocatalyst for various processes, using the method of the selective dissolution. The key feature of the synthesis of alloys of the Zn-Ni system is the anomalous nature of codeposition of components, during which the prevailing reduction of a more electronegative component, zinc, occurs at the cathode. Electrodeposition of zinc-nickel alloys is conducted from various acid and alkaline electrolytes. The use of additives allows regulating certain properties of the coatings, such as chemical and/or phase composition, morphology, and anticorrosive characteristics. Aminoacetic acid (glycine) is a promising organic additive to acid (chloride, ammonia, and sulphate) electrolytes for the deposition of alloys of the Zn-Ni system. At the same time, according to previous studies, the influence of the addition of glycine is not clear as the current efficiency of the target process of the deposition of alloys can either increase or decrease depending on the composition of the solution and other conditions. Also, there are practically no data on the influence of glycine on the kinetics of zinc and nickel reduction and the mechanism of their nucleation. Therefore, it is important to

conduct studies aimed at the establishment of the kinetics of electrodeposition of zinc-nickel alloy coatings, assessment of the effectiveness of their corrosion resistance, as well as study the patterns of selective dissolution of alloys in order to obtain nanoporous nickel electrocatalysts.

## Conflict of interests

The authors declare that they have no known competing financial interests or personal relationships that could have influenced the work reported in this paper.

## References

1. Anwar S., Khan F., Zhang Y., Caines S. Optimization of zinc-nickel film electrodeposition for better corrosion resistant characteristics. *The Canadian Journal of Chemical Engineering*. 2019;97(9): 2426–2439. <https://doi.org/10.1002/cjce.23521>
2. Fedi B., Gigandet M. P., Hihn J. Y., Mierzejewski S. Structure determination of electrodeposited zinc-nickel alloys: thermal stability and quantification using XRD and potentiodynamic. *Electrochimica Acta*. 2016;215: 652–666. <https://doi.org/10.1016/j.electacta.2016.08.141>
3. Conde A., Arenas M. A., Damborenea J. J. Electrodeposition of Zn-Ni coatings as Cd replacement for corrosion protection of high strength steel. *Corrosion Science*. 2011;53(4): 1489–1497. <https://doi.org/10.1016/j.corsci.2011.01.021>
4. Maizelis A., Bairachny B. Voltammetric Analysis of phase composition of Zn-Ni alloy thin films electrodeposited from weak alkaline polyligand electrolyte. *Journal of Nano- and Electronic Physics*. 2017;9(5): 7. [https://doi.org/10.21272/jnep.9\(5\).05010](https://doi.org/10.21272/jnep.9(5).05010)
5. Blejan D., Muresan L. M. Corrosion behavior of Zn-Ni- $\text{Al}_2\text{O}_3$  nanocomposite coatings obtained by electrodeposition from alkaline electrolytes. *Materials and Corrosion*. 2013;64(5): 433–438. <https://doi.org/10.1002/maco.201206522>
6. Nash P. *Phase diagrams of binary nickel alloys*. USA: ASM International; 1991. 394 p.
7. Liu X. D. Effect of nickel pre-plating on the plating of Zn-Ni alloy coating on stainless steel substrate. In: *2nd Annual International Conference on Advanced Material Engineering, 15–17 April 2016, Wuhan*. Wuhan, Hubei, China: Southwest University; 2016. p. 410–415. <https://doi.org/10.2991/ame-16.2016.67>
8. Huang K. L. Experiment study of the phase analysis on the Ni-Zn alloys. *Physics Experimentation*. 2010;30: 8–11. Available at: [http://en.cnki.com.cn/Article\\_en/CJFDTotal-WLSL201004004.htm](http://en.cnki.com.cn/Article_en/CJFDTotal-WLSL201004004.htm)
9. Rajagopalan S. K. *Characterization of electrodeposited Zn-Ni alloy coatings as a replacement for electrodeposited Zn and Cd coatings*. Montreal: McGill University; 2012. 221 p.

10. Brooks I. Erb U. Hardness of electrodeposited microcrystalline and nanocrystalline gamma-phase Zn-Ni alloys. *Scripta Mater.* 2001;44(5): 853–858. [https://doi.org/10.1016/S1359-6462\(00\)00680-1](https://doi.org/10.1016/S1359-6462(00)00680-1)
11. Kozaderov O. A., Burlyayev D. V. Elektroosazhdenie tsink-nikelevykh splavov iz glitsin-soderzhashchego ammiachno-khloridnogo elektrolita [Electrodeposition of zinc-nickel alloys from a glycine-containing ammonium chloride electrolyte]. In: *Physico-chemical processes in condensed media and interphase boundaries. 8th All-Russian Conference with international participation Voronezh, Russia, 8–11 October 2018.* Voronezh: Nauchnaya kniga Publ.; 2018. pp. 118–119. Available at: <https://www.elibrary.ru/item.asp?id=36837752> (In Russ.)
12. El-Sayed A.-R., Mohran H. S., Abd El-Lateef H. M. Corrosion study of zinc, nickel, and zinc-nickel alloys in alkaline solutions by tafel plot and impedance techniques. *Metallurgical and Materials Transactions A.* 2012;43(2): 619–632. <https://doi.org/10.1007/s11661-011-0908-4>
13. Conrad H. A., Golden T. D., McGuire M. R., Zhou T., Coskun M. I. Improved corrosion resistant properties of electrochemically deposited zinc-nickel alloys utilizing a borate electrolytic alkaline solution. *Surface & Coatings Technology.* 2015;272: 50–57. <https://doi.org/10.1016/j.surfcoat.2015.04.025>
14. Maizelis A. Voltammetric analysis of phase composition of Zn-Ni alloy thin films electrodeposited under different electrolyze modes. In: *7th International Conference on Nanomaterials: Applications and Properties, 2017, Kharkiv.* Kharkiv: Kharkiv Polytechnic Institute; 2017. p. 1. <https://doi.org/10.1109/NAP.2017.8190373>
15. Nayana O., Venkatesha T. V. Effect of ethyl vanillin on ZnNi alloy electrodeposition and its properties. *Bulletin of Materials Science.* 2014;37(5): 1137–1146. <https://doi.org/10.1007/s12034-014-0054-x>
16. Chouchane S. Microstructural analysis of low Ni content Zn alloy electrodeposited under applied magnetic field. *Surface & Coatings Technology.* 2007;201(14): 6212–6216. <https://doi.org/10.1016/j.surfcoat.2006.11.015>
17. Petrauskas A. Studies of phase composition of Zn-Ni alloy obtained in acetate-chloride electrolyte by using XRD and potentiodynamic stripping. *Electrochimica Acta.* 2005;50(5): 1189–1196. <https://doi.org/10.1016/j.electacta.2004.07.044>
18. Petrauskas A. Influence of  $\text{Co}^{2+}$  and  $\text{Cu}^{2+}$  on the phase composition of Zn-Ni alloy. *Electrochimica Acta.* 2006;51(27): 6135–6139. <https://doi.org/10.1016/j.electacta.2006.01.064>
19. Koura N., Suzuki Y., Idemoto I., Kato T., Matsumoto F. Electrodeposition of Zn-Ni alloy from  $\text{ZnCl}_2$ - $\text{NiCl}_2$ -EMIC and  $\text{ZnCl}_2$ - $\text{NiCl}_2$ -EMIC-EtOH ambient-temperature molten salts. *Surface & Coatings Technology.* 2003;169-170: 120–123. [https://doi.org/10.1016/S0257-8972\(03\)00183-X](https://doi.org/10.1016/S0257-8972(03)00183-X)
20. Lehmberg C. E. Composition and structure of thin electrodeposited zinc-nickel coatings. *Surface & Coatings Technology.* 2005;192(2-3): 269–277. <https://doi.org/10.1016/j.surfcoat.2004.07.109>
21. Aaboubi O. Magneto-hydrodynamic analysis of silver electrocrystallization from a nitric and tartaric solution. *Journal of the Electrochemical Society.* 2004;151(2): 112. <https://doi.org/10.1149/1.1635829>
22. Uhlemann M. Electrochemical deposition of Cu under superimposition of high magnetic fields. *Journal of the Electrochemical Society.* 2004;151(9): 598. <https://doi.org/10.1149/1.1782991>
23. Hajjami A. E. Characterization of thin Zn-Ni alloy coatings electrodeposited on low carbon steel. *Applied Surface Science.* 2007;254(2): 480–489. <https://doi.org/10.1016/j.apsusc.2007.06.016>
24. Feng Z., Li Q., Zhang J., Tang P., Song H., An M. Electrodeposition of nanocrystalline Zn-Ni coatings with single gamma phase from an alkaline bath. *Surface & Coatings Technology.* 2015;270: 47–56. <https://doi.org/10.1016/j.surfcoat.2015.03.020>
25. Shekhanov R. F., Gridchin, S. N., Balmasov A. V. Electrodeposition of zinc-nickel alloys from ammonium oxalate electrolytes. *Russian Journal of Electrochemistry.* 2018;54(4): 355–362. <https://doi.org/10.1134/S1023193518040079>
26. Garcia J. R., Lago D. C. B., Senna L. F. Electrodeposition of cobalt rich Zn-Co alloy coatings from citrate bath. *Materials Research.* 2014;17(4): 947–957. <https://doi.org/10.1590/S1516-14392014005000096>
27. Faid H., Mentar L., Khelladi M. R., Azizi A. Deposition potential effect on surface properties of Zn-Ni coatings. *Surface Engineering.* 2017;33(7): 529–535. <https://doi.org/10.1080/02670844.2017.1287836>
28. Fashu S., Gu C. D., Wang X. L., Tu J. P. Influence of electrodeposition conditions on the microstructure and corrosion resistance of Zn-Ni alloy coatings from a deep eutectic solvent. *Surface & Coatings Technology.* 2014;242: 34–41. <https://doi.org/10.1016/j.surfcoat.2014.01.014>
29. Chernaya E. V., Bobrikova I. G. Zakonomernosti elektroosazhdeniya splava tsink-nikel' v ammiakatnykh elektrolitakh [Regularities of the electrodeposition of zinc-nickel alloy in ammoniacal electrolytes]. *Tekhnicheskije nauki.* 2011;(5): 112. Available at: <https://cyberleninka.ru/article/n/zakonomernosti-elektroosazhdeniya-splava-tsink-nikel-v-ammiakatnyh-elektrolitah> (In Russ.)
30. Nakano H., Arakawa S., Oue S., Kobayashi S. Electrodeposition behavior of Zn-Ni alloys from an alkaline zincate solution containing ethylenediamine. *ISIJ International.* 2013;53(10): 1864–1870. <https://doi.org/10.2355/isijinternational.53.1864>
31. Byk T. V., Gaevskaya T. V., Tsybul'skaya L. S. Effect of electrodeposition conditions on the composition, microstructure, and corrosion resistance of Zn-Ni alloy coatings. *Surface & Coatings Technology.*

- 2008;202(24): 5817–5823. <https://doi.org/10.1016/j.surfcoat.2008.05.058>
32. Conrad H. A., Corbett J. R., Golden T. D. Electrochemical deposition of  $\gamma$ -phase zinc-nickel alloys from alkaline solution. *Journal of the Electrochemical Society*. 2012;159(1): 29–32. <https://doi.org/10.1149/2.027201jes>
33. Mosavat S. H., Bahroloroom M. E., Shariat M. H. Electrodeposition of nanocrystalline Zn–Ni alloy from alkaline glycinate bath containing saccharin as additive. *Applied Surface Science*. 2011;257(20): 8311–8316. <https://doi.org/10.1016/j.apsusc.2011.03.017>
34. Muresan L. M. Zn–Ni alloy coatings from alkaline bath containing triethanolamine. Influence of additives. *Studia Universitatis Babeş-Bolyai Chemia*. 2010;55(1): 37–43. Available at: [https://www.researchgate.net/publication/235654567\\_Zn-Ni\\_alloy\\_coatings\\_from\\_alkaline\\_bath\\_containing\\_triethanolamine\\_influence\\_of\\_additives](https://www.researchgate.net/publication/235654567_Zn-Ni_alloy_coatings_from_alkaline_bath_containing_triethanolamine_influence_of_additives)
35. Soares M. E., Souza C. A. C., Kuri S. E. Corrosion resistance of a Zn–Ni electrodeposited alloy obtained with a controlled electrolyte flow and gelatin additive. *Surface & Coatings Technology*. 2006;201(6): 2953–2959. <https://doi.org/10.1016/j.surfcoat.2006.06.006>
36. Oliveira E. M., Carlos I. A. Chemical, physical and morphological characterization of ZnNi films electrodeposited on 1010 steel substrate from acid baths containing polyalcohol. *Surface & Coatings Technology*. 2011;206(2): 250–256. <https://doi.org/10.1016/j.surfcoat.2011.06.061>
37. Oliveira E. M., Carlos I. A. Study of the effect of mannitol on ZnNi alloy electrodeposition from acid baths and on the morphology, composition, and structure of the deposit. *Journal of Applied Electrochemistry*. 2009;39(10): 1849–1856. <https://doi.org/10.1007/s10800-009-9888-0>
38. Burliaev D. V., Kozaderov O. A., Tinaeva A. E., Tinaeva K. E. Elektroosazhdenie tsink-nikelevykh pokrytii iz glitsin-soderzhashchego ammiachno-khlordnogo elektrolita [Electrodeposition of zinc-nickel coatings from glycine-containing ammonium chloride electrolyte]. *Protection of Metals and Physical Chemistry of Surfaces*. 2020;56(3): 301–308. <https://doi.org/10.31857/S0044185620030079> (In Russ.)
39. Thangaraj V., Chitharanjan Hegde A. Electrodeposition and compositional behaviour of Zn–Ni alloy. *Indian Journal of Chemical Technology*. 2007;14(3): 246–252. Available at: <http://nopr.niscair.res.in/handle/123456789/1116>
40. Bajat J. B. Protective properties of epoxy coatings electrodeposited on steel electrochemically modified by Zn–Ni alloys. *Progress in Organic Coating*. 2004;49(3): 183–196. <https://doi.org/10.1016/j.porgcoat.2003.09.019>
41. Li G. Y. Investigation of nanocrystalline zinc–nickel alloy coatings in an alkaline zincate bath. *Surface & Coatings Technology*. 2005;191(1): 59–67. <https://doi.org/10.1016/j.surfcoat.2004.04.062>
42. Ghaziof S. Electrodeposition of single gamma phased Zn–Ni alloy coatings from additive-free acidic bath. *Applied Surface Science*. 2014;311(30): 635–642. <https://doi.org/10.1016/j.apsusc.2014.05.127>
43. Lotfi N., Aliofkhaezai M., Rahmani H., Barati Darband Gh. Zinc–nickel alloy electrodeposition: characterization, properties, multilayers and composites. *Protection of Metals and Physical Chemistry of Surfaces*. 2018;54: 1102–1140. Available at: [https://www.researchgate.net/publication/329246287\\_Zinc-Nickel\\_Alloy\\_Electrodeposition\\_Characterization\\_Properties\\_Multilayers\\_and\\_Composites](https://www.researchgate.net/publication/329246287_Zinc-Nickel_Alloy_Electrodeposition_Characterization_Properties_Multilayers_and_Composites)
44. Grilikhes S. Ya., Tikhonov K. I. *Elektroliticheskie i khimicheskie pokrytiya. Teoriya i praktika* [Electrolytic and chemical coatings. Theory and practice.]. Leningrad: Khimiya Publ.; 1990. pp. 113–125. (In Russ.)
45. Minin I. V., Solovyeva N. D. Kinetics of zinc electroreduction from the sulfate electrolyte in the presence of surfactant additives. *Vestnik Saratovskogo gosudarstvennogo tekhnicheskogo universiteta*. 2013;69(1): 57–62. Available at: <https://cyberleninka.ru/article/n/kinetika-elektrovsstanovleniya-tsinka-iz-sulfatnogo-elektrolita-v-prisutstvii-dobavok-pav> (In Russ.)
46. Pchelintseva Yu. V. *Kineticheskie zakonomernosti elektroosazhdeniya tsinka iz khlorammoniinogo elektrolita* [Kinetic regularities of zinc electrodeposition from chlorammonium electrolyte]. Abstract of thesis Cand. Chem. Sci. Saratovskii gosudarstvennyi tekhnicheskii universitet; 2004. 20 p. (In Russ.)
47. Berezin N. B., Berezina T. N., Mezhevich Zh. V. Kinetika i mekhanizm vosstanovleniya kompleksov tsinka [Kinetics and mechanism of recovery of zinc complexes]. *Vestnik Kazanskogo tekhnologicheskogo universiteta*. 2014;17(23): 374–379. Available at: <https://cyberleninka.ru/article/n/kinetika-i-mekhanizm-vosstanovleniya-kompleksov-tsinka> (In Russ.)
48. Proskurkin E. V., Popovich V. A., Moroz A. T. *Tsinkovanie: Spravochnik / pod red. E. V. Proskurkina* [Zinc plating: A Handbook, E. V. Proskurkina (ed.)]. Moscow: Metallurgiya Publ.; 1988. 528 p. (In Russ.)
49. Raeissi K., Saatchi A., Golozar M. A. Nucleation and growth of zinc electrodeposited onto electropolished and mechanically polished steel surfaces. *Transactions of the IMF*. 2003;81(6): 186–189. <https://doi.org/10.1080/00202967.2003.11871537>
50. Trejo G., Ortega R., Meas Y. Nucleation and growth of zinc from chloride concentrated solutions. *Journal of the Electrochemical Society*. 1998;145(12): 4090–4097. <https://doi.org/10.1149/1.1838919>
51. Orinakova R., Streckova M. Comparison of chloride and sulphate electrolytes in nickel electrodeposition on a paraffin impregnated graphite electrode. *Journal of Electroanalytical Chemistry*. 2006;549(2): 152–159. <https://doi.org/10.1016/j.jelechem.2006.05.031>

52. Orinakova R., Turonova A., Kladenkova D., Galova M. Recent developments in the electrodeposition of nickel and some nickel-based alloys. *Journal of Applied Electrochemistry*. 2006;36: 957–972. <https://doi.org/10.1007/s10800-006-9162-7>
53. Palomar-Pardave M., Scharifker B. R., Arce E. M., Romero-Romo M. Nucleation and diffusion-controlled growth of electroactive centers. Reduction of protons during cobalt electrodeposition. *Electrochimica Acta*. 2005;50(24): 4736–4745. <https://doi.org/10.1016/j.electacta.2005.03.004>
54. Hosseini M. G. Electrochemical studies of Zn–Ni alloy coatings from non-cyanide alkaline bath containing tartrate as complexing agent. *Surface & Coatings Technology*. 2008;202(13): 2897–2904. <https://doi.org/10.1016/j.surfcoat.2007.10.022>
55. Elkhatabi F. Chemical and phase compositions of zinc + nickel alloys determined by stripping techniques. *Journal of Electroanalytical Chemistry*. 1996;404(1): 45–53. [https://doi.org/10.1016/0022-0728\(95\)04359-4](https://doi.org/10.1016/0022-0728(95)04359-4)
56. Elkhatabi F. Dependence of coating characteristics on deposition potential for electrodeposited Zn–Ni alloys. *Electrochimica Acta*. 1999;44(10): 1645–1653. [https://doi.org/10.1016/S0013-4686\(98\)00286-2](https://doi.org/10.1016/S0013-4686(98)00286-2)
57. Abou-Krishna M. M. Electrochemical studies of zinc–nickel codeposition in sulphate bath. *Applied Surface Science*. 2005;252(4): 1035–1048. <https://doi.org/10.1016/j.apsusc.2005.01.161>
58. Abou-Krishna M. M., Rageh H. M., Matter E. A. Electrochemical studies on the electrodeposited Zn–Ni–Co ternary alloy in different media. *Surface and Coatings Technology*. 2008;202(15): 3739–3746. <https://doi.org/10.1016/j.surfcoat.2008.01.015>
59. Hegde A. C., Venkatakrishna K., Eliaz N. Electrodeposition of Zn–Ni, Zn–Fe and Zn–Ni–Fe alloys. *Surface and Coatings Technology*. 2010;205(7): 2031–2041. <https://doi.org/10.1016/j.surfcoat.2010.08.102>
60. Tozar A., Karahan I. H., Structural and corrosion protection properties of electrochemically deposited nano-sized Zn–Ni alloy coatings. *Applied Surface Science*. 2014;318: 15–23. <https://doi.org/10.1016/j.apsusc.2013.12.020>
61. Damaskin B. B. *Elektrokhimiya: uchebnik dlya vuzov* [Electrochemistry: a textbook for universities]. Moscow: Khimiya Publ.; 2001. 624 p. (In Russ.)
62. Saponova L. V., Sotskaya N. V., Dolgikh O. V. Kinetika elektroosazhdeniya nikelya iz kompleksnykh elektrolitov, sodержashchikh aminokisloty [Kinetics of nickel electrodeposition from complex electrolytes containing amino acids]. *Kondensirovannye sredy i mezhfaznye granitsy = Condensed Matter and Interphases*. 2013;15(4): 446–452. Available at: <https://journals.vsu.ru/kcmf/article/download/933/1015> (In Russ.)
63. Sotskaya N. V., Dolgikh O. V. Nickel electroplating from glycine containing baths with different pH. *Protection of Metals*. 2008;44(5): 479–486. <https://doi.org/10.1134/s0033173208050123>
64. Dolgikh O. V., Sotskaya N. V., Duyen Vu Thi, Kotlyarova E. A., Agapov B. L. Electroplating of catalytically active nickel coatings from baths of various anionic compositions. *Protection of Metals and Physical Chemistry of Surfaces*. 2009;45(6): 718–723. <https://doi.org/10.1134/s2070205109060148>
65. Bard A. J. *Electrochemical Methods: Fundamentals and Applications*. NY: John Wiley & Sons. Inc.; 2001. 833 p.
66. Dolgikh O. V., Sotskaya N. V., Saponova L. V. Kinetika elektroosazhdeniya nikelya iz asparaginatnykh i suktsinatnykh elektrolitov [Kinetics of nickel electrodeposition from aspartate and succinate electrolytes]. *Kondensirovannye sredy i mezhfaznye granitsy = Condensed Matter and Interphases*. 2012;14(2): 175–181. Available at: [http://www.kcmf.vsu.ru/resources/t\\_14\\_2\\_2012\\_006.pdf](http://www.kcmf.vsu.ru/resources/t_14_2_2012_006.pdf) (In Russ.)
67. Ghaziof S., Kilmartin P. A., Gao W. Electrochemical studies of sol-enhanced Zn–Ni–Al<sub>2</sub>O<sub>3</sub> composite and Zn–Ni alloy coatings. *Journal of Electroanalytical Chemistry*. 2015;755: 63–70. <https://doi.org/10.1016/j.jelechem.2015.07.041>
68. Ibrahim M. A. M., Al Radadi R. M. Role of glycine as a complexing agent in nickel electrodeposition from acidic sulphate bath. *International Journal of Electrochemical Science*. 2015;10(6): 4946–4971. Available at: <http://www.electrochemsci.org/papers/vol10/100604946.pdf>
69. Saponova L. V., Sotskaya N. V., Dolgikh O. V., Zorina A. V., Kushan E. V. Kinetika elektrokristallizatsii nikelya iz gliksinsoderzhashchikh elektrolitov [Kinetics of nickel electrocrystallization from glycine-containing electrolytes]. *Proceedings of Voronezh State University. Series: Chemistry. Biology. Pharmacy*. 2012;(2): 87–91. Available at: <http://www.vestnik.vsu.ru/pdf/chembio/2012/02/2012-02-13.pdf> (In Russ.)
70. Torabi M., Dolati A. A kinetic study on the electrodeposition of nickel nanostructure and its electrocatalytic activity for hydrogen evolution reaction. *Journal of Applied Electrochemistry*. 2010;40: 1941–1947. <https://doi.org/10.1007/s10800-010-0170-2>
71. Basavanna S., Naik Y. A. Electrochemical studies of Zn–Ni alloy coatings from acid chloride bath. *Journal of Applied Electrochemistry*. 2009;39: 1975–1982. <https://doi.org/10.1007/s10800-009-9907-1>
72. Tsay P., Hu C. C. Non-anomalous codeposition of iron–nickel alloys using pulse–reverse electroplating through means of experimental strategies. *Journal of the Electrochemical Society*. 2002;149(10): 492–497. <https://doi.org/10.1149/1.1504718>
73. Basavanna S., Naik Y. A. Study of the effect of new brightener on Zn–Ni alloy electrodeposition from acid sulphate bath. *Journal of Applied Electrochemistry*. 2011;41(5): 535–541. <https://doi.org/10.1007/s10800-011-0263-6>

74. Asseli R., Benaicha M., Derbal S., Allam M., Dilmi O. Electrochemical nucleation and growth of Zn-Ni alloys from chloride citrate-based electrolyte. *Journal of Electroanalytical Chemistry*. 2019;847: 1–10. <https://doi.org/10.1016/j.jelechem.2019.113261>
75. Li C., Li X., Wang Z., Guo H. Mechanism of nanocrystalline nickel electrodeposition from novel citrate bath. *Rare Metal Materials and Engineering*. 2015;44(7): 1561–1567. [https://doi.org/10.1016/S1875-5372\(15\)30093-X](https://doi.org/10.1016/S1875-5372(15)30093-X)
76. Díaz-Morales O., Mostany J., Borrás C., Scharifker B. R. Current transient study of the kinetics of nucleation and diffusion-controlled growth of bimetallic phases. *Journal of Solid State Electrochemistry*. 2013;17: 345–351. <https://doi.org/10.1007/s10008-012-1881-6>
77. Pochkina S. Yu. *Elektroosazhdenie splavov tsinka s nikel'm i kobal'tom s povyshennymi antikorroziionnymi svoystvami iz sul'fatno-glitsinatnykh elektrolitov* [Electrodeposition of zinc-nickel and cobalt alloys with enhanced anti-corrosion properties from sulfate-glycinate electrolytes] Abstract of thesis Cand. Chem. Sci. Saratov State Technical University; 2020. 20 p. (In Russ.)
78. Selvaraju V., Thangaraj V. Influence of  $\gamma$ -phase on corrosion resistance of Zn-Ni alloy electrodeposition from acetate electrolytic bath. *Materials Research Express*. 2018;5(5): 1–14. <https://doi.org/10.1088/2053-1591/aabe64>
79. Tian W. Study on corrosion resistance of electroplating zinc-nickel alloy coatings. *Surface and Interface Analysis*. 2009;41(3): 251–254. <https://doi.org/10.1002/sia.3017>
80. Abd El-Lateef H. M. Role of Ni content in improvement of corrosion resistance of Zn-Ni alloy in 3.5% NaCl solution. Part I: Polarization and impedance studies. *Transactions of Nonferrous Metals Society of China*. 2015;25(8): 2807–2816. [https://doi.org/10.1016/S1003-6326\(15\)63906-1](https://doi.org/10.1016/S1003-6326(15)63906-1)
81. Feng Z., Ren L., Zhang J., Yang P. Effect of additives on corrosion mechanism of nanocrystalline zinc-nickel alloys in an alkaline bath. *RSC Advances*. 2016;6(91): 1–47. <https://doi.org/10.1039/C6RA18476F>
82. Gavrila M. Corrosion behavior of zinc-nickel coatings, electrodeposited on steel. *Surface & Coatings Technology*. 2000;123(2-3): 164–172. [https://doi.org/10.1016/S0257-8972\(99\)00455-7](https://doi.org/10.1016/S0257-8972(99)00455-7)
83. Soleimangoli F., Hosseini S. A., Davoodi A., Mokhtari A., Alishahi M. Effect of  $\text{NH}_4\text{Cl}$  on the microstructure, wettability and corrosion behavior of electrodeposited Ni-Zn coatings with hierarchical nano/microstructure. *Surface & Coatings Technology*. 2020;394: 1–9. <https://doi.org/10.1016/j.surfcoat.2020.125825>
84. Baldwin K. R. The corrosion resistance of electrodeposited zinc-nickel alloy coatings. *Corrosion Science*. 1993;35(5-8): 1267–1272. [https://doi.org/10.1016/0010-938X\(93\)90347-J](https://doi.org/10.1016/0010-938X(93)90347-J)
85. Rahsepar M. Corrosion study of Ni/Zn compositionally modulated multilayer coatings using electrochemical impedance spectroscopy. *Corrosion Science*. 2009;51(11): 2537–2543. <https://doi.org/10.1016/j.corsci.2009.06.030>
86. Rashmi D, Pavithra G. P., Praveen B. M., Devapal D. Electrodeposition of Zn-Ni monolithic coatings, characterization, and corrosion analysis. *Journal of Failure Analysis and Prevention*. 2020;20(5-8): 513–522. <https://doi.org/10.1007/s11668-020-00848-3>
87. Exbrayat L., Rébéré C., Ndong Eyame R., Steyer P., Creus J. Corrosion behavior in saline solution of pulsed-electrodeposited zinc-nickel-ceria nanocomposite coatings. *Materials and Corrosion*. 2017;68(10): 1129–1142. <https://doi.org/10.1002/maco.201709419>
88. Fashu S., Gu C., Zhang J., Huang M., Wang X., Tu J. Effect of EDTA and  $\text{NH}_4\text{Cl}$  additives on electrodeposition of Zn-Ni films from choline chloride-based ionic liquid. *Transactions of Nonferrous Metals Society of China*. 2015;25(6): 2054–2064. [https://doi.org/10.1016/S1003-6326\(15\)63815-8](https://doi.org/10.1016/S1003-6326(15)63815-8)
89. Beheshti M., Ismail M. C., Kakooei S., Shahrestani S., Mohan G., Zabihiadzboni M. Influence of deposition temperature on the corrosion resistance of electrodeposited zinc-nickel alloy coatings. *Materialwissenschaft und Werkstofftechnik*. 2018;49(4): 472–482. <https://doi.org/10.1002/mawe.201700284>
90. Feng Z., Li D., Wang L., Sun Q., Lu P., Xing P., An M. Theoretical and experimental studies of 2,2-bipyridine for nanocrystalline zinc-nickel deposition. *Ionics*. 2019;25: 1857–1867. <https://doi.org/10.1007/s11581-018-2786-x>
91. Stein M., Ovens S. P., Pickers H. W., Weil K. G. Dealloying studies with electrodeposited zinc-nickel alloy films. *Electrochimica Acta*. 1998;43(1-2): 223–226. [https://doi.org/10.1016/S0013-4686\(97\)00228-4](https://doi.org/10.1016/S0013-4686(97)00228-4)
92. Ivaskevicius E., Selskis A., Sudavicius A., Ramanauskas R. Dealloying of electrodeposited zinc-nickel alloy coatings. *Chemija*. 2001;12(3): 204–209. Available at: <http://www.elibrary.lt/resursai/LMA/Chemija/C-204.pdf>
93. Ding Y., Zhang J. *Nanoporous metals for advanced energy technologies*. Moosseedorf: Springer International Publishing Switzerland; 2016. 223 p. <https://doi.org/10.1007/978-3-319-29749-1>
94. El-Sayed A.-R., Mohran H. S., Abd El-Lateef H. M. Role of nickel alloying on anodic dissolution behavior of zinc in 3.5% NaCl solution. Part II: Potentiodynamic, potentiostatic and galvanostatic studies. *Transactions of Nonferrous Metals Society of China*. 2015;25(9): 3152–3164. [https://doi.org/10.1016/S1003-6326\(15\)63946-2](https://doi.org/10.1016/S1003-6326(15)63946-2)
95. Badawya W. A., Ismaila K. M., Fathib A. M. Effect of Ni content on the corrosion behavior of Cu-Ni alloys in neutral chloride solutions. *Electrochimica*

*Acta*. 2005;50(18): 3603–3608. <https://doi.org/10.1016/j.electacta.2004.12.030>

96. Kozaderov O., Światowska J., Dragoe D., Volovitch P. Effect of Cr(III) passivation layer on surface modifications of zinc-nickel coatings in chloride solutions. *Journal of Solid State Electrochemistry*. 2021;25(4): 1161–1173. <https://doi.org/10.1007/s10008-021-04898-x>

97. Marygina Yu. I., Kaluzhina S. A., Protasova I. V. Phase composition and morphology of Ni, Zn-alloy surface, electrodeposited from sulfate-ammonium solution *Kondensirovannye sredy i mezhfaznye granitsy = Condensed Matter and Interphases*. 2018;20(1): 93–101. DOI: <https://doi.org/10.17308/kcmf.2018.20/481> (In Russ., abstract in Eng.)

98. Rouya E., Mallett J. J., Salvi P., Villa M., Begley M., Kelly R. G., Reed M., Zangari G. Nanoporous nickel by electrochemical dealloying. *Transactions of the Materials Research Society of Japan*. 2010;35(1): 23–26. <https://doi.org/10.14723/tmrj.35.23>

99. McCue I., Benn E., Gaskey B., Erlebacher J. Dealloying and dealloyed materials. *The Annual Review of Materials Research*. 2016;46(1): 263–284. <https://doi.org/10.1146/annurev-matsci-070115-031739>

100. Gopal F., Faraji M. Fabrication of nanoporous nickel oxide by de-zincification of Zn–Ni/(TiO<sub>2</sub>-nanotubes) for use in electrochemical supercapacitors. *Electrochimica Acta*. 2013;100: 133–139. <https://doi.org/10.1016/j.electacta.2013.03.155>

101. Balej J., Divisek J., Schmitz H., Mergel J. Preparation and properties of Raney nickel electrodes on Ni–Zn base for H<sub>2</sub> and O<sub>2</sub> evolution from alkaline solutions. Part II: Leaching (activation) of the Ni–Zn electrodeposits in concentrated KOH solutions and H<sub>2</sub> and O<sub>2</sub> overvoltage on activated Ni–Zn Raney electrodes. *Journal of Applied Electrochemistry*. 1992;22: 711–716. Available at: <https://link.springer.com/content/pdf/10.1007%2FBF01027498.pdf>

102. Katagiri A., Nakata M. Preparation of a high surface area nickel electrode by alloying and dealloying in a ZnCl<sub>2</sub>–NaCl Melt. *Journal of the Electrochemical Society*. 2003;150(9): 585–590. <https://doi.org/10.1149/1.1595662>

103. Wang T., Ren D., Huo Z., Song Z., Jin F., Chen M. Nanoporous nickel catalyst for selective hydrogenation of carbonates into formic acid in water. *Green Chemistry*. 2016;19(3): 1–7. <https://doi.org/10.1039/C6GC02866G>

104. Zuo L., Li R., Jin Y., Xu H., Zhang T. Fabrication of three-dimensional nanoporous nickel by dealloying Mg–Ni–Y metallic glasses in citric acid solutions for high-performance energy storage. *Journal of The Electrochemical Society*. 2017;164(2): 348–354. <https://doi.org/10.1149/2.1131702jes>

105. Gan Y. X., Zhang Y., Gan J. B. Nanoporous metals processed by dealloying and their applications. *AIMS Materials Science*. 2018;5(6): 1141–1183. <https://doi.org/10.3934/matrics.2018.6.1141>

106. Luo X. K., Li R., Huang L., Zhang T. Nucleation and growth of nanoporous copper ligaments during electrochemical dealloying of Mg-based metallic glasses. *Corrosion Science*. 2013;67: 100–108. <https://doi.org/10.1016/j.corsci.2012.10.010>

107. Hosseini M. G. Preparation, characterization, and application of alkaline leached Ni/Zn–Ni binary coatings for electro-oxidation of methanol in alkaline solution. *Journal of Applied Electrochemistry*. 2012;42(3): 153–162. <https://doi.org/10.1007/s10800-012-0382-8>

108. Cai J. Fabrication of three-dimensional nanoporous nickel films with tunable nanoporosity and their excellent electrocatalytic activities for hydrogen evolution reaction. *International Journal of Hydrogen Energy*. 2013;38(2): 934–941. <https://doi.org/10.1016/j.ijhydene.2012.10.084>

109. Herraiz-Cardona I., Ortega E., Perez-Herranz V. Impedance study of hydrogen evolution on Ni/Zn and Ni–Co/Zn stainless steel based electrodeposits. *Electrochimica Acta*. 2011;56(3): 1308–1315. <https://doi.org/10.1016/j.electacta.2010.10.093>

110. Singh H., Yadav R., Farooqui S. A., Dudnyk O., Sinha A. K. Nanoporous nickel oxide catalyst with uniform Ni dispersion for enhanced hydrogen production from organic waste. *International Journal of Hydrogen Energy*. 2019;44(36): 19573–19584. <https://doi.org/10.1016/j.ijhydene.2019.05.203>

111. Gao Y., Ding Y. Nanoporous metals for heterogeneous catalysis: following the success of Raney nickel. *Chemistry—A European Journal*. 2020;26(41): 8845–8856. <https://doi.org/10.1002/chem.202000471>

### Information about the authors

Oleg A. Kozaderov, DSc in Chemistry, Head of the Department of Physical Chemistry, Faculty of Chemistry, Voronezh State University, Voronezh, Russian Federation; e-mail: ok@chem.vsu.ru. ORCID id: <https://orcid.org/0000-0002-0249-9517>.

Dmitrii V. Burliaev, postgraduate student, Department of Physical Chemistry, Faculty of Chemistry, Voronezh State University, Voronezh, Russian Federation; e-mail: dimn0@yandex.ru. ORCID id: <https://orcid.org/0000-0003-3826-686X>.

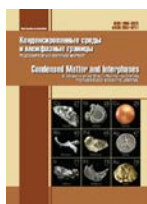
Polina Volovitch, Professor, PSL University, CNRS-Chimie ParisTech, Institut de Recherche de Chimie Paris, Paris, France; e-mail: polina.volovitch@chimieparistech.psl.eu. ORCID id: <https://orcid.org/0000-0001-5729-9830>

All authors have read and approved the final manuscript.

Received 30 January 2021; Approved after reviewing 15 February 2021; Accepted 15 March 2021; Published online 25 March 2021

Translated by Marina Strepetova  
Edited and proofread by Simon Cox





# Condensed Matter and Interphases

Kondensirovannye Sredy i Mezhfaznye Granitsy  
<https://journals.vsu.ru/kcmf/>

## Original articles

Original article

<https://doi.org/10.17308/kcmf.2021.23/3293>

## Liquidus surface of the quasi-ternary system $\text{Cu}_2\text{S}-\text{In}_2\text{S}_3-\text{FeS}$

I. B. Bakhtiyarly, R. J. Kurbanova, Sh. S. Abdullaeva<sup>✉</sup>, \* Z. M. Mukhtarova, F. M. Mammadova

*Institute of Catalysis and Inorganic Chemistry, Azerbaijan National Academy of Sciences,  
113 H. Javid pr., Baku AZ-1143, Azerbaijan*

### Abstract

A projection of the liquidus surface of the quasi-ternary system  $\text{Cu}_2\text{S}-\text{In}_2\text{S}_3-\text{FeS}$  was constructed as a result of experimental studies of quasi-binary and non-quasi-binary sections and based on the data on binary systems comprising a ternary system. Each section (six quasi-binary and four non-quasi-binary ones) was studied separately using complex methods of physicochemical analysis: differential thermal analysis, X-ray phase analysis, and microstructural analysis.

It was found that the quasi-ternary system  $\text{Cu}_2\text{S}-\text{In}_2\text{S}_3-\text{FeS}$  has six fields of primary crystallisation of separate phases and eleven monovariant equilibrium curves along which two phases are co-crystallised. Non-variant equilibrium points were obtained through the extrapolation of the direction of monovariant equilibrium curves.

The quasi-ternary system  $\text{Cu}_2\text{S}-\text{In}_2\text{S}_3-\text{FeS}$  is characterised by 17 non-variant equilibrium points, where  $E_1-E_5$  are triple eutectic points.

The projection diagram of the liquidus surface is characterised by three crystallisation fields of the initial components ( $\text{Cu}_2\text{S}$ ,  $\text{In}_2\text{S}_3$ ,  $\text{FeS}$ ), four fields of binary compounds, and one field of a complex compound ( $\text{CuFeIn}_3\text{S}_6$ ).

Since complete solubility of the initial components in liquid and solid states is observed in the quasi-binary section  $\text{CuIn}_5\text{S}_8-\text{FeIn}_2\text{S}_4$ , the fields of primary crystallisation of  $\text{CuIn}_5\text{S}_8$  and  $\text{FeIn}_2\text{S}_4$  are absent; they are replaced by an unlimited solid solution based on these components.

The fields of primary crystallisation of  $\text{Cu}_2\text{S}$ ,  $\text{FeS}$ , and  $\text{CuInS}_2$  are the most extensive in the ternary system  $\text{Cu}_2\text{S}-\text{In}_2\text{S}_3-\text{FeS}$ . The reactions occurring at monovariant equilibrium points are presented.

**Keywords:** system, quasi-ternary, eutectic, liquidus, section

**Acknowledgements:** the study was supported by the Science Development Foundation under the President of the Republic of Azerbaijan, grant EIF/MQM/Elm-Tehsil-1-2016-1(26)-71/15/1.

**For citation:** Bakhtiyarly I. B., Kurbanova R. J., Abdullaeva Sh. S., Mukhtarova Z. M., Mammadova F. M. Liquidus Surface of the Quasi-ternary System  $\text{Cu}_2\text{S}-\text{In}_2\text{S}_3-\text{FeS}$ . *Kondensirovannye sredy i mezhfaznye granitsy = Condensed Matter and Interphases*. 2021;23(1): 16–24. <https://doi.org/10.17308/kcmf.2021.23/3293>

**Для цитирования:** Бахтиярлы И. Б., Курбанова Р. Дж., Абдуллаева Ш. С., Мухтарова З. М., Маммадова Ф. М. Поверхность ликвидуса квазитройной системы  $\text{Cu}_2\text{S}-\text{In}_2\text{S}_3-\text{FeS}$ . *Конденсированные среды и межфазные границы*. 2021;23(1): 16–24. <https://doi.org/10.17308/kcmf.2021.23/3293>

✉ Abdullaeva Shahri Seyfaly, email: [sehri.abdullayeva.83@mail.ru](mailto:sehri.abdullayeva.83@mail.ru)

© Bakhtiyarly I. B., Kurbanova R. J., Abdullaeva Sh. S., Mukhtarova Z. M., Mammadova F. M., 2021



## 1. Introduction

The object of the study was the quasi-ternary system  $\text{Cu}_2\text{S}-\text{In}_2\text{S}_3-\text{FeS}$ .

The  $\text{Cu}_2\text{S}-\text{In}_2\text{S}_3-\text{FeS}$  system is formed by congruently melting binary compounds [1–5]. The  $\text{Cu}_2\text{S}$  compound exists in the form of three modifications: a low-temperature modification  $\alpha\text{-Cu}_2\text{S}$  is stable below 376 K, a  $\beta\text{-Cu}_2\text{S}$  form of hexagonal syngony exists in the 376–708 K temperature range, and above 708 K there is a  $\gamma\text{-Cu}_2\text{S}$  form with FCC structure which melts at 1402 K [6–8].

The  $\text{In}_2\text{S}_3$  compound also exists in several structural modifications and belongs to semiconductor materials of type  $\text{A}_2^{\text{III}}\text{B}_3^{\text{VI}}$ . This compound is a wide-band semiconductor. In recent years, it has been of great interest to researchers as the “window” material in thin-film photovoltaic devices with the purpose of substitution of CdS. It is used in optoelectronics to create light-sensitive heterostructures as well as in microelectronics and solar energy as a material with a number of unique properties [9, 10].

Ferric sulphides are usually found in the form of natural compounds. They have been attracting a lot of interest from researchers for many years as they possess various crystal structures and phase transformations as well as unusual electric and magnetic properties [11]. Metal-insulator phase transformations, transitions into superconductive state, etc., are observed in these compounds. FeS is used in some technical areas, and another developing application of the compound is the substitution of silicon in solar photovoltaic industry [12].

Therefore, the study of the patterns of physico-chemical interaction and phase formation between the specified chalcogenides is of special scientific and practical interest and it allows developing new multi-functional materials based on them.

There is a number of works in scientific literature dedicated to binary chalcogenide compounds  $\text{Cu}_2\text{S}$ , FeS, and  $\text{In}_2\text{S}_3$  [13–15] that were necessary for the discussion of the obtained results in the present work.

It should be noted that there are no publications on the study of the ternary system. However, there is some literature data on the study of two quasi-binary sections ( $\text{CuIn}_5\text{S}_8-\text{FeIn}_2\text{S}_4$  and  $\text{CuInS}_2-\text{FeS}$  [16–18]). We studied the  $\text{CuInS}_2-\text{FeS}$  section [21].

The purpose of the work was to construct a projection of the liquidus surface of the  $\text{Cu}_2\text{S}-\text{In}_2\text{S}_3-\text{FeS}$  system: to establish the position of the fields of primary crystallisation of phases in the system, to compose equations of non-variant phase transformations, and to identify the nature of interactions in subordinate triangles.

## 2. Experimental

For the experimental part of the study of the  $\text{Cu}_2\text{S}-\text{In}_2\text{S}_3-\text{FeS}$  system we used a complex of physicochemical methods: differential thermal analysis (DTA), microstructural analysis (MSA), X-ray diffraction analysis (XRD) as well as microhardness measurement, and density determination [21]. DTA was conducted using a Jupiter STA 449 F3 (NETZSCH, Germany) in synchronous thermal analysis mode. The accuracy of detection of thermal effects was 0.10–0.15 K/deg. XRD was conducted using a “D2 Phaser” X-ray diffractometer (Bruker, Germany). Microhardness of the phases in the alloys was measured on a PMT-3 tester using a well-known method [19]. The load on the diamond pyramid was 0.01–0.02 N. The microstructure was studied on a MIM-8 metallographic microscope. The density was determined at a temperature of 300 K using a pycnometer (with toluene as the filler).

The samples were synthesised from the elements (reduced iron, In – 000 indium, copper with 99.999 % purity, extra pure sulphur 99.9999 %) in evacuated to 1.33 Pa and vacuum-sealed quartz ampoules with the length of 15–18 cm and the diameter of 1.5 cm using direct ampoule method in a single temperature furnace while stirring the samples. Before being put into electrical furnace, the ampoules were heated up to 800 K, then gradually immersed into the furnace together with the samples while the temperature was increased by 50 – 70° C above the melting temperature. The melt was kept at this temperature for 7 hours. The process was repeated several times. After that, the ampoule was hardened in iced water. Then the ingot was subjected to homogenizing annealing. Homogenizing annealing was conducted at a temperature of 900 K for 200 h.

## 3. Results and discussion

In order to understand fully the processes occurring in the quasi-ternary system  $\text{Cu}_2\text{S}-\text{In}_2\text{S}_3-\text{FeS}$ , we studied the following quasi-binary

and non-quasi-binary sections:  $\text{CuInS}_2\text{-FeIn}_2\text{S}_4$ ,  $\text{Cu}_3\text{In}_5\text{S}_9\text{-FeIn}_2\text{S}_4$ ,  $\text{Cu}_3\text{In}_5\text{S}_9\text{-CuFeIn}_3\text{S}_6$ ,  $\text{CuFeIn}_3\text{S}_6\text{-FeS}$ ,  $\text{CuInS}_2\text{-FeS}$  were quasi-binary;  $\text{FeIn}_2\text{S}_4\text{-}(5\text{Cu}_2\text{S})_{0.83}(\text{3In}_2\text{S}_3)_{0.17}$ ,  $(5\text{Cu}_2\text{S})_{0.50}(\text{7.5FeS})_{0.50}\text{-}(5\text{Cu}_2\text{S})_{0.16}(\text{3In}_2\text{S}_3)_{0.84}$ ,  $(5\text{Cu}_2\text{S})_{0.16}(\text{3In}_2\text{S}_3)_{0.84}\text{-FeIn}_2\text{S}_4$ ,  $(5\text{Cu}_2\text{S})_{0.350}(\text{3In}_2\text{S}_3)_{0.650}\text{-}(7.5\text{FeS})_{0.350}(\text{3In}_2\text{S}_3)_{0.650}$  were non-quasi-binary.

Among the studied sections, a complex phase was found only in the  $\text{CuInS}_2\text{-FeIn}_2\text{S}_4$  section – a compound of the  $\text{CuFeIn}_3\text{S}_6$  composition that participates in the triangulation of the quasi-ternary system  $\text{Cu}_2\text{S-In}_2\text{S}_3\text{-FeS}$ . Below is a brief description of the studied sections of the quasi-ternary system  $\text{Cu}_2\text{S-In}_2\text{S}_3\text{-FeS}$ .

**The  $\text{CuInS}_2\text{-FeIn}_2\text{S}_4$  section** is a quasi-binary section of the quasi-ternary system  $\text{Cu}_2\text{S-In}_2\text{S}_3\text{-FeS}$ . A compound of the  $\text{CuFeIn}_3\text{S}_6$  composition which melts congruently at a temperature of 1365 K was found with the component ratio of 1:1. Coordinates of the eutectic point were 31 mol. % and 68 mol. %  $\text{FeIn}_2\text{S}_4$  at temperatures of 1240 and 1290 K respectively.

Based on the initial components and the compound of the  $\text{CuFeIn}_3\text{S}_6$  composition, solubility was observed. The limits of solid solutions were specified and it was established that the resulting solid solutions based on the modifications of the  $\text{CuInS}_2$  ( $\alpha$ ,  $\beta$ ,  $\gamma$ ) compound reached 12 mol. %  $\text{FeIn}_2\text{S}_4$  at 300 K and 20 mol. %  $\text{FeIn}_2\text{S}_4$  at 1175 K [20].

**The  $\text{Cu}_3\text{In}_5\text{S}_9\text{-CuFeIn}_3\text{S}_6$  section** is a quasi-binary section of the quasi-ternary system. Its phase diagram is of the simple eutectic type. The eutectic composition corresponds to 55 mol. %  $\text{CuFeIn}_3\text{S}_6$  at a temperature of 1200 K. The solubility based on  $\text{Cu}_3\text{In}_5\text{S}_9$  at 900 K is 13 mol. %  $\text{CuFeIn}_3\text{S}_6$  and 20 mol. %  $\text{CuFeIn}_3\text{S}_6$  at 1200 K.

**The  $\text{CuInS}_2\text{-FeS}$  section** is a quasi-binary section [21] of the quasi-ternary system  $\text{Cu}_2\text{S-In}_2\text{S}_3\text{-FeS}$ . The liquidus of the section consists of the primary crystallisation branches  $\alpha$ ,  $\beta$ ,  $\gamma$  of the modification of the  $\text{CuInS}_2$  compound. Under the influence of  $\text{FeS}$  the temperature of the  $\gamma\text{CuInS}_2 \leftrightarrow \beta\text{CuInS}_2$  phase transition decreased and belonged to the eutectoid type. The crystallisation of the alloys ended at 1130 K and 50 mol. % by the reaction  $\text{liq}(\text{e}) \leftrightarrow \alpha + \text{FeS}$ .

It was found that the solubility reached 12 mol. %  $\text{FeS}$  at room temperature (300 K) [21].

**The  $\text{CuIn}_5\text{S}_8\text{-FeIn}_2\text{S}_4$  section** is quasi-binary. Based on the initial components  $\text{CuIn}_5\text{S}_8$  and

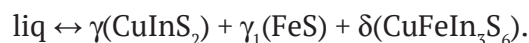
$\text{FeIn}_2\text{S}_4$ , we observed their complete solubility in liquid and solid states. The liquidus of the section consisted of one curve of primary crystallisation  $\sigma$ -solid solution. A continuous series of the  $\sigma$ -solid solution solidified below the solidus line.

The data that we have obtained corresponds well with the results of the authors who studied the  $\text{CuIn}_5\text{S}_8\text{-FeIn}_2\text{S}_4$  system [16].

**The  $\text{Cu}_3\text{In}_5\text{S}_9\text{-FeIn}_2\text{S}_4$  section** is a quasi-binary section of the eutectic type. Co-crystallisation of the branches of the solid solutions based on the initial components occurred with the composition of 42 mol. %  $\text{FeIn}_2\text{S}_4$  at a temperature of 1150 K. The solubility at room temperature was 3 mol. %  $\text{FeIn}_2\text{S}_4$  based on  $\text{Cu}_3\text{In}_5\text{S}_9$  and 5 mol. % based on  $\text{FeIn}_2\text{S}_4$ .

**The  $\text{CuFeIn}_3\text{S}_6\text{-FeS}$  section** is a quasi-binary section of the quasi-ternary system of the simple eutectic type. Co-crystallisation of the initial components finished at a temperature of 1100 K and had the composition of 30 mol. %  $\text{FeS}$ . There was solubility based on both components.

**The  $(5\text{Cu}_2\text{S})_{0.50}(\text{7.5FeS})_{0.50}\text{-}(5\text{Cu}_2\text{S})_{0.16}(\text{3In}_2\text{S}_3)_{0.84}(\text{e6-e2})$  section** is a non-quasi-binary section (Fig. 1). This section of the ternary system crossed the fields of subordinate ternary systems  $\text{Cu}_2\text{S-CuInS}_2\text{-FeS}$ ,  $\text{CuInS}_2\text{-CuFeIn}_3\text{S}_6\text{-FeS}$ ,  $\text{CuInS}_2\text{-Cu}_3\text{In}_5\text{S}_9\text{-CuFeIn}_3\text{S}_6$ ;  $\text{Cu}_3\text{In}_5\text{S}_9\text{-CuFeIn}_3\text{S}_6\text{-FeIn}_2\text{S}_4$ , and  $\text{CuInS}_2\text{-FeIn}_2\text{S}_4\text{-CuIn}_5\text{S}_8$ . Therefore, its phase diagram consisted of five independent parts. The liquidus of the section had the form of four branches of primary separation of  $\alpha$ ,  $\gamma$ ,  $\sigma$ ,  $\delta$ -phases. A part of the section went through the subordinate ternary system  $\text{Cu}_2\text{S-CuInS}_2\text{-FeS}$  in the range of the concentration 0–61 mol. %  $(5\text{Cu}_2\text{S})_{0.50}(\text{7.5FeS})_{0.50}$ . There was one ternary eutectic ( $E_3$ ) equilibrium at 990 K in this part of the section. The second part of the section crossed the secondary ternary system  $\text{CuInS}_2\text{-CuFeIn}_3\text{S}_6\text{-FeS}$  in the range of 61–79 mol. %  $(5\text{Cu}_2\text{S})_{0.16}(\text{3In}_2\text{S}_3)_{0.84}$ , where a non-variant eutectic reaction was formed:



The crystallisation of the alloys in the third part of the section ended with the solidification of the triple eutectic at  $E_2$  at a temperature of 1100 K (Fig. 2).

**The  $(5\text{Cu}_2\text{S})_{0.350}(\text{3In}_2\text{S}_3)_{0.650}\text{-}(7.5\text{FeS})_{0.350}(\text{3In}_2\text{S}_3)_{0.650}(\text{c-d})$  section.** To study the processes occurring in compound triangles  $\text{Cu}_2\text{S-CuInS}_2\text{-FeS}$ ,  $\text{CuInS}_2\text{-CuFeIn}_3\text{S}_6\text{-FeS}$ , and

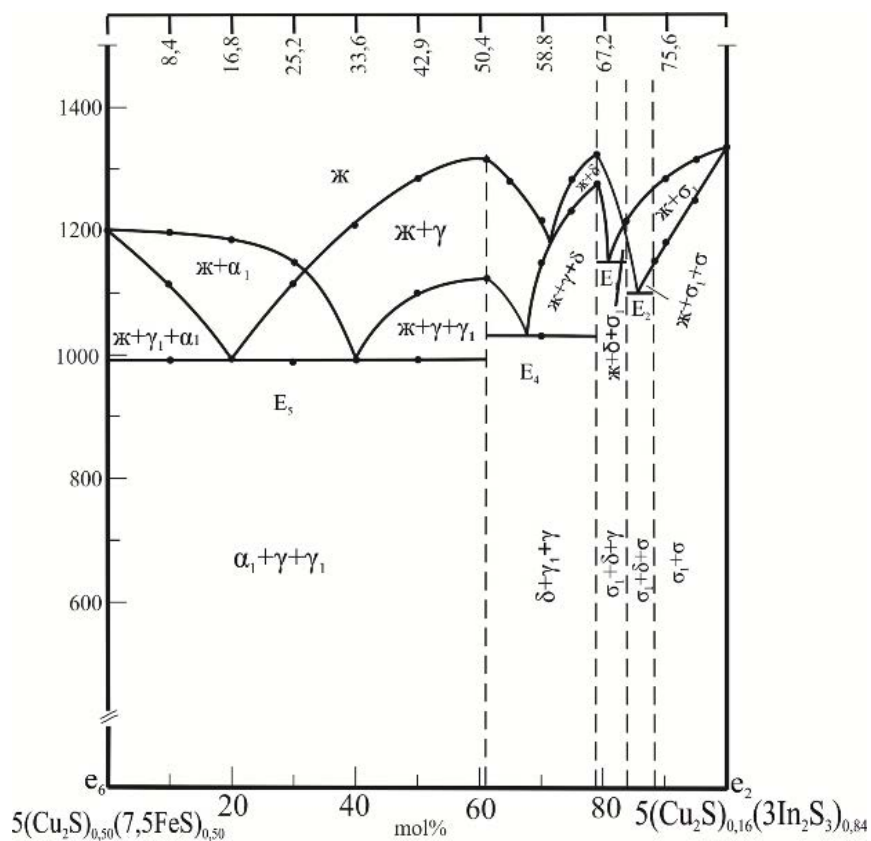


Fig. 1. Phase diagram of the  $5(\text{Cu}_2\text{S})_{0.50}7.5(\text{FeS})_{0.50}-5(\text{Cu}_2\text{S})_{0.16}3(\text{In}_2\text{S}_3)_{0.84}$  system

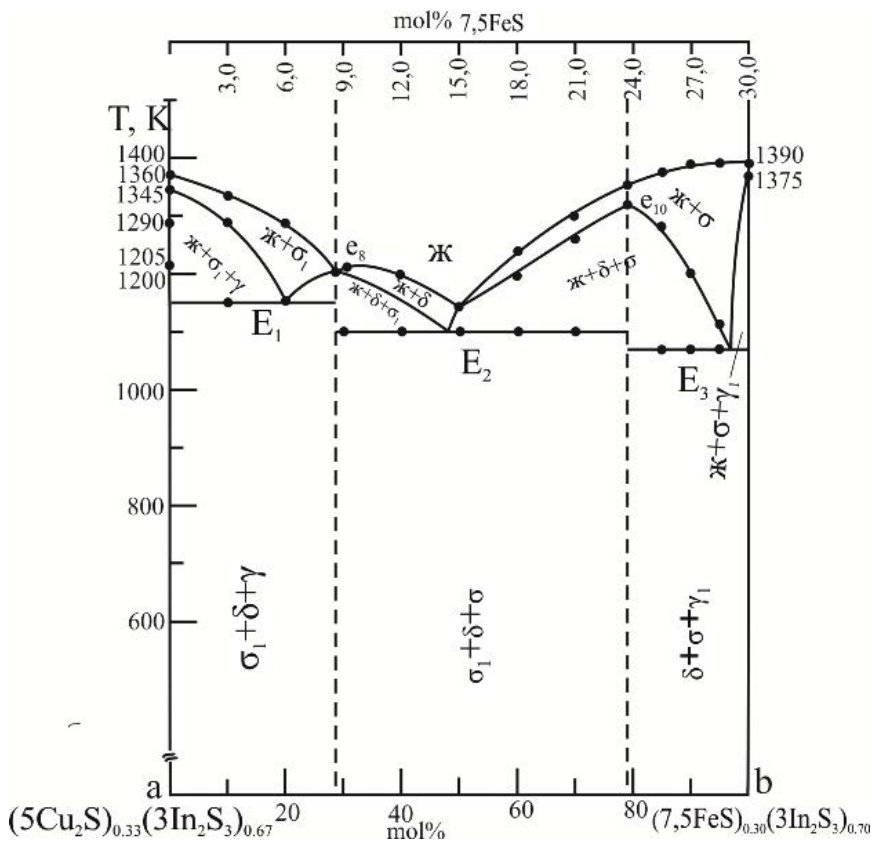


Fig. 2. Phase diagram of the  $5(\text{Cu}_2\text{S})_{0.33}3(\text{In}_2\text{S}_3)_{0.67}-5(\text{FeS})_{0.30}3(\text{In}_2\text{S}_3)_{0.70}$  system

CuFeIn<sub>3</sub>S<sub>6</sub>–FeIn<sub>2</sub>S<sub>4</sub>–FeS, as well as to determine the composition and temperature of triple non-variant points, we studied the interaction in the (5Cu<sub>2</sub>S)<sub>0.350</sub>(3In<sub>2</sub>S<sub>3</sub>)<sub>0.650</sub>–(7.5FeS)<sub>0.350</sub>(3In<sub>2</sub>S<sub>3</sub>)<sub>0.650</sub> section. This section is non-quasi-binary and it crossed two extensive areas of primary crystallisation. Its liquidus is shown as two curves of primary crystallisation of the components (5Cu<sub>2</sub>S)<sub>0.350</sub>(3In<sub>2</sub>S<sub>3</sub>)<sub>0.650</sub> and (7.5FeS)<sub>0.350</sub>(3In<sub>2</sub>S<sub>3</sub>)<sub>0.650</sub>. A part of the section went through the ternary system Cu<sub>2</sub>S–CuInS<sub>2</sub>–FeS in the range of concentration of 0–68 mol. % (7.5FeS)<sub>0.350</sub>(3In<sub>2</sub>S<sub>3</sub>)<sub>0.650</sub>. There was one ternary eutectic equilibrium E<sub>3</sub> at 990 K in this part of the section. The second part of the section went through the ternary system CuInS<sub>2</sub>–CuFeIn<sub>3</sub>S<sub>6</sub>–FeS in the range of concentration of 68–84 mol. % (7.5FeS)<sub>0.350</sub>(3In<sub>2</sub>S<sub>3</sub>)<sub>0.650</sub> where the equilibrium ended at a temperature of 1030 K in the triple eutectic E<sub>4</sub>. The third part of the section crossed the ternary system FeIn<sub>2</sub>S<sub>4</sub>–CuFeIn<sub>3</sub>S<sub>6</sub>–FeS in the range of concentration of 84–0 mol. % (7.5FeS)<sub>0.350</sub>(3In<sub>2</sub>S<sub>3</sub>)<sub>0.650</sub>. There was also one triple eutectic equilibrium E<sub>3</sub> here.

Depending on the concentration below the solidus line, the section is represented as a mechanical mix of the three phases.

The (5Cu<sub>2</sub>S)<sub>0.33</sub>(3In<sub>2</sub>S<sub>3</sub>)<sub>0.67</sub>–(7.5FeS)<sub>0.30</sub>(3In<sub>2</sub>S<sub>3</sub>)<sub>0.70</sub> (a–b) section is a non-quasi-binary section of the quasi-ternary system Cu<sub>2</sub>S–In<sub>2</sub>S<sub>3</sub>–FeS which crossed three secondary triangles (Fig. 2).

The phase diagram consisted of three parts. The liquidus of the system which went through the subordinate system CuInS<sub>2</sub>–Cu<sub>3</sub>In<sub>5</sub>S<sub>9</sub>–CuFeIn<sub>3</sub>S<sub>6</sub> consisted of the primary crystallisation of the high-temperature modification of σ<sub>1</sub>(Cu<sub>3</sub>In<sub>5</sub>S<sub>9</sub>). In this part the crystallisation ended at the temperature of triple eutectic E<sub>1</sub> (1150 K). The liquidus of the system which went through the subordinate system Cu<sub>3</sub>In<sub>5</sub>S<sub>9</sub>–CuFeIn<sub>3</sub>S<sub>6</sub>–FeIn<sub>2</sub>S<sub>4</sub> consisted of two branches: primary crystallisation δ-modification of the CuFeIn<sub>3</sub>S<sub>6</sub> compound and σ-solid solution based on FeIn<sub>2</sub>S<sub>4</sub>.

Final crystallisation occurred at 1100 K, the temperature of triple eutectic (E<sub>2</sub>).

The third part of the section crossed the Cu–FeIn<sub>3</sub>S<sub>6</sub>–FeIn<sub>2</sub>S<sub>4</sub>–FeS phase triangle. There was one triple eutectic point E<sub>3</sub> here. The liquidus of this part consisted of the branches of primary crystallisation of the solid solution σ(FeIn<sub>2</sub>S<sub>4</sub>)<sub>1-x</sub>(CuIn<sub>5</sub>S<sub>9</sub>)<sub>x</sub>.

The (7.5FeS)<sub>2.86</sub>(3In<sub>2</sub>S<sub>3</sub>)<sub>0.714</sub>–(5Cu<sub>2</sub>S)<sub>0.83</sub>(3In<sub>2</sub>S<sub>3</sub>)<sub>0.17</sub> (D<sub>4</sub>–e<sub>4</sub>) section is a non-

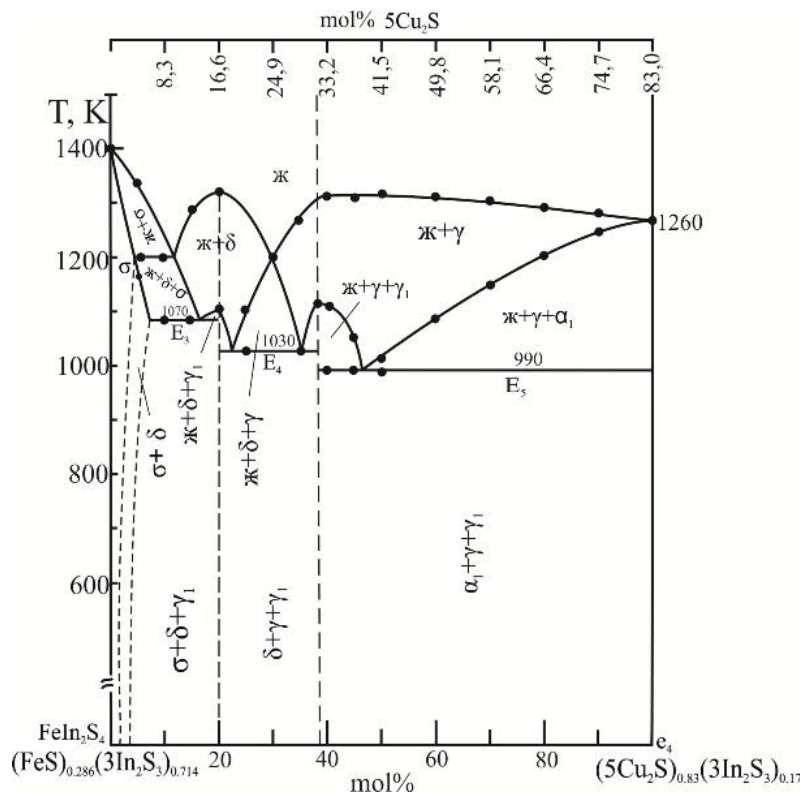
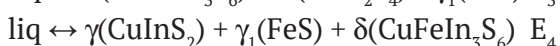
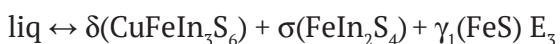


Fig. 3. Phase diagram of the (FeS)<sub>0.286</sub>3(In<sub>2</sub>S<sub>3</sub>)<sub>0.714</sub>–5(Cu<sub>2</sub>S)<sub>0.83</sub>3(In<sub>2</sub>S<sub>3</sub>)<sub>0.17</sub> system

quasi-binary section of the ternary system. Its phase diagram consisted of three parts (Fig. 3).

The liquidus of the section consisted of the curves of primary crystallisation  $\sigma$ -,  $\delta$ - and  $\gamma$ -phases of solid solutions based on the compound  $\text{Cu}_3\text{In}_5\text{S}_9$ ,  $\text{FeIn}_2\text{S}_4$ , and solid solution of  $\gamma$ -phase transition  $\text{CuInS}_2$ , respectively. There were three triple eutectic transformations  $E_3$ ,  $E_4$ , and  $E_5$  in the section. We present the reactions occurring in these non-variant eutectic points as follows:



### 3.1. Projection of the liquidus surface

Through the quasi-binary sections (there are 6 of them), which are triangulating section lines, the quasi-ternary system  $\text{Cu}_2\text{S}$ – $\text{In}_2\text{S}_3$ – $\text{FeS}$  was triangulated into six subordinate triangles:

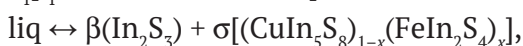
1.  $\text{Cu}_3\text{In}_5\text{S}_9$ – $\text{In}_2\text{S}_3$ – $\text{FeIn}_2\text{S}_4$
2.  $\text{CuInS}_2$ – $\text{Cu}_3\text{In}_5\text{S}_9$ – $\text{CuFeIn}_3\text{S}_6$
3.  $\text{CuFeIn}_3\text{S}_6$ – $\text{Cu}_3\text{In}_5\text{S}_9$ – $\text{FeIn}_2\text{S}_4$
4.  $\text{Cu}_2\text{S}$ – $\text{CuInS}_2$ – $\text{FeS}$
5.  $\text{CuInS}_2$ – $\text{CuFeIn}_3\text{S}_6$ – $\text{FeS}$
6.  $\text{CuFeIn}_3\text{S}_6$ – $\text{FeIn}_2\text{S}_4$ – $\text{FeS}$

Each of them can be represented separately as an independent ternary system.

Below we provide the nature of the chemical interaction for individual secondary ternary systems.

#### The $\text{Cu}_3\text{In}_5\text{S}_9$ – $\text{In}_2\text{S}_3$ – $\text{FeIn}_2\text{S}_4$ system

A quasi-binary section  $D_1(\text{CuIn}_5\text{S}_8)$ – $D_4(\text{FeIn}_2\text{S}_4)$ , where a continuous series of solid solution was formed, did not participate in the triangulation of the ternary system. Therefore, crystallisation in the  $\text{Cu}_3\text{In}_5\text{S}_9$ – $\text{In}_2\text{S}_3$ – $\text{FeIn}_2\text{S}_4$  system ended in curves  $e_1p_1$  and  $e_2e_7$  in a double non-variant point instead of a triple non-variant point. A monovariant curve  $e_1p_1$  characterises the equilibrium:

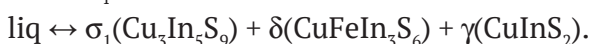


while curve  $e_2e_7$  characterises the following one:



#### $\text{CuInS}_2$ – $\text{Cu}_3\text{In}_5\text{S}_9$ – $\text{CuFeIn}_3\text{S}_6$

One eutectic transformation occurred in this compound triangle, therefore this system is characterised by the presence of one non-variant point  $E_1$  where the reaction occurs:



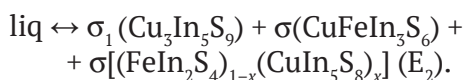
The crystallisation field of this system is mainly represented by fields  $\text{CuInS}_2$  (5),  $\text{Cu}_3\text{In}_5\text{S}_9$  (3), and  $\text{CuFeIn}_3\text{S}_6$  (4).

Three monovariant equilibrium curves  $e_3E_1$ ,  $e_8E_1$ , and  $e_9E_1$  converge in a non-variant point  $E_1$  at a temperature of 1150 K.

#### The $\text{CuFeIn}_3\text{S}_6$ – $\text{Cu}_3\text{In}_5\text{S}_9$ – $\text{FeIn}_2\text{S}_4$ system

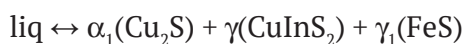
The liquidus of this system is represented by the fields  $\text{Cu}_3\text{In}_5\text{S}_9$ ,  $\text{CuFeIn}_3\text{S}_6$ ,  $\sigma(\text{FeIn}_2\text{S}_4)_{1-x}(\text{CuIn}_5\text{S}_8)_x$  separated by monovariant equilibrium curves  $e_8E_2$ ,  $e_7E_2$ , and  $e_{10}E_2$ .

The system is characterised by one non-variant point  $E_2$  where these monovariant equilibrium curves converge, and the chemical reaction occurred here at a temperature of 1150 K:



#### The $\text{Cu}_2\text{S}$ – $\text{CuInS}_2$ – $\text{FeS}$ system

The crystallisation surface of this secondary system was occupied by the fields  $\text{Cu}_2\text{S}$ ,  $\text{CuInS}_2$ , and  $\text{FeS}$ . One eutectic transformation  $E_5$  occurred in this compound triangle, and the following chemical reaction occurred here:



Three monovariant equilibrium curves  $e_4E_5$ ,  $e_6E_5$ , and  $E_5e_{12}$  converged at this point separating the fields  $\text{Cu}_2\text{S}$ ,  $\text{CuInS}_2$ , and  $\text{FeS}$ .

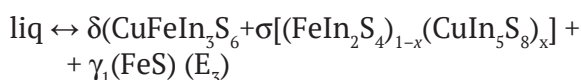
#### The $\text{CuInS}_2$ – $\text{CuFeIn}_3\text{S}_6$ – $\text{FeS}$ system

Only one eutectic transformation  $E_4$  occurred in this secondary ternary system. Monovariant curves  $e_9E_4$ ,  $e_{12}E_4$ , and  $e_{11}E_4$  converged at this point. Three phases  $\text{CuInS}_2$ ,  $\text{CuFeIn}_3\text{S}_6$ , and  $\text{FeS}$  were co-crystallised in a non-variant point  $E_4$  at a temperature of 1030 K.

#### The $\text{CuFeIn}_3\text{S}_6$ – $\text{FeIn}_2\text{S}_4$ – $\text{FeS}$ system

The field of this secondary system is mainly occupied by the area  $\text{FeS}$  as well as by the fields  $\text{CuFeIn}_3\text{S}_6$  and  $(\text{FeIn}_2\text{S}_4)_{1-x}(\text{CuIn}_5\text{S}_8)_x$ . Only eutectic transformations occur on the three sides of this triangle. This triangle has one non-variant eutectic point  $E_5$  at a temperature of 1070 K where three monovariant equilibrium curves  $e_{10}E_5$ ,  $e_{11}E_5$ , and  $e_5E_5$  converge.

The following chemical reaction occurred in this compound triangle:



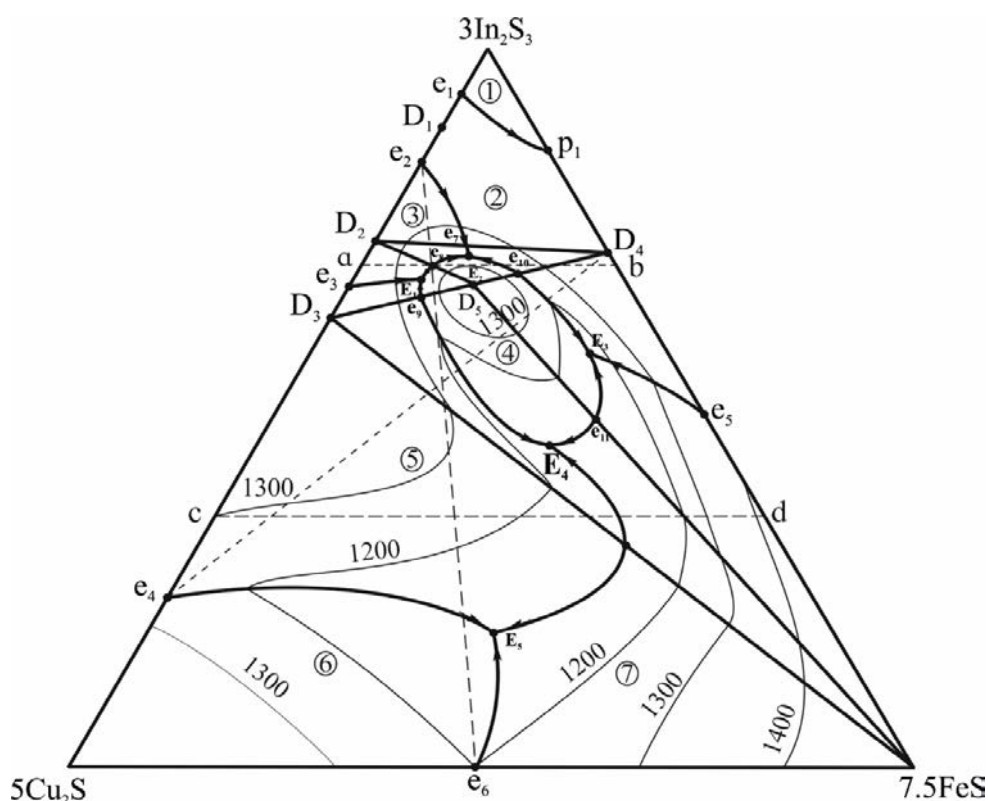


Fig. 4. Liquidus surface of the  $\text{Cu}_2\text{S}$ - $\text{In}_2\text{S}_3$ - $\text{FeS}$  system

The projection of the liquidus surface of the ternary quasi-ternary system  $\text{Cu}_2\text{S}$ - $\text{In}_2\text{S}_3$ - $\text{FeS}$  (Fig. 4) was constructed based on the data on phase equilibria in double systems comprising a ternary system and on a number of experimentally studied internal sections which were briefly characterised above.

The diagram of the projection of the liquidus surface is characterised by three fields of crystallisation of the initial components (Fig. 2) ( $\text{Cu}_2\text{S}$ ,  $\text{In}_2\text{S}_3$ ,  $\text{FeS}$ ), four fields of double compounds, and one field of a complex compound ( $\text{CuFeIn}_3\text{S}_6$ ).

Since complete solubility of the initial components in liquid and solid states was observed in the quasi-binary section  $\text{CuIn}_5\text{S}_8$ - $\text{FeIn}_2\text{S}_4$ , primary crystallisation fields  $\text{CuIn}_5\text{S}_8$  and  $\text{FeIn}_2\text{S}_4$  are absent; they are replaced by an unlimited solid solution based on these components.

The solid solution area found in the  $\text{CuIn}_5\text{S}_8$ - $\text{FeIn}_2\text{S}_4$  section occupied a part of the crystallisation field of the secondary ternary systems  $\text{CuIn}_5\text{S}_8$ - $\text{FeIn}_2\text{S}_4$ - $\text{Cu}_3\text{In}_5\text{S}_9$  and  $\text{In}_2\text{S}_3$ - $\text{CuIn}_5\text{S}_8$ - $\text{FeIn}_2\text{S}_4$ . There are 7 fields of primary crystallisation of separate phases in the ternary system. The most extensive fields in the ternary

system  $\text{Cu}_2\text{S}$ - $\text{In}_2\text{S}_3$ - $\text{FeS}$  are primary crystallisation fields  $\text{Cu}_2\text{S}$  (6),  $\text{FeS}$  (7), and  $\text{CuIn}_2\text{S}_5$  (5).

The separating primary crystallisation fields of the line of monovariant equilibria intersect at ternary non-variant points (Tables 1 and 2).

#### 4. Conclusions

There are 5 non-variant equilibrium points in the system, which are triple eutectic points, and there are nine monovariant equilibrium curves. The temperatures and compositions of the discovered non-variant points were compared to the data obtained during the study of non-quasi-binary sections as well as to the thermograms of alloys near the alleged points.

Therefore, for the first time, we constructed the projection of the liquidus surface of the quasi-ternary system  $\text{Cu}_2\text{S}$ - $\text{In}_2\text{S}_3$ - $\text{FeS}$ . We also determined the areas of primary crystallisation of the phases and the coordinates of all non-variant and monovariant equilibria.

#### Conflict of interests

The authors declare that they have no known competing financial interests or personal relationships that could have influenced the work reported in this paper.

**Table 1.** Non-variant reactions in the quasi-ternary system  $\text{Cu}_2\text{S}-\text{In}_2\text{S}_3-\text{FeS}$ 

Symbols	Equilibriums	Compositions, %			T, K
		5Cu <sub>2</sub> S	3In <sub>2</sub> S <sub>3</sub>	7.5FeS	
e <sub>1</sub>	liq ↔ β(In <sub>2</sub> S <sub>3</sub> ) + σ(D <sub>1</sub> )(CuIn <sub>5</sub> S <sub>8</sub> )	7.00	93.00	–	1340
e <sub>2</sub>	liq ↔ σ(D <sub>1</sub> )(CuIn <sub>5</sub> S <sub>8</sub> ) + σ <sub>1</sub> (D <sub>2</sub> )(Cu <sub>3</sub> In <sub>5</sub> S <sub>9</sub> )	16.00	84.00	–	1330
e <sub>3</sub>	liq ↔ σ <sub>1</sub> (D <sub>2</sub> )(Cu <sub>3</sub> In <sub>5</sub> S <sub>9</sub> ) + γ(D <sub>3</sub> )(CuInS <sub>2</sub> )	33.00	67.00	–	1345
e <sub>4</sub>	liq ↔ α <sub>1</sub> (Cu <sub>2</sub> S) + γ(D <sub>3</sub> )(CuInS <sub>2</sub> )	77.00	23.00	–	1260
e <sub>5</sub>	liq ↔ σ(D <sub>4</sub> )(FeInS <sub>4</sub> ) + γ <sub>1</sub> (FeS)	–	51.00	49.00	1375
e <sub>6</sub>	liq ↔ α <sub>1</sub> (Cu <sub>2</sub> S) + γ <sub>1</sub> (FeS)	52.00	–	48.00	1200
e <sub>7</sub>	liq ↔ σ <sub>1</sub> (D <sub>2</sub> )(Cu <sub>3</sub> In <sub>5</sub> S <sub>9</sub> ) + σ(D <sub>4</sub> )(FeInS <sub>4</sub> )	15.50	72.50	12.00	1150
e <sub>8</sub>	liq ↔ σ <sub>1</sub> (D <sub>2</sub> )(Cu <sub>3</sub> In <sub>5</sub> S <sub>9</sub> ) + δ(D <sub>5</sub> )(CuFeIn <sub>3</sub> S <sub>6</sub> )	22.00	70.00	8.00	1200
e <sub>9</sub>	liq ↔ γ(D <sub>3</sub> )(CuInS <sub>2</sub> ) + δ(D <sub>5</sub> )(CuFeIn <sub>3</sub> S <sub>6</sub> )	25.50	66.00	8.500	1285
e <sub>10</sub>	liq ↔ δ(D <sub>5</sub> )(CuFeIn <sub>3</sub> S <sub>6</sub> ) + σ(D <sub>4</sub> )(FeInS <sub>4</sub> )	12.00	69.00	19.00	1290
e <sub>11</sub>	liq ↔ δ(D <sub>5</sub> )(CuFeIn <sub>3</sub> S <sub>6</sub> ) + γ <sub>1</sub> (FeS)	12.50	46.50	41.00	1100
e <sub>12</sub>	liq ↔ γ(D <sub>3</sub> )(CuInS <sub>2</sub> ) + γ <sub>1</sub> (FeS)	18.50	31.50	50.00	1130
E <sub>1</sub>	liq ↔ σ <sub>1</sub> (D <sub>2</sub> )(Cu <sub>3</sub> In <sub>5</sub> S <sub>9</sub> ) + δ(D <sub>5</sub> )(CuFeIn <sub>3</sub> S <sub>6</sub> ) + γ(D <sub>3</sub> )(CuInS <sub>2</sub> )	24.00	68.00	8.00	1150
E <sub>2</sub>	liq ↔ σ <sub>1</sub> (D <sub>2</sub> )(Cu <sub>3</sub> In <sub>5</sub> S <sub>9</sub> ) + δ(D <sub>5</sub> )(CuFeIn <sub>3</sub> S <sub>6</sub> ) + σ((D <sub>4</sub> ) <sub>1-x</sub> (D <sub>1</sub> ) <sub>x</sub> )	16.00	71.50	12.50	1100
E <sub>3</sub>	liq ↔ δ(D <sub>5</sub> )(CuFeIn <sub>3</sub> S <sub>6</sub> ) + σ((D <sub>4</sub> ) <sub>1-x</sub> (D <sub>1</sub> ) <sub>x</sub> ) + γ <sub>1</sub> (FeS)	7.00	58.00	35.00	1070
E <sub>4</sub>	liq ↔ γ(D <sub>3</sub> )(CuInS <sub>2</sub> ) + γ <sub>1</sub> (FeS) + δ(D <sub>5</sub> )(CuFeIn <sub>3</sub> S <sub>6</sub> )	17.50	45.00	37.50	1030
E <sub>5</sub>	liq ↔ α <sub>1</sub> (Cu <sub>2</sub> S) + γ(D <sub>3</sub> )(CuInS <sub>2</sub> ) + γ <sub>1</sub> (FeS)	38.50	18.50	43.00	1090

**Table 2.** Monovariant reactions in the quasi-ternary system  $\text{Cu}_2\text{S}-\text{In}_2\text{S}_3-\text{FeS}$ 

Symbols	Equilibriums	T, K
e <sub>2</sub> e <sub>7</sub> E <sub>2</sub>	liq ↔ σ(CuIn <sub>5</sub> S <sub>8</sub> ) <sub>1-x</sub> (FeIn <sub>2</sub> S <sub>4</sub> ) <sub>x</sub> + σ <sub>1</sub> (Cu <sub>3</sub> In <sub>5</sub> S <sub>9</sub> )	1330–1150–1100
e <sub>3</sub> E <sub>1</sub>	liq ↔ σ <sub>1</sub> (Cu <sub>3</sub> In <sub>5</sub> S <sub>9</sub> ) + γ(CuInS <sub>2</sub> )	1345–1150
E <sub>1</sub> e <sub>8</sub> E <sub>2</sub>	liq ↔ σ <sub>1</sub> (Cu <sub>3</sub> In <sub>5</sub> S <sub>9</sub> ) + δ(CuFeIn <sub>3</sub> S <sub>6</sub> )	1150–1200–1100
E <sub>1</sub> e <sub>9</sub> E <sub>4</sub>	liq ↔ δ(CuFeIn <sub>3</sub> S <sub>6</sub> ) + γ(CuInS <sub>2</sub> )	1150–1285–1030
E <sub>4</sub> e <sub>12</sub> E <sub>5</sub>	liq ↔ γ(CuInS <sub>2</sub> ) + γ <sub>1</sub> (FeS)	1030–1130–1090
e <sub>4</sub> E <sub>5</sub>	liq ↔ γ(CuInS <sub>2</sub> ) + α <sub>1</sub> (Cu <sub>2</sub> S)	1260–1090
e <sub>6</sub> E <sub>5</sub>	liq ↔ α <sub>1</sub> (Cu <sub>2</sub> S) + γ <sub>1</sub> (FeS)	1200–1090
E <sub>4</sub> e <sub>11</sub> E <sub>3</sub>	liq ↔ δ(CuFeIn <sub>3</sub> S <sub>6</sub> ) + γ <sub>1</sub> (FeS)	1030–1100–1070
e <sub>5</sub> E <sub>3</sub>	liq ↔ σ(CuIn <sub>5</sub> S <sub>8</sub> ) <sub>1-x</sub> (FeIn <sub>2</sub> S <sub>4</sub> ) <sub>x</sub> + γ <sub>1</sub> (FeS)	1375–1070
E <sub>2</sub> e <sub>10</sub> E <sub>3</sub>	liq ↔ σ(CuIn <sub>5</sub> S <sub>8</sub> ) <sub>1-x</sub> (FeIn <sub>2</sub> S <sub>4</sub> ) <sub>x</sub> + δ(CuFeIn <sub>3</sub> S <sub>6</sub> )	1100–1315–1070
e <sub>1</sub> p <sub>1</sub>	liq ↔ β(In <sub>2</sub> S <sub>3</sub> ) + σ(CuIn <sub>5</sub> S <sub>8</sub> ) <sub>1-x</sub> (FeIn <sub>2</sub> S <sub>4</sub> ) <sub>x</sub>	1340–1305
e <sub>2</sub> e <sub>7</sub>	liq ↔ σ(CuIn <sub>5</sub> S <sub>8</sub> ) <sub>1-x</sub> (FeIn <sub>2</sub> S <sub>4</sub> ) <sub>x</sub> + σ <sub>1</sub> (Cu <sub>3</sub> In <sub>5</sub> S <sub>9</sub> )	1330–1150

## References

1. Tomashik V. Cu–In–S (Copper – Indium - Sulfur). *Non-Ferrous Metal Systems*. 2006;V11C1(1): 1–19. [https://doi.org/10.1007/10915981\\_24](https://doi.org/10.1007/10915981_24)

2. Binsma J. J. M., Giling L. J., Bloem J. Phase relations in the system  $\text{Cu}_2\text{S}-\text{In}_2\text{S}_3$ . *Journal of Crystal Growth*. 1980;50(2): 429–436. [https://doi.org/10.1016/0022-0248\(80\)90090-1](https://doi.org/10.1016/0022-0248(80)90090-1)

3. Rustamov P. Q., Babaeva P. K., Allazov M. R. State diagram of the section  $\text{FeS}-\text{In}_2\text{S}_3$ . *Russian Journal of Inorganic Chemistry*. 1979;24(8): 2208–2211. (In Russ.)

4. Raghavan V. Fe–In–S (Iron – Indium - Sulfur). *Journal of Phase Equilibria*. 1998;19(3): 270. <https://doi.org/10.1361/105497198770342337>

5. Manual G. J., Patino F., Salinas E. Medición del contenido calórico de la mata de cobre ( $\text{Cu}_2\text{S}-\text{FeS}$ ) usando un calorímetro de gota. *Revista de la Sociedad Química de México*. 2001;45(1): 13–16. Available at: [https://www.researchgate.net/publication/26465784\\_Medicion\\_del\\_contenido\\_calorico\\_de\\_la\\_mata\\_de\\_cobre\\_Cu2S-FeS\\_usando\\_un\\_calorimetro\\_de\\_gota](https://www.researchgate.net/publication/26465784_Medicion_del_contenido_calorico_de_la_mata_de_cobre_Cu2S-FeS_usando_un_calorimetro_de_gota)



6. Patil M., Sharma D., Dive A., Mahajan S., Sharma R. Synthesis and characterization of  $\text{Cu}_2\text{S}$  thin film deposited by chemical bath deposition method. *Procedia Manufacturing*. 2018;20: 505–508. <https://doi.org/10.1016/j.promfg.2018.02.075>
7. Li S., Wang H., Xu W., Si H., Tao X., Lou S., et al. Synthesis and assembly of monodisperse spherical  $\text{Cu}_2\text{S}$  nanocrystals. *Journal of Colloid and Interface Science*. 2009;330(2): 483–487. <https://doi.org/10.1016/j.jcis.2008.10.062>
8. Kozer V. R., Parasyuk O. V. Phase equilibria in the quasi-ternary system  $\text{Cu}_2\text{S}$ - $\text{In}_2\text{S}_3$ - $\text{CdS}$ . *Chemistry of Metals and Alloys*. 2009;2(1/2): 102–107. <https://doi.org/10.30970/cma2.0087>
9. Gorai S., Guha P., Ganguli D., Chaudhuri S. Chemical synthesis of  $\beta$ - $\text{In}_2\text{S}_3$  powder and its optical characterization. *Materials Chemistry and Physics*. 2003;82(320): 974–979. <https://doi.org/10.1016/j.matchemphys.2003.08.013>
10. Bodnar I. V., Polubok V. A., Rud V. Yu., Rud Yu. V. Photosensitive structures based on  $\text{In}_2\text{S}_3$  crystals. *Semiconductors*. 2003; 37(11): 1308–1310. <https://doi.org/10.1134/1.1626214>
11. Mitsui H., Sasaki T., Oikawa K., Ishida K. Phase equilibria in  $\text{FeS}$ - $\text{XS}$  and  $\text{MnS}$ - $\text{XS}$  ( $\text{X} = \text{Ti}, \text{Nb}$  and  $\text{V}$ ) systems. *ISIJ International*. 2009;49(7): 936–941. <https://doi.org/10.2355/isijinternational.49.936>
12. Terranova U., de Leeuw N. H. Phase stability and thermodynamic properties of  $\text{FeS}$  polymorphs. *Journal of Physics and Chemistry of Solids*. 2017;111: 317–323. <https://doi.org/10.1016/j.jpcs.2017.07.033>
13. Thomere A., Guillot-Deudon C., Caldes M. T., Bodeux R., Barreau N., Jobic S., Lafond A. Chemical crystallographic investigation on  $\text{Cu}_2\text{S}$ - $\text{In}_2\text{S}_3$ - $\text{Ga}_2\text{S}_3$  ternary system. *Thin Solid Films*. 2018;665: 46–50. <https://doi.org/10.1016/j.tsf.2018.09.003>
14. Hurman Eric R. Activities in  $\text{CuS}$ - $\text{FeS}$ - $\text{SnS}$  melts at 1200. *Metallurgical Transactions B*. 1993;24(2):301–308. <https://doi.org/10.1007/bf02659132>
15. Womes M., Olivier-Fourcade J., Jumas J.-C., Aubertin F., Gonser U. Characterization of the single phase region with spinel structure in the ternary system  $\text{In}_2\text{S}_5$ - $\text{FeS}$ - $\text{FeS}_2$ . *Journal of Solid State Chemistry*. 1992;97(2): 249–256. [https://doi.org/10.1016/0022-4596\(92\)90032-q](https://doi.org/10.1016/0022-4596(92)90032-q)
16. Olekseyuk I. D., Parasyuk O. V., Kozer V. R. Research of systems of type  $\text{Cu}$  ( $\text{Ag}$ )  $\text{In}_3\text{S}_8$  -  $\text{FeIn}_2\text{S}_4$ . *Naukovii visnik Volins'kogo natsional'nogo universitetu im. Lesi Ukraïnki: Khimichni nauki*. 2009;24: 3-8. (In Ukrainian)
17. Mirzoeva R. J., Shikhalibeyli S. Sh., Allazov M. R. Investigation of the  $\text{CuInS}_2$ - $\text{FeS}$  semiconductor system. In: *Physico-chemical processes in condensed matter and interphase boundaries: Proc. 7th All-Russian Conf., 10–13 November 2015*. Voronezh: Nauchnaya Kniga Publ.; 2015. p. 371. (In Russ.)
18. Trukhanov S. V., Bodnar I. V., Zhafar M. A. Magnetic and electrical properties of  $(\text{FeIn}_2\text{S}_4)_{1-x}(\text{CuIn}_5\text{S}_8)_x$  solid solutions. *Journal of Magnetism and Magnetic Materials*. 2015;379: 22–27. <https://doi.org/10.1016/j.jmmm.2014.10.120>
19. Glazov V. M., Vigodorovich V. K. *Microtverdst metallo v i poluprovodnikov* [Microhardness of metals and semiconductors]. Moscow: Metallurgy; 1969. 248 p. (In Russ.)
20. Abdullayeva Sh. S., Mammadov F. M., Bakhtiyarly İ. B. Quasi-binary section  $\text{CuInS}_2$ - $\text{FeIn}_2\text{S}_4$ . *Russian Journal of Inorganic Chemistry*. 2020;65(1): 100–105. <https://doi.org/10.1134/s0036023619110020>
21. Bakhtiyarly I. B., Abdullayeva Sh. S., Gurbanova R. J., Mammadova F. M. Guseynova Sh. B. Study of interactions in the  $\text{CuInS}_2$ - $\text{FeS}$  system. *Russian Journal of General Chemistry*. 2019;89(8):1281–1284. <https://doi.org/10.1134/s1070363219080188>

### Information about the authors

*Bakhtiyarly Ikhtiyar Bahram oglu*, DSc in Chemistry, Professor, Institute of Catalysis and Inorganic Chemistry of the National Academy of Sciences of Azerbaijan, Baku, Azerbaijan; e-mail: [ibakhtiyarli@mail.ru](mailto:ibakhtiyarli@mail.ru). ORCID iD: <https://orcid.org/0000-0002-7765-0672>.

*Kurbanova Ruksana Jalal kizi*, DSc of Philosophy in Chemistry, Associate Professor, Institute of Catalysis and Inorganic Chemistry of the National Academy of Sciences of Azerbaijan, Baku, Azerbaijan; ORCID iD: <https://orcid.org/0000-0001-6467-0079>.

*Abdullaeva Shahri Seyfaly kizi*, postgraduate student, Junior Researcher, Institute of Catalysis and Inorganic Chemistry of the National Academy of Sciences of Azerbaijan, Baku, Azerbaijan; e-mail: [sehri.abdullayeva.83@mail.ru](mailto:sehri.abdullayeva.83@mail.ru). ORCID iD: <https://orcid.org/0000-0003-1723-2783>.

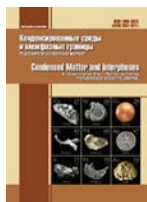
*Mukhtarova Ziyafat Mamed kizi*, DSc of Philosophy in Chemistry, Associate Professor, Institute of Catalysis and Inorganic Chemistry of the National Academy of Sciences of Azerbaijan, Baku, Azerbaijan; e-mail [ziyafatmuxtarova@mail.ru](mailto:ziyafatmuxtarova@mail.ru). ORCID iD: <https://orcid.org/0000-0001-5962-3710>.

*Mammadova Fatmahanum Mamed*, Researcher, Institute of Catalysis and Inorganic Chemistry of the National Academy of Sciences of Azerbaijan, Baku, Azerbaijan; e-mail: [Fatma.mammadova.1959@mail.ru](mailto:Fatma.mammadova.1959@mail.ru). ORCID iD: <https://orcid.org/0000-0002-8848-1018>.

All authors have read and approved the final manuscript.

*Received 3 September 2020; Approved after reviewing 15 December 2020; Accepted 15 March 2021; Published online 25 March 2021.*

*Translated by Marina Strepetova  
Edited and proofread by Simon Cox*



## Original articles

Original article

<https://doi.org/10.17308/kcmf.2021.23/3294>

## Spectral manifestations of the exciton-plasmon interaction of Ag<sub>2</sub>S quantum dots with silver and gold nanoparticles

I. G. Grevtseva, T. A. Chevychelova, V. N. Derepko, O. V. Ovchinnikov✉, M. S. Smirnov, A. S. Perepelitsa, A. S. Parshina

Voronezh State University,  
1 Universitetskaya pl., Voronezh 394018, Russian Federation

Abstract

The purpose of our study was to develop methods for creating hybrid nanostructures based on colloidal Ag<sub>2</sub>S quantum dots, pyramidal silver nanoparticles, Au nanorods, and to determine the spectral-luminescent manifestations of exciton-plasmon interactions in these structures. The objects of the study were Ag<sub>2</sub>S quantum dots passivated with thioglycolic acid (Ag<sub>2</sub>S/TGA QDs) and 2-mercaptopropionic acid (Ag<sub>2</sub>S/2-MPA QDs), gold nanorods (Au NRs), silver nanoparticles with pyramidal geometry (Ag NPs), and their mixtures. The spectral properties were studied using a USB2000+ with a PMC-100-20 photomultiplier system (Becker & Hickl Germany). The article considers the transformation of the luminescence spectra of colloidal Ag<sub>2</sub>S/TGA QDs and Ag<sub>2</sub>S/2-MPA QDs in mixtures with pyramidal Ag NPs and Au NRs. The study demonstrated the presence of the effects of the contour transformation of the luminescence spectra due to the Fano effect, as well as the luminescence quenching following direct contact between QDs and NPs.

**Keywords:** silver and gold nanoparticles, silver sulfide quantum dots, hybrid nanostructures, luminescence spectrum

**Acknowledgements:** The reported study was supported by a grant of the President of the Russian Federation to support leading scientific schools of the Russian Federation, project No. NSh-2613.2020.2. The results of transmission electron microscopy were obtained using the equipment of the Center for Collective Use of Scientific Equipment of Voronezh State University.

**For citation:** Grevtseva I. G., Chevychelova T. A., Derepko V. N., Ovchinnikov O. V., Smirnov M. S., Perepelitsa A. S., Parshina A. S. Spectral manifestations of exciton-plasmon interaction of Ag<sub>2</sub>S quantum dots with silver and gold nanoparticles. *Kondensirovannyyesredy i mezhfaznyegranitsy = Condensed Matter and Interphases*. 2021;23(1): 25–31. <https://doi.org/10.17308/kcmf.2021.23/3294>

**Для цитирования:** Гревцева И. Г., Чевычелова Т. А., Дерепко В. Н., Овчинников О. В., Смирнов М. С., Перепелица А. С., Паршина А. С. Спектральные проявления плазмон-экситонного взаимодействия квантовых точек Ag<sub>2</sub>S с наночастицами серебра и золота. *Конденсированные среды и межфазные границы*. 2021;23(1): 25–31. <https://doi.org/10.17308/kcmf.2021.23/3294>

✉ Oleg V. Ovchinnikov, e-mail: [ovchinnikov\\_o\\_v@rambler.ru](mailto:ovchinnikov_o_v@rambler.ru)

© Grevtseva I. G., Chevychelova T. A., Derepko V. N., Ovchinnikov O. V., Smirnov M. S., Perepelitsa A. S., Parshina A. S., 2021



## 1. Introduction

Metal nanoparticles (NPs), semiconductor quantum dots (QDs), and hybrid structures based on them can be used to solve certain basic and applied science problems in biology, medicine, chemistry, optoelectronics, photocatalysis, etc. [1–10]. Most of these spheres require sensors which can be used for various purposes. These sensors include fluorescent thermometers, pH sensors, fluorescent indicators of impurity ions, and biosensors based on the luminescence of QDs and dyes as well as on light scattering from plasmonic NP, etc. It is possible to control the spectral position of the plasmon resonance of metal NPs using their size [3, 4], shape [11], and dielectric environment [12], as well as by changing the structure of their interface. Thus, NPs can be decorated with semiconductor QDs, whose luminescence spectra partially or completely overlap with the plasmon peak of the extinction spectrum. Creation of hybrid structures with plasmon-exciton coupling based on plasmonic NPs and semiconductor QDs, may result in the high sensitivity of the structures' spectra to impurities, the environment, and the properties of the surrounding solution or matrix. As a result, hybrid nanostructures demonstrate both the additive properties of their components and novel unique sensory properties arising from direct interaction between the components and their close proximity to each other [6–18]. Variations in the regime of exciton-plasmon coupling (weak, intermediate and strong) enable resonance spectral-luminescent effects in the weak (Purcell effect), intermediate (Fano effect), and strong (Rabi splitting) regimes of exciton-plasmon coupling [14, 19–21]. The type of interaction and the distance between the components are crucial for such hybrid nanostructures. Of vital importance is to predict the spectral-luminescent properties of hybrid nanostructures. This problem has not been thoroughly studied yet. It is thus important to study the optical properties of synthesised nanostructures. To solve this problem, it is necessary to develop approaches to the synthesis of hybrid nanostructures based on technologies that allow for various regimes of exciton-plasmon interaction of metal NPs with QDs and dye molecules, as well as for the tuning of the

optical resonance of the components of hybrid nanostructures.

The purpose of our study was to develop methods for creating hybrid nanostructures based on colloidal Ag<sub>2</sub>S quantum dots (Ag<sub>2</sub>S QDs), pyramidal silver nanoparticles (Ag NPs), gold nanorods (Au NRs), and to determine the spectral-luminescent manifestations of exciton-plasmon interactions in these structures.

## 2. Experimental

### 2.1. Samples

Colloidal Ag<sub>2</sub>S QDs, passivated using molecules of thioglycolic acid (Ag<sub>2</sub>S/TGA QDs) and 2-Mercaptopropionic acid (Ag<sub>2</sub>S/2-MPA QDs) with an average size of 2.0 nm and 2.8 nm respectively, were synthesised using a one-step method. The method involves using TGA and 2-MPA molecules in the crystallisation both as the sources of sulphur and as passivators of QDs interfaces [22,23]. The approach involves mixing the initial reagent AgNO<sub>3</sub> (2.4 mM) and TGA (2-MPA) (4.8 mM). When TGA was used to passivate the QDs interfaces, distilled water was used as a solvent. When 2-MPA was used, the synthesis was performed in viscous medium (ethylene glycol).

The method of synthesising pyramidal Ag NPs was based on a combination of two methods: reduction of Ag with trisodium citrate (Na<sub>3</sub>C<sub>6</sub>H<sub>5</sub>O<sub>7</sub>) and reduction of Ag with sodium borohydride (NaBH<sub>4</sub>). To do this we subsequently poured 0.5 ml of PVP (0.003 M), 3 ml of Na<sub>3</sub>C<sub>6</sub>H<sub>5</sub>O<sub>7</sub> (0.03 M), 0.2 ml of H<sub>2</sub>O<sub>2</sub> (30%), and 0.5 ml of NaBH<sub>4</sub> (0.05 моль) into the AgNO<sub>3</sub> (50 мл, 0.02 M) aqueous solution with constant stirring at room temperature. At this stage the formed particles were predominantly spherical. When the constantly stirred colloidal solution was subjected to optical radiation with a wavelength of 520 nm, pyramidal Ag NPs were formed.

The colloidal synthesis of Au nanorods was performed in the presence of a surface-active substance (SAS), cetyltrimethylammonium bromide (CTAB), whose aqueous solution forms cylindrical micelle, thus creating anisotropic environment for the growth of NRs. Au NRs were formed in several stages, which included subsequent preparation and mixing of the seeds and growth solutions. As a seed solution we used spherical Au NPs (3 nm), obtained by means of the

chemical reduction of  $\text{HAuCl}_4$  (7  $\mu\text{l}$ , 0.36 M) with a  $\text{NaBH}_4$  solution (1.0 ml, 5mM) in the presence of CTAB (20 ml, 0.02 mM). The growth solution was a mixture of  $\text{HAuCl}_4$  (28  $\mu\text{l}$ , 0.36 M), CTAB (50 ml, 0.1 mM),  $\text{AgNO}_3$  (100  $\mu\text{l}$ , 0.02 M), and  $\text{C}_6\text{H}_8\text{O}_6$  (5 ml, 0.05  $\mu\text{M}$ ). After adding the seed solution to the growth solution, the reaction mixture gradually becomes blue, purple, or brown-red depending on the ratio of the length of the Au NRs to their diameter. By adding variable concentrations of  $\text{AgNO}_3$  to the growth solution we could regulate the ratio of the length of the Au NRs to their diameter. The obtained Au NRs were purified from reaction products by means of several cycles of centrifugation and dispersion.

Hybrid structures were formed by mixing colloidal solutions of Au NRs (pyramidal Ag NPs) and  $\text{Ag}_2\text{S}$  QDs/TGA (or  $\text{Ag}_2\text{S}$  QDs/2-MPA) with a molar ratio of  $[\nu(\text{NPs})]:[\nu(\text{QDs})] \sim 10^{-4}$  mole fraction (m.f.).

## 2.2. Methods of experimental studies

The size and morphology of  $\text{Ag}_2\text{S}$ /TGA QDs,  $\text{Ag}_2\text{S}$ /2-MPA QDs, pyramidal Ag NPs and Au NRs were determined by means of a Libra 120 transmission electron microscope (TEM) (Carl Zeiss, Germany). The absorption properties were studied using a USB2000+ spectrometer (Ocean Optics, USA) with a USB-DT light source (Ocean Optics, USA). The luminescence spectra and the luminescence decay kinetics of  $\text{Ag}_2\text{S}$ /TGA QDs,  $\text{Ag}_2\text{S}$ /2-MPA QDs, and their mixtures with plasmonic NPs were studied using the USB2000+ and a TimeHarp-260 system for time correlated photon counting (PicoQuant Germany) with a PMC-100-20 photomultiplier tube (Becker&Hickl

Germany) with a time resolution of 0.2 ns. A diode laser NDV7375 (Nichia, Japan) with a wavelength of 405 nm (200 mW) was used to stimulate the luminescence.

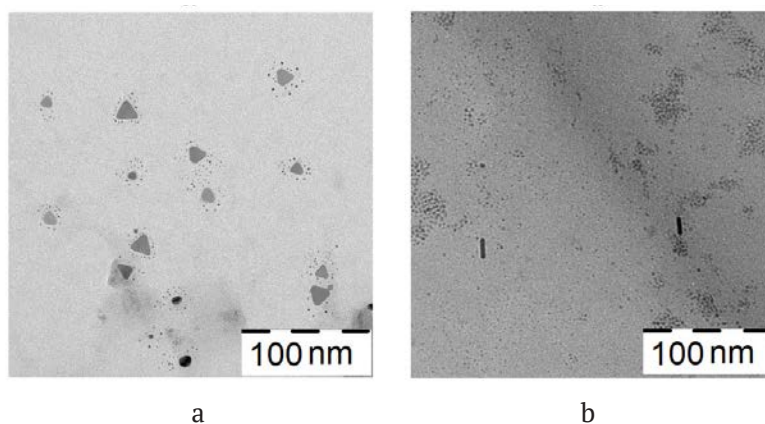
## 3. Results and discussion

Figure 1 presents TEM images of pyramidal Ag NPs and Au NRs. The analysis of TEM images demonstrated that pyramidal Ag NPs are formed with an average edge length of 19 nm (Fig. 1a). The photo-induced transformation of Ag NPs from spherical to pyramidal, followed by a growth in size, results in the shift of the extinction peak to longer wavelengths, from 480 nm to 590 nm (Fig. 2a, dotted line).

The described approach to the synthesis of Au NRs allowed us to obtain Au NRs with a size from  $20 \div 9$  nm to  $25 \div 9$  nm (Fig. 1b) and regulate their average size (ratio of the length to the diameter) by adding 100  $\mu\text{l}$  and 70  $\mu\text{l}$  of  $\text{AgNO}_3$  (0.02 M) to the growth solution of Au NRs. The increased length of Au NRs results in the shift of the extinction peak to longer wavelengths, from 640 to 690 nm respectively (Fig. 2b, dotted line).

According to the results of TEM, the suggested methods of synthesising  $\text{Ag}_2\text{S}$  QDs and Ag and Au NPs provided for the compatibility of the components and the formation of hybrid structures. TEM images demonstrate that the largest number of QDs are observed next to Ag and Au NPs (Fig. 1).

The spectra of optical absorption of  $\text{Ag}_2\text{S}$ /TGA QDs and  $\text{Ag}_2\text{S}$ /2-MPA QDs shifted to shorter wavelengths relative to the edge of the fundamental absorption of single crystals of silver sulphide (1.09 eV). This happened due



**Fig. 1.** TEM images demonstrating the formation of associates of  $\text{Ag}_2\text{S}$  QDs with pyramidal Ag nanoparticles (a) and Au nanorods (b)

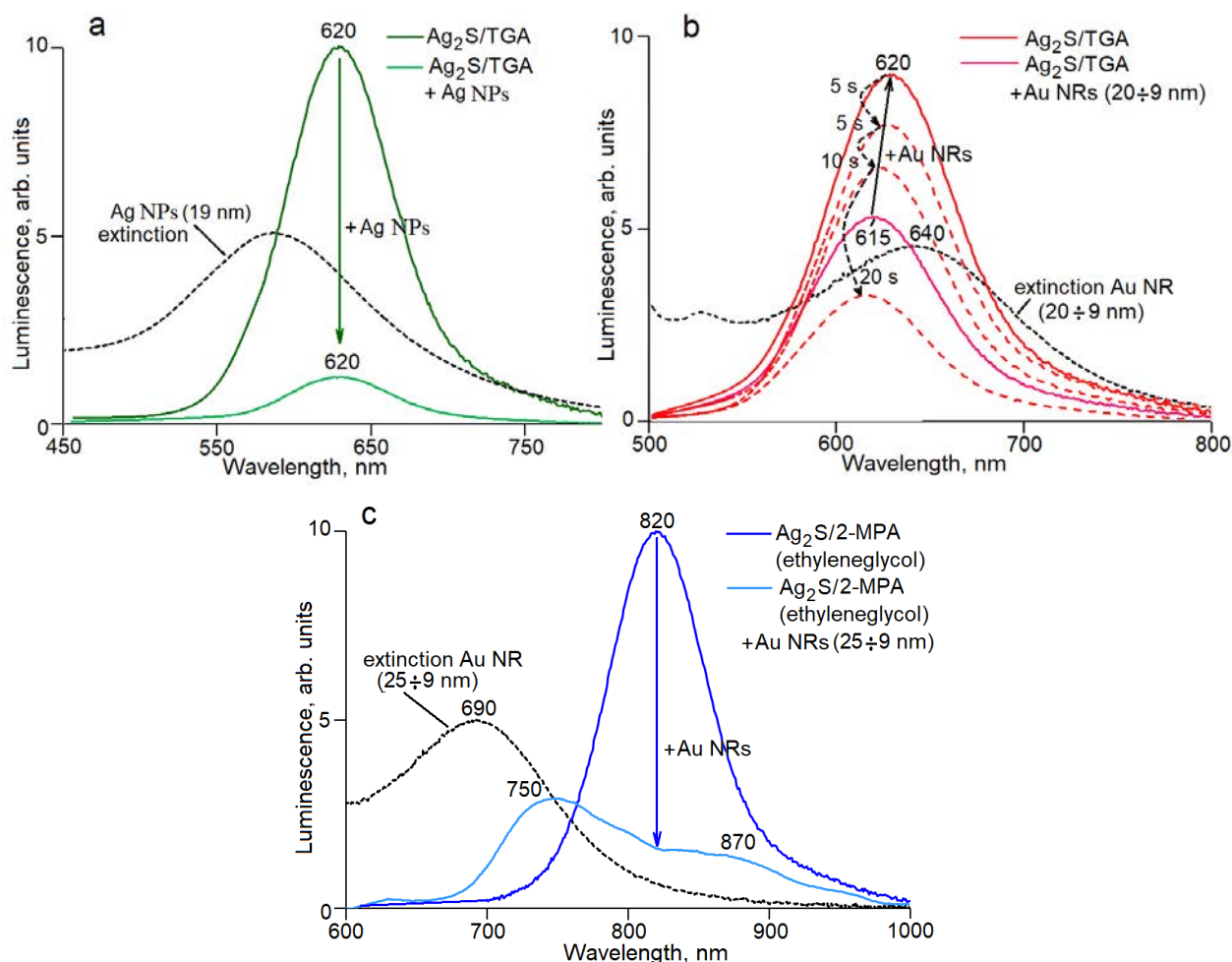
to the quantum size effect. In the absorption spectrum of colloidal  $\text{Ag}_2\text{S}/\text{TGA}$  QDs, we observed a specific feature in the 590 nm region, which was characteristic of the most probable excitonic transition in the absorption spectrum. When colloidal  $\text{Ag}_2\text{S}/\text{TGA}$  QDs were excited at the wavelength of 405 nm, we observed recombination luminescence, with the absorption band peak at 615–620 nm (Fig. 2a, b).

The absorption spectrum of colloidal  $\text{Ag}_2\text{S}/2\text{-MPA}$  QDs has a prominent peak at about 690 nm, corresponding to the most probable excitonic transition in the optical absorption spectrum. For colloidal  $\text{Ag}_2\text{S}/2\text{-MPA}$  QDs a recombination luminescence was observed with the peak at 820 nm (Fig. 2c).

Thus, the geometry and size of pyramidal Ag NPs (19 nm) and Au NRs (20÷9) ensured a significant overlap between their extinction

spectra and the luminescence spectra of  $\text{Ag}_2\text{S}/\text{TGA}$  QDs (620 nm) (Fig. 2a, b). The mixture of Au NRs (25÷9) and  $\text{Ag}_2\text{S}/2\text{-MPA}$  QDs (820 nm) did not yield any significant overlap between their extinction spectra and the luminescence spectra of  $\text{Ag}_2\text{S}/2\text{-MPA}$  QDs (Fig. 2c).

Mixtures of  $\text{Ag}_2\text{S}/\text{TGA}$  QDs and  $\text{Ag}_2\text{S}/2\text{-MPA}$  QDs with plasmonic pyramidal Ag NPs and Au NRs demonstrated complex bands in the extinction spectra, which were not simply a sum of the spectra of mixtures components. It was also noted that the optical density increased over the whole extinction spectrum, when QDs and NPs were mixed. The difference in the location of the stop band peaks of the components and redistribution of the intensity within the resulting contours indicate the presence of exciton-plasmon interaction between the components.



**Fig. 2.** The extinction spectra of pyramidal Ag NPs (a) and Au NRs with size of (20÷9) nm (b) and (25÷9) nm (c), the luminescence spectra of  $\text{Ag}_2\text{S}/\text{TGA}$  QDs (a and b),  $\text{Ag}_2\text{S}/2\text{-MPA}$  QDs (c), and their mixtures with NPs

The most interesting patterns, however, were observed in luminescence spectra of QDs mixed with plasmonic NPs. Mixtures of  $\text{Ag}_2\text{S}/\text{TGA}$  QDs (luminescence peak at 620 nm) with Ag NPs (light extinction peak at 590 nm) demonstrated a decrease in the luminescence intensity of QDs by 8 times (Fig. 2a) together with a decrease in the luminescence lifetime by 5–7 %. The observed patterns indicate that the effects of exciton-plasmon coupling are dominated by the carrier phototransfer between the components of the associates. The phototransfer blocks QDs luminescence, when the overlap between the extinction peak of Ag NPs (nanoresonator mode) and  $\text{Ag}_2\text{S}/\text{TGA}$  QDs luminescence is not complete [10, 24].

On the contrary, when the overlap between the luminescence spectra (620 nm) and the plasmon peak (640 nm) was greater, mixtures of the same samples of  $\text{Ag}_2\text{S}/\text{TGA}$  QDs with plasmonic Au NPs (20÷9 nm), demonstrated an increase in luminescence quantum yield by 1.5 times (Fig. 2b). At the same time, the intensity of QDs recombination luminescence fell below the luminescence level of the initial QD sample after a 20-second exposure to luminescence excitement. The initial increase in the intensity of  $\text{Ag}_2\text{S}/\text{TGA}$  QDs luminescence is accounted for by the Purcell effect, which presumes greater probability of optical transition in proximity to the nanoresonator [25]. However, the following significant decrease in the luminescence intensity may be caused by the photo-stimulated charge transfer between the components of the studied associates, which, as we know, blocks the luminescence [10, 24]. Incomplete luminescence quenching indicates that some of QDs are not in full contact with NPs, which is necessary for the injection of photostimulated charge carriers.

Mixtures of Au NRs (25÷9 nm, extinction peak at 690 nm) and  $\text{Ag}_2\text{S}/2\text{-MPA}$  QDs demonstrated a decrease in QDs luminescence intensity at the band peak (820 nm). In this case, a dramatic transformation of the spectral contour of  $\text{Ag}_2\text{S}/2\text{-MPA}$  QDs luminescence band was registered. However, the peak intensity grew in the region with the wavelengths shorter than 700 nm (Fig. 2b). Apparently, such a behaviour of the luminescence spectrum is connected with the quantum interference (Fano antiresonance)

during exciton-plasmon interaction [26]. At the same time, the average luminescence lifetime increased from 94 to 115 ns at the wavelength of 750 nm and decreased from 94 to 16 ns at the wavelength of 820 nm. This also indicates the presence of exciton-plasmon interaction. The enhancement of luminescence at 700 nm may be accounted for by the Purcell effect, when there is direct contact between a plasmonic nanoparticle and quantum dots. A slowdown in the luminescence decay is explained by a decrease in the effectiveness of the non-radiative recombination caused by the difference in the immediate environment of the QDs.

#### 4. Conclusions

The article suggests a new method for synthesising hybrid associates based on  $\text{Ag}_2\text{S}/\text{TGA}$  QDs,  $\text{Ag}_2\text{S}/2\text{-MPA}$  QDs, pyramidal Ag NPs, and Au NRs. The study determined the transformation effects of the luminescence spectra contours resulting from the quantum interference (the Fano effect), and the luminescence quenching occurring when there is direct contact between QDs and NPs. The observed interaction between  $\text{Ag}_2\text{S}$  QDs and plasmonic NPs indicates the possibility to regulate the spectrum and the quantum efficiency of QDs IR luminescence. However, the results of the latest experiments definitely indicate the complexity of exciton-plasmon interaction in the studied systems, as several effects are observed at the same time, including the Purcell effect, the Fano effect, and the photo-induced charge transfer between QDs and NPs.

#### Conflict of interests

The authors declare that they have no known competing financial interests or personal relationships that could have influenced the work reported in this paper.

#### References

1. Fantoni A., Fernandes M., Vygranenko Y., Louro P., Vieira M., Silva R. P. O., Texeira D., Ribeiro A. P. C., Prazeres M., Alegria E. C. B. A. Analysis of metallic nanoparticles embedded in thin film semiconductors for optoelectronic applications. *Optical and Quantum Electronics*. 2018;50(246): 1–12. <https://doi.org/10.1007/s11082-018-1523-z>
2. Hentschel M., Metzger B., Knabe B., Buse K., Giessen H. Linear and nonlinear optical properties of

- hybrid metallic–dielectric plasmonic nanoantennas. *Beilstein J. Nanotechnol.* 2016;7(111): 111–120. <https://doi.org/10.3762/bjnano.7.13>
3. Khan I., Saeed K., Khan I. Nanoparticles: Properties, applications and toxicities. *Arabian Journal of Chemistry.* 2019;12(7): 908–931. <https://doi.org/10.1016/j.arabj.2017.05.011>
4. Daniel M. C., Astruc D. Gold nanoparticles: assembly, supramolecular chemistry, quantum-size-related properties, and applications toward biology, catalysis, and nanotechnology. *Chemical Reviews.* 2004;104(1): 293–346. <https://doi.org/10.1021/cr030698+>
5. Garcia M. A. Surface plasmons in metallic nanoparticles: fundamentals and applications. *Journal of Physics D: Applied Physics.* 2011;44(28): 283001(1–20). <https://doi.org/10.1088/0022-3727/44/28/283001>
6. Luo Y., Zhao J. Plasmon-exciton interaction in colloiddally fabricated metal nanoparticle-quantum emitter nanostructures. *Nano Research.* 2019;12(9): 2164–2171. <https://doi.org/10.1007/s12274-019-2390-z>
7. Kim K.-S., Kim J.-H., Kim H., Laquai F., Arifin E., Lee J.-K., Yoo S., Sohn B.-H. Switching Off FRET in the hybrid assemblies of diblock copolymer micelles, quantum dots, and dyes by plasmonic nanoparticles. *ACS Nano.* 2012;6(6): 5051–5059. <https://doi.org/10.1021/nn301893e>
8. Ovchinnikov O. V., Kondratenko T. S., Grevtseva I. G., Smirnov M. S., Pokutnyi S. I. Sensitization of photoprocesses in colloidal Ag<sub>2</sub>S quantum dots by dye molecules. *Journal of Nanophotonics.* 2016;10(3): 033505. <https://doi.org/10.1117/1.JNP.10.033505>
9. Ovchinnikov O. V., Smirnov M. S., Shapiro B. I., Shatskikh T. S., Latyshev A. N., Mien Ph. Thi Hai, Khokhlov V. Yu. Spectral manifestations of hybrid association of CdS colloidal quantum dots with methylene blue molecules. *Optics and Spectroscopy.* 2013;115(3): 389–397. <https://doi.org/10.7868/S0030403413090195>
10. Kondratenko T. S., Ovchinnikov O. V., Grevtseva I. G., Smirnov M. S. Organic–inorganic nanostructures for luminescent indication in the near-infrared range. *Technical Physics Letters.* 2016;42(4): 365–367. <https://doi.org/10.1134/S1063785016040088>
11. Etacheri V., Georgekutty R., Seery M. K., Pillai S. C. Single step morphology-controlled synthesis of silver nanoparticles. *MRS Proceedings.* 2009;1217: 1217-Y08-40. <https://doi.org/10.1557/PROC-1217-Y08-40>
12. Shah K. W., Sreethawong T., Liu S. H., Zhang S. Y., Li S. T., Han M. Y. Aqueous route to facile, efficient and functional silica coating of metal nanoparticles at room temperature. *Nanoscale.* 2014;6(19): 11273–11282. <https://doi.org/10.1039/c4nr03306j>
13. Fedutik Y., Temnov V. V., Schöps O., Woggon U., Artemyev M. V. Exciton-plasmon-photon conversion in plasmonic nanostructures. *Physical Review Letters.* 2007;99(13): 136802. <https://doi.org/10.1103/PhysRevLett.99.136802>
14. Zhang W., Govorov A. O., Bryant G. W. Semiconductor-metal nanoparticle molecules: hybrid excitons and the nonlinear fano effect. *Physical Review Letters.* 2006;97(14): 146804. <https://doi.org/10.1103/PhysRevLett.97.146804>
15. Hildebrandt N., Spillmann Ch. M., Algar W. R., Pons T., Stewart M. H., Oh E., Susumu K., Díaz S. A., Delehanty J. B., Medintz I. L. Energy transfer with semiconductor quantum dot bioconjugates: A versatile platform for biosensing, energy harvesting, and other developing applications. *Chemical Reviews.* 2017; 117(2): 536–711. <https://doi.org/10.1021/acs.chemrev.6b00030>
16. Resch-Genger U., Grabolle M., Cavaliere-Jaricot S., Nitschke R., Nann T. Quantum dots versus organic dyes as fluorescent labels. *Nature Methods.* 2008;5(5): 763–775. <https://doi.org/10.1038/nmeth.1248>
17. Ievlev V. M., Latyshev A. N., Ovchinnikov O. V., Smirnov M. S., Klyuev V. G., Kholkina A. M., Utekhin A. N., Evlev A. B. Photostimulated formation of anti-stokes luminescence centers in ionic covalent crystals. *Doklady Physics.* 2006;51(8): 400–402. <https://doi.org/10.1134/S1028335806080027>
18. Ovchinnikov O. V., Smirnov M. S., Latyshev A. N., Stasel'ko D. I. Photostimulated formation of sensitized anti-stokes luminescence centers in AgCl(I) microcrystals. *Optics and Spectroscopy.* 2007;103(3): 482–489. <https://doi.org/10.1134/S0030400X07090172>
19. Durach M., Rusina A., Stockman M. I., Nelson K., Toward full spatiotemporal control on the nanoscale. *Nano Letters.* 2007;7(10): 3145–3149. <https://doi.org/10.1021/nl071718g>
20. Komarala V. K., Rakovich Yu. P., Bradley A. L. Off-resonance surface plasmon enhanced spontaneous emission from CdTe quantum dots. *Applied Physics Letters.* 2006;89(25): 253118. <https://doi.org/10.1063/1.2422906>
21. Gong H. M., Wang X. H., Du Y. M., Wang Q. Q. Optical nonlinear absorption and refraction of CdS and CdS-Ag core-shell quantum dots. *The Journal of Chemical Physics.* 2006;125(2): 024707. <https://doi.org/10.1063/1.2212400>
22. Ovchinnikov O. V., Aslanov S. V., Smirnov M. S., Grevtseva I. G., Perepelitsa A. S. Photostimulated control of luminescence quantum yield for colloidal Ag<sub>2</sub>S/2-MPA quantum dots. *RSC Advances.* 2019;9(64): 37312–37320. <https://doi.org/10.1039/C9RA07047H>
23. Kondratenko T. S., Zvyagin A. I., Smirnov M. S., Grevtseva I. G., Perepelitsa A. S., Ovchinnikov O. V. Luminescence and nonlinear optical properties of

colloidal Ag<sub>2</sub>S quantum dots. *Journal of Luminescence*. 2019;208: 193-200. <https://doi.org/10.1016/j.jlumin.2018.12.042>

24. Kondratenko T. S., Grevtseva I. G., Zvyagin A. I., Ovchinnikov O. V., Smirnov M. S. Luminescence and nonlinear optical properties of hybrid associates of Ag<sub>2</sub>S quantum dots with molecules of thiazine dyes. *Optics and Spectroscopy*. 2018;124(5): 673–680. <https://doi.org/10.21883/OS.2018.05.45945.310-17>

25. Purcell E. M. Spontaneous emission probabilities at radio frequencies. *Physical Review*. 1946;69: 681. [https://doi.org/10.1007/978-1-4615-1963-8\\_40](https://doi.org/10.1007/978-1-4615-1963-8_40)

26. Fano U. Effects of configuration interaction on intensities and phase shifts. *Physical Review*. 1961;124: 1866–1878. <https://doi.org/10.1103/PhysRev.124.1866>

### Information about the authors

*Irina G. Grevtseva*, PhD in Physics and Mathematics, lecturer, Department of Optics and Spectroscopy, Voronezh State University, Voronezh, Russian Federation; e-mail: [grevtseva\\_ig@inbox.ru](mailto:grevtseva_ig@inbox.ru). ORCID iD: <https://orcid.org/0000-0002-1964-1233>.

*Tamara A. Chevychelova*, postgraduate student Department of Optics and Spectroscopy, Voronezh State University, Voronezh, Russian Federation; e-mail: [t.chevychelova@rambler.ru](mailto:t.chevychelova@rambler.ru). ORCID iD: <https://orcid.org/0000-0001-8097-0688>.

*Violetta N. Derepko*, postgraduate student Department of Optics and Spectroscopy, Voronezh State University, Voronezh, Russian Federation;

e-mail: [viol.physics@gmail.com](mailto:viol.physics@gmail.com). ORCID iD: <https://orcid.org/0000-0002-9096-5388>

*Oleg V. Ovchinnikov*, DSc in Physics and Mathematics, Professor, Department of Optics and Spectroscopy, Voronezh State University, Voronezh, Russian Federation; e-mail: [ovchinnikov\\_o\\_v@rambler.ru](mailto:ovchinnikov_o_v@rambler.ru). ORCID iD: <https://orcid.org/0000-0001-6032-9295>

*Mikhail S. Smirnov*, PhD in Physics and Mathematics, Associate Professor, Department of Optics and Spectroscopy, Voronezh State University, Voronezh, Russian Federation; e-mail: [smirnov\\_m\\_s@mail.ru](mailto:smirnov_m_s@mail.ru). ORCID iD: <https://orcid.org/0000-0001-8765-0986>

*Aleksey S. Perepelitsa*, PhD in Physics and Mathematics, senior lecturer, Department of Optics and Spectroscopy, Voronezh State University, Voronezh, Russian Federation; e-mail: [a-perepelitsa@yandex.ru](mailto:a-perepelitsa@yandex.ru). ORCID iD: <https://orcid.org/0000-0001-8097-0688>.

*Anna S. Parshina*, master's degree student, Department of Materials Science and Nanotechnology, Voronezh State University, Voronezh, Russian Federation; e-mail: [anyuta\\_parshina@mail.ru](mailto:anyuta_parshina@mail.ru). ORCID iD: <https://orcid.org/0000-0002-9455-2062>

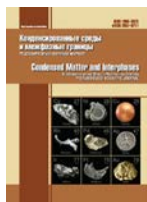
All authors have read and approved the final manuscript.

*Received 25 December 2020; Approved after reviewing 13 January 2021; Accepted 15 March 2021; Published online 25 March 2021*

*Translated by Yulia Dymant*

*Edited and proofread by Simon Cox*





# Condensed Matter and Interphases

Kondensirovannyye Sredy i Mezhhfaznye Granitsy  
<https://journals.vsu.ru/kcmf/>

## Original articles

Original article

<https://doi.org/10.17308/kcmf.2021.23/3296>

## Phase relations in the $Tl_2Te-TlBiTe_2-TlTbTe_2$ system

S. Z. Imamaliyeva<sup>1</sup>✉, G. I. Alakbarzade<sup>2</sup>, D. M. Babanly<sup>1,3</sup>, M. V. Bulanova<sup>4</sup>,  
V. A. Gasymov<sup>1</sup>, M. B. Babanly<sup>1</sup>

<sup>1</sup>Institute of Catalysis and Inorganic Chemistry of the Azerbaijan National Academy of Sciences,  
113 H. Javid ave., Baku AZ-1143, Azerbaijan

<sup>2</sup>Azerbaijan National Aerospace Agency,  
159 Azadlig ave, AZ-1106, Baku, Azerbaijan

<sup>3</sup>Azerbaijan State Oil and Industry University, French-Azerbaijani University (UFAZ),  
16/21 Azadliq prospekti, Baku AZ-1101, Azerbaijan

<sup>4</sup>Frantsevich Institute for Problems of Materials Science, NASU,  
3 Krzhizhanovskiy st., Kiev 03142, Ukraine

### Abstract

The phase equilibria in the  $Tl_2Te-TlBiTe_2-TlTbTe_2$  concentration area of the Tl–Bi–Tb–Te quaternary system were investigated by using the differential thermal analysis and powder X-ray diffraction techniques. The diagram of the solid-phase equilibria of this system at room temperature was constructed. It was established that the  $Tl_9BiTe_6-Tl_9TbTe_6$  section divides the  $Tl_2Te-TlBiTe_2-TlTbTe_2$  system into two independent subsystems. It was found that the  $Tl_2Te-Tl_9BiTe_6-Tl_9TbTe_6$  subsystem is characterized by the formation of a wide field of solid solutions with a  $Tl_5Te_3$  structure ( $\delta$ -phase) that occupy more than 90% of the area of the concentration triangle. The results of X-ray phase analysis of alloys of the  $Tl_9BiTe_6-Tl_9TbTe_6-TlTbTe_2-TlBiTe_2$  subsystem showed the formation of wide regions of solid solutions based on  $TlTbTe_2$  and  $TlBiTe_2$  along the section of  $TlTbTe_2-TlBiTe_2$  ( $\beta_1$ - and  $\beta_2$ -phases) and made it possible to determine the location of the heterogeneous phase regions in this subsystem. The parameters of crystal lattices of mutually saturated compositions of the  $\beta_1$ -,  $\beta_2$ -, and  $\delta$ -phases are calculated from powder diffraction patterns.

The paper also presents some polythermal sections, isothermal sections at 740 and 780 K of the phase diagram, as well as projections of the liquidus and solidus surfaces of the  $Tl_2Te-Tl_9BiTe_6-Tl_9TbTe_6$  subsystem. The liquidus surface consists of three fields of the primary crystallization of  $\alpha$  ( $Tl_2Te$ )-,  $\delta$ - and  $\beta_1$ -phase. The constructed isothermal sections clearly demonstrate that the directions of the tie lines do not coincide with the T–x planes of the studied internal sections, which is characteristic of non-quasi-binary polythermal sections. The obtained new phases are of interest as potential thermoelectric and magnetic materials.

**Keywords:**  $Tl_2Te-TlBiTe_2-TlTbTe_2$  system, phase equilibria, solid solutions, powder X-ray diffraction, crystal lattice, topological insulators

**Acknowledgements:** the work has been carried out within the framework of the international joint research laboratory “Advanced Materials for Spintronics and Quantum Computing” (AMSQC) established between the Institute of Catalysis and Inorganic Chemistry of ANAS (Azerbaijan) and Donostia International Physics Center (Basque Country, Spain) and partially supported by the Science Development Foundation under the President of the Republic of Azerbaijan, a grant EİF/MQM/Elm-Tehsil-1-2016-1(26)-71/01/4-M-33.

**For citation:** Imamaliyeva S. Z., Alakbarzade G. I., Babanly D. M., Bulanova M. V., Gasymov V. A., Babanly M. B. Phase relations in the  $Tl_2Te-TlBiTe_2-TlTbTe_2$  system. *Kondensirovannyye sredy i mezhhfaznye granitsy = Condensed Matter and Interphases*. 2021;23 (1): 32–40. <https://doi.org/10.17308/kcmf.2021.23/3296>

✉ Samira Zakir Imamaliyeva, e-mail: samira9597a@gmail.com

© Imamaliyeva S. Z., Alakbarzade G. I., Babanly D. M., Bulanova M. V., Gasymov V. A., Babanly M. B., 2021



The content is available under Creative Commons Attribution 4.0 License.

**Для цитирования:** Имамалиева С. З., Алекберзаде Г. И., Бабанлы Д. М., Буланова М. В., Гасымов В. А., Бабанлы М. Б. Фазовые равновесия в системе  $Tl_2Te-TlBiTe_2-TlTbTe_2$ . *Конденсированные среды и межфазные границы*. 2021;23(1): 32–40. <https://doi.org/10.17308/kcmf.2021.23/3296>

## 1. Introduction

Binary and multinary chalcogenides of metals are of great interest as prospective materials with different functional properties such as electronic, optical, thermoelectric, topological insulators et al. [1–9].

Despite the toxicity of thallium, complex thallium chalcogenides are closely monitored as topological insulators [10–15], Weyl semimetals [16, 17], photodetectors [18, 19], X-ray and gamma radiation detectors [20, 21], as well as materials which exhibit abnormally low thermal conductivity [22–25].

Insertion to the crystal structure of chalcogenides of d- and f- elements can improve their properties and give them additional functionality, for example, the magnetic properties [26–29].

For the optimization of the functional properties of the above materials, it is necessary to plot phase diagrams of these systems, especially for the systems consisting of structural analogues, since it can be expected that they form wide areas of solid solutions [7, 30–32].

This work is a continuation of our studies on the phase equilibria in systems based on thallium-REE tellurides, in which wide areas of solid solutions with a  $Tl_5Te_3$  structure are revealed, which are of practical interest as thermoelectric materials with anomalously low thermal conductivity [32–36].

The aim of the present work is the investigation of the solid-phase relations in the  $Tl_2Te-TlBiTe_2-TlTbTe_2$  system.

The starting compounds and phase equilibria in the boundary systems were studied in a number of works [33, 37–43].

$Tl_2Te$  melts congruently at 698 K [37], and has a monoclinic structure (Sp.Gr.  $C_2/C$ ;  $a = 15.662$ ;  $b = 8.987$ ;  $c = 31.196 \text{ \AA}$ ,  $\beta = 100.76^\circ$ ,  $z = 44$ ) [38].

$TlBiTe_2$  melts congruently at 820 K [39], and crystallizes in a hexagonal structure (Sp. Gr.  $R\bar{3}m$ ) with parameters  $a = 4.526$ ;  $c = 23.12 \text{ \AA}$ ;  $z = 3$  [40].

$TlTbTe_2$  compound is structural analogue of  $TlBiTe_2$  and has the following lattice parameters:  $a = 4.416$ ;  $c = 24.27 \text{ \AA}$ ;  $z = 3$  [41].

$Tl_2Te-TlBiTe_2$  system studied by the authors of [38] is characterized by the formation of the

$Tl_9BiTe_6$  compound which melts congruently at 830 K. This compound crystallizes in a tetragonal structure with the following lattice parameters:  $a = 8.855$ ;  $c = 13.048 \text{ \AA}$ ,  $z = 2$  [42]. According to Ref. [39], in the  $Tl_2Te-Tl_9BiTe_6$  system, continuous solid solutions with a morphotropic phase transition near  $Tl_2Te$  were detected. Considering that  $Tl_2Te$  and  $Tl_9BiTe_6$  crystallize in different crystal structures, this statement seems unlikely. Therefore, the authors of [43] re-studied the phase relations in the  $Tl_2Te-Tl_9BiTe_6$  system and showed that the system is a quasi-binary system of the peritectic type and is characterized by the formation of limited solid solutions based on the initial compounds.

$Tl_2Te-TlTbTe_2$  system was studied only in the composition interval of  $\geq 80 \text{ mol\% } Tl_2Te$ . It is shown that it is characterized by the formation of a tetragonal  $Tl_9TbTe_6$  compound which melts with decomposition by a peritectic reaction at 780 K and has the following lattice parameters:  $a = 8.871$ ;  $c = 12.973 \text{ \AA}$ ,  $z = 2$  [35]. The  $Tl_2Te-Tl_9TbTe_6$  subsystem is characterized by the formation of solid solutions with  $Tl_5Te_3$  type tetragonal structure based on  $Tl_9TbTe_6$ .

In the  $Tl_9TbTe_6-Tl_9BiTe_6$  system, continuous solid solutions based on the starting compounds were found [33].

In the  $TlBiTe_2-TlTbTe_2$  system, it was shown that despite the isostructural character of the initial compounds, the system is characterized by the limited mutual solubility of the initial components. The solubility based on  $TlBiTe_2$  reaches  $\sim 45 \text{ mol\%}$  and the solubility based on  $TlTbTe_2$  is about  $22 \text{ mol\%}$  [44].

## 2. Experimental

### 2.1. Materials and synthesis

Initial binary and ternary compounds were synthesized by the direct interaction of the high purity elements, all from Alfa Aesar (Germany): (thallium, CAS No 7440-28-0; tellurium, 13494-80-9; bismuth, 7440-69-9; terbium, 7440-27-9).

$Tl_2Te$ ,  $Tl_9BiTe_6$ , and  $TlBiTe_2$ , 10 grams each, were prepared by the melting of the elements in evacuated ( $\sim 10^{-2} \text{ Pa}$ ) quartz ampoules in a single-zone electric furnace at 850 K. To

achieve an equilibrium state, after synthesis, the intermediate ingot of  $\text{TlBiTe}_2$  was subjected to heat treatment 700 K for 500 h.

The synthesis of the incongruently melting compounds,  $\text{Tl}_9\text{TbTe}_6$  and  $\text{TlTbTe}_2$ , was carried out by the ceramic method at 1000 K for 100 h. We used a graphitized ampoule in order to prevent the reaction of terbium with quartz. Then the ingots were slowly cooled down to room temperature, crushed in an agate mortar, pressed into pellets and the heating procedure was repeated at 900 K for 500 h.

The purity of the synthesized compounds was controlled by the differential thermal analysis (DTA) and powder X-ray diffraction (PXRD) method.

Samples of the  $\text{Tl}_2\text{Te}-\text{TlSbTe}_2-\text{TlTbTe}_2$  system, 1 g each, were prepared by fusing pre-synthesized and identified binary and ternary compounds in evacuated quartz ampoules in a single-zone electric furnace at a temperature 30–50° higher than the melting temperature of the compounds, followed by cooling in a switched off furnace.

## 2.2. Methods

The PXRD (Bruker D8 diffractometer,  $\text{CuK}_\alpha$  radiation) was used to control the purity of the synthesized compounds and intermediate

samples. The analysis was carried out at room temperature between  $10^\circ \leq 2\theta \leq 70^\circ$ . The lattice constants were calculated by indexing of powder patterns using Topas V3.0 software.

DTA was performed using a NETZSCH 404 F1 Pegasus differential scanning calorimeter within room temperature and ~1400 K depending on the composition of the alloys at a heating rate of  $10 \text{ K} \times \text{min}^{-1}$ . The temperatures of thermal effects were taken mainly from the heating curves.

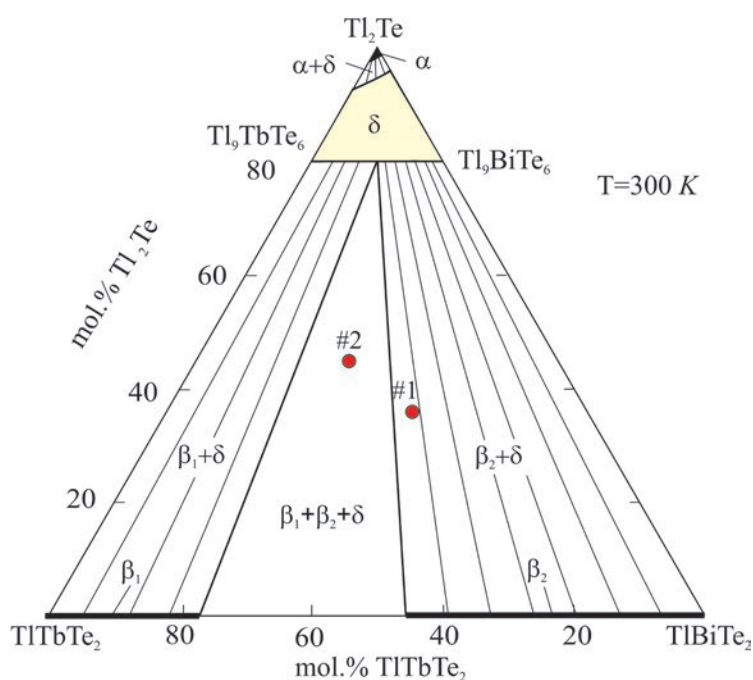
## 3. Results and discussion

### 3.1. Solid-phase equilibria diagram of the $\text{Tl}_2\text{Te}-\text{TlBiTe}_2-\text{TlTbTe}_2$ system

Fig. 1 presents the solid-phase equilibria diagram of the  $\text{Tl}_2\text{Te}-\text{TlBiTe}_2-\text{TlTbTe}_2$  system.

As can be seen, the stable section  $\text{Tl}_9\text{BiTe}_6-\text{Tl}_9\text{TbTe}_6$  characterized by the formation of a continuous series of solid solutions [36] divides this system into two independent subsystems.

$\text{Tl}_2\text{Te}-\text{Tl}_9\text{BiTe}_6-\text{Tl}_9\text{TbTe}_6$  subsystem is characterized by the formation of a wide field of solid solutions with a  $\text{Tl}_5\text{Te}_3$  structure ( $\delta$ -phase) that occupy more than 90% of the area of the concentration triangle. Solid solutions based on  $\text{Tl}_2\text{Te}$  ( $\alpha$ -phase) form within a narrow region. The regions of the  $\alpha$ - and  $\delta$ -phases are separated by a two-phase region  $\alpha + \delta$ . It should be noted



**Fig. 1.** The solid-phase equilibria diagram of the  $\text{Tl}_2\text{Te}-\text{TlBiTe}_2-\text{TlTbTe}_2$  system

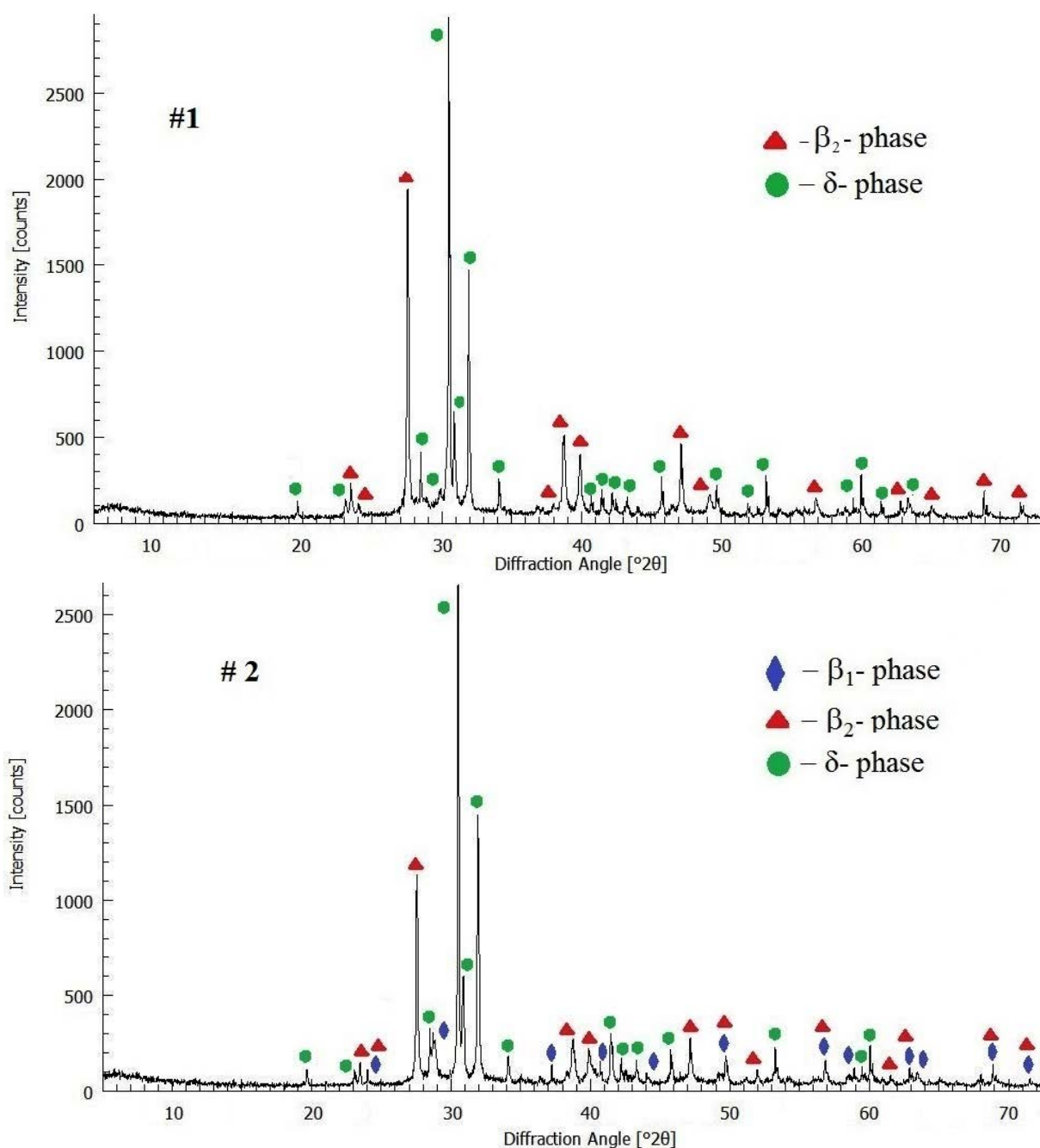
that a similar scheme of phase equilibria was found when studying the  $\text{Tl}_2\text{Te}-\text{Tl}_9\text{BiTe}_6-\text{Tl}_9\text{ErTe}_6$  system [43].

While studying the  $\text{Tl}_9\text{BiTe}_6-\text{Tl}_9\text{TbTe}_6-\text{TlTbTe}_2-\text{TlBiTe}_2$  subsystem, a number of alloys from this concentration region were investigated. Also, we used the results from our previous papers [36, 44].

The interaction of the  $\delta$ -phase with solid solutions based on  $\text{TlTbTe}_2$  ( $\beta_1$ ) and  $\text{TlBiTe}_2$  ( $\beta_2$ )

leads to the formation of wide two-phase ( $\beta_1+\delta$  and  $\beta_2+\delta$ ) fields separated by a  $\beta_1+\beta_2+\delta$  three-phase area. The location and extent of the phase regions are confirmed by XRD data. As an example, Fig. 2 shows PXRD patterns from the  $\beta_1+\delta$  two-phase (# 1) and  $\beta_1+\beta_2+\delta$  three-phase (# 2) regions.

Based on the index of the PXRD patterns of the samples # 1 and # 2, we obtained the following crystal lattice parameters:



**Fig. 2.** The PXRD patterns of samples #1 and #2 from the two- and three-phase areas of the  $\text{Tl}_9\text{BiTe}_6-\text{Tl}_9\text{TbTe}_6-\text{TlTbTe}_2-\text{TlBiTe}_2$  subsystem

Sample #1:  $a=4.4883$ ,  $c=23.580$  Å ( $\beta_1$ -phase);  
 $a=8.8626$ ,  $c=13.008$  Å ( $\delta$ -phase)

Sample #2:  $a=4.4793$ ,  $c=23.481$  Å ( $\beta_1$ -phase);  
 $a=4.4472$ ,  $c=24.007$  Å ( $\beta_2$ -phase);  $a=8.8630$ ,  
 $c=13.005$  Å ( $\delta$ -phase).

A comparison of these data with the results of [36, 44] shows that sample #1 consists of a two-phase mixture of a  $\beta_1$ -phase with a composition of 40 mol%  $\text{TlTbTe}_2$  along the  $\text{TlBiTe}_2$ – $\text{TlTbTe}_2$  and a  $\delta$ -phase with a composition of 50 mol%  $\text{Tl}_9\text{TbTe}_6$  along the  $\text{Tl}_9\text{BiTe}_6$ – $\text{Tl}_9\text{TbTe}_6$  section. Sample #2 consist of a three-phase mixture of  $\beta_1+\beta_2+\delta$  with the following phase compositions:  $\beta_1$  and  $\beta_2$  – respectively, 45 and 77 mol%  $\text{TlTbTe}_2$  along the  $\text{TlBiTe}_2$ – $\text{TlTbTe}_2$  section, and  $\delta$  – 50 mol%  $\text{Tl}_9\text{TbTe}_6$ . These coincide with the data in Fig. 1.

### 3.2. The liquidus surface of the $\text{Tl}_2\text{Te}$ – $\text{Tl}_9\text{BiTe}_6$ – $\text{Tl}_9\text{TbTe}_6$ subsystem

The liquidus surface of the  $\text{Tl}_2\text{Te}$ – $\text{Tl}_9\text{BiTe}_6$ – $\text{Tl}_9\text{TbTe}_6$  system consists of three fields of the primary crystallization of the  $\alpha$ - and  $\delta$ -phases and the  $\beta_2$ -phase based on the  $\text{TlTbTe}_2$  compound (Fig. 3). These fields are separated by  $p_1p_1'$  and  $p_2p_2'$  lines, which correspond to the  $L+\beta_2 \leftrightarrow \beta$  and  $L+\delta \leftrightarrow \alpha$  monovariant peritectic process. The solidus surface consists of two areas of

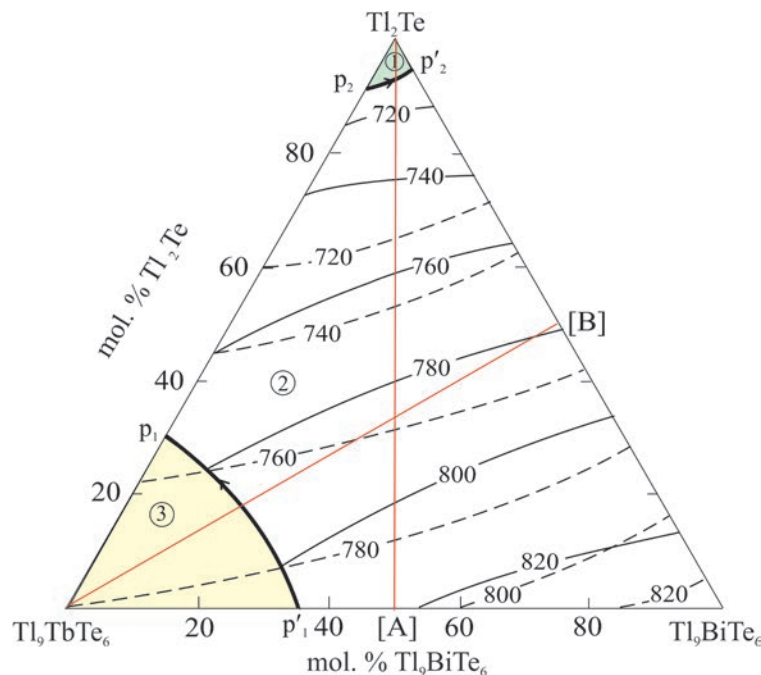
the completion of crystallization of the  $\alpha$ - and  $\delta$ -phases.

### 3.3. Some polythermal and isothermal sections of the phase diagram of the $\text{Tl}_2\text{Te}$ – $\text{Tl}_9\text{BiTe}_6$ – $\text{Tl}_9\text{TbTe}_6$ subsystem

In order to confirm the correct construction of the liquidus surface of the  $\text{Tl}_2\text{Te}$ – $\text{Tl}_9\text{BiTe}_6$ – $\text{Tl}_9\text{TbTe}_6$  subsystem and to refine the boundaries of areas of primary crystallization of the  $\delta$ -phase and  $\text{TlTbTe}_2$ , the isopleth sections  $\text{Tl}_2\text{Te}$ –[A] and  $\text{Tl}_9\text{TbTe}_6$ –[B] (A and B – are alloys with compositions 1:1 from the boundary sections  $\text{Tl}_9\text{BiTe}_6$ – $\text{Tl}_9\text{TbTe}_6$  and  $\text{Tl}_2\text{Te}$ – $\text{Tl}_9\text{BiTe}_6$ ) of the phase diagram were constructed.

The liquidus curve along the  $\text{Tl}_2\text{Te}$ –[A] section consists of two curves corresponding to the primary crystallization of the  $\alpha$ - and  $\delta$ -phases. Their intersection point corresponds with the onset of the monovariant peritectic reaction  $L+\delta \leftrightarrow \alpha$ .

In the  $\text{Tl}_9\text{TbTe}_6$ –[B] section, in the composition range up to ~65 mol%  $\text{Tl}_9\text{TbTe}_6$ , the  $\delta$ -phase crystallizes from the melt, while in the  $\text{TlTbTe}_2$ –rich alloys the  $\beta_1$ -phase based on  $\text{TlTbTe}_2$  first crystallizes, then the monovariant peritectic equilibrium  $L+\beta_1 \leftrightarrow \delta$  takes place. In the latter reaction, the  $\beta_1$ -phase is completely consumed and the excess of melt crystallizes into the  $\delta$ -phase.



**Fig. 3.** Projections of the liquidus (solid lines) and solidus (dashed lines) surfaces of the  $\text{Tl}_2\text{Te}$ – $\text{Tl}_9\text{BiTe}_6$ – $\text{Tl}_9\text{TbTe}_6$  subsystem. Primary crystallization fields of phases: 1 –  $\alpha$ ; 2 –  $\delta$ ; 3 –  $\beta_1$ . Red lines show the studied  $\text{Tl}_2\text{Te}$ –[A] and  $\text{Tl}_9\text{TbTe}_6$ –[B] polythermal sections of the subsystem

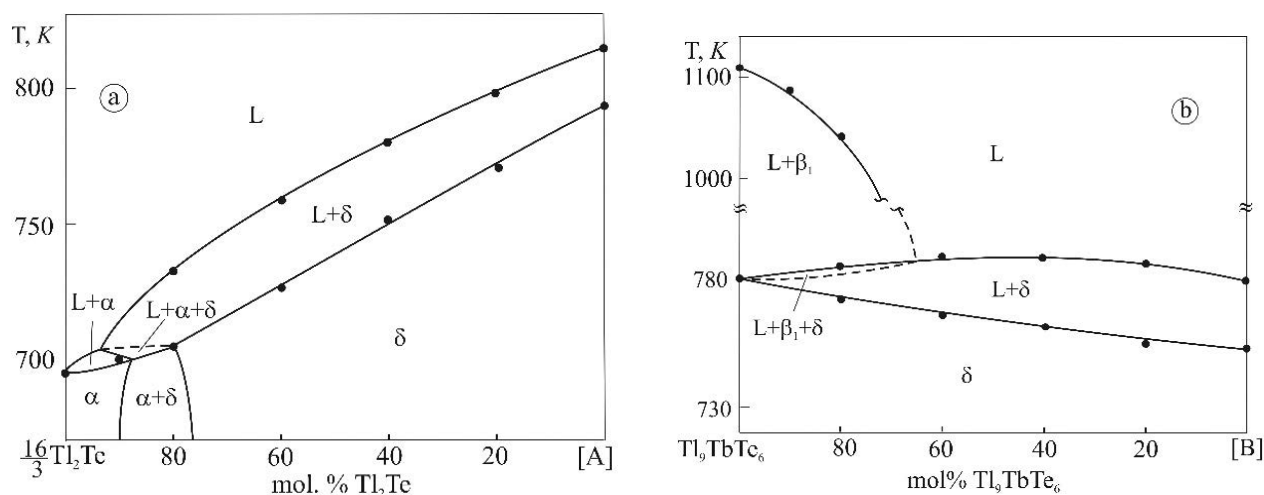
The presence of monovariant peritectic reactions  $L+\beta_1 \leftrightarrow \delta$  and  $L+\delta \leftrightarrow \delta$  (Fig. 3,  $p_2p_2'$  and  $p_2p_2$  curves) in the  $Tl_2Te-Tl_9BiTe_6-Tl_9TbTe_6$  system should lead to the formation of  $L+\alpha+\delta$  and  $L+\beta_1+\delta$  three-phase regions on the polythermal sections of  $Tl_2Te$ -[A] and  $Tl_9TbTe_6$ -[B], accordingly (Fig. 4). The very narrow temperature ranges of these reactions do not allow us to determine these areas by the DTA method. Taking into account the well-known principles [45] of the construction of polythermal sections, the regions  $L+\beta_1+\delta$  and  $L+\alpha+\delta$  in the relevant section were delimited by dashed lines.

The isothermal sections of the phase diagram are important for choosing the composition of

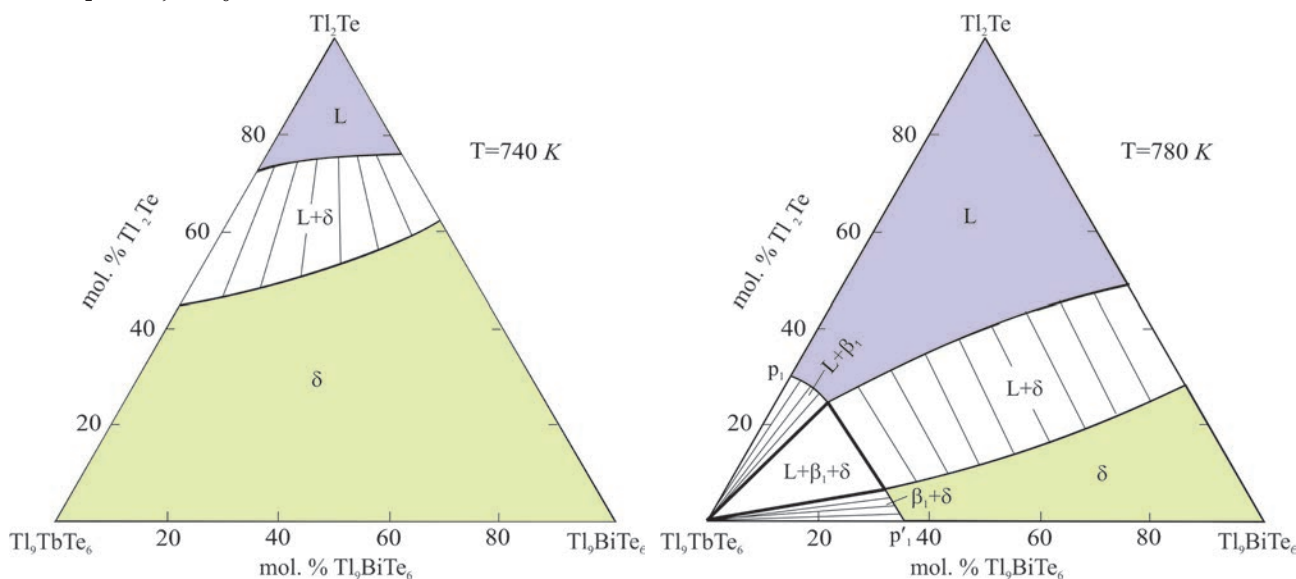
solution-melts when growing single crystals by directional crystallization.

As can be seen, from the isothermal sections at 740 and 780 K, the first consists of conjugated liquidus and solidus curves, delimiting single-phase regions L and  $\delta$ . These curves are connected by tie lines and delimit the  $L + \delta$  two-phase area. The isothermal section at 780 K in addition to these phase regions, also reflects the heterogeneous regions  $L+\beta_1$ ,  $\beta_1+\delta$ , and  $L+\beta_1+\delta$ , which are delimited taking into account data on the  $Tl_2Te-Tl_9TbTe_6$  and  $Tl_2Te-Tl_9TbTe_6$  boundary systems [35, 43].

A comparison of the isothermal (Fig. 5) and polythermal (Fig. 4) sections of the phase diagram



**Fig. 4.**  $Tl_2Te$ -[A] and  $Tl_9TbTe_6$ -[B] polythermal sections of the phase diagram of the  $Tl_2Te-Tl_9BiTe_6-Tl_9TbTe_6$  subsystem of the Tl-Bi-Tb-Te quaternary system. A and B are equimolar compositions of the  $Tl_9BiTe_6-Tl_9TbTe_6$  and  $Tl_2Te-Tl_9BiTe_6$  boundary systems on Fig. 3



**Fig. 5.** Isothermal sections at 740 and 780 K of the  $Tl_2Te-Tl_9BiTe_6-Tl_9TbTe_6$  subsystem

of the  $Tl_2Te-Tl_9BiTe_6-Tl_9TbTe_6$  system clearly demonstrates that the directions of the tie lines do not coincide with the  $T-x$  planes of the studied internal sections, which is characteristic of non-quasi-binary polythermal sections.

#### 4. Conclusion

The character of the solid-phase equilibria in the  $Tl_2Te-TlBiTe_2-TlTbTe_2$  system is established by using the DTA and powder XRD. A diagram of solid-phase equilibria at room temperature of this system is constructed, as well as a number of polythermal and isothermal sections and projections of the surfaces of liquidus and solidus in the  $Tl_2Te-Tl_9BiTe_6-Tl_9TbTe_6$  composition range. The  $Tl_9BiTe_6-Tl_9TbTe_6$  section, characterized by the formation of a continuous series of solid solutions ( $\delta$ -phase), divides the  $Tl_2Te-TlBiTe_2-TlTbTe_2$  system into two independent subsystems. The  $Tl_9BiTe_6-TlBiTe_2-TlTbTe_2-Tl_9TbTe_6$  subsystem is characterized by the formation of the wide areas of the solid solutions based on  $TlTbTe_2$  ( $\beta_1$ -phase) and  $TlBiTe_2$  ( $\beta_2$ -phase). The homogeneity region of the  $\delta$ -phase covers a large (> 90% of the  $Tl_2Te-Tl_9BiTe_6-Tl_9TbTe_6$  subsystem area). The obtained solid solutions  $\beta_1$ ,  $\beta_2$ , and  $\delta$  are of great interest as potential magnetic topological insulators and thermoelectric materials.

#### Conflict of interests

The authors declare that they have no known competing financial interests or personal relationships that could have influenced the work reported in this paper.

#### References

1. Ahluwalia G. K. (ed.). *Applications of chalcogenides: S, Se, and Te*. Switzerland: Springer; 2017. 461 p. <https://doi.org/10.1007/978-3-319-41190-3>
2. Alonso-Vante N. Outlook. In: *Chalcogenide materials for energy conversion: Pathways to oxygen and hydrogen reactions. Nanostructure Science and Technology*. Springer, Cham; 2018. 226 p. [https://doi.org/10.1007/978-3-319-89612-0\\_7](https://doi.org/10.1007/978-3-319-89612-0_7)
3. Scheer R., Schock H.-W. *Chalcogenide photovoltaics: physics, technologies, and thin film devices*. Wiley-VCH; 2011. 368 p. <https://doi.org/10.1002/9783527633708>
4. Palchoudhury S., Ramasamy K., Gupta A. Multinary copper-based chalcogenide nanocrystal systems from the perspective of device applications. *Nanoscale Advances*. 2020;2(8): 3069–3082. <https://doi.org/10.1039/D0NA00399A>
5. Lin S., Li W., Bu Z., Shan B., Pei Y. Thermoelectric p-type  $Ag_5GaTe_6$  with an intrinsically low lattice thermal conductivity. *ACS Applied Energy Materials*. 2020;3(2): 1892–1898. <https://doi.org/10.1021/acsaem.9b02330>
6. Banik A., Roychowdhury S., Biswas K. The journey of tin chalcogenides towards high-performance thermoelectrics and topological materials. *Chemical Communications*. 2018;54(50): 6573–6590. <https://doi.org/10.1039/C8CC02230E>
7. Otrokov M. M., Klimovskikh I. I., Bentmann H., Zeugner A., Aliev Z. S., Gass S., Wolter A. U. B., Koroleva A. V., Estyunin D., Shikin A. M., Blanco-Rey M., Hoffmann M., Vyazovskaya A. Yu., Ereemeev S. V., Koroteev Y. M., Amiraslanov I. R., Babanly M. B., Mamedov N. T., Abdullayev N. A., Zverev V. N., Büchner B., Schiwer E. F., Kumar S., Kimura A., Petaccia L., Di Santo G., Vidal R. C., Schatz S., Kisner K., Min C.-H., Moser S. K., Peixoto T. R. F., Reinert F., Ernst A., Echenique P. M., Isaeva A., Chulkov E. V. Prediction and observation of the first antiferromagnetic topological insulator. *Nature*. 2019;576(7787): 416–422. <https://doi.org/10.1038/s41586-019-1840-9>
8. Babanly M. B., Chulkov E. V., Aliev Z. S., Shevel'kov A. V., Amiraslanov I. R. Phase diagrams in the materials science of topological insulators based on metal chalcogenides. *Russian Journal of Inorganic Chemistry*. 2017;62(13): 1703–1729. <https://doi.org/10.1134/S0036023617130034>
9. Ding J., Liu C., Xi L., Xi J., Yang J. Thermoelectric transport properties in chalcogenides  $ZnX$  ( $X=S, Se$ ): From the role of electron-phonon couplings. *Journal of Materiomics*. 2021;7(2): 310–319. <https://doi.org/10.1016/j.jmat.2020.10.007>
10. Segawa K. Synthesis and characterization of 3D topological insulators: a case  $TlBi(S_{1-x}Se_x)_2$ . *Science and Technology of Advanced Materials*. 2015;16(1): 014405–8. <https://doi.org/10.1088/1468-6996/16/1/014405>
11. Usanmaz D., Nath P., Toher C., Plata J. J., Friedrich R., Fornari M., Nardelli M. B., Curtarolo S. Spinodal superlattices of topological insulators. *Chemistry of Materials*. 2018;30(7): 2331–2340. <https://doi.org/10.1021/acs.chemmater.7b05299>
12. Wang Z., Segawa K., Sasaki S., Taskin A. A., Ando Y. Ferromagnetism in Cr-doped topological insulator  $TlSbTe_2$ . *APL Materials*. 2015;3: 083302–7. <https://doi.org/10.1063/1.4922002>
13. Ereemeev S. V., Koroteev Y. M., Chulkov E. V. Ternary thallium-based semimetal chalcogenides  $Tl-V-VI_2$  as a new class of three-dimensional topological insulators. *JETP Letters*. 2010;91(11): 594–598. <https://doi.org/10.1134/S0021364010110111>
14. Filnov S. O., Klimovskikh I. I., Estyunin D. A., Fedorov A., Voroshnin V., Koroleva A. V., Shevchenko E. V., Rybkin A. G., Aliev Z. S., Babanly M. B.,

- Amiraslanov I. R., Mamedov N. T., Schwier E. F., Miyamoto K., Okuda T., Kumar S., Kimura A., Misheneva V. M., Shikin A. M., Chulkov E. V. Probe-dependent Dirac-point gap in the gadolinium-doped thallium-based topological insulator  $\text{TlBi}_{0.9}\text{Gd}_{0.1}\text{Se}_2$ . *Physical Review B*. 2020;102: 085149-7. <https://doi.org/10.1103/PhysRevB.102.085149>
15. Arpino K. E., Wasser B. D., McQueen T. M. Superconducting dome and crossover to an insulating state in  $[\text{Tl}_4]\text{Tl}_{1-x}\text{Sn}_x\text{Te}_3$ . *APL Materials*. 2015;3(4): 041507-8. <https://doi.org/10.1063/1.4913392>
16. Ruan J., Jian S.-K., Zhang D., Yao H., Zhang H., Zhang S.-C., Xing D. Ideal Weyl semimetals in the chalcopyrites  $\text{CuTlSe}_2$ ,  $\text{AgTlTe}_2$ ,  $\text{AuTlTe}_2$ , and  $\text{ZnPbAs}_2$ . *Physical Review Letters*. 2016;116: 226801-5. <https://doi.org/10.1103/PhysRevLett.116.226801>
17. Singh B., Sharma A., Lin H., Hasan M. Z., Prasad R., Bansil A. Topological electronic structure and Weyl semimetal in the  $\text{TlBiSe}_2$  class of semiconductors. *Physical Review B*. 2012;86: 115208-7. <https://doi.org/10.1103/PhysRevB.86.115208>
18. Piasecki M., Brik M. G., Barchiy I. E., Ozga K., Kityk I. V., El-Naggar A. M., Albassam A. A., Malakhovskaya T. A., Lakshminarayana G. Band structure, electronic and optical features of  $\text{Tl}_4\text{SnX}_3$  ( $X = \text{S}, \text{Te}$ ) ternary compounds for optoelectronic applications. *Journal of Alloys and Compounds*. 2017;710: 600–607. <https://doi.org/10.1016/j.jallcom.2017.03.280>
19. Barchiy I., Sabov M., El-Naggar A. M., AlZayed N. S., Albassam A. A., Fedorchuk A. O., Kityk I. V.  $\text{Tl}_4\text{SnS}_3$ ,  $\text{Tl}_4\text{SnSe}_3$  and  $\text{Tl}_4\text{SnTe}_3$  crystals as novel IR induced optoelectronic materials. *Journal of Materials Science: Materials in Electronic*. 2016;27: 3901-5. <https://doi.org/10.1007/s10854-015-4240-4>
20. Shi H., Lin W., Kanatzidis M. G., Szeles C., Du M.-H. Impurity-induced deep centers in  $\text{Tl}_6\text{SI}_4$ . *Journal of Applied Physics*. 2017;121(14): 145102-5. <https://doi.org/10.1063/1.4980174>
21. Das S., Peters J. A., Lin W. W., Kostina S. S., Chen P., Kim J., Kanatzidis M. G., Wessels B. W. Charge transport and observation of persistent photoconductivity in  $\text{Tl}_6\text{SeI}_4$  single crystals. *Journal of Physical Chemistry Letters*. 2017;8(7): 1538–1544. <https://doi.org/10.1021/acs.jpcclett.7b00336>
22. Ding G., He J., Cheng Z., Wang X., Li S. Low lattice thermal conductivity and promising thermoelectric figure of merit of Zintl type  $\text{TlInTe}_2$ . *Journal of Materials Chemistry C*. 2018;6: 13269–13274. <https://doi.org/10.1039/C8TC03492C>
23. Shi Y., Assoud A., Ponou S., Lidin S., Kleinke H. A. New material with a composite crystal structure causing ultralow thermal conductivity and outstanding thermoelectric properties:  $\text{Tl}_2\text{Ag}_{12}\text{Te}_{7+8}$ . *Journal of American Chemical Society*. 2018;140(27): 8578–8585. <https://doi.org/10.1021/jacs.8b04639>
24. Han C., Sun Q., Li Z., Dou S. X. Thermoelectric enhancement of different kinds of metal chalcogenides. *Advanced Energy Materials*. 2016;6(15): 1600498-1-1600498-36. <https://doi.org/10.1002/aenm.201600498>
25. Heinke F., Eisenburger L., Schlegel R., Schwarzmüller S., Oeckler O. The influence of nanoscale heterostructures on the thermoelectric properties of Bi-substituted  $\text{Tl}_5\text{Te}_3$ . *Zeitschrift für anorganische und allgemeine Chemie*. 2017;643: 447–454. <https://doi.org/10.1002/zaac.201600449>
26. Maier S., Lefèvre R., Lin X., Nunna R., Berthebaud D., Hébert S., Mar A., Gascoin F. The solid solution series  $\text{Tl}(\text{V}_{1-x}\text{Cr}_x)_5\text{Se}_8$ : crystal structure, magnetic and thermoelectric properties. *Journal of Materials Chemistry C*. 2015;3: 10509–10517. <https://doi.org/10.1039/C5TC01766A>
27. Guo Q., Kleinke H. Thermoelectric properties of hot-pressed ( $\text{Ln} = \text{La}, \text{Ce}, \text{Pr}, \text{Nd}, \text{Sm}, \text{Gd}, \text{Tb}$ ) and  $\text{Tl}_{10-x}\text{La}_x\text{Te}_6$  ( $0,90 < x < 1,05$ ). *Journal of Alloys and Compounds*. 2015;630: 37–42. <https://doi.org/10.1016/j.jallcom.2015.01.025>
28. Isaeva A., Schoenemann R., Doert T. Syntheses, Crystal structure and magnetic properties of  $\text{Tl}_9\text{RETe}_6$  ( $\text{RE} = \text{Ce}, \text{Sm}, \text{Gd}$ ). *Crystals*. 2020;10(4): 277-11. <https://doi.org/10.3390/cryst10040277>
29. Bangarigadu-Sanasy S., Sankar C. R., Dube P. A., Greedan J. E., Kleinke H. Magnetic properties of  $\text{Tl}_9\text{LnTe}_6$ ,  $\text{Ln} = \text{Ce}, \text{Pr}, \text{Tb}$  and  $\text{Sm}$ . *Journal of Alloys and Compounds*. 2014;589: 389–392. <https://doi.org/10.1016/j.jallcom.2013.11.229>
30. Villars P., Prince A. Okamoto H. Handbook of ternary alloy phase diagrams (10 volume set). Materials Park, OH: ASM International; 1995. 15000 p.
31. Babanly M. B., Mashadiyeva L. F., Babanly D. M., Imamaliyeva S. Z., Taghiyev D. B., Yusibov Y. A. Some aspects of complex investigation of the phase equilibria and thermodynamic properties of the ternary chalcogenid systems by the EMF method. *Russian Journal of Inorganic Chemistry*. 2019;64(13): 1649–1671. <https://doi.org/10.1134/S0036023619130035>
32. Imamaliyeva S. Z. Phase diagrams in the development of thallium-REE tellurides with  $\text{Tl}_5\text{Te}_3$  structure and multicomponent phases based on them. Overview. *Kondensirovannye sredy i mezhfaznye granitsy = Condensed Matter and Interphases*. 2018;20(3): 332–347. <https://doi.org/10.17308/kcmf.2018.20/570> (In Russ., abstract in Eng.)
33. Imamaliyeva S. Z., Alakbarzade G. I., Mahmudova M. A., Amiraslanov I. R., Babanly M. B. Experimental study of the  $\text{Tl}_4\text{PbTe}_3$ – $\text{Tl}_9\text{TbTe}_6$ – $\text{Tl}_9\text{BiTe}_6$  section of the  $\text{Tl}$ – $\text{Pb}$ – $\text{Bi}$ – $\text{Tb}$ – $\text{Te}$  system. *Materials Research*. 2018;21(4): e20180189-6. <https://doi.org/10.1590/1980-5373-mr-2018-0189>
34. Imamaliyeva S. Z., Alakbarova G. I., Babanly K. N., Amiraslanov I. R., Babanly M. B.  $\text{Tl}_2\text{Te}$ –



Tl<sub>9</sub>SbTe<sub>6</sub>–Tl<sub>9</sub>TbTe<sub>6</sub> system. *New Materials, Compounds and Applications*. 2018;2(3): 221–230. Available at: <http://jomardpublishing.com/UploadFiles/Files/journals/NMCA/V2N3/Imamaliyeva%20et%20al.pdf>

35. Imamaliyeva S. Z., Gasanly T. M., Zlomanov V. P., Babanly M. B. Phase Equilibria in the Tl<sub>2</sub>Te–Tl<sub>5</sub>Te<sub>3</sub>–Tl<sub>9</sub>TbTe<sub>6</sub> system. *Inorganic Materials*. 2017;53(4): 361–368. <https://doi.org/10.1134/S0020168517040069>

36. Imamaliyeva S. Z., Gasanly T. M., Zlomanov V. P., Babanly M. B. Phase equilibria in the Tl<sub>5</sub>Te<sub>3</sub>–Tl<sub>9</sub>BiTe<sub>6</sub>–Tl<sub>9</sub>TbTe<sub>6</sub> system. *Inorganic Materials*. 2017;53(7): 685–689. <https://doi.org/10.1134/S0020168517070093>

37. Asadov M. M., Babanly M. B., Kuliev A. A. Phase equilibria in the system Tl–Te. *Izvestiya Akademii Nauk SSSR. Neorganicheskie Materiali*. 1977;13(8): 1407–1410. (In Russ.)

38. Cerny R., Joubert J., Filinchuk Y., Feutelais Y. Tl<sub>2</sub>Te and its relationship with Tl<sub>5</sub>Te<sub>3</sub>. *Acta Crystallographica Section C*. 2002;58(5): 163. <https://doi.org/10.1107/s0108270102005085>

39. Babanly M. B., Azizulla A., Kuliev A. A. System Tl<sub>2</sub>Te–Bi<sub>2</sub>Te<sub>3</sub>–Te. *Russian Journal of Inorganic Chemistry*. 1985;30(9): 2356–2359. (In Russ.)

40. Pradel A., Tedenac J. C., Brun G., Maurin M. Mise au point dans le ternaire Tl–Bi–Te. Existence de deux phases nonstoechiométriques de type TlBiTe<sub>2</sub>. *Journal of Solid State Chemistry*. 1982;5(1): 99–111. [https://doi.org/10.1016/0022-4596\(82\)90296-1](https://doi.org/10.1016/0022-4596(82)90296-1)

41. Duczmal M. Structure, właściwości magnetyczne i pole krystaliczne w potrójnych chalcogenkach lantanowcow i talu TlLnX<sub>2</sub> (X = S, Se lub Te). Monografie. Wrocław: Politechniki Wrocławskiej; 2003. 67 p. (In Polish)

42. Doert T., Böttcher P. Crystal structure of bismuth nonathallium hexatelluride BiTl<sub>9</sub>Te<sub>6</sub>. *Zeitschrift für Kristallographie*. 1994;209: 95. <https://doi.org/10.1524/zkri.1994.209.1.95>

43. Imamaliyeva S. Z., Mekhdiyeva I. F., Gasyimov V. A., Babanly M. B. Tl–Bi–Er–Te system in the composition region Tl<sub>2</sub>Te–Tl<sub>9</sub>BiTe<sub>6</sub>–Tl<sub>9</sub>ErTe<sub>6</sub>. *Russian Journal of Inorganic Chemistry*. 2019;64(7): 907–913. <https://doi.org/10.1134/S0036023619070192>

44. Alakbarzade G. I. Solid-phase equilibria in the TlBiTe<sub>2</sub>–TlTbTe<sub>2</sub> system. *Chemical Problems*. 2019;4: 565–570. <https://doi.org/10.32737/2221-8688-2019-4-565-570>

45. Afinogenov Yu. P., Goncharov E. G., Semenova G. V., Zlomanov V. P. *Fiziko-khimicheskii analiz mnogokomponentnykh sistem* [Physicochemical analysis of multicomponent systems]. Moscow: MFTIB; 2006. 332 p. (In Russ.)

### Information about the authors

*Samira Z. Imamaliyeva*, PhD in Chemistry, Assistance Professor, Institute of Catalysis and Inorganic Chemistry, Azerbaijan National Academy of Sciences, Baku, Azerbaijan; e-mail: [samira9597a@gmail.com](mailto:samira9597a@gmail.com). ORCID iD: <https://orcid.org/0000-0001-8193-2122>.

*Ganira I. Alakbarzade*, PhD student, Azerbaijan National Aerospace Agency, Baku, Azerbaijan; e-mail: [alakbarzadegi@gmail.com](mailto:alakbarzadegi@gmail.com) ORCID iD: <https://orcid.org/0000-0001-8500-0007>

*Dunya M. Babanly*, DSc in Chemistry, Assistance Professor, Institute of Catalysis and Inorganic Chemistry, Azerbaijan National Academy of Sciences, Azerbaijan State Oil and Industry University, Baku, Azerbaijan; e-mail: [dunya.babanly@ufaz.az](mailto:dunya.babanly@ufaz.az). ORCID iD: <https://orcid.org/0000-0002-8330-7854>.

*Marina V. Bulanova*, DSc in Chemistry, Leading Researcher, I. M. Frantsevich Institute for Problems of Materials Science, NAS of Ukraine, Kiev, Ukraine; e-mail: [mvbulanova2@gmail.com](mailto:mvbulanova2@gmail.com). ORCID iD: <https://orcid.org/0000-0002-8691-0982>.

*Vagif A. Gasymov*, PhD in Chemistry, Assistance Professor, Institute of Catalysis and Inorganic Chemistry, Azerbaijan National Academy of Sciences, Baku, Azerbaijan; e-mail: [v-gasymov@rambler.ru](mailto:v-gasymov@rambler.ru). ORCID iD: <https://orcid.org/0000-0001-6233-5840>.

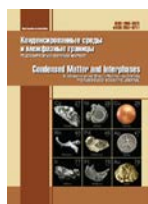
*Mahammad B. Babanly*, DSc in Chemistry, Professor, Associate Member of the Azerbaijan National Academy of Sciences, Deputy-director of the Institute of Catalysis and Inorganic Chemistry, Azerbaijan National Academy of Sciences, Baku State University, Baku, Azerbaijan; e-mail: [babanlymb@gmail.com](mailto:babanlymb@gmail.com). ORCID iD: <https://orcid.org/0000-0001-5962-3710>.

All authors have read and approved the final manuscript.

*Received 8 January 2021; Approved after reviewing 9 February 2021; Accepted 15 March 2021; Published online 25 March 2021.*

*Translated by Samira Imamaliyeva*

*Edited and proofread by Simon Cox*



## Original articles

Original article

<https://doi.org/10.17308/kcmf.2021.23/3300>

## Features of the two-stage formation of macroporous and mesoporous silicon structures

A. S. Lenshin<sup>✉</sup>, A. N. Lukin, Ya. A. Peshkov, S. V. Kannykin, B. L. Agapov,  
P. V. Seredin, E. P. Domashevskaya

Voronezh State University,  
1 Universitetskaya pl., Voronezh 394018, Russian Federation

### Abstract

The aim of this work was the formation of multilayer structures of macroporous silicon and the study of their structural, morphological, and optical properties in comparison with the properties of multilayer structures of mesoporous silicon.

The paper presents the results of the development of techniques for the formation of multilayer structures of porous silicon *por-Si* by stepwise change in the current with two-stage modes of electrochemical etching.

The data on the morphology, composition, and porosity of macroporous and mesoporous silicon samples were obtained using scanning electron microscopy, IR spectroscopy, and X-ray reflectivity. It was shown that with the two-stage growth of porous silicon layers, the depth of the boundary between the layers of the structure was determined by the primary mode of electrochemical etching, while the total layer thickness increased with an increase in the current density of electrochemical etching.

A comparative analysis of the relative intensity and fine structure of vibrational modes of IR spectra indicated a significantly more developed specific pore surface and greater sorption capacity of mesoporous silicon as compared to macroporous silicon.

**Keywords:** macroporous silicon, mesoporous silicon, electrochemical etching, porosity, IR spectra, X-ray reflectivity

**Acknowledgements:** The study was supported by the Russian Foundation for Basic Research and the Government of the Voronezh Region in the framework of the scientific project No. 19-42-363004. The work on the development of techniques for the formation of porous silicon layers with different porosity was carried out with the financial support of the Russian Science Foundation grant 19-72-10007. This work was partially supported by the Ministry of Science and Higher Education of the Russian Federation within the framework of the state assignment to universities in the field of scientific activity for 2020-2022, project No. FZGU-2020-0036. The studies were conducted in the Centre for Collective Use of Scientific Equipment of Voronezh State University (<http://ckp.vsu.ru>).

**For citation:** Lenshin A. S., Lukin A. N., Peshkov Ya. A., Kannykin S. V., Agapov B. L., Seredin P. V., Domashevskaya E. P. Features of two-stage formation of macroporous and mesoporous silicon structures. *Kondensirovannye sredy i mezhfaznye granitsy = Condensed Matter and Interphases*. 2021; 23 (1): 41–49. <https://doi.org/10.17308/kcmf.2021.23/3300>

**Для цитирования:** Леншин А. С., Лукин А. Н., Пешков Я. А., Канныкин С. В., Агапов Б. Л., Середин П. В., Домашевская Э. П. Особенности двухстадийного формирования структур макропористого и мезопористого кремния. *Конденсированные среды и межфазные границы*. 2021;23(1): 41-48. <https://doi.org/10.17308/kcmf.2021.23/3300>

✉ Alexander S. Lenshin, e-mail: [lenshinas@phys.vsu.ru](mailto:lenshinas@phys.vsu.ru)

© Lenshin A. S., Lukin A. N., Peshkov Ya. A., Kannykin S. V., Agapov B. L., Seredin P. V., Domashevskaya E. P., 2021



## 1. Introduction

The use of porous silicon *por*-Si as one of the materials of modern solid-state functional electronics is due to the presence of many practically useful functional properties of this material and its compatibility with most technological production processes. It is known that depending on the method of its production, *por*-Si can have an extremely large area of specific surface of pores (up to 500 m<sup>2</sup>/g), high reactivity, and intense photoluminescence (PL) in the visible range of wavelengths [1–4].

Previously in the 20<sup>th</sup> century, before the concept of “nano” and the nanoscopic scale were introduced into scientific terminology, according to the IUPAC classification, pores with a radius of up to 0.2 nm were called submicropores, pores with a radius of 0.2–1.0 nm were called micropores, pores with a radius of 1–25 nm were called mesopores, and those with a radius of more than 25 nm were called macropores [5]. Currently there are different variants of systematisation of porous materials by their morphology and physicochemical properties. Regardless of the size of the pores, porous silicon is usually characterised by such parameter as “porosity” *P*, which is the ratio of the volume of pores to the total volume of the porous layer of the sample, as well as by the average size of the structural elements. With a low value of porosity, the properties of *por*-Si are similar to the properties of crystal silicon, although they can change if the value increases. For instance, photoluminescence was found in the samples of *por*-Si with a value of porosity of at least 50 % [6].

Depending on the initial material, porosity, and formation conditions, porous silicon has a wide range of values of resistivity (10<sup>-2</sup>–10<sup>11</sup> Ohm-cm), absolute permittivity (1.75–12), and refractive index (1.2–3.5) [7]. In a number of works [1–4] it is shown that changes in the modes of formation of *por*-Si and post-processing

of its surface allow effectively controlling the morphology, surface composition, and optical and adsorption properties of *por*-Si [6].

The possibilities of creating gas sensors, optical sensors, and moisture sensors were demonstrated on the structures of porous silicon. The use of multi-stage modes of formation of a porous layer on single-crystal silicon can also be promising for fine adjustment of the functional properties of its surface and volume for the further formation of thin layers of such modern nanoelectronic materials as metal oxide structures or structures of the A3B5 type on its surface [1–4, 8–10].

The aim of this work was the study of multi-layer structures of macroporous silicon and their structural, morphological, and optical characteristics in comparison with the characteristics of multilayer structures of mesoporous silicon that we previously obtained [11].

## 2. Experimental

Multilayer structures of porous silicon (henceforth referred to as “macroporous silicon”) were formed on the surface of crystal silicon substrates *c*-Si (100) with a resistivity of 0.3 Ohm-cm, doped with phosphorus. Electrochemical etching (ECE) was performed in a solution of hydrofluoric acid and dimethylformamide with the addition of hydrogen peroxide and sulphuric acid while periodically changing the current density. At the same time, the current density gradually changed during the process of the two-stage ECE. The modes of electrochemical etching are presented in table 1.

The samples were obtained in the modes similar to those that were used to synthesise the samples of mesoporous silicon in our previous work [11]. Only the composition of the ECE solution was changed towards a lower content of hydrofluoric acid. The morphological features of the samples were studied using scanning electron microscopy SEM (JEOL JSM 6380 LV).

**Table 1.** Conditions for obtaining the samples of porous silicon

No.	Etching mode	Anodic current density, mA/cm <sup>2</sup>	Etching time, minutes
1	single-stage	15	10
2	single-stage	50	10
3	two-stage	50/15	5/5
4	two-stage	15/50	5/5

IR spectra of multilayer structures were obtained on a Vertex 70 (Bruker) IR Fourier spectrometer using an attachment for disturbed total internal reflection (ATR) spectroscopy [9] in the range of  $400\text{--}4000\text{ cm}^{-1}$ . IR spectra were collected two weeks after the samples had been obtained.

To determine the porosity of the surface layer of *por*-Si with the thickness of 10 nm, the samples obtained using single-stage ECE were studied using X-ray reflectivity (XRR) on a laboratory diffractometer ARL X'TRA (Cu  $K\alpha$ ) with Bragg-Brentano geometry within a small angle range of ( $2\theta = 0.1\text{--}1^\circ$ ).

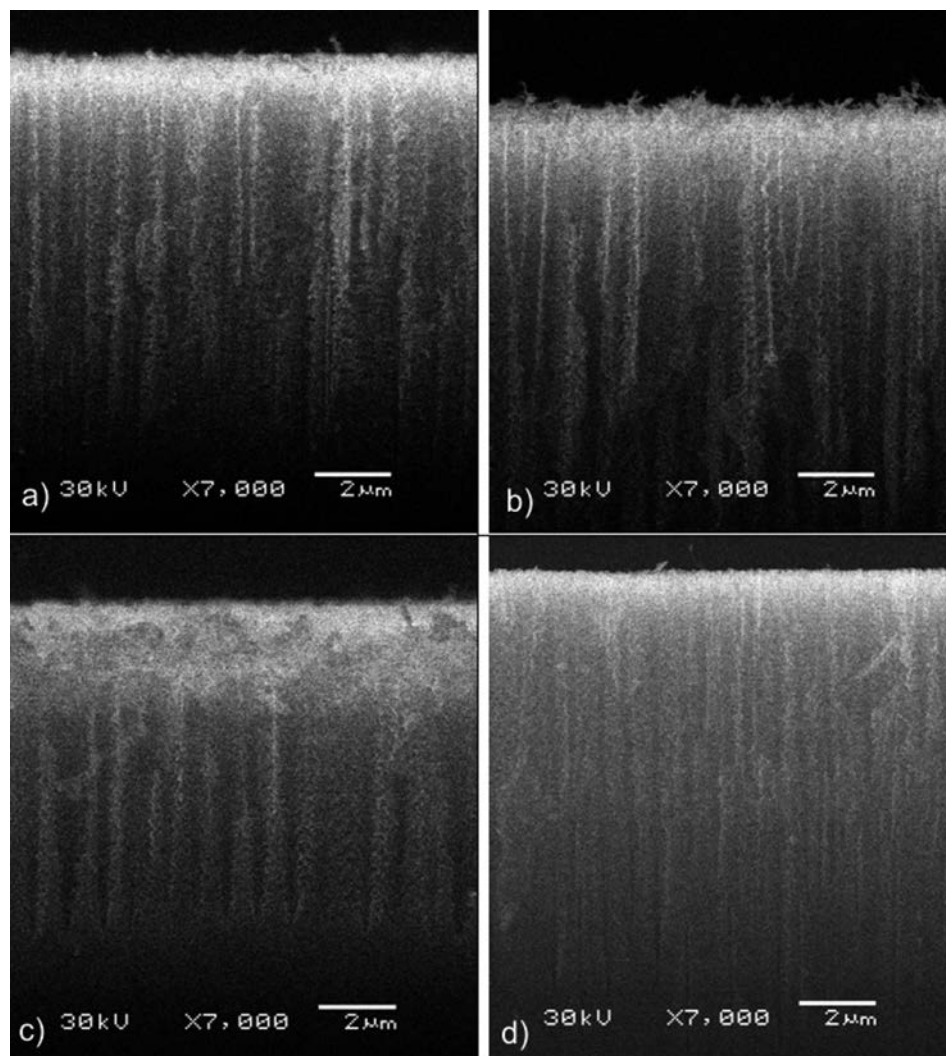
### 3. Results and discussion

#### 3.1. Structural and morphological SEM data

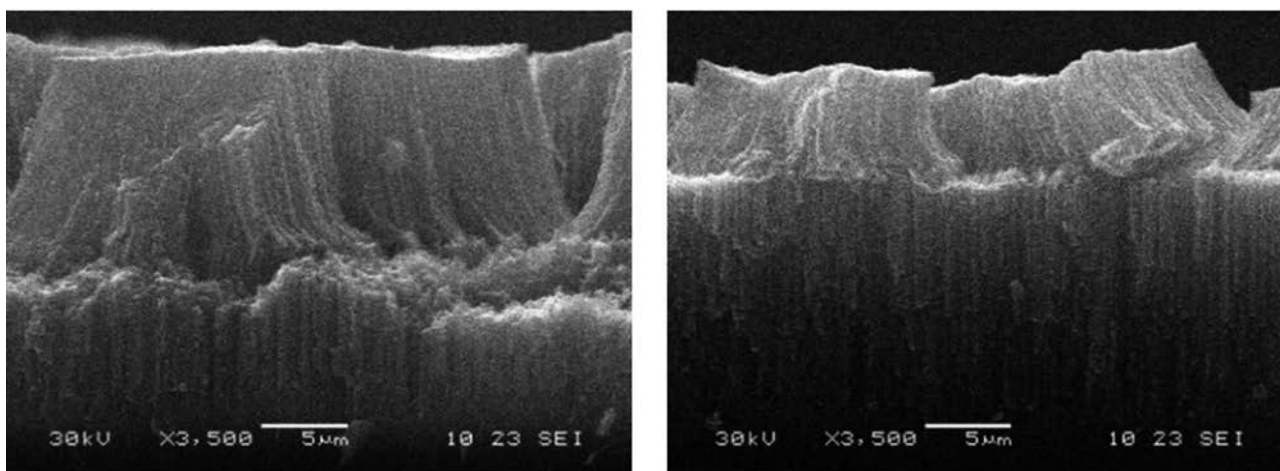
Figure 1 presents SEM microphotographs of cleavages of macroporous *por*-Si samples

with an average diameter of the main type of pores of approximately 150–200 nm obtained in single-stage and two-stage ECE modes with the following anodic current densities: 15 mA/cm<sup>2</sup> (No. 1) and 50 mA/cm<sup>2</sup> (No. 2), 50/15 mA/cm<sup>2</sup> (No. 3) and 15/50 mA/cm<sup>2</sup> (No. 4).

The analysis of the SEM data shows that an increase in the current density in the specified range causes an increase in the thickness of the porous layer and in the size of the pores, but, unlike mesoporous silicon [11] obtained with the same ECE modes (Fig. 2), there is no partial cracking of the porous layer, and the boundary between the porous layers is less pronounced. For example, the thickness of the porous layer of sample No. 1 obtained using a single-stage mode with the current density of  $j = 15\text{ mA/cm}^2$  was~



**Fig. 1.** SEM images of cleavages of porous silicon samples obtained in single and two-stage etching modes a) No. 1,  $j_a = 15\text{ mA/cm}^2$ ; b) No. 2,  $j_a = 50\text{ mA/cm}^2$ ; c) No. 3,  $j_a = 50/15\text{ mA/cm}^2$ ; d) No. 4,  $j_a = 15/50\text{ mA/cm}^2$



**Fig. 2.** SEM images of cleavages of mesoporous silicon samples obtained in two-stage etching modes: a) No. 208,  $j_a = 50/15$  mA/cm<sup>2</sup>; b) No. 207,  $j_a = 15/50$  mA/cm<sup>2</sup> [8]

15  $\mu$ , while the thickness of the porous layer of sample No. 2 obtained with the current density of  $j = 50$  mA/cm<sup>2</sup> was  $\sim 25$   $\mu$  (Fig. 1). The average diameter of the main type of pores in the samples was 150–200 nm.

The smaller thickness of the macroporous silicon layer, as compared to the mesoporous silicon, as well as the absence of stratification in the surface layer, can be explained by the lower concentration of hydrofluoric acid in the ECE solution. Taking into account the etching time of 10 min, the etching rate of the porous layer was  $\sim 1.5$   $\mu$ /min and  $2.5$   $\mu$ /min for samples No. 1 and No. 2 respectively, and it increased by 1.5 times with more than a threefold increase in the current density (similar to mesoporous silicon). The average size of vertical pores in mesoporous silicon was  $\sim 50$ – $100$  nm.

As for samples No. 3 and 4 (fig. 1c, d), obtained using two-stage modes of changing the anodic current density, that is in the modes of decreasing ( $j = 50/15$  mA/cm<sup>2</sup>) and increasing ( $j = 15/50$  mA/cm<sup>2</sup>) the ECE current density, the thickness of the porous layer of the samples was  $\sim 15$   $\mu$  and  $\sim 18$   $\mu$  respectively. An analysis of the images of sample cleavages indicates that the depth of the boundary between the layers of the structure, similar to mesoporous silicon, is determined by the primary ECE mode [11].

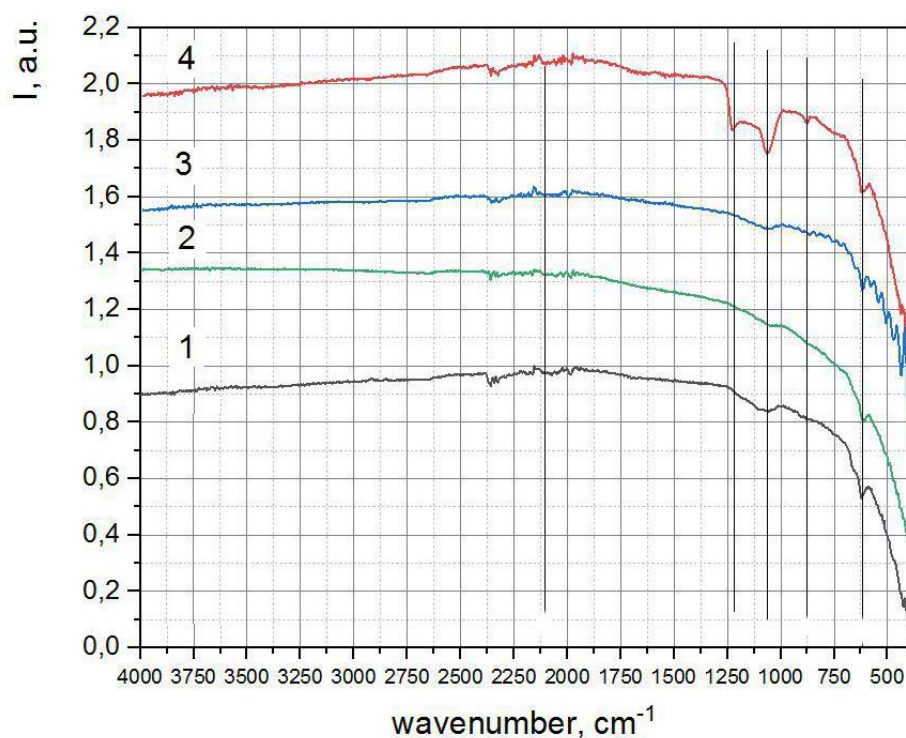
### 3.2. IR spectra of macroporous and mesoporous silicon

To obtain information on the composition of the chemical bonds in porous layers, all samples

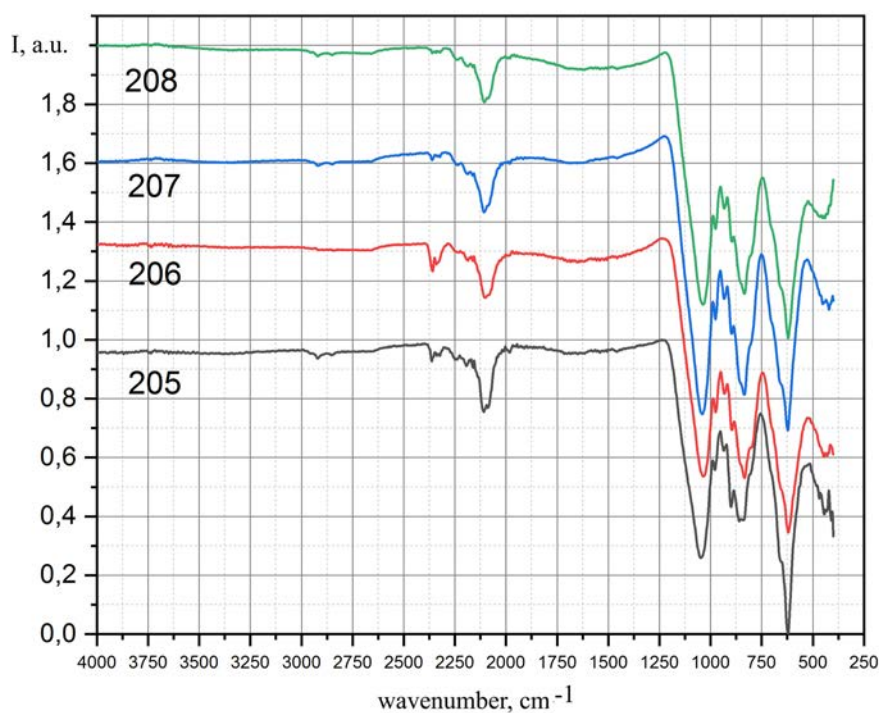
of macroporous and mesoporous silicon were studied using IR spectroscopy.

Fig. 3 presents the IR spectra of ATR showing the effect of an increase in the ECE current density and changes in the sequence of values of currents during a two-stage ECE on the composition of chemical bonds of macroporous silicon samples. A band of  $1000$ – $1200$  cm<sup>-1</sup> corresponding to Si–O–Si bonds and an intensity mode corresponding to the vibrations of Si–Si bonds ( $616$  cm<sup>-1</sup>) are observed on these IR spectra. The Si–O–Si band is shown most clearly and intensively in sample No. 4 obtained in a two-stage ECE mode,  $j_a = 15/50$  mA/cm<sup>2</sup>. In addition, a low-intensity features appear in the IR spectra in the regions of  $\sim 900$  cm<sup>-1</sup> and  $2060$ – $2120$  cm<sup>-1</sup> which are typical for various configurations of the Si–H<sub>x</sub> and O<sub>x</sub>–SiH bonds. The presented results correlate well with the previously obtained results for different single layer structures of porous silicon [9].

Fig. 4 shows the IR spectra of ATR of mesoporous silicon samples obtained in the modes of single-stage and two-stage etching with a different sequence of changes in the ECE current values. At first glance, these spectra stand out due to their significantly higher intensity and pronounced structuredness of all modes that were barely visible in the IR spectra of the macroporous silicon samples presented in Fig. 3. The most intensive and clearly structured modes in the spectra of mesoporous silicon are those in the region of  $400$ – $1200$  cm<sup>-1</sup> which are typical for this material [9] and correspond to the vibrations of the following bonds: Si–Si ( $616$



**Fig. 3.** IR-spectra of macroporous silicon samples obtained in single and two-stage etching modes: a) No. 1,  $j_a = 15 \text{ mA/cm}^2$ ; b) No. 2,  $j_a = 50 \text{ mA/cm}^2$ , c) No. 3,  $j_a = 50/15 \text{ mA/cm}^2$ ; d) No. 4,  $j_a = 15/50 \text{ mA/cm}^2$

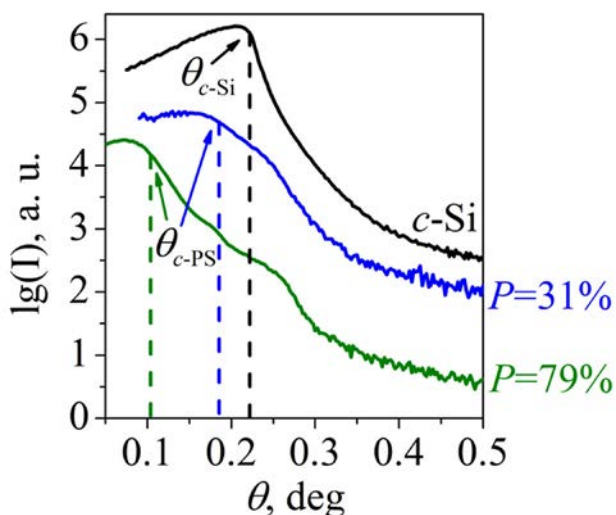


**Fig. 4.** IR-spectra of mesoporous silicon samples obtained in single and two-stage etching modes: No. 205,  $j_a = 15 \text{ mA/cm}^2$ ; No. 206,  $j_a = 50 \text{ mA/cm}^2$ ; No. 207,  $j_a = 15/50 \text{ mA/cm}^2$ ; No. 208,  $j_a = 50/15 \text{ mA/cm}^2$

$\text{cm}^{-1}$ ),  $\text{Si-H}_x$  (664, 906, 2100–2250  $\text{cm}^{-1}$ ),  $\text{Si-O-Si}$  (490, 1060–1170  $\text{cm}^{-1}$ ),  $\text{O}_2\text{-Si-OH}$  ( $\sim 830 \text{ cm}^{-1}$ ),  $\text{O}_3\text{-SiH}$  (880  $\text{cm}^{-1}$ ).

In addition, there are noticeable bands in the region of 2060–2120  $\text{cm}^{-1}$  on the spectra of the samples. These bands are typical for various configurations of  $\text{Si-H}_x$  and  $\text{O}_x\text{-SiH}_y$  bonds as well as adsorbed  $\text{CO}_2$  (2360  $\text{cm}^{-1}$ ). The presence of these bonds indicates a significantly greater sorption capacity of mesoporous silicon with a larger specific surface area of smaller pores as compared to macroporous silicon.

While comparing mesoporous samples obtained in single-stage modes (No. 205 and No. 206), it should be noted that an increased ECE current density leads to an increase in relative intensity of absorption bands in the regions of 750–900  $\text{cm}^{-1}$  ( $\text{Si-H}_x$ ,  $\text{O}_2\text{-Si-OH}$ , and  $\text{O}_x\text{-SiH}_y$  bonds) and the 1000–1200  $\text{cm}^{-1}$  band corresponding to  $\text{Si-O-Si}$  bonds. In combination with the SEM data, this indicates an increase in the specific surface area of the porous layer  $S_{\text{sp}}$  for the samples obtained with a higher ECE current density. At the same time, increased  $S_{\text{sp}}$  contributes to a more active interaction of the material with the environment, which leads to stronger oxidation of the porous layer and adsorption of hydrogen and hydroxyl groups on it [8, 9].



**Fig. 5.** XRR profiles of the samples of macroporous (the blue curve) and mesoporous silicon (the green curve) and single-crystal silicon substrate  $c\text{-Si}$ . The dotted lines indicate the positions of the critical angles of total external reflection

A similar situation is observed when changing the sequence of changes in the current values during ECE. The IR spectrum of sample No. 207 obtained in a two-stage mode  $j_a = 15/50 \text{ mA/cm}^2$  shows more intensive, as compared to the spectrum of a single-stage sample No. 205 (obtained in the mode with minimal current density  $j_a = 15 \text{ mA/cm}^2$ ), absorption bands 50–900  $\text{cm}^{-1}$  and 1000–1200  $\text{cm}^{-1}$  corresponding to  $\text{Si-O-Si}$ ,  $\text{Si-H}_x$ ,  $\text{O}_2\text{-Si-OH}$ , and  $\text{O}_x\text{-SiH}_y$  bonds. These modes are less intensive as compared to the spectrum of the mode obtained with maximum ECE current density (No. 208,  $j_a = 50/15 \text{ mA/cm}^2$ ) in a two-stage mode.

Thus, a comparative analysis of the relative intensity and fine structure of vibrational modes of IR spectra indicated a significantly more developed specific pore surface and greater sorption capacity of mesoporous silicon as compared to macroporous silicon.

### 3.3. X-ray reflectivity

Fig. 5 shows XRR reflectograms of mesoporous and macroporous silicon samples (No. 206 and No. 2) obtained in single-stage modes and a silicon substrate of single-crystal silicon  $\text{Si}(100)$  on which porous layers were formed. The results show that the intensity of the XRR curves begins to decrease significantly after passing the critical angle  $\theta_c$  of the total external reflection (TER) of X-ray radiation where the intensity of the reflected X-ray radiation is reduced by half. In this case, the values of critical angles of TER for the three studied samples were markedly different. The critical angle of TER for a single-crystal silicon wafer  $c\text{-Si}$  is  $\theta_{c\text{-Si}} = 0.223^\circ$ , which correlates well with theoretical calculations ( $0.226^\circ$ ). At the same time, the values of critical angles for macroporous and mesoporous silicon are considerably lower:  $\theta_{c\text{-PS}} = 0.186^\circ$  and  $\theta_{c\text{-PS}} = 0.105^\circ$  respectively.

The porosity ( $P$ ) of the surface layer of the samples can be evaluated using ratio (1) presented in [12]:

$$P(\%) = \left[ 1 - \left( \theta_{c\text{-PS}} / \theta_{c\text{-Si}} \right)^2 \right] \times 100, \quad (1)$$

where  $\theta_{c\text{-Si}}$  is the critical angle of TER of single-crystal silicon  $c\text{-Si}$ ,  $\theta_{c\text{-PS}}$  is a critical angle of TER of the porous layer of the samples of macroporous or mesoporous silicon. In accordance with ratio (1), the value of porosity of mesoporous

silicon  $P = 79\%$  is 2.5 times higher than the corresponding value of macroporous silicon  $P = 31\%$ .

The measurements of the photoluminescence of porous silicon samples using the technique described in [13] showed the absence of PL in a sample of macroporous silicon with porosity of 31% (sample No. 2) and the presence of typical PL for sample No. 206 of mesoporous silicon with porosity of  $P = 79\%$ . This correlates with the results of previous studies, according to which porous silicon begins to luminesce with the value of porosity  $P$  higher than 50% [13, 14].

#### 4. Conclusions

The paper presented the results related to the development of techniques or the two-stage formation of multilayer structures of porous silicon with various porosity and various sizes of pores.

Using scanning electron microscopy, it was shown that with the two-stage growth of porous silicon layers, the depth of the boundary between the layers of the structure was determined by the primary mode of electrochemical etching, while the total layer thickness increased with an increase in the ECE current density.

The average diameter of the main type of pores in the samples of macroporous silicon was 150–200 nm, while the average diameter vertical pores in mesoporous silicon was two-three times less, ~ 50–100 nm.

Comparative analysis of the relative intensity and fine structure of vibrational modes of IR spectra indicated that multilayer samples of macroporous silicon were less oxidated as compared to the samples of mesoporous silicon and that the surface of pores contained fewer bonds of the Si–OH and Si–H type.

The porosity of the surface layer of mesoporous silicon  $P = 79\%$  determined by the X-ray reflectivity was 2.5 times higher than the corresponding value of macroporous silicon  $P = 31\%$ , which correlated well with the significantly more developed specific surface of pores and greater sorption capacity of mesoporous silicon as compared to macroporous silicon.

#### Conflict of interests

The authors declare that they have no known competing financial interests or personal

relationships that could have influenced the work reported in this paper.

#### References

1. Pacholski C. Photonic crystal sensors based on porous silicon. *Sensors*. 2013;13(4): 4694–4713. <https://doi.org/10.3390/s130404694>
2. Harraz F. A. Porous silicon chemical sensors and biosensors: A review. *Sensors and Actuators B: Chemical*. 2014;202: 897–912. <https://doi.org/10.1016/j.snb.2014.06.048>
3. Qian M., Bao X. Q., Wang L. W., Lu X., Shao J., Chen X. S. Structural tailoring of multilayer porous silicon for photonic crystal application. *Journal of Crystal Growth*. 2006;292(2): 347–350. <https://doi.org/10.1016/j.jcrysgro.2006.04.033>
4. Len'shin A. S., Kashkarov V. M., Turishchev S. Yu., Smirnov M. S., Domashevskaya E. P. Effect of natural aging on photoluminescence of porous silicon. *Technical Physics Letters*. 2011;37(9): 789–792. <https://doi.org/10.1134/S1063785011090124>
5. Kheifets L. I., Neimark A. B. *Multiphase processes in porous media*. Moscow: Khimiya Publ.; 1982. 320 p. (In Russ.)
6. Canham L. *Handbook of porous silicon*. Switzerland: Springer International Publishing; 2014. 733 p.
7. Zimin S. P. Porous silicon – material with new properties. *Soros Educational Journal*. 2004;8(1): 101–107. Available at: [http://window.edu.ru/resource/217/21217/files/0401\\_101.pdf\\_\(In\\_Russ.,\\_abstract\\_in\\_Eng.\)](http://window.edu.ru/resource/217/21217/files/0401_101.pdf_(In_Russ.,_abstract_in_Eng.))
8. Seredin P. V., Lenshin A. S., Goloshchapov D. L., Lukin A. N., Arsentyev I. N., Bondarev A. D., Tarasov I. S. Investigations of nanodimensional  $Al_2O_3$  films deposited by ion-plasma sputtering onto porous silicon. *Semiconductors*. 2015;49(7): 915–920. <https://doi.org/10.1134/S1063782615070210>
9. Seredin P. V., Lenshin A. S., Mizerov A. M., Leiste H., Rinke M. Structural, optical and morphological properties of hybrid heterostructures on the basis of GaN grown on compliant substrate por-Si(111). *Applied Surface Science*. 2019;476: 1049–1060. <https://doi.org/10.1016/j.apsusc.2019.01.239>
10. Seredin P. V., Leiste H., Lenshin A. S., Mizerov A. M. Effect of the transition porous silicon layer on the properties of hybrid GaN/SiC/por-Si/Si(111) heterostructures. *Applied Surface Science*. 2020;508(145267): 1–14. <https://doi.org/10.1016/j.apsusc.2020.145267>
11. Lenshin A. S., Barkov K. A., Skopintseva N. G., Agapov B. L., Domashevskaya E. P. Influence of electrochemical etching modes under one stage and two Stage formation of porous silicon on the degree of oxidation of its surface layer under natural conditions. *Kondensirovannye sredy i mezhfaznye*



*granitsy = Condensed Matter and Interphases*. 2019;21(4): 534–543. <https://doi.org/10.17308/kcmf.2019.21/2364> (In Russ., abstract in Eng.)

12. Buttard D., Dolino G., Bellet D., Baumbach T., Rieutord F. X-ray reflectivity investigation of thin p-type porous silicon layers. *Solid State Communications*. 1998;109(1): 1–5. [https://doi.org/10.1016/S0038-1098\(98\)00531-6](https://doi.org/10.1016/S0038-1098(98)00531-6)

13. Lenshin A. S., Seredin P. V., Agapov B. L., Minakov D. A., Kashkarov V. M. Preparation and degradation of the optical properties of nano-, meso-, and macroporous silicon. *Materials Science in Semiconductor Processing*. 2015;30: 25–30. <https://doi.org/10.1016/j.mssp.2014.09.040>

14. Ksenofontova O. I., Vasin A. V., Egorov V. V., Bobyl' A. V., Soldatenkov F. Yu., Terukov E. I., Ulin V. P., Ulin N. V., Kiselev O. I. Porous silicon and its applications in biology and medicine. *Technical Physics*. 2014;59(1): 66–77. <https://doi.org/10.1134/S1063784214010083>

### Information about the authors

*Alexander S. Lenshin*, PhD in Physics and Mathematics, Senior Researcher, Department of Solid State Physics and Nanostructures, Voronezh State University, Voronezh, Russian Federation; e-mail: [lenshinas@phys.vsu.ru](mailto:lenshinas@phys.vsu.ru). ORCID iD: <https://orcid.org/0000-0002-1939-253X>.

*Anatoly N. Lukin*, PhD in Physics and Mathematics, Associate Professor, Department of Solid State Physics and Nanostructures, Voronezh State University, Voronezh, Russian Federation; e-mail: [ckp\\_49@mail.ru](mailto:ckp_49@mail.ru). ORCID iD: <https://orcid.org/0000-0001-6521-8009>.

*Yaroslav A. Peshkov*, PhD student, Department of Solid State Physics and Nanostructures, Voronezh State University, Voronezh, Russian Federation; e-mail: [Tangar77@mail.ru](mailto:Tangar77@mail.ru). ORCID iD: <https://orcid.org/0000-0002-2918-3926>.

*Sergey V. Kannykin*, PhD in Physics and Mathematics, Associate Professor, Department of Materials Science and the Industry of Nanosystems, Voronezh State University, Voronezh, Russian Federation; e-mail: [svkannykin@gmail.com](mailto:svkannykin@gmail.com). ORCID iD: <https://orcid.org/0000-0001-8756-5722>.

*Boris L. Agapov*, PhD in Technical Science, Centre for Collective Use of Scientific Equipment, Voronezh State University, Voronezh, Russian Federation; e-mail: [b.agapov2010@yandex.ru](mailto:b.agapov2010@yandex.ru).

*Pavel V. Seredin*, DSc in Physics and Mathematics, Head of the Department of Solid State Physics and Nanostructures, Voronezh State University, Voronezh, Russian Federation; e-mail: [paul@phys.ru](mailto:paul@phys.ru). ORCID iD: <https://orcid.org/0000-0002-6724-0063>.

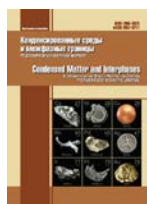
*Evelina P. Domashevskaya*, DSc in Physics and Mathematics, Full Professor, Department of Solid State Physics and Nanostructures, Voronezh State University, Voronezh, Russian Federation; e-mail: [ftt@phys.vsu.ru](mailto:ftt@phys.vsu.ru). ORCID iD: <https://orcid.org/0000-0002-6354-4799>.

All authors have read and approved the final manuscript.

*Received 5 February 2021; Approved after reviewing 15 February 2021; Accepted 15 March 2021; Published online 25 March 2021.*

*Translated by Marina Strepetova*

*Edited and proofread by Simon Cox*



## Original articles

Original article

<https://doi.org/10.17308/kcmf.2021.23/3302>

## Luminescent properties of colloidal mixtures of $Zn_{0.5}Cd_{0.5}S$ quantum dots and gold nanoparticles

O. V. Ovchinnikov✉, M. S. Smirnov, I. G. Grevtseva, V. N. Derepko, T. A. Chevychelova, L. Yu. Leonova, A. S. Perepelitsa, T. S. Kondratenko

Voronezh State University,  
1 Universitetskaya ploshad, Voronezh 394018, Russian Federation

### Abstract

The aim of the study is to establish spectral-luminescent interaction effects in mixtures of colloidal  $Zn_{0.5}Cd_{0.5}S$  quantum dots passivated with 2-mercaptopropionic acid and Au and Au/SiO<sub>2</sub> nanoparticles. The studied samples of  $Zn_{0.5}Cd_{0.5}S$  quantum dots, Au and Au/SiO<sub>2</sub> nanoparticles and their mixtures were obtained by methods of colloidal synthesis and were characterised using transmission electron microscopy. The absorption, luminescence and time-resolved luminescence spectroscopy were used as the main investigation methods. The measurements were carried out at temperatures of 77 K and 300 K. The spectral-luminescent properties of “free”  $Zn_{0.5}Cd_{0.5}S$  quantum dots and those interacting with Au and Au/SiO<sub>2</sub> nanoparticles were compared. It was found that the luminescence properties of  $Zn_{0.5}Cd_{0.5}S$  quantum dots can be controlled under conditions of changing plasmon–exciton coupling achieved during the formation of a dielectric SiO<sub>2</sub> shell on the surface of Au nanoparticles as well as a result of a polymer introduced into the colloidal mixture.

**Keywords:**  $Zn_{0.5}Cd_{0.5}S$  quantum dots, gold nanoparticles, core/shell, silicon dioxide (SiO<sub>2</sub>), extinction spectrum, plasmon–exciton interaction

**Acknowledgements:** the study was carried out within the framework of the Grant of the President of the Russian Federation to Support Leading Scientific Schools of the Russian Federation, project NSH-2613.2020.2. The results of transmission electron microscopy using a Libra 120 microscope were obtained with the help of the equipment of the Center for Collective Use of Voronezh State University.

**For citation:** Ovchinnikov O. V., Smirnov M. S., Grevtseva I. G., Derepko V. N., Chevychelova T. A., Leonova L. Yu., Perepelitsa A. S., Kondratenko T. S. Luminescent properties of colloidal mixtures of  $Zn_{0.5}Cd_{0.5}S$  quantum dots and gold nanoparticles. *Kondensirovannye sredy i mezhfaznye granitsy = Condensed Matter and Interphases*. 2021;23(1): 49–55. <https://doi.org/10.17308/kcmf.2021.23/3302>

Овчинников О. В., Смирнов М. С., Гревцева И. Г., Дерепко В. Н., Чевычелова Т. А., Леонова Л. Ю., Перепелица А. С., Кондратенко Т. С. Люминесцентные свойства коллоидных смесей квантовых точек  $Zn_{0.5}Cd_{0.5}S$  с наночастицами золота. *Конденсированные среды и межфазные границы*. 2021;23(1): 40–55. <https://doi.org/10.17308/kcmf.2021.23/3302>

✉ Oleg V. Ovchinnikov, e-mail: [ovchinnikov\\_o\\_v@rambler.ru](mailto:ovchinnikov_o_v@rambler.ru)

© Ovchinnikov O. V., Smirnov M. S., Grevtseva I. G., Derepko V. N., Chevychelova T. A., Leonova L. Yu., Perepelitsa A. S., Kondratenko T. S., 2021



## 1. Introduction

Much attention has been recently paid to attempts to create hybrid plasmon-exciton nanostructures based on metal (plasmonic) nanoparticles (NPs), semiconductor quantum dots (QDs), and/or dye molecules [1-10]. For such hybrid systems, QDs and dye luminescence spectra are heavily affected by the presence of metal nanoparticles (nanoresonators) which have modes with frequencies similar to the frequency of the luminescence maximum. Spatial distribution of the mixture components is also essential for the resulting spectral pattern. The variation of these parameters allows adjusting the modes of plasmon-exciton coupling (weak, intermediate, and strong), which opens the possibility to control the parameters of the spectral-luminescence properties of the emitter [10–12].

Some sources describe research aimed at identifying conditions for the formation of plasmon-exciton nanostructures providing resonance effects in the modes of weak (Purcell effect), intermediate (Fano effect), and strong (Rabi splitting) plasmon-exciton interaction [1, 2, 6–13]. Moreover, the researchers have detected plasmon-induced fluorescence amplification/quenching [9], the plasmon-enhanced Förster energy transfer [9], and induced exciton-plasmon-photon conversion [8]. However, the available results of the studies of plasmon-exciton interaction do not allow finding a solution to the fundamental problem of predicting the final luminescent properties of hybrid nanostructures.

It is important that there has not been developed yet a unified approach to creating hybrid nanostructures to adjust the modes of plasmon-exciton coupling from weak to intermediate and strong. Experimental data obtained by different research teams are contradictory and vary mainly between fluorescence amplification and quenching. Moreover, they do not provide major parameters and physically important experimental characteristics to explain the processes of plasmon-exciton interactions. The absence of detailed experimental data and their weak correlation with the results of theoretical calculations are due to the complicated nature

of plasmon-exciton interactions. Also, the researchers have not developed the problem of the formation of QD luminescence quenching centres when QDs interact with plasmonic NPs, as well as their role in shaping the final “hybrid” luminescent properties of plasmon-exciton nanostructures. Therefore, the development of techniques to control luminescent properties of hybrid nanostructures based on plasmonic NPs and QDs and/or dye molecules is a pressing problem.

This paper presents experimental data which show the possibility to control the luminescent properties of  $\text{Zn}_{0.5}\text{Cd}_{0.5}\text{S}$  QDs in the near field of spherical gold (Au) NPs. The research involved creating special conditions which made it possible to change a plasmon-exciton coupling by forming Au/SiO<sub>2</sub> core/shell NPs and to further separate the mixture components by introducing a polymer, which allowed changing the distance between them.

## 2. Experimental

Colloidal  $\text{Zn}_{0.5}\text{Cd}_{0.5}\text{S}$  QDs passivated with 2-mercaptopropionic acid (2-MPA) were synthesized using aqueous synthesis techniques [16, 17]. This approach involves mixing aqueous solutions of precursors for  $\text{CdBr}_2$  (224 mg, 50 ml), and  $\text{Zn}(\text{ClO}_4)_2$  (242 mg, 10 ml), followed by the introduction of 2-MPA (230  $\mu\text{l}$ ) into the reaction mixture and adjusting the pH level to 7 with 1 M of NaOH solution. Then,  $\text{Na}_2\text{S}$  aqueous solution (30 mg, 10 ml) was added to the colloidal solution.

The synthesis of spherical Au NPs was carried out by the Turkevich method [14]. 1.4 ml of 1%  $\text{Na}_3\text{C}_6\text{H}_5\text{O}_7$  solution was added to the boiling 0.01%  $\text{HAuCl}_4$  solution (200 ml). The resulting mixture was boiled for 30 minutes with constant stirring. The SiO<sub>2</sub> shell on the surface of Au NPs (Au/SiO<sub>2</sub> core/shell NPs) was formed by Au NPs surface functionalisation by a monolayer of (3-mercaptopropyl)trimethoxysilane (3-MPTMS) with a subsequent formation of dense SiO<sub>2</sub> layers by sodium metasilicate ( $\text{Na}_2\text{O}(\text{SiO}_2)$ ). For this, 0.4 ml of 0.035% hydrolysed solution of 3-MPTMS was mixed with 30 ml of solution of colloidal Au NPs. Then the  $\text{Na}_2\text{SiO}_3$  aqueous solution (96 mg, 10 ml) was added to the reaction mixture. The flask with the reaction mixture was placed in a

water bath at 60 °C and was held there for 6 hours with continuous stirring.

Hybrid structures were formed by mixing colloidal solutions of  $Zn_{0.5}Cd_{0.5}S$  QDs with Au NPs, Au NPs in the presence of 4 % polymer solution of poly-(diallyldimethylammonium chloride) (PolyDADMAC), and Au/SiO<sub>2</sub> core/shell NPs in an approximate molar ratio  $[v(QDs)]:[v(NPs)]$  of  $\sim 10^4$  mole fraction (m.f.).

The size and morphology of  $Zn_{0.5}Cd_{0.5}S$  QDs, Au NPs, and Au/SiO<sub>2</sub> NPs were determined using a Libra 120 transmission electron microscope (TEM) (Carl Zeiss, Germany). Absorption properties were studied using a USB2000+ spectrometer (Ocean Optics, USA) with a USB-DT light source (Ocean Optics, USA). The luminescence spectra and the luminescence decay kinetics of  $Zn_{0.5}Cd_{0.5}S$  QDs were studied by a USB2000+ and a TimeHarp 260 time-correlated single-photon counting board (PicoQuant, Germany) with a PMC-100-20 module (Becker&Hickl, Germany) with the time resolution of 0.2 ns. A HPL-H77GV1BT-V1BT-V1 diode module with the wavelength of 380 nm was used to stimulate the luminescence.

### 3. Results and discussion

#### 3.1. Structural data

The analysis of TEM images showed that the approach to the synthesis of  $Zn_{0.5}Cd_{0.5}S$  QDs ensures the formation of individual nanocrystals with an average size of  $4.0 \pm 0.5$  nm (Fig. 1a). The existing dispersion in size in  $Zn_{0.5}Cd_{0.5}S$  QDs ensembles  $\sim 35\%$  is due to the chosen approach to colloidal synthesis in aqueous solution.

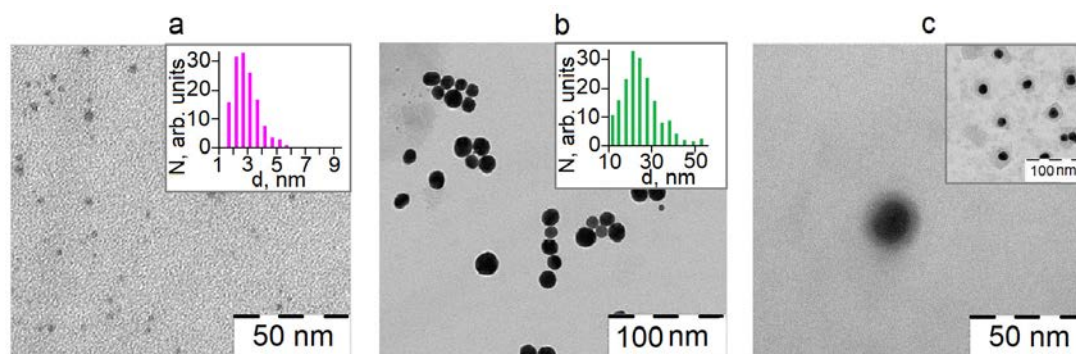
Fig. 1b and c show TEM images of Au NPs and Au/SiO<sub>2</sub> core/shell NPs. It is shown that the

Turkevich method results in the formation of Au NPs with a spherical shape. The average diameter of spherical Au NPs in the ensemble is  $20 \pm 3$  nm with a size distribution within 30% (Fig. 1b). The analysis of TEM images of Au/SiO<sub>2</sub> core/shell NPs (Fig. 1c) showed the formation of a SiO<sub>2</sub> shell on the surface of Au NPs with a thickness of  $10 \pm 03$  nm. There was practically no coagulation of Au/SiO<sub>2</sub> core/shell NPs.

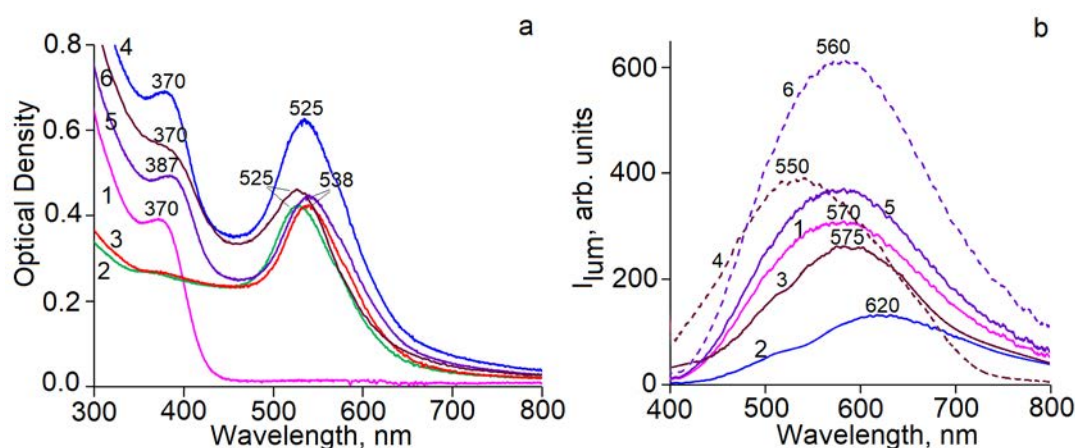
#### 3.2. Spectral-luminescent properties of mixtures of colloidal $Zn_{0.5}Cd_{0.5}S$ QDs and Au, Au/SiO<sub>2</sub> nanoparticles

A characteristic feature for the exciton transition [18] in the optical absorption of  $Zn_{0.5}Cd_{0.5}S$  QDs is in the region of 370 nm (Fig. 2a, curve 1). The maximum of the light extinction spectrum for Au NPs is in the range of 525 nm (Fig. 2a, curve 2). Adding 4% PolyDADMAC polymer solution to Au NPs does not influence the position of the light extinction maximum in the region of 525 nm. The formation of a SiO<sub>2</sub> shell with a thickness of 10 nm on the surface of Au NPs leads to a long-wave spectral shift of the maximum of the light extinction spectrum of Au NPs from 525 to 538 nm as a result of changes in the total permittivity of the core/shell system (Fig. 2a, curve 3).

For mixtures of  $Zn_{0.5}Cd_{0.5}S$  QDs and Au NPs, the resulting light extinction spectrum is not a simple sum of the spectra of the mixture's components. The shift of the maximums of the attenuation bands of the mixture components and an increase in optical density throughout the extinction spectrum indicates a strong plasmon-exciton interaction between the components



**Fig. 1.** TEM images and size distribution's histogram of  $Zn_{0.5}Cd_{0.5}S$  QDs - (a); Au NPs - (b); Au/SiO<sub>2</sub> core/shell NPs with a shell thickness of 10 nm - (c)



**Fig. 2.** (a) Optical absorption spectra of Zn<sub>0.5</sub>Cd<sub>0.5</sub>S QDs (1), extinction spectra of Au NPs, Au NPs (PolyDADMAC) (2), Au/SiO<sub>2</sub> core/shell NPs (3), extinction spectra of mixtures of Zn<sub>0.5</sub>Cd<sub>0.5</sub>S QDs and Au NPs (4), Zn<sub>0.5</sub>Cd<sub>0.5</sub>S QDs and Au NPs (PolyDADMAC) (5), Zn<sub>0.5</sub>Cd<sub>0.5</sub>S QDs and Au/SiO<sub>2</sub> core/shell NPs (6). (b) Luminescence spectra of Zn<sub>0.5</sub>Cd<sub>0.5</sub>S QDs (1), mixtures of Zn<sub>0.5</sub>Cd<sub>0.5</sub>S QDs and Au NPs at  $T = 300$  K and  $T = 77$  K (2), Zn<sub>0.5</sub>Cd<sub>0.5</sub>S QDs and Au NPs (PolyDADMAC) at  $T = 300$  K (3) and at  $T = 77$  K (4), Zn<sub>0.5</sub>Cd<sub>0.5</sub>S QDs and Au/SiO<sub>2</sub> core/shell NPs at  $T = 300$  K (5) and at  $T = 77$  K (6)

of the mixture (Fig. 2a, curve 4). In case of the mixtures of Zn<sub>0.5</sub>Cd<sub>0.5</sub>S QDs and Au NPs in the presence of a PolyDADMAC polymer, as well as core/shell Au/SiO<sub>2</sub> NPs, in the resulting extinction spectra there was an increase in the optical density in the region of exciton transition of Zn<sub>0.5</sub>Cd<sub>0.5</sub>S QDs (Fig. 2a, curves 5 and 6) which can be explained not only by a contribution of Au NPs to the overall spectral contour of the light extinction, but a weak interaction between the components of the mixture.

The control of the size and the morphology of mixture components using the applied synthesis methods provided a considerable overlap between Au NPs light extinction peak (525 nm) and Au/SiO<sub>2</sub> core/shell NPs (538 nm) and Zn<sub>0.5</sub>Cd<sub>0.5</sub>S QDs luminescence spectrum (570 nm), which is crucial for the appearance of effects of plasmon-exciton interaction in the luminescent properties of the emitter.

For mixtures of Zn<sub>0.5</sub>Cd<sub>0.5</sub>S QDs and Au NPs, there was luminescence quenching accompanied by a transformation of the spectral contour of QD emission band resulting in a dip in the region of 525 nm (Fig. 2b, curve 2). At the same time, the luminescence lifetime was reduced from 21 ns to 4 ns. Lowering the temperature of the samples to 77 K did not qualitatively change the luminescent properties of the mixtures of Zn<sub>0.5</sub>Cd<sub>0.5</sub>S QDs and Au NPs. Such behaviour

of luminescent properties indicates a complex character of plasmon-exciton interaction in the studied mixtures due to several simultaneous effects, such as the Fano effect [1, 5, 10] and nonradiative recombination [15, 19] caused by changes in the immediate environment of Zn<sub>0.5</sub>Cd<sub>0.5</sub>S QDs. Increasing the distance between Zn<sub>0.5</sub>Cd<sub>0.5</sub>S QDs and Au NPs by a PolyDADMAC polymer led to a decreased quenching of QDs luminescence intensity, also accompanied by a transformation of the spectral contour (Fig. 2b, curve 3). What is more, the luminescence lifetime did not change. Lowering the temperature to 77 K contributed to a hypsochromic shift in Zn<sub>0.5</sub>Cd<sub>0.5</sub>S QDs luminescence band to the region of 550 nm and 1.5 times increase in its intensity (Fig. 2b, curve 4) accompanied by an increase in the luminescence lifetime from 23 to 25 ns. The control of the distance between the mixture components by means of a SiO<sub>2</sub> shell with a thickness of 10 nm on Au NPs surface led to a slight enhancement of QDs luminescent properties at a temperature of 300 K (Fig. 2b, curve 5). At a temperature of 77 K, Zn<sub>0.5</sub>Cd<sub>0.5</sub>S QDs luminescence intensity grew 8 times, whereas the luminescence lifetime rose from 23 to 40 ns (Fig. 2b, curve 6). Such behaviour of luminescent properties can be a manifestation of the Purcell effect complicated by the influence of the effects of exciton-phonon interaction, concentration

quenching, and possible exchange of electronic excitations which always occur in hybrid systems, including those involving a SiO<sub>2</sub> shell [1, 4, 11, 12, 20, 21].

Thus, the spatial distribution of plasmonic Au NPs and Zn<sub>0.5</sub>Cd<sub>0.5</sub>S QDs under strong spectral resonance enables controlling luminescent properties of Zn<sub>0.5</sub>Cd<sub>0.5</sub>S QDs. Obviously, this is due to switching between the modes of the plasmon-exciton coupling. Resonance effects in their pure form are complicated by multiple interfering factors, such as the electron-phonon interaction and the resonant nonradiative energy transfer between the components of the mixture.

### 3. Conclusions

The study demonstrated new experimental effects of interaction between Zn<sub>0.5</sub>Cd<sub>0.5</sub>S QDs and Au NPs resulting from changes in the plasmon-exciton coupling between the mixture components due to the formation of SiO<sub>2</sub> shells with a thickness of 10 nm on Au NPs surface and the introduction of a polymer in the colloidal mixture. It was shown that the formation of mixtures of Zn<sub>0.5</sub>Cd<sub>0.5</sub>S QDs and plasmonic Au NPs is accompanied by the intensity quenching, a transformation of the spectral contour of QD luminescence, and a decrease in the luminescence lifetime. Increasing the distance between the mixture components by introducing a PolyDADMAC polymer and the formation of SiO<sub>2</sub> shell with a thickness of 10 nm on Au NPs surface block the process of luminescence quenching at a temperature of 300 K and lead to an increase in the luminescence intensity at 77 K accompanied by an increase in the luminescence lifetime. The obtained data demonstrate the possibility of controlling Zn<sub>0.5</sub>Cd<sub>0.5</sub>S QDs luminescent properties under conditions of changing modes of plasmon-exciton interaction between the mixtures components. They also clearly indicate a complex character of the exciton-plasmon interaction in the studied mixtures due to several simultaneous effects, such as the Purcell effect, the Fano effect, nonradiative energy transfer from QDs to plasmonic particles, and resonance detuning.

### Conflict of interests

The authors declare that they have no known competing financial interests or personal relationships that could have influenced the work reported in this paper.

### References

1. Luo Y., Zhao J. Plasmon-exciton interaction in colloidally fabricated metal nanoparticle-quantum emitter nanostructures. *Nano Research*. 2019;12(9): 2164–2171. <https://doi.org/10.1007/s12274-019-2390-z>
2. Lepeshov S. I., Krasnok A. E., Belov P. A., Miroshnichenko A. E. Hybrid nanophotonics. *Physics-Uspekhi*. 2018;61(11): 1035–1050. <https://doi.org/10.3367/UFNe.2017.12.038275>
3. Khan I., Saeed K., Khan I. Nanoparticles: properties, applications and toxicities. *Arabian Journal of Chemistry*. 2019;12(7): 908–931. <https://doi.org/10.1016/j.arabjc.2017.05.011>
4. Kim K.-S., Kim J.-H., Kim H., Laquai F., Arifin E., Lee J.-K., Yoo S., Sohn B.-H. Switching Off FRET in the hybrid assemblies of diblock copolymer micelles, quantum dots, and dyes by plasmonic nanoparticles. *ACS Nano*. 2012;6(6): 5051–5059. <https://doi.org/10.1021/nn301893e>
5. Andreeva O. V., Sidorov A. I., Staselko D. I., Khrushcheva T. A. Synthesis and optical properties of hybrid “plasmon-exciton” nanostructures based on Ag-AgI in nanoporous silica glass. *Physics of the Solid State*. 2012;54(6): 1293–1297. <https://doi.org/10.1134/S1063783412060029>
6. Chen G. Y., Chen Y. N., Chuu D. S. Spontaneous emission of quantum dot excitons into surface plasmons in a nanowire. *Optics Letters*. 2008;33(19): 2212–2214. <https://doi.org/10.1364/OL.33.002212>
7. Akimov A. V., Mukherjee A., Yu C. L., Chang D. E., Zibrov A. S., Hemmer P. R., Park H., Lukin M. D. Generation of single optical plasmons in metallic nanowires coupled to quantum dots. *Nature*. 2007;450(7168): 402–406. <https://doi.org/10.1038/nature06230>
8. Fedutik Y., Temnov V. V., Schöps O., Woggon U., Artemyev M. V. Exciton-plasmon-photon conversion in plasmonic nanostructures. *Physical Review Letters*. 2007;99(13): 136802. <https://doi.org/10.1103/PhysRevLett.99.136802>
9. Govorov A. O., Lee J., Kotov N. A. Theory of plasmon-enhanced Förster energy transfer in optically excited semiconductor and metal nanoparticles. *Physical Review B*. 2007;76: 125308. <https://doi.org/10.1103/PhysRevB.76.125308>

10. Zhang W., Govorov A. O., Bryant G. W. Semiconductor-metal nanoparticle molecules: hybrid excitons and the nonlinear Fano effect. *Physical Review Letters*. 2006;97: 146804. <https://doi.org/10.1103/PhysRevLett.97.146804>
11. Leng H., Szychowski B., Daniel M.-Ch., Pelton M. Strong coupling and induced transparency at room temperature with single quantum dots and gap plasmons. *Nature Communications*. 2018;9: 4012. <https://doi.org/10.1038/s41467-018-06450-4>
12. Cao En, Lin W., Sun M., Liang W., Song Yu. Exciton-plasmon coupling interactions: from principle to applications. *Nanophotonics*. 2018;7(1): 145–167. <https://doi.org/10.1515/nanoph-2017-0059>
13. Pompa P. P., Martiradonna L., Torre A. D., Sala F. D., Manna L., Vittorio M. De, Calabi F., Cingolani R., Rinaldi R. Metal-enhanced fluorescence of colloidal nanocrystals with nanoscale control. *Nature Nanotechnology*. 2006;1: 126–130. <https://doi.org/10.1038/nnano.2006.93>
14. Turkevich J., Stevenson P. C., Hillier J. A study of the nucleation and growth processes in the synthesis of colloidal gold. *Discussion Faraday Society*. 1951;11: 55–75. <https://doi.org/10.1039/df9511100055>
15. Krivenkov V., Dyagileva D., Samokhvalov P., Nabiev I., Rakovich Yu. Effect of spectral overlap and separation distance on exciton and biexciton quantum yields and radiative and nonradiative recombination rates in quantum dots near plasmon nanoparticles. *Annalen der Physik*. 2020;532(8): 2000236. <https://doi.org/10.1002/andp.202000236>
16. Smirnov M. S., Ovchinnikov O. V., Hazal N. A. R., Zvyagin A. I. Control over the size effect in the spectroscopic properties of  $Zn_xCd_{1-x}S$  colloidal quantum dots. *Inorganic Materials*. 2018;54(5): 413–420. <https://doi.org/10.1134/S002016851805014X>
17. Kondratenko T. S., Smirnov M. S., Ovchinnikov O. V., Shabunya-Klyachkovskaya E. V., Matsukovich A. S., Zvyagin A. I., Vinokur Y. A. Size-dependent optical properties of colloidal CdS quantum dots passivated by thioglycolic acid. *Semiconductors*. 2018;52(9): 1137–1144. <https://doi.org/10.1134/S1063782618090087>
18. Ovchinnikov O. V., Smirnov M. S., Shapiro B. I., Shatskikh T. S., Latyshev A. N., Mien Ph. Thi Hai, Khokhlov V. Yu. Spectral manifestations of hybrid association of CdS colloidal quantum dots with methylene blue molecules. *Optics and Spectroscopy*. 2013;115(3): 340–348. <https://doi.org/10.1134/S0030400X1309018X>
19. Smirnov M. S., Buganov O. V., Shabunya-Klyachkovskaya E. V., Tikhomirov S. A., Ovchinnikov O. V., Vitukhnovsky A. G., Perepelitsa A. S., Matsukovich A. S., Katsaba A. V. Dynamics of electronic excitations decay in hydrophilic colloidal CdS quantum dots in gelatin with involvement of localized states. *Physica E: Low-dimensional Systems and Nanostructures*. 2016;84: 511–518. <https://doi.org/10.1016/j.physe.2016.07.004>
20. Kondratenko T. S., Grevtseva I. G., Zvyagin A. I., Ovchinnikov O. V., Smirnov M. S. Luminescence and nonlinear optical properties of hybrid associates of  $Ag_2S$  quantum dots with molecules of thiazine dyes. *Optics and Spectroscopy*. 2018;124(5): 673–680. <https://doi.org/10.1134/S0030400X18050090>
21. Ievlev V. M., Latyshev A. N., Ovchinnikov O. V., Smirnov M. S., Klyuev V. G., Kholkina A. M., Utekhin A. N., Evlev A. B. Photostimulated formation of anti-stokes luminescence centers in ionic covalent crystals. *Doklady Physics*. 2006;51(8): 400–402. <https://doi.org/10.1134/S1028335806080027>

### Information about the authors

*Oleg V. Ovchinnikov*, DSc in Physics and Mathematics, Professor, Department of Optics and Spectroscopy, Voronezh State University, Voronezh, Russian Federation; e-mail: ovchinnikov\_o\_v@rambler.ru. ORCID iD: <https://orcid.org/0000-0001-6032-9295>.

*Mikhail S. Smirnov*, PhD in Physics and Mathematics, Associate Professor, Department of Optics and Spectroscopy, Voronezh State University, Voronezh, Russian Federation; e-mail: smirnov\_m\_s@mail.ru. ORCID iD: <https://orcid.org/0000-0001-8765-0986>.

*Irina G. Grevtseva*, PhD in Physics and Mathematics, Lecturer, Department of Optics and Spectroscopy, Voronezh State University, Voronezh, Russian Federation; e-mail: grevtseva\_ig@inbox.ru. ORCID iD: <https://orcid.org/0000-0002-1964-1233>.

*Violetta N. Derepko*, PhD student, Department of Optics and Spectroscopy, Voronezh State University, Voronezh, Russian Federation; e-mail: viol.physics@gmail.com. ORCID iD: <https://orcid.org/0000-0002-9096-5388>.

*Tamara A. Chevychelova*, PhD student, Department of Optics and Spectroscopy, Voronezh State University, Voronezh, Russian Federation; e-mail: t.chevychelova@rambler.ru. ORCID iD: <https://orcid.org/0000-0001-8097-0688>.

*Liana Yu. Leonova*, PhD in Physics and Mathematics, Associate Professor, Department of Optics and Spectroscopy, Voronezh State University, Voronezh, Russian Federation; e-mail: liana.leonova@mail.ru. ORCID iD: <https://orcid.org/0000-0003-4171-4176>.

*Aleksey S. Perepelitsa*, PhD in Physics and Mathematics, senior lecturer, Department of Optics and Spectroscopy, Voronezh State University, Voronezh, Russian Federation; e-mail: a-perepelitsa@yandex.ru. ORCID iD: <https://orcid.org/0000-0001-8097-0688>.

*Tamara S. Kondratenko*, PhD in Physics and Mathematics, Associate Professor, Department of

Optics and Spectroscopy, Voronezh State University, Voronezh, Russian Federation; e-mail: tamara-shatskikh@rambler.ru. ORCID iD: <https://orcid.org/0000-0003-4936-0130>.

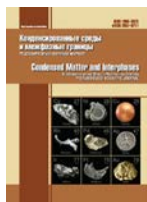
All authors read and approved the final manuscript.

*Received 25 December 2020; Approved after reviewing 15 February 2021; Accepted 15 March 2021; Published online 25 March 2021.*

*Translated by Irina Charychanskaya*

*Edited and proofread by Simon Cox*





## Original articles

Original article

<https://doi.org/10.17308/kcmf.2021.23/3303>

## Ozone detection by means of semiconductor gas sensors based on palladium (II) oxide

S. V. Ryabtsev<sup>1</sup>✉, D. A. A. Ghareeb<sup>1</sup>, A. A. Sinelnikov<sup>1</sup>, S. Yu. Turishchev<sup>1</sup>, L. A. Obvintseva<sup>2</sup>,  
A. V. Shaposhnik<sup>3</sup>

<sup>1</sup> Voronezh State University,  
1 Universitetskaya pl., Voronezh 394018, Russian Federation

<sup>2</sup> Russian State University named after A. N. Kosygin,  
1 Malaya Kaluzhskaya str., Moscow 119071, Russian Federation

<sup>3</sup> Voronezh State Agricultural University,  
1 Michurina ul., Voronezh 394087, Russian Federation

### Abstract

Thin film semiconductor sensors based on palladium oxide were produced to analyse the concentration of ozone in the air. The palladium oxide films were obtained by means of thermal oxidation of ~ 20-30 nm metal in air at various temperatures. The oxide films were studied using electron microscopy and reflection high-energy electron diffraction. The optical, electrophysical, and gas sensitivity properties of the films were investigated. The study determined the optimal oxidation annealing temperature that ensures the uniform composition of the films and absence of electrical noise affecting the gas detection process. The article explains that electrical noise in ultrathin films is caused by their fragmentation during oxidation annealing. The study demonstrated the high sensitivity of the obtained films to oxide.

**Keywords:** Palladium oxide, Ultrathin films, Electron microscopy, Reflection high-energy electron diffraction, Phase composition, Electrical noise, Gas sensitivity properties, Ozone

**Acknowledgements:** the study was supported by the Russian Foundation for Basic Research (project No. 20-03-00901). TEM was conducted at the Centre for Collective Use of Scientific Equipment of Voronezh State University (<http://ckp.vsu.ru>).

**For citation:** Ryabtsev S. V., Ghareeb D. A. A., Sinelnikov A. A., Turishchev S. Yu., Obvintseva L. A., Shaposhnik A. V. Ozone detection by means of semiconductor gas sensors based on palladium (II) oxide. *Kondensirovannye sredy i mezhfaznye granitsy = Condensed Matter and Interphases*. 2021;23(1): 56–61. <https://doi.org/10.17308/kcmf.2021.23/3303>

**Для цитирования:** Рябцев С. В., Гхариб Д. А. А., Синельников А. А., Турищев С. Ю., Обвинцева Л. А., Шапошник А. В. Детектирование озона в воздухе полупроводниковыми газовыми сенсорами на основе оксида палладия (II). *Конденсированные среды и межфазные границы*. 2021;23(1): 56–61. <https://doi.org/10.17308/kcmf.2021.23/3303>

✉ Stanislav V. Ryabtsev, e-mail: [ryabtsev@phys.vsu.ru](mailto:ryabtsev@phys.vsu.ru)

© Ryabtsev S. V., Ghareeb D. A. A., Sinelnikov A. A., Turishchev S. Yu., Obvintseva L. A., Shaposhnik A. V., 2021



The content is available under Creative Commons Attribution 4.0 License.

## 1. Introduction

At the moment, ozone-based technologies are widely used for the disinfection of water in water supply lines, swimming pools, and indoor water parks, as well as for sewage water treatment, the bleaching of paper, etc. Ozone is obtained in large quantities by means of special on-site generators. However, ozone is very toxic. The maximum acceptable concentration (MAC) of ozone in the operational area is  $0.1 \text{ mg/m}^3$  or  $\sim 50 \text{ ppb}$  ( $1 \text{ ppb} = 10^{-7} \text{ vol. \%}$ ). For comparison, the MACs of other toxic gases, including  $\text{Cl}_2$ ,  $\text{NO}_2$ , and  $\text{CO}$ ,  $\text{NH}_3$  are within the range of  $300\text{--}3 \cdot 10^4 \text{ ppb}$ . Therefore, in order to ensure safety at the ozone generation stations, it is necessary to organise continuous and multipoint monitoring of the concentration of ozone in the air. The existing monitoring devices are based on optical techniques for ozone detection and have a number of drawbacks: they are expensive, require a lot of energy, and are difficult to service. Moreover, they only analyse the ozone concentration at a single point, the place where the optical sensor is located. An alternative solution involves using semiconductor-based resistive sensors. Devices with such sensors have a number of advantages: they do not require consumables and allow multipoint continuous monitoring of the air in the operational area.

The production technology of the gas sensitive layer and the choice of the sensor material largely determine the sensitivity of the sensor. The sol-gel method is the most commonly used. It helps to obtain highly developed surfaces available for the adsorption of gases. The article describes a thin-film technology involving the vacuum deposition of gas sensitive layers, because it combines well with established microelectronic technologies. The cost of gas analysers produced using this technology is significantly lower.

$\text{In}_2\text{O}_3$ ,  $\text{WO}_3$ ,  $\text{ZnO}$ , and  $\text{SnO}_2$  oxides are most commonly used as sensor materials for ozone detection, either in pure forms or with additives. In our study, we used PdO, which was first suggested as a sensor material for ozone analysis in our previous articles [1-3].

The purpose of the study was to optimise the technology of the production of thin gas sensitive PdO films that ensure detection of ozone, when its concentration is below the MAC.

## 2. Experimental

Thin PdO films were obtained by thermal sputtering of metallic Pd on various substrates: glass substrates for the study of the optical properties, alumina ceramic ( $\text{Al}_2\text{O}_3$ ) substrates for the analysis of the electrophysical and sensitivity properties, KCl single crystal substrates with an amorphous carbon sublayer in the experiments conducted using transmission electron microscopy (TEM). Fixed sputtering parameters, including the speed of the deposition of the metal on the substrate ( $\sim 1 \text{ nm/min}$ ), the pressure of the residual gases in the vacuum chamber ( $\sim 10^{-6} \text{ Torr}$ ), and the distance between the evaporator and the substrate, allowed us to obtain metallic Pd films with reproducible thickness. The thickness of the films was determined by studying the film edge on a single crystal carbon substrate using a scanning electron microscope. The thickness of the experimental samples was  $\sim 20\text{--}30 \text{ nm}$ . These metal films were annealed in air at 240, 400, and 600 °C for one hour. The obtained films were then characterised.

Optical analysis was performed using an Ocean Optics fibre optic spectrometer in transmission mode.

The phase composition and the microstructure of the films were studied by means of reflection high-energy electron diffraction (RHEED) and transmission electron microscopy (Karl Zeiss Libra 120).

The electrophysical and gas sensitivity properties of the films were studied on special alumina ceramic test structures. An alumina ceramic substrate (2-3 mm) plated with Pt electrodes used for measuring the resistance of PdO films is presented in Fig.1.



**Fig. 1.** The test structure used for the analysis of the electrophysical and gas sensitivity properties of the PdO films

On the back side of the substrate a meander Pt heater was made. It served as a temperature sensor. The temperature of the sensors during the experiments was maintained with an accuracy of 1 °C.

A GS-024-25 ozone generator (“OPTEC”) was used in the gas sensitivity experiments.

### 3. Results and discussion

PdO is a semiconductor oxide of the *p*-type with the bandgap of 2.2–2.7 eV [4–6]. The semiconductor nature of the obtained films was proved by means of optical spectroscopy and electrophysical methods. The transmission spectra of PdO films are characteristic of semiconductor materials with transmission rapidly reducing next to the band-to-band electronic transition  $E_v-E_c$  (Fig. 2). A Tauc plot  $E-(\alpha d h\nu)^2$  was applied to determine the bandgap of the semiconductor  $E_g$ . Extrapolation of the straight line drawn to the linear region of the optical spectrum to the X-axis results in  $E_g = 2.27$  eV (Fig. 2), which complies with the results of previous studies [4–6].

The *p*-type conductivity of PdO was determined earlier in the study of the Seebeck effect in thin films [3]. This is also proved by the

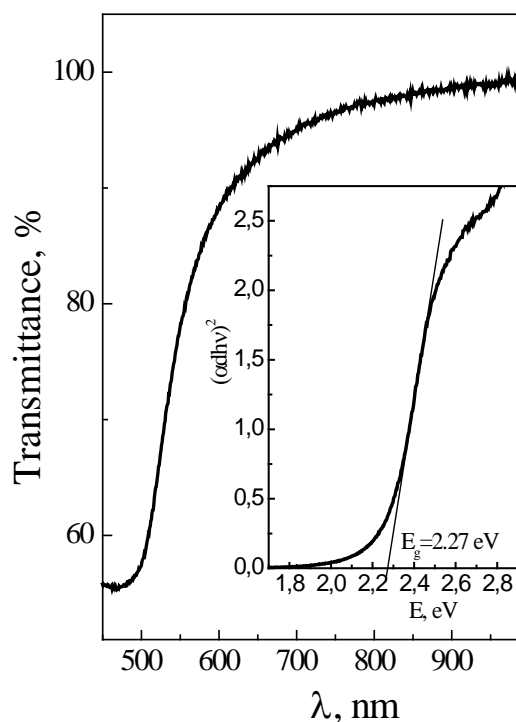


Fig. 2. Optical spectra of PdO

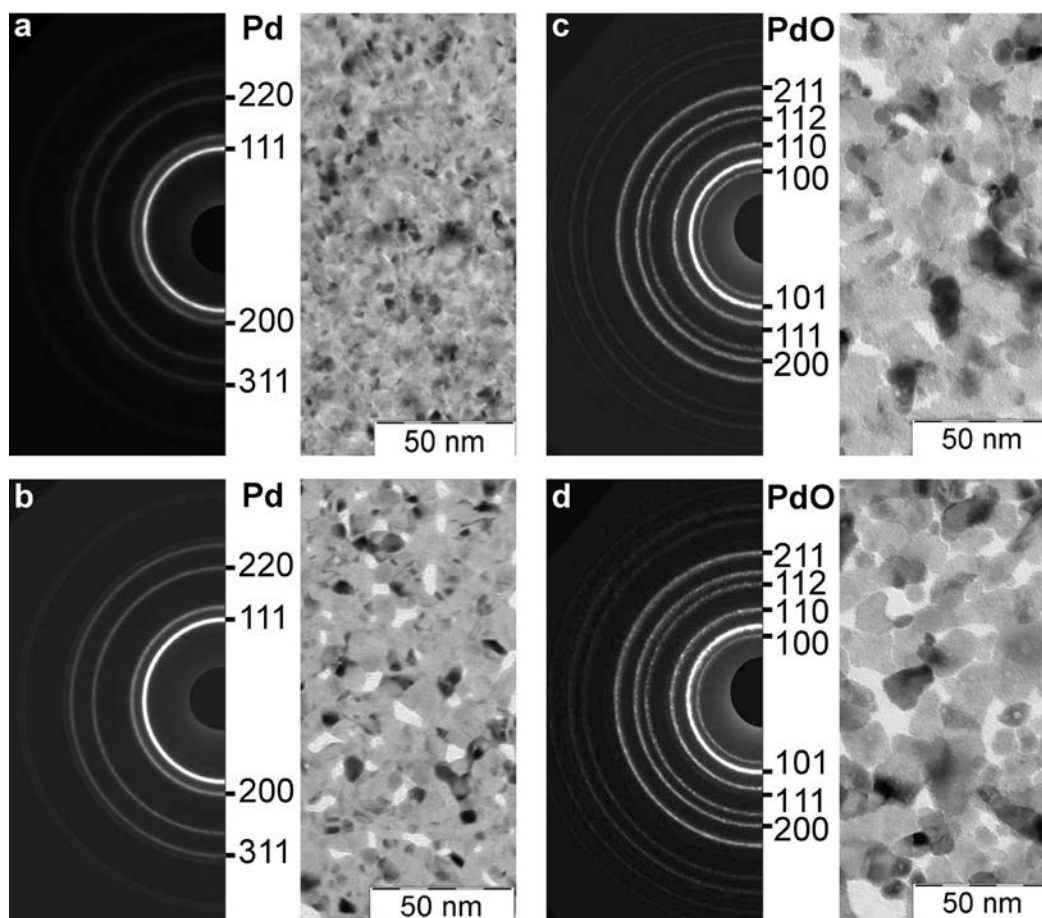
nature of the resistance response of PdO films in the ozone - oxide gas environment (Fig. 4). The resistance of the PdO films, as expected from a *p*-type semiconductor, reduces in the oxidizing environment of ozone (Fig. 4) in full compliance with the known patterns of sensory response [7].

Fig. 3 presents X-ray diffraction patterns and TEM images of the Pd films in various stages of oxidation. The analysis of the X-ray diffraction patterns demonstrated that the initial films (Fig. 3a) are metallic palladium with no visible traces of oxide phases. Films annealed in air at 240 °C (PDF card 00-041-1043 [8]) have the same phase composition.

Increasing the temperature of annealing of Pd films in air up to 400 and 600 °C results in the formation of the tetragonal oxide phase of PdO with the following parameters of the crystal lattice:  $a = 0.3036$  nm,  $c = 0.5339$  nm (PDF card 00-041-1107). In this case, RHEED does not show the metallic palladium phase in the films, which means that the oxidation of palladium is complete and the film now has a single phase - PdO.

One of the features of the oxidation annealing is the growth of crystallites both in the Pd film (Fig. 3b) and in the PdO films (Fig. 3c, d). In this case the films lose their initial uniform structure. The growth of crystallites and formation of gaps in the film proceeds in proportion to the growth of the annealing temperature. Such secondary recrystallization significantly affects the electrophysical properties of the films. During the oxidation annealing of the films applied to test structures (Fig. 1) we registered their current resistance, which monotonously grew with the growth of temperature. This was mainly accounted for by the oxidation of metallic palladium to the semiconductor oxide which has higher resistance.

It is noteworthy, that at annealing temperatures of more than 550 °C, electrical noise was observed which, according to the microscopic study (Fig. 3), was directly connected to the fragmentation of the thin films. We assume that the increasing fragmentation of the films results in worse contact between the crystallites, which causes the electrical noise. At a temperature of above 600 °C, the noise level and the resistance grow dramatically. At a temperature of 650–700 °C, the films fragmentation ends and as a



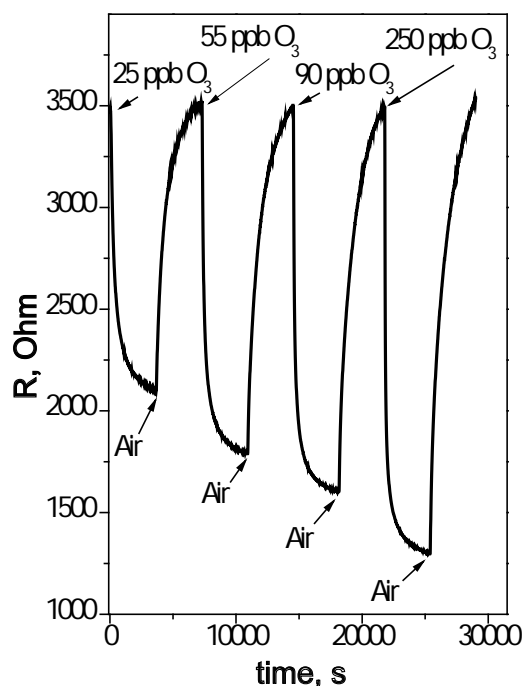
**Fig. 3.** X-ray diffraction patterns and TEM images of the initial Pd film (a) and the films annealed at 240 (b), 400 (c), and 600 °C (d)

result the films lose their electrical conductivity.

The described patterns are characteristic for the thin films (~ 20–30 nm) described in this article. The thickness of the films was chosen because of the ratio of the surface area to the volume, i.e. the sensory effect of the films depends on the gas chemisorption. The inner “exchange” layers of the films remain passive and shunt the changes in the electrical conductivity of the surface layers, thus reducing the sensory effect.

Therefore, the optimal annealing temperature for PdO thin films should not exceed 550 °C. This ensures the single-phase composition of the films and the absence of electrical noise that interferes with accurate resistance measurements.

The gas sensitive properties of PdO thin films were studied, when the concentrations of ozone in the air were 25, 55, 90, and 250 ppb. The operating temperature of the PdO films during the ozone detection experiments was 150 °C. The resistance response of the PdO based thin



**Fig. 4.** The resistance response of the PdO films to various concentrations of ozone in the air

film sensor obtained by means of the described technology is presented in Fig. 4.

The literature review demonstrated that the minimal concentrations of ozone registered by semiconductor sensors are from single digit to several tens of ppb [9–12]. Fig. 4 demonstrates that the elaborated technology for the production of ultrathin layers of PdO can detect significantly lower concentrations of ozone in the operation area.

#### 4. Conclusions

In our research, we analysed PdO ultrathin films and their potential as sensor materials for the detection of ozone in the air. The films were obtained by means of thermal oxidation of the layers of metallic palladium. TEM registered the fragmentation of PdO films at higher annealing temperatures, which results in electrical noise occurring during resistance measurements. The optimal oxidation annealing temperature is 550 °C. The sensory layers obtained using this technology can detect ozone at concentrations significantly lower than 25 ppb.

#### Conflict of interests

The authors declare that they have no known competing financial interests or personal relationships that could have influenced the work reported in this paper.

#### References

1. Ryabtsev S. V., Ievlev V. M., Samoylov A. M., Kushev S. B., Soldatenko S. A. Microstructure and electrical properties of palladium oxide thin films for oxidizing gases detection. *Thin Solid Films*. 2017;636: 751–759. <https://doi.org/10.1016/j.tsf.2017.04.009>
2. Ryabtsev S. V., Shaposhnik A. V., Samoylov A. M., Sinelnikov A. A., Soldatenko S. A., Kushev S. B., Ievlev V. M. Thin films of palladium oxide for gas sensors. *Doklady Physical Chemistry*. 2016;470(2): 158–161. <https://doi.org/10.1134/S0012501616100055>
3. Ievlev V. M., Ryabtsev S. V., Samoylov A. M., Shaposhnik A. V., Kushev S. B., Sinelnikov A. A. Thin and ultrathin films of palladium oxide for oxidizing gases detection. *Sensors and Actuators B*. 2018;255(2): 1335–1342. <https://doi.org/10.1016/j.snb.2017.08.121>
4. Heras J. M., Estiu G., Viscido L. Annealing behaviour of clean and oxygen covered polycrystalline palladium films: a work function and electrical resistance study. *Thin Solid Films*. 1990;188(1): 165–172. [https://doi.org/10.1016/0040-6090\(90\)90202-O](https://doi.org/10.1016/0040-6090(90)90202-O)

5. Nilsson P. O., Shivaraman M. S. Optical properties of PdO in the range 0.5–5.4 eV. *Journal of Physics C: Solid State Physics*. 1979;12(7): 1423–1427. <https://doi.org/10.1088/0022-3719/12/7/030>

6. Sobolev V. Val., Mordas D. O., Sobolev V. V. Optical spectra of palladium oxide. *Glass Physics and Chemistry*. 2003;29(4): 360–363. <https://doi.org/10.1023/a:1025116708801>

7. Semiconductor sensors in physico-chemical studies. In: *Handbook of sensors and actuators Vol. 4*. Kupriyanov L. Yu. (ed.). Amsterdam-Lausanna-New York-Oxford-Shannon-Tokio: Elsevier; 1996. 412 p. ISBN 5-02-001542-3

8. *Powder Diffraction File*. Alphabetical Index. Inorganic Compounds. JCPDS.

9. Korotcenkov G., Brinzari V., Cho B. K. In<sub>2</sub>O<sub>3</sub>- and SnO<sub>2</sub>-based ozone sensors: Design and characterization. *Critical Reviews in Solid State and Materials Sciences* 2017;43(2): 83–132. <https://doi.org/10.1080/10408436.2017.1287661>

10. Takada T. Ozone detection by In<sub>2</sub>O<sub>3</sub> thin film gas sensor. In: *Chemical Sensor Technology. V. 2*. Seiyama T. (ed.). Tokyo: Koudansha, Amsterdam: Elsevier; 1989. 59–70 p. <https://doi.org/10.1016/b978-0-444-98784-6.50009-x>

11. Takada T., Tanjou H., Saito T., Harada K. Aqueous ozone detector using In<sub>2</sub>O<sub>3</sub> thin-film semiconductor gas sensor. *Sensors and Actuators B*. 1995;25(1-3): 548–551. [https://doi.org/10.1016/0925-4005\(95\)85119-4](https://doi.org/10.1016/0925-4005(95)85119-4)

12. Obvintseva L. A. Poluprovodnikovye metallo-oksidsnyye sensory dlya opredeleniya khimicheskii aktivnykh gazovykh primesei v vozduшной srede [Semiconductor metal oxide sensors for the determination of chemically active gas impurities in air]. *Rossiiskii khimicheskii zhurnal*. 2008;52(2): 113–121. Available at: <https://www.elibrary.ru/item.asp?id=11629686> (In Russ.)

#### Information about the authors

*Stanislav V. Ryabtsev*, DSc in Physics and Mathematics, Senior Researcher, Department of Solid State Physics and Nanostructures, Voronezh State University, Voronezh, Russian Federation; e-mail: ryabtsev@phys.vsu.ru. ORCID iD: <https://orcid.org/0000-0001-7635-8162>.

*Dina A. A. Ghareeb*, postgraduate student, Department of Solid State Physics and Nanostructures, Voronezh State University; Voronezh, Russian Federation.

*Alexander A. Sinelnikov*, PhD in Physics and Mathematics, Head of the Department of Materials Science and Nanotechnology, Voronezh State University, Voronezh, Russian Federation; e-mail: rnileme@mail.ru.

*Sergey Yu. Turishchev*, DSc in Physics and Mathematics, Associate Professor, Department of Solid State Physics and Nanostructures, Voronezh State University, Voronezh, Russian Federation; e-mail: [tsu@phys.vsu.ru](mailto:tsu@phys.vsu.ru). ORCID iD: <https://orcid.org/0000-0003-3320-1979>.

*Lyudmila A. Obvintseva*, PhD in Physics and Mathematics, Russian State University named after A. N. Kosygin, Moscow, Russian Federation; e-mail: [obvint@yandex.ru](mailto:obvint@yandex.ru).

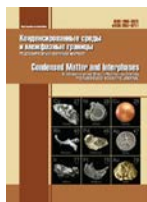
*Aleksey V. Shaposhnik*, DSc in Chemical Sciences, Professor, Head of the Department of Chemistry, Voronezh State Agrarian University named after Emperor Peter the Great, Voronezh, Russian Federation; e-mail: [ash@agrochem.vsau.ru](mailto:ash@agrochem.vsau.ru). ORCID iD: <https://orcid.org/0000-0002-1214-2730>.

All authors have read and approved the final manuscript.

*Received 25 December 2020; Approved after reviewing 15 January 2021; Accepted 15 March 2021; Published online 25 March 2021.*

*Translated by Yulia Dymant*

*Edited and proofread by Simon Cox*



# Condensed Matter and Interphases

Kondensirovannye Sredy i Mezhfaznye Granitsy  
<https://journals.vsu.ru/kcmf/>

## Original articles

Original article

<https://doi.org/10.17308/kcmf.2021.23/3305>

## Calculation of the nonstoichiometry area of nanocrystalline palladium (II) oxide films

A. M. Samoylov<sup>✉</sup>, D. I. Pelipenko, N. S. Kuralenko

<sup>2</sup>Voronezh State University,  
1 Universitetskaya pl., Voronezh 394018, Russian Federation

### Abstract

Nanocrystalline palladium (II) oxide films were synthesised using thermal oxidation in the oxygen atmosphere of the initial ultradispersed metal palladium layers with a thickness of ~ 35 nanometres that were obtained on SiO<sub>2</sub>/Si (100) substrates using the method of thermal sublimation in high vacuum. Using X-ray analysis, it was established that during thermal oxidation in the oxygen atmosphere within the temperature range  $T = 670\text{--}970\text{ K}$  the values of the  $a$  and  $c$  parameters of the tetragonal lattice as well as the unit cell volume of nanocrystalline PdO films increased monotonously with the rise of the temperature reaching the maximum values at  $T = 950\text{--}970\text{ K}$ . It was found that the parameters of the tetragonal lattice and the unit cell volume of nanocrystalline PdO films decreased as the oxidation temperature increased up to  $T > 970\text{ K}$ . Based on the ratio of the  $c/a$  parameters, it was shown that the main contribution to the deformation phenomena of the tetragonal lattice were mostly due to the increase in the elementary translations along the coordination axes  $Ox$  and  $Oy$ . Based on an assumption that the ionic component of the chemical bond is essential to the palladium (II) oxide structure, we suggested a method for the calculation of the range of the nonstoichiometry area for nanocrystalline PdO films, using the reported data on the radii of cation Pd<sup>2+</sup> and anion O<sup>2-</sup> taking into account their coordination environment. The results of the calculations showed that nanocrystalline PdO films synthesised with an oxygen pressure of ~ 105 kPa are characterised by the two-sided homogeneity region in relation to the stoichiometric ratio of the components. The homogeneity region of nanocrystalline PdO films is characterised by the retrograde solidus line in the range of the temperatures  $T = 770\text{--}1070\text{ K}$ .

**Keywords:** Palladium (II) oxide, Nanostructures, Thermal oxidation, Crystal structure, Nonstoichiometry, Point defects, Gas sensors

**Acknowledgements:** the work was supported by the Ministry of Science and Higher Education of the Russian Federation in the framework of the government order to higher education institutions in the sphere of scientific research for years 2020-2022, project No. FZGU-2020-0036.

**For citation:** Samoylov A. M., Pelipenko D. I., Kuralenko N. S. Calculation of the nonstoichiometry area of nanocrystalline palladium (II) oxide films *Kondensirovannye sredy i mezhfaznye granitsy = Condensed Matter and Interphases*. 2021;23(1): 62–72. <https://doi.org/10.17308/kcmf.2021.23/3305>

**Для цитирования:** Самойлов А. М., Пелипенко Д. И., Кураленко Н. С. Расчет области нестехиометрии нанокристаллических пленок оксида палладия (II). *Конденсированные среды и межфазные границы*. 2021;23(1): 62–72. <https://doi.org/10.17308/kcmf.2021.23/3305>

✉ Alexander M. Samoylov, e-mail: [samoylov@chem.vsu.ru](mailto:samoylov@chem.vsu.ru).

© Самойлов А. М., Пелипенко Д. И., Кураленко Н. С., 2021



The content is available under Creative Commons Attribution 4.0 License.

## 1. Introduction

Gas sensors of various types are designed for the accurate, fast, and reliable determination of concentrations of toxic and explosive gases in the atmospheric air [1–3]. Such devices are necessary for the prevention of technological and household incidents with explosive gases, as well as for security systems in different industrial processes that use poisonous or flammable volatile substances [1–4]. The creation of effective resistive gas sensors based on wide-band metal oxide semiconductors is a relevant scientific and technical task as it will allow producing portable individual devices [5–7]. Over the past fifty years, metal oxide semiconductors with *n*-type conductivity have been the main objects of research and development, and tin dioxide SnO<sub>2</sub> has undoubtedly been the leader among them [1–3, 5, 6].

Impressive success in the development of sensors based on *n*-type semiconductors can be explained by the results of studying the physicochemical patterns that describe and predict the nature of the interaction of the active layer surface with the molecules of detected gases [3–4, 8]. It was established that *n*-type wide-band semiconductors, particularly SnO<sub>2</sub>, are characterised by a rather narrow homogeneity region [1, 5–6, 8]. As we know [1–2, 3, 9], point defects are highly significant in the interaction of the surface of *n*-type semiconductors with the molecules of the analysed gases. Various authors have proved the nature of point defects, mainly oxygen vacancies, which are responsible for nonstoichiometry and electronic type of conductivity of these compounds [1, 5–6, 8, 9].

Over the past decade, there has been a considerable increase in the interest in the study of sensory properties of wide-band metal oxide semiconductors with the *p*-type surface and the composites based on them [10]. So far, the functional properties of metal oxide semiconductors with *p*-type conductivity, such as Cr<sub>2</sub>O<sub>3</sub>, Cu<sub>2</sub>O, PdO, etc., have been studied only partially despite the fact that these materials possess great potential when being used in gas sensors [10]. In a number of publications, it was suggested that metal oxide semiconductors with the *p*-type conductivity would be highly effective for the detection of such toxic gases as ozone, chlorine, nitrogen oxide, and sulphur dioxide [10].

The gas-sensitive properties of nanostructures based on palladium (II) oxide, which is characterised by *p*-type conductivity [11, 12], have only recently become the object of studies. Over the past five years, it has been experimentally proved that nanostructures with different morphological organisation based on palladium (II) oxide possess high sensitivity, sensory response stability, short recovery period, as well as good reproducibility of the sensor signal when detecting hydrogen, carbon monoxide, vapours of organic compounds, nitrogen (IV) oxide, and ozone in the atmospheric air [12–18].

However, as the analysis of the literature shows, unlike wide-band metal oxide materials with *n*-type conductivity, the phase diagram of palladium – oxide system has not been thoroughly studied, and the homogeneity region of palladium (II) oxide has not been experimentally determined so far [18, 19]. In addition, authors express different opinions on the nature of point defects in this compound [12, 18, 20]. The lack of this information makes it impossible to establish the mechanisms of interaction of the detected gases with the surface of nanostructures of palladium (II) oxide and largely hinders the practical application of gas sensors based on them.

Therefore, the aim of this work was to calculate the range of the nonstoichiometry area of nanocrystalline palladium (II) oxide films based on experimental X-ray diffraction data on the change in the parameters of the tetragonal crystal lattice depending on the conditions of their synthesis.

## 2. Experimental

A two-stage process was used to synthesise nanocrystalline films of palladium (II) oxide in the present work. During the first stage, using thermal sublimation of palladium foil with a purity of 99.98% in high vacuum (residual pressure in the reaction chamber ~ 10<sup>-5</sup> Pa), initial microdispersed Pd films were obtained on Si (100) substrates with a buffer layer of the SiO<sub>2</sub> oxide with a thickness of *d* ~ 300 nm without heating. The method of formation of thin and ultrathin layers of metallic Pd was described in detail in previous works [11, 13–16].

As was established in [20], thermal oxidation of initial ultradispersed layers of metallic Pd in



dry oxygen in the temperature range of  $T_{\text{ox}} = 670\text{--}1070$  K leads to the formation of single-phase PdO nanocrystalline films. Taking into account the experimental data [20], in the present work the initial heterostructures Pd/SiO<sub>2</sub>/Si (100) were thermally oxidised in a dry oxygen atmosphere at a pressure of  $p(\text{O}_2) \sim 1.1 \cdot 10^5$  Pa in the continuous flow mode with the oxygen consumption of 5 dm<sup>3</sup> per hour. The Pd/SiO<sub>2</sub>/Si (100) heterostructures were kept at temperatures  $T_{\text{ox}} = 570, 670, 770, 870, 1070,$  and 1120 K for 2 hours and then cooled to room temperature in a dry oxygen stream.

The change in the phase composition and crystal lattice parameters of palladium (II) oxide synthesised using thermal oxidation of Pd/SiO<sub>2</sub>/Si (100) heterostructures was characterized using X-ray diffractometry on DRON-4-07 and Philips PANanalytical X'Pert devices with CuK<sub>α</sub> and CoK<sub>α</sub>-radiation. Diffraction patterns of the samples were registered with rotation of the samples, while the profiles of X-ray reflections were constructed pointwise with the step of the counter being 0.01°. The clearly recorded reflection (400) of the Si (100) substrate served as an internal standard to prevent accidental errors.

Precise determination of the tetragonal crystal lattice period of palladium (II) oxide films was conducted by extrapolating the diffraction angle to  $\theta = 90$  degrees. For this, an extrapolation function  $f(\theta)$  was chosen so that the dependence of parameters  $a$  and  $c$  on the value of  $f(\theta)$  was closest to linear. The best results were

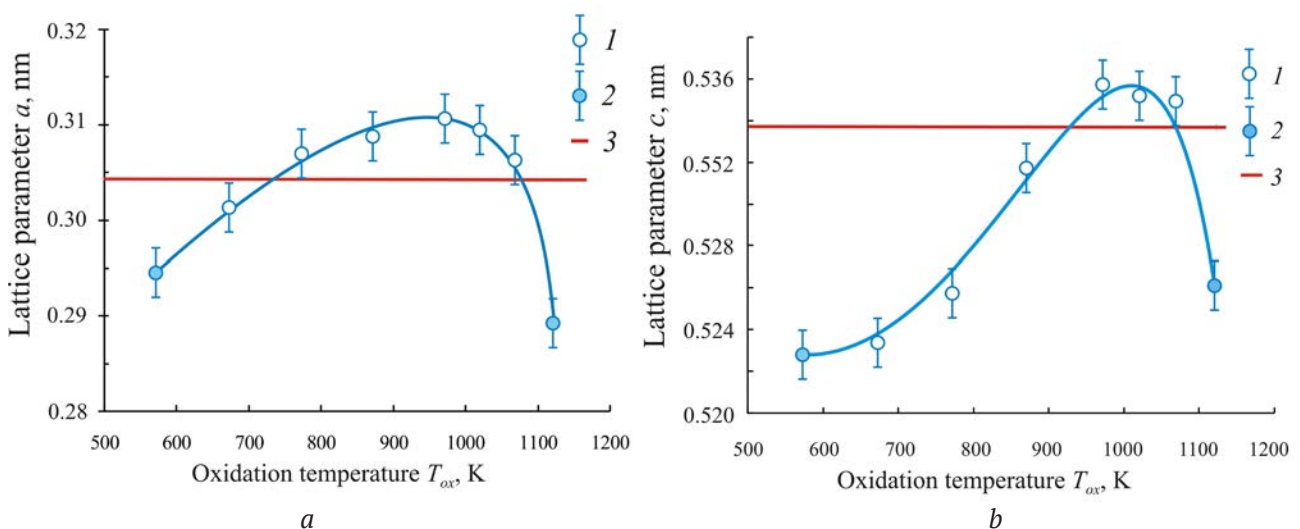
obtained using the Nelson-Riley extrapolation function [21]. The lattice constants  $a$  and  $c$  of the tetragonal structure of nanocrystalline PdO films were calculated using the MATHCAD 10 software based on an algorithm for solving a system of quadratic equations with two non-obvious parameters. The desired value of the lattice parameters  $a_0$  and  $c_0$  were obtained using linear function approximation:

$$a = k \times f(\sin\theta) + a_0 \quad (1 a)$$

$$c = k \times f(\sin\theta) + c_0 \quad (1 b)$$

using the least-squares method.

The values of the parameters  $a$  and  $c$  of the tetragonal crystal lattice of nanocrystalline PdO films calculated on the basis of the obtained experimental X-ray diffraction data, depending on the oxidation temperature  $T_{\text{ox}}$ , are shown in figs. 1a and 1b as compared to the values of the lattice parameters of the ASTM standard [22, 23]. It must be emphasised that heterophase PdO + Pd films were synthesised as a result of oxidation of the initial ultradispersed films of metal Pd at  $T_{\text{ox}} = 570$  K and  $T_{\text{ox}} = 1120$  K. The samples synthesised at  $T_{\text{ox}} = 570$  K should be considered as products of incomplete transformation of the initial Pd layers into PdO oxide, while the samples obtained at  $T_{\text{ox}} = 1120$  K are products of the partial thermal decomposition of nanocrystalline PdO films. The authors [20] indicated that there were reflections on the diffraction patterns of the films synthesised at  $T_{\text{ox}} = 1120$  K which could



**Fig. 1.** Dependences of the parameters  $a$  and  $c$  of the tetragonal lattice of nanocrystalline PdO films on the oxidation temperature  $T_{\text{ox}}$ : 1 – homogeneous PdO films, 2 – heterogeneous PdO + Pd films; 3 – data of the ASTM standard [22, 23]

correspond to the structure of palladium (I) oxide Pd<sub>2</sub>O [24]. Nevertheless, the formation of Pd<sub>2</sub>O cannot be considered fully proved. The number of low-intensity reflections established in this work is insufficient for the accurate identification of the phase.

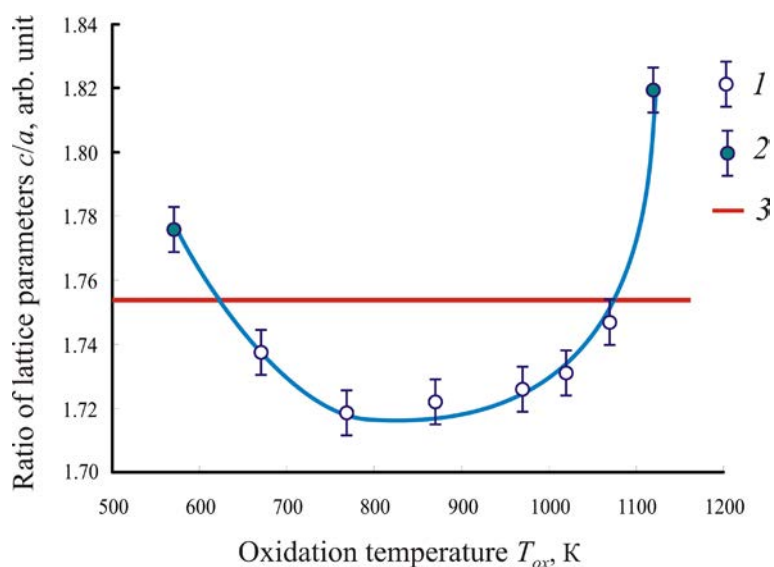
As Fig. 1a and Fig. 1b show, the dependencies  $a = f(T_{\text{ox}})$  and  $c = f(T_{\text{ox}})$  for nanocrystalline PdO films are characterised by similar behaviour: the values of both parameters monotonously increase with an increase in the oxidation temperature up to  $T_{\text{ox}} = 970$  K, and with a further increase in  $T_{\text{ox}} > 970$  K their sharp decrease is observed. In this case, the values of the lattice constant  $a$  of nanocrystalline PdO films for the temperature range  $T_{\text{ox}} = 770$ –1070 K, is higher than the value of the similar parameter of the ASTM standard [23] (Fig. 1a). The range of oxidation temperatures where the values of parameter  $c$  is higher than the values of the ASTM standard is more specific: from  $T_{\text{ox}} = 870$  K to  $T_{\text{ox}} = 1070$  K (Fig. 1b). It should be noted that heterogeneous nanocrystalline PdO films obtained at  $T_{\text{ox}} = 570$  K and  $T_{\text{ox}} = 1120$  K are characterised by the minimal values of the parameters of the tetragonal lattice (Fig. 1a and Fig. 1b).

The results of the calculations of the values of the tetragonal lattice parameters (Fig. 1a and Fig. 1b) indicate that the structure of nanocrystalline PdO is considerably transformed when the space group remains unchanged during thermal oxidation.

In this work, the values of the ratio of the  $c/a$  parameters were calculated for a more accurate estimate of the contribution of changes in the  $a$  and  $c$  parameters to the overall picture of deformation phenomena in the tetragonal lattice of nanocrystalline PdO films. It is known that the  $c/a$  ratio is a parametric feature of crystals of the middle category and it reflects the degree of anisotropy of the crystal structure and a number of physical properties [25].

The change in the  $c/a$  values for nanocrystalline PdO films depending on the oxidation temperature  $T_{\text{ox}}$  is presented in Fig. 2. As the figure shows, the  $c/a$  values for all single-phase nanocrystalline PdO films obtained by oxidation in oxygen in the temperature range  $600 < T_{\text{ox}} < 1050$  K are significantly lower than the value calculated for the reference sample from the ASTM database [23]. On the contrary, the  $c/a$  values are higher than the similar value of the reference sample for heterogeneous samples (PdO + Pd) and (PdO + Pd + Pd<sub>2</sub>O).

There is a flat minimum in the temperature range  $800 < T_{\text{ox}} < 850$  K on the  $c/a = f(T_{\text{ox}})$  curve presented in Fig. 2. The established nature of the behaviour of the  $c/a = f(T_{\text{ox}})$  curve indicates that the increase in the tetragonal lattice parameters of nanocrystalline PdO films is uneven. The main contribution to the distortions of the tetragonal crystal structure of palladium (II) oxide occurs mainly due to an increase in the values of



**Fig. 2.** Dependence of the  $c/a$  ratio of the parameters of the tetragonal lattice of nanocrystalline PdO films on the oxidation temperature  $T_{\text{ox}}$ : 1 – homogeneous polycrystalline PdO samples; 2 – heterogeneous polycrystalline (PdO + Pd) samples; 3 – data of the ASTM standard [23]

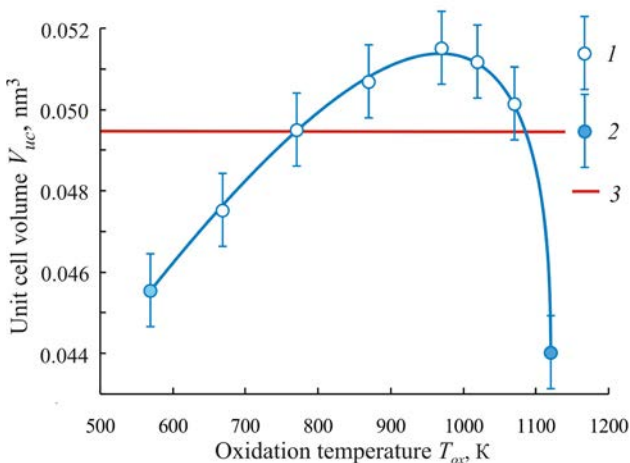
the  $a$  parameter, that is due to an increase in elementary translations along the  $OX$  and  $OY$  coordinate axes. Thus, the deformation of the tetragonal crystal structure of nanocrystalline PdO films observed in the oxidation temperature range  $670 < T_{ox} < 1070$  K is accompanied by a decrease in the values of the parametric ratio  $c/a$ , which leads to a reduction in the degree of anisotropy of the crystal structure.

An analysis of the nature of the transformation of the tetragonal structure of nanocrystalline PdO films during their synthesis needs to be complemented with the calculations of the unit cell volume of the crystal structure using the formula:

$$V_{uc} = a^2c, \quad (2)$$

where  $V_{uc}$  – is the unit cell volume;  $a$  and  $c$  – are parameters of the tetragonal crystal structure of palladium (II) oxide. Such calculations allow assessing the average degree of distortion of the tetragonal structure of nanocrystalline PdO films depending on the oxidation temperature due to changes in the values of both parameters  $a$  and  $c$ .

The results of the calculations are presented in Fig. 3 as a dependence  $V_{uc} = f(T_{ox})$ . As the figure shows, the unit cell volume  $V_{uc}$  of the crystal structure of single-phase nanocrystalline films of palladium (II) oxide monotonously grow with an increase in the oxidation temperature from



**Fig. 3.** Dependence of the unit cell volume  $V_{uc}$  of the tetragonal lattice of nanocrystalline PdO films on the oxidation temperature  $T_{ox}$ : 1 – homogeneous polycrystalline PdO samples; 2 – heterogeneous polycrystalline (PdO + Pd) samples; 3 – data of the ASTM standard [23]

$T_{ox} = 670$  K to  $T_{ox} = 970$  K. The maximum values of  $V_{uc}$  are found in the temperature range  $950 < T_{ox} < 970$  K. At the same time, in the temperature range  $T_{ox} = 770 – 1070$  K the values of the unit cell volume  $V_{uc}$  for homogeneous PdO films exceed the volume of the reference unit cell ASTM [23].

In the present work, the values of the X-ray density were calculated for a fuller picture of the analysis of the deformations in the structure of nanocrystalline PdO films depending on the oxidation temperature. As there are two formula units of palladium (II) oxide in a unit cell [20, 23], the X-ray density  $\rho_{Xray}(PdO)$  was calculated using the formula:

$$\rho_{Xray}(PdO) = \frac{2M(PdO)}{V_{uc} \cdot N_A}, \quad (3)$$

where  $M(PdO)$  is the molar mass of palladium (II) oxide;  $V_{uc}$  is the unit cell volume;  $N_A$  is Avogadro number.

The results of the calculation using formula (3) for palladium (II) oxide of stoichiometric composition in the form of a dependence  $\rho_{Xray}(PdO) = f(T_{ox})$  are presented in Fig. 4. As the figure shows, the values  $\rho_{Xray}(PdO)$  monotonously decrease with an increase in the oxidation temperature in the range of  $570 < T_{ox} < 970$  K. Minimal values of  $\rho_{Xray}(PdO)$  were established for the oxidation temperature  $T_{ox} \sim 970$  K. Further increase in the oxidation temperature  $T_{ox} > 970$  K is accompanied by a sharp increase in the X-ray density. It should be noted that maximum values of density were obtained for heterogeneous samples (PdO + Pd) and (PdO + Pd + Pd<sub>2</sub>O) synthesised at  $T_{ox} = 570$  K and  $T_{ox} = 1120$  K respectively.

The comparison of the obtained experimental data on the change in the tetragonal lattice parameters of nanocrystalline PdO films synthesised at different temperatures (Fig. 1), as well as the calculated dependences of the change in the unit cell volume  $V_{uc} = f(T_{ox})$  and X-ray density  $\rho_{Xray}(PdO) = f(T_{ox})$ , presented in Fig. 3 and Fig. 4 respectively, indicate that the authors' suggestions [20] about the causes of the distortion of the tetragonal of palladium (II) oxide were appropriate. The increase in the unit cell volume of the PdO tetragonal lattice with an increase in the oxidation temperature at the constant value of oxygen pressure is most likely

due to the incorporation of oxygen atoms into the crystal structure of PdO [20]. It is known [26] that the surface of nanostructures of wide-band metal oxide semiconductors adsorbs oxygen molecules. Moreover, depending on the temperature, the ionisation of the adsorbed molecules of  $O_2$  are observed with the formation of oxygen diatomic and monoatomic anions:  $O_2^-$ ,  $O^-$ , and  $O^{2-}$  [26]. The nature of the ionised oxygen particles depends on the temperature [26]. It was shown that double-charged monoatomic anions of oxygen  $O^{2-}$  are formed at the temperature of  $T_{ox} > 570$  K [26].

The obtained calculation data on the change in the X-ray density  $\rho_{Xray}(PdO)$  of nanocrystalline PdO films with an increase in the temperature also support this hypothesis (Fig. 4). A decrease in the values of density  $\rho_{Xray}(PdO)$  can be explained by the incorporation of oxygen atoms into the lattice whose atomic mass is 6.6515 times smaller than the mass of palladium atoms:

$$\frac{A_r(O)}{A_r(Pd)} = \frac{15.9994}{106.42} = 0.150342. \quad (4)$$

### 3. Methodology for the calculation of nonstoichiometry areas

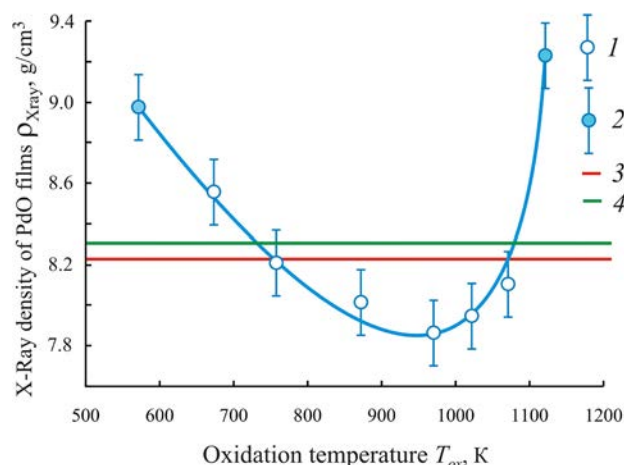
In the present work, based on the obtained experimental and calculation data, we propose a method for the calculation of the range of the nonstoichiometric areas of nanocrystalline PdO films within the above-mentioned hypothesis, which explains the deformation of the crystal lattice depending on the oxidation temperature.

During the calculation of the nonstoichiometric areas of nanocrystalline PdO films, boundary conditions were established and three main assumptions were specified.

1. High proportion of the ionic component of the chemical bond in palladium (II) oxide.

The review of the literature data shows that, as for its chemical properties, palladium (II) oxide is a sparingly soluble basic oxide, similar to MnO, NiO, FeO, etc. [25, 27, 28]. This fact indicates that despite the low values of the coordination numbers in the tetragonal structure:  $CN(Pd_o) = CN(O_{pd}) = 4$ , the proportion of the ionic component of the chemical bond in palladium (II) oxide is rather high.

The proportion of the ionic bond in palladium (II) oxide can be assessed using the method



**Fig. 4.** Dependence of the X-ray density  $\rho_{Xray}$  nanocrystalline PdO films on the oxidation temperature  $T_{ox}$ : 1 – homogeneous polycrystalline PdO samples; 2 – heterogeneous polycrystalline PdO + Pd samples; 3 – data of the ASTM standard [23]; 4 – density values of polycrystalline PdO samples obtained using the hydrostatic method [26]

proposed by the authors of [29] based on the comparison of the relative electronegativity (ENE) of the elements that form the binary compound of the AB composition. Within this method, an elementary substance with semiconducting properties, for example, single-crystal Si, has a proportion of ionicity equal to zero, while caesium fluoride CsF is characterised by a proportion of ionicity equal to 1 (Fig. 5). The values of relative electronegativity (ENE) of chemical elements that form some binary compounds of the AB composition are presented in Table 1.

A comparison of the values of the relative electronegativity (ENE) of the elements by the Pauling scale [30] is shown (Table 1):

$$\Delta\chi(CsF) = \chi(F) - \chi(Cs) = 3.98 - 0.79 = 3.19 \quad (5 a)$$

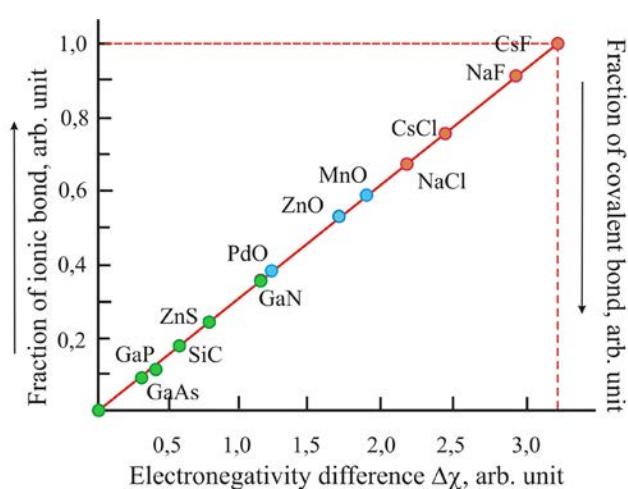
$$\Delta\chi(NaCl) = \chi(Cl) - \chi(Na) = 3.16 - 0.93 = 2.27 \quad (5 b)$$

$$\Delta\chi(PdO) = \chi(O) - \chi(Pd) = 3.44 - 2.20 = 1.24 \quad (5 c)$$

Using this method [29] and its graphic interpretation (Fig. 5), it is possible to determine the proportion of the ionic component of the chemical bond in palladium (II) oxide. As Fig. 5 shows, based on the value of the difference between ENE of oxygen and palladium  $\Delta\chi(PdO) = 1.24$  calculated using formula (5 c), the proportion of the ionic component of the chemical bond in palladium (II) oxide is approximately 39%.

**Table 1.** The values of relative electronegativity (ENE) of some chemical elements [30] and the proportion of the ionic component of the chemical bond in binary compounds of the AB composition formed by these elements

Compound	Relative electronegativity of the elements (ENE) $\chi$ , r.u.		Difference between ENE elements $\Delta\chi$ , r.u.	Degree of ionicity, r.u.
CsF	$\chi(\text{Cs}) = 0.79$	$\chi(\text{F}) = 3.98$	$\Delta\chi = 3.19$	1.0
CsCl	$\chi(\text{Cs}) = 0.79$	$\chi(\text{Cl}) = 3.16$	$\Delta\chi = 2.37$	0.76
NaF	$\chi(\text{Na}) = 0.93$	$\chi(\text{F}) = 3.98$	$\Delta\chi = 3.05$	0.92
NaCl	$\chi(\text{Na}) = 0.93$	$\chi(\text{Cl}) = 3.16$	$\Delta\chi = 2.23$	0.68
MnO	$\chi(\text{Mn}) = 1.55$	$\chi(\text{O}) = 3.44$	$\Delta\chi = 1.89$	0.59
PdO	$\chi(\text{Pd}) = 2.20$	$\chi(\text{O}) = 3.44$	$\Delta\chi = 1.24$	0.39
ZnO	$\chi(\text{Zn}) = 1.65$	$\chi(\text{O}) = 3.44$	$\Delta\chi = 1.79$	0.5
ZnS	$\chi(\text{Zn}) = 1.65$	$\chi(\text{S}) = 2.58$	$\Delta\chi = 0.93$	0.28



**Fig. 5.** Dependence of the proportion of the ionic component of the chemical bond in AB binary compounds on the value of the difference between the relative electronegativity of the elements calculated using the method [29]

The obtained values of  $\Delta\chi(\text{PdO})$  elements and the value of the proportion of ionicity allow concluding that the chemical bond in palladium (II) oxide is covalent with a significant proportion of the ionic component. Therefore, it is quite reasonable to assume that it is possible to consider palladium and oxygen particles in the crystal structure of palladium (II) oxide as ions with spherical symmetry. For this reason, to conduct the calculations it is reasonable to use the data on the ionic radii of elements  $R(\text{Pd}^{2+})$  and  $R(\text{O}^{2-})$  presented in Table 2 [30–32].

2. As a sample of palladium (II) oxide, the composition of which corresponds to the stoichiometric ratio of the components, we used a standard from the ASTM database [23] with the

following parameters of the tetragonal lattice:  $a = 0.30434$  nm,  $c = 0.5337$  nm. Thus, the unit cell volume  $V_{\text{uc}}^0$  of the standard sample of PdO can be expressed by the following equation:

$$V_{\text{uc}}^0 = 2V(\text{Pd}^{2+}) + 2V(\text{O}^{2-}) + V_{\text{void}}, \quad (6)$$

where  $V(\text{Pd}^{2+})$  and  $V(\text{O}^{2-})$  are the volumes of palladium and oxygen anion respectively;  $V_{\text{void}}$  is the total volume of the tetrahedral and octahedral voids.

3. To calculate the range of the homogeneity (nonstoichiometry) area of nanocrystalline PdO films, in the present work we used the variant of the unit cell of the crystal structure of palladium (II) oxide suggested in [20]. This variant of the representation of the PdO unit cell (Fig. 6) completely corresponds to the latest experimental data [23], in particular, to a set of elements of the space group symmetry (SGS)  $P4_2/mmc$ , Pearson symbol  $tP4$ , Wyckoff position of the atoms of Pd and O, as well as their multiplicity [20, 23].

When calculating the values of deviation from stoichiometry  $\delta$  of nanocrystalline films of palladium (II) oxide, we used the concept of the “effective volume” of the particles of palladium  $V_{\text{eff}}(\text{Pd}^{2+})$  and oxygen  $V_{\text{eff}}(\text{O}^{2-})$  in a unit cell. The “effective volume” of the particles of palladium and oxygen were determined using the ratio:

$$2V_{\text{eff}}(\text{Pd}^{2+}) + 2V_{\text{eff}}(\text{O}^{2-}) = V_{\text{uc}}^0, \quad (7)$$

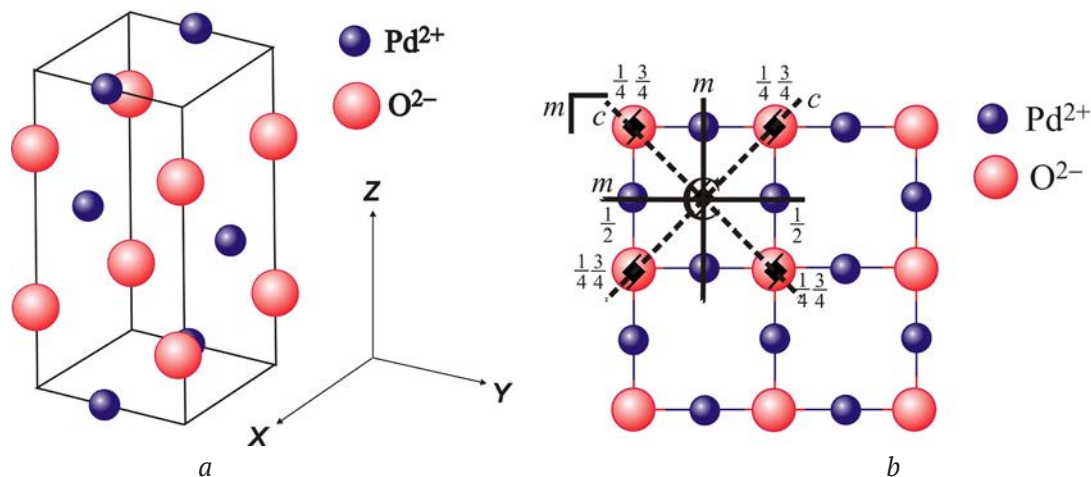
where  $V_{\text{uc}}^0$  is the unit cell volume of the standard of the ASTM data [23].

The values of  $\delta$  were determined when solving the equation system:

**Table 2.** Values of palladium Pd<sup>2+</sup> and oxygen O<sup>2-</sup> ionic radii [30 – 32]

Ion	Coordination number CN	Coordination polyhedron	Values of ionic radii $R_{\text{ion}}$ , nm
Pd <sup>2+</sup>	4	Square (rectangular)	0.078 [30]; 0.086 [31]; 0.078 [32]
O <sup>2-</sup>	4	Tetragonal tetrahedron	0.132 [30]; 0.140 [31]; 0.124* [31]; 0.132 [32]

\*The values of ionic radius were obtained on the basis of quantum mechanical calculations.



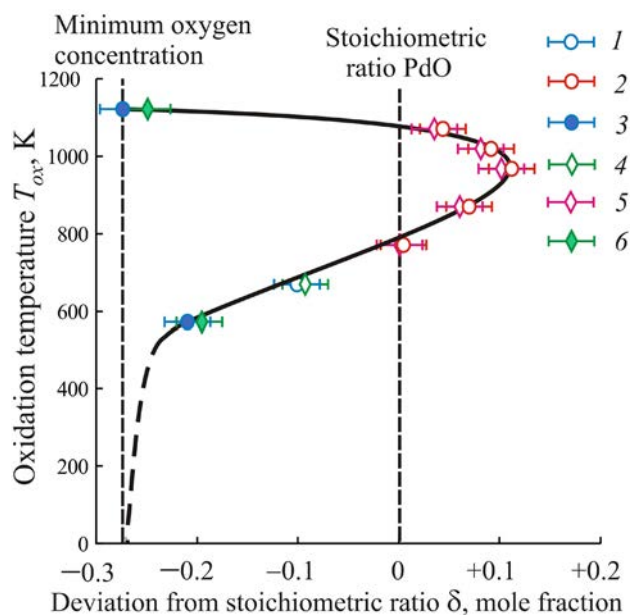
**Fig. 6.** Unit cell of palladium (II) oxide tetragonal crystal structure (a) and projection of four unit cells on XOY plane (b) with the indication of the elements of symmetry typical for SG  $P4_2/mmc$  [20]

$$\left\{ \begin{array}{l} V_{\text{uc}}^0(T_{\text{ox}}) = 2V_{\text{eff}}(\text{Pd}^{2+}) + 2V_{\text{eff}}(\text{O}^{2-}) + 2\delta \times V_{\text{eff}}(\text{O}^{2-}) \\ V_{\text{eff}}(\text{Pd}^{2+}) = \frac{R^5(\text{Pd}^{2+})}{R^3(\text{O}^{2-})} \\ V_{\text{eff}}(\text{O}^{2-}) = \frac{R^5(\text{O}^{2-})}{R^3(\text{O}^{2-})} \end{array} \right\} \quad (8)$$

It was solved using MATCAD 10.

The results of the conducted calculations are presented in Fig. 7 in the form of a calculated diagram of the homogeneity region of nanocrystalline PdO films. As the figure shows, the values of the oxidation temperature  $T_{\text{ox}}$  are presented as a function of deviation from the stoichiometric ratio  $\delta$  of the elements in the composition of nanocrystalline palladium (II) oxide films. The values  $\delta$  were calculated for two different values of the radius of oxygen anion  $R(\text{O}^{2-}) = 0.124$  nm and  $R(\text{O}^{2-}) = 0.140$  nm known from previous works (Table. 2). The calculation of the values of deviation from stoichiometry  $\delta$  using these values of radii of oxygen anion leads to very similar results (Fig. 7).

According to the calculation results, the nonstoichiometry area of nanocrystalline PdO films obtained using oxidation in oxygen is rather wide and varies in the range from  $-0.20 + 0.04 \leq \delta \leq 0.12 + 0.04$  mol. f. (Fig. 6). As Fig. 7 shows, heterogeneous samples (Pd + PdO) synthesised at  $T_{\text{ox}} = 570$  K and  $T_{\text{ox}} = 1120$  K are



**Fig. 7.** The calculated model of the nonstoichiometry area of nanocrystalline palladium (II) oxide films prepared by oxidation in the oxygen atmosphere ( $\text{O}_2$  partial pressure is 105–110 kPa); 1, 4 – homogeneous PdO samples with a deficiency of oxygen atoms; 2, 5 – homogeneous PdO samples with an excess of oxygen atoms; 3, 6 – heterogeneous PdO + Pd samples; 1, 2, 3 – calculation for the ionic radius of oxygen  $\text{O}^{2-}$   $R(\text{O}^{2-}) = 0.124$  nm; 4, 5, 6 – calculation for the ionic radius of oxygen  $R(\text{O}^{2-}) = 0.140$  nm.

characterised by the least content of oxygen atoms (the area of negative values of  $\hat{\delta}$ ). In the latter case, nanocrystalline films show all the signs of thermal decomposition. With the same value of partial pressure  $O_2$ , an increase in the oxidation temperature from  $T_{ox} = 570$  to  $T_{ox} = 970$ – $1020$  K leads to an increase in the concentration of oxygen atoms in nanocrystalline PdO films, which is accompanied by an anisotropic increase in the volume of the unit cell of the crystal structure (Fig. 3) and a decrease in the X-ray density (Fig. 4).

Generalisation of the experimental and calculation data obtained in the present work allows stating the strong influence of the oxidation temperature on the change in the concentration of oxygen atoms in nanocrystalline PdO films, which leads to the distortion of their crystal structure.

Altogether, the obtained experimental and calculated data indicate that the deviation from stoichiometry can be caused by point defects in the anion sublattice. As for nanocrystalline PdO films that were synthesised at  $T_{ox} = 570$ – $670$  K, a deficiency of oxygen atoms can be explained by the formation of oxygen vacancies  $V_o$ . It is likely that these vacancies are filled with oxygen atoms when the oxidation temperature is increased up to  $T_{ox} = 770$  K. PdO samples obtained at  $T_{ox} = 870$ – $1070$  K are characterised by an excess of oxygen atoms in relation to the stoichiometry and minimal density values due to embedded interstitial atoms of oxygen  $O_i$ . Further increase in the oxidation temperature leads to a decrease in the concentration of oxygen atoms in the PdO films, which indicates the retrograde nature of the solidus line in this region of the composition and temperature (Fig. 7).

The results of the conducted calculations allow stating that single-phase nanocrystalline PdO films possess a two-sided homogeneity region in relation to the stoichiometric ratio of the components. The data obtained in the present work will contribute to the development of effective gas sensors with best functional parameters based on the nanostructures of palladium (II) oxide.

#### 4. Conclusions

1. Based on X-ray analysis, it was established that the parameters of the tetragonal structure

of nanocrystalline films of palladium (II) oxide monotonously increase with an increase in the oxidation temperature from  $T_{ox} = 570$  K to  $T_{ox} = 970$  K and decrease at  $T_{ox} > 970$  K.

2. It was shown that the distortions of the tetragonal lattice of nanocrystalline films of palladium (II) oxide were mainly due to an increase in the value of parameter  $a$ .

3. Based on the obtained experimental and calculation data, an assumption was made that the distortions of the tetragonal lattice of nanocrystalline palladium (II) oxide films were caused by the incorporation of excess oxygen atoms.

4. Based on an assumption that the ionic component of the chemical bond is essential, we developed a calculation method for the nonstoichiometry area of nanocrystalline palladium (II) oxide films.

5. Based on the conducted calculations, we developed a model for the nonstoichiometry areas of nanocrystalline palladium (II) oxide films. It was shown that the nonstoichiometry area is two-sided in relation to the stoichiometric composition and is characterised by the retrograde solidus line.

#### Conflict of interests

The authors declare that they have no known competing financial interests or personal relationships that could have influenced the work reported in this paper.

#### References

1. Korotcenkov G. *Handbook of gas sensor materials. Properties, advantages and shortcomings for applications. Volume 1: Conventional approaches*. New York, Heidelberg Dordrecht London: Springer, New York, NY; 2013. 442 p. <https://doi.org/10.1007/978-1-4614-7165-3>
2. Yamazoe N. Toward innovations of gas sensor technology. *Sensors and Actuators B*. 2005;108: 2–14. <https://doi.org/10.1016/j.snb.2004.12.075>
3. Marikutsa A. V., Rumyantseva M. N., Gaskov A. M., Samoylov A. M. Nanocrystalline tin dioxide: Basics in relation with gas sensing phenomena. Part I. Physical and chemical properties and sensor signal formation. *Inorganic Materials*. 2015;51(13): 1329–1347. <https://doi.org/10.1134/S002016851513004X>
4. Marikutsa A. V., Rumyantseva M. N., Gaskov A. M., Samoylov A. M. Nanocrystalline tin dioxide: Basics in relation with gas sensing phenomena. Part II. Active

centers and sensor behavior. *Inorganic Materials*. 2016;52(13): 1311–1338. <https://doi.org/10.1134/S0020168516130045>

5. Seiyama T., Kato A., Fujiishi K., Nagatani M. A new detector for gaseous components using semiconductive thin films. *Analytical Chemistry*. 1962;34(11): 1502–1503. <https://doi.org/10.1021/ac60191a001>

6. Korotcenkov G. Metal oxides for solid-state gas sensors: What determines our choice? *Materials Science and Engineering: B*. 2007;139(1): 1–23. <https://doi.org/10.1016/j.mseb.2007.01.044>

7. Toda K., Furue R., Hayami S. Recent progress in applications of graphene oxide for gas sensing: A review. *Analytica Chimica Acta*. 2015;878: 43–53. <https://doi.org/10.1016/J.ACA.2015.02.002>

8. Chin Boon Ong, Law Yong Ng, Abdul Wahab Mohammad. A review of ZnO nanoparticles as solar photocatalysts: Synthesis, mechanisms and applications. *Renewable and Sustainable Energy Reviews*. 2018;81: 536–551. <https://doi.org/10.1016/j.rser.2017.08.020>

9. Al-Hashem M., Akbar S., Morris P. Role of oxygen vacancies in nanostructured metal-oxide gas sensors: A Review. *Sensors Actuators B*. 2019;301: 126845. <https://doi.org/10.1016/j.snb.2019.126845>

10. Kim H.-J., Lee J.-H. Highly sensitive and selective gas sensors using *p*-type oxide semiconductors: Overview. *Sensors and Actuators B*. 2014;192: 607–627. <https://doi.org/10.1016/j.snb.2013.11.005>

11. Ryabtsev S. V., Ievlev V. M., Samoylov A. M., Kushev S. B., Soldatenko S. A. Microstructure and electrical properties of palladium oxide thin films for oxidizing gases detection. *Thin Solid Films*. 2017;636: 751–759. <https://doi.org/10.1016/j.tsf.2017.04.009>

12. García-Serrano O., López-Rodríguez C., Andraca-Adame J. A., Romero-Paredes G., Pena-Sierra R. Growth and characterization of PdO films obtained by thermal oxidation of nanometric Pd films by electroless deposition technique. *Materials Science and Engineering B*. 2010;174(1-3): 273–278. <https://doi.org/10.1016/j.mseb.2010.03.064>

13. Ryabtsev S. V., Shaposhnik A. V., Samoylov A. M., Sinelnikov A. A., Soldatenko S. A., Kushchev S. B., Ievlev V. M. Thin films of palladium oxide for gas sensors. *Doklady Physical Chemistry*. 2016;470(2): 158–161. <https://doi.org/10.1134/s0012501616100055>

14. Samoylov A., Ryabtsev S., Shaposhnik A., Kushev S., Soldatenko S., Ievlev V. Palladium oxide thin film for oxidizing gases detecting. In: *The 16-th International Meeting on Chemical Sensors IMCS 2016. Jeju, Jeju Island, Korea, July 10–13, 2016: Final Program & Abstracts Book*. Korea: 2016. 96 p.

15. Ryabtsev S. V., Ievlev V. M., Samoylov A. M., Kushev S. B., Soldatenko S. A. Real microstructure

and electrical properties of palladium oxide thin films for oxidizing gases detecting. In: *Science and Application of Thin Films, Conference & Exhibition (SATF-2016) Çeşme, Izmir, Turkey, September 19–23, 2016. Book of Abstract: Izmir Institute of Technology*. Izmir: 2016. 44 p.

16. Ievlev V. M., Ryabtsev S. V., Shaposhnik A. V., Samoylov A. M., Kushev S. B., Sinelnikov A. A. Ultrathin films of palladium oxide for oxidizing gases detecting. *Procedia Engineering*. 2016;168: 1106–1109. <https://doi.org/10.1016/j.proeng.2016.11.357>

17. Ievlev V. M., Ryabtsev S. V., Samoylov A. M., Shaposhnik A. V., Kushev S. B., Sinelnikov A. A. Thin and ultrathin films of palladium oxide for oxidizing gases detection. *Sensors and Actuators B*. 2018;255 (2): 1335–1342. <https://doi.org/10.1016/j.snb.2017.08.121>

18. Samoylov A. M., Ryabtsev S. V., Popov V. N., Badica P. Palladium (II) oxide nanostructures as promising materials for gas sensors. In: *Novel nanomaterials synthesis and applications*. George Kyzas (ed.). UK, London: IntechOpen; 2018. pp. 211–229. <http://dx.doi.org/10.5772/intechopen.72323>

19. *Diagrammy sostoyaniya dvoynikh metallicheskih sistem: Spravochnik: v 3 tomakh* [Phase diagrams of binary metal systems: Handbook: in 3 volumes]. Lyakishev N. P. (ed.) Moscow: Metallurgy Publ.; 1996–2000. (In Russ.)

20. Samoylov A. M., Ivkov S. A., Pelipenko D. I., Sharov M. K., Tsyganova V. O., Agapov B. L., Tutov E. A., Badica P. Structural changes in palladium nanofilms during thermal oxidation. *Inorganic Materials*. 2020;56(10): 1020–1026. <https://doi.org/10.1134/S0020168520100131>

21. Hammond C. The basics of crystallography and diffraction. Fourth edition. International Union of Crystallography. Oxford University Press; 2015. 519 p. <https://doi.org/10.1093/acprof:oso/9780198738671.003.0009>

22. *ASTM JCPDS - International Centre for Diffraction Data*. © 1987–2009. JCPDS-ICDD. Newtown Square, PA 19073. USA.

23. Grier D., McCarthy G., North Dakota. State University, Fargo, N. Dakota, USA, ICDD Grant-in-Aid, JCPDS-ICDD, 1991. Card no. 43-1024.

24. Kumar J., Saxena R. Formation of NaCl- and Cu<sub>2</sub>O-type oxides of platinum and palladium on carbon and alumina support films. *Journal of the Less Common Metals*. 1989;147(1): 59–71. [https://doi.org/10.1016/0022-5088\(89\)90148-3](https://doi.org/10.1016/0022-5088(89)90148-3)

25. Wiberg, E., Wiberg, N., Holleman, A. F. *Inorganic Chemistry. 1st English Edition*. San Diego: Academic Press; Berlin: New York: De Gruyter; 2001. 1884 p.

26. Al-Hashem M., Akbar S., Morris P. Role of oxygen vacancies in nanostructured metal-oxide gas sensors: A Review. *Sensors and Actuators B*. 2019;301: 126–154. <https://doi.org/10.1016/j.snb.2019.126845>



27. Ugay Ya. A. *Neorganicheskaya khimiya* [Inorganic chemistry]. Moscow: Vysshaya shkola Publ.; 1989. 483 p. (In Russ.)

28. Greenwood N. N., Earnshaw A. *Chemistry of the Elements, 2nd Ed.* Oxford: A division of Reed Educational and Professional Publishing Ltd., 1998. 1341 p.

29. Goncharov E. G., Semenova G. V., Ugay Ya. A. *Khimiya poluprovodnikov* [Chemistry of semiconductors]. Voronezh: Voronezh State University Publ.; 1995. 272 p. (In Russ.)

30. [https://www.webelements.com/palladium/atom\\_sizes.html](https://www.webelements.com/palladium/atom_sizes.html) WebElements: The periodic table on the WWW [www.webelements.com] Copyright 1993–2018 Mark Winter [The University of Sheffield and Web Elements Ltd, UK]. All rights reserved.

31. Shannon R. D. Revised effective ionic radii and systematic studies of interatomic distances in halides and chalcogenides. *Acta Crystallographica Section A*. 1976;32(5): 751–767. <https://doi.org/10.1107/s0567739476001551>

32. Emsley J. *The elements. 3-d Edition*. United Kingdom, Oxford: Clarendon Press; 1998. 298 p.

## Information about the authors

*Alexander M. Samoylov*, DSc in Chemistry, Associate Professor, Professor at the Department of Materials Science and the Industry of Nanosystems, Voronezh State University, Voronezh, Russian Federation; e-mail: samoylov@chem.vsu.ru. ORCID iD: <https://orcid.org/0000-0003-4224-2203>.

*Dmitry I. Pelipenko*, post-graduate student at the Department of Materials Science and the Industry of Nanosystems, Voronezh State University, Voronezh, Russian Federation; e-mail: pelipenko.dmitry@yandex.com. ORCID iD: <https://orcid.org/0000-0002-7698-7249>

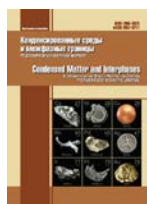
*Natalia S. Kuralenko*, student, Faculty of Chemistry, Department of Materials Science and the Industry of Nanosystems, Voronezh State University, Voronezh, Russian Federation; e-mail: nataliprosto99@gmail.com. ORCID iD: <https://orcid.org/0000-0001-9604-1058>

All authors have read and approved the final manuscript.

*Received 09 February 2021; Approved after reviewing 15 February 2021; Accepted 15 March 2021; Published online 25 March 2021.*

*Translated by Marina Strepetova*

*Edited and proofread by Simon Cox*



# Condensed Matter and Interphases

Kondensirovannye Sredy i Mezhfaznye Granitsy  
<https://journals.vsu.ru/kcmf/>

## Original articles

Original article

<https://doi.org/10.17308/kcmf.2021.23/3306>

## New compounds $\text{Li}_3\text{Ba}_2\text{Bi}_3(\text{XO}_4)_8$ ( $X = \text{Mo}, \text{W}$ ): synthesis and properties

T. S. Spiridonova<sup>1</sup> ✉, A. A. Savina<sup>1,2</sup>, Yu. M. Kadyrova<sup>1,3</sup>, E. P. Belykh<sup>3</sup>, E. G. Khaikina<sup>1,3</sup>

<sup>1</sup>Baikal Institute of Nature Management, Siberian Branch of the Russian Academy of Sciences, 6 Sakhyanova str., Ulan-Ude 670047, Republic of Buryatia, Russian Federation

<sup>2</sup>Skolkovo Institute of Science and Technology, 30 Bolshoy Boulevard, bld. 1, Moscow 121205, Russian Federation

<sup>3</sup>Dorji Banzarov Buryat State University (BSU), 24a Smolin str., Ulan-Ude 670000, Republic of Buryatia, Russian Federation

### Abstract

New compounds  $\text{Li}_3\text{Ba}_2\text{Bi}_3(\text{XO}_4)_8$  ( $X = \text{Mo}, \text{W}$ ) were obtained by the ceramic technology. Those are the first representatives of the ternary molybdates and tungstates  $\text{Li}_3\text{Ba}_2\text{R}_3(\text{XO}_4)_8$  family, which contain different from the rare earth elements trivalent metal. The sequence of chemical transformations occurring during the  $\text{Li}_3\text{Ba}_2\text{Bi}_3(\text{WO}_4)_8$  formation has been established. The primary characterization of the obtained phases was carried out and their ion-conducting properties were studied. The synthesized compounds are shown to melt incongruently, isostructural to the lanthanide-containing analogues (structural type of  $\text{BaNd}_2(\text{MoO}_4)_4$ , sp. gr.  $C2/c$ ) and crystallize in the monoclinic crystal system with unit cell parameters  $a = 5.2798(1)$ ,  $b = 12.8976(4)$ ,  $c = 19.2272(5)$  Å,  $\beta = 90.978(2)^\circ$  ( $X = \text{Mo}$ ),  $a = 5.2733(2)$ ,  $b = 12.9032(4)$ ,  $c = 19.2650(6)$  Å,  $\beta = 91.512(3)^\circ$  ( $X = \text{W}$ ).  $\text{Li}_3\text{Ba}_2\text{Bi}_3(\text{XO}_4)_8$  are found to undergo the diffuse first-order phase transitions at 441°C (molybdate) and 527°C (tungstate), after that their conductivity reaches values of  $10^{-3}$ – $10^{-4}$  S/cm.

**Keywords:** triple molybdates and tungstates, solid-state synthesis, powder X-ray diffraction study, thermal properties, ionic conductivity

**Acknowledgements:** the work was carried out in accordance with the state assignment of the BINM SB RAS and with partial support from the Russian Foundation for Basic Research (project No. 20-03-00533).

**For citation:** Spiridonova T.S., Savina A.A., Kadyrova Yu. M., Belykh E. P., Khaikina E. G. New compounds  $\text{Li}_3\text{Ba}_2\text{Bi}_3(\text{XO}_4)_8$  ( $X = \text{Mo}, \text{W}$ ): synthesis and properties. *Kondensirovannye sredy i mezhfaznye granitsy = Condensed Matter and Interphases*. 2021;23(1): 73–80. <https://doi.org/10.17308/kcmf.2021.23/3306>

**Для цитирования:** Спиридонова Т. С., Савина А. А., Кадырова Ю. М., Бельх Е. П., Хайкина Е. Г. Новые соединения  $\text{Li}_3\text{Ba}_2\text{Bi}_3(\text{XO}_4)_8$  ( $X = \text{Mo}, \text{W}$ ): синтез и свойства. *Конденсированные среды и межфазные границы*. 2021;23(1): 73–80. <https://doi.org/10.17308/kcmf.2021.23/3306>

✉ Tatyana S. Spiridonova, e-mail: spiridonova-25@mail.ru

© Spiridonova T.S., Savina A.A., Kadyrova Yu. M., Belykh E. P., Khaikina E. G., 2021



The content is available under Creative Commons Attribution 4.0 License.

## 1. Introduction

Currently, the class of ternary molybdates includes more than 700 representatives, characterized by a large stoichiometric and structural diversity, and belongs to the most dynamically replenished groups of complex oxide compounds containing a tetrahedral anion and three different cations. Triple molybdates of different valence metals not only have a high material science potential, but also due to the wide possibilities of varying the elemental and quantitative compositions are convenient model objects for establishing genetic relationships in the series of composition – structure – properties of compound – properties of materials. A significant place among them is occupied by the family of triple molybdates obtained for all lanthanides and yttrium with the composition  $\text{Li}_3\text{Ba}_2\text{R}_3(\text{MoO}_4)_8$ , belonging to the structure type  $\text{BaNd}_2(\text{MoO}_4)_4$  (sp. gr.  $C2/c$ ,  $Z = 2$ ) and related to scheelite. These compounds are shown to possess promising luminescent and generation properties [1–3], as well as the properties of solid electrolytes [1, 4]. In particular, the obtained results aimed at study of  $\text{Li}_3\text{Ba}_2\text{R}_3(\text{MoO}_4)_8$  ( $R = \text{La, Gd, Y}$ ) doped with  $\text{Eu}^{3+}$ ,  $\text{Tb}^{3+}$ ,  $\text{Er}^{3+}$ ,  $\text{Nd}^{3+}$ , indicate the prospects for their use as new photo- and IR-luminophores and laser materials [2, 5–7]. Since 2009, studies on the preparation of ternary tungstates of lithium-barium-lanthanides, isoformular and isostructural to the  $\text{Li}_3\text{Ba}_2\text{Ln}_3(\text{WO}_4)_8$  which are, like them, are of great not only scientific but also practical interest started to appear [8–17]. Sizes and quality of grown crystals  $\text{Li}_3\text{Ba}_2\text{Ln}_3(\text{WO}_4)_8$  ( $\text{Ln} = \text{La, Gd, Y}$ ) [9–12, 18] doped with  $\text{Nd}^{3+}$ ,  $\text{Eu}^{3+}$ ,  $\text{Tm}^{3+}$  and other ions, allowed proceeding to a detailed study of the optical-generation characteristics of these new highly efficient laser media. Ceramics  $\text{Li}_3\text{Ba}_2\text{La}_3(\text{WO}_4)_8$ :  $\text{Eu}^{3+}$  [8] and  $\text{Li}_3\text{Ba}_2\text{Gd}_3(\text{WO}_4)_8$ :  $\text{Tb}^{3+}$  [15] can be used as red and green luminophores, respectively.

In this study, the first representatives of the considered family of phases containing in their composition a different from the rare earth trivalent element – ternary bismuth – containing molybdate and tungstate of composition  $\text{Li}_3\text{Ba}_2\text{Bi}_3(\text{XO}_4)_8$  ( $X = \text{Mo, W}$ ) were obtained by directed solid state synthesis. The primary characterization of the obtained compounds was carried out and their electrophysical properties were studied.

## 2. Experimental

Industrial reagents  $\text{Li}_2\text{MoO}_4$ ,  $\text{Li}_2\text{WO}_4$ ,  $\text{XO}_3$  ( $X = \text{Mo, W}$ ),  $\text{Bi}_2\text{O}_3$ ,  $\text{BaMoO}_4$ ,  $\text{BaCO}_3$  (chemically pure) were used as source components for the synthesis of  $\text{Li}_3\text{Ba}_2\text{Bi}_3(\text{XO}_4)_8$  ( $X = \text{Mo, W}$ ).  $\text{BaWO}_4$  was obtained by annealing of the stoichiometric mixture of  $\text{BaCO}_3$  and  $\text{WO}_3$  (600–850 °C, 70 h),  $\text{Bi}_2(\text{MoO}_4)_3$  – by the reaction:  $\text{Bi}_2\text{O}_3 + 3\text{MoO}_3 = \text{Bi}_2(\text{MoO}_4)_3$  (450–500 °C, 50 h). Tertiary bismuth tungstate does not exist; it could not be obtained by the solid-state method, as it was shown in the literature data [19] and proved by our unsuccessful attempts to synthesize those. Therefore, in this case the source component was an oxide mixture of  $\text{Bi}_2\text{O}_3$  and  $\text{WO}_3$ .  $\text{AXO}_4$  ( $A = \text{Ca, Sr, Cd, Pb}$ ;  $X = \text{Mo, W}$ ), required to study of the possibility of realizing the considered structure in ternary molybdates and bismuth tungstates with complete or partial substitution of barium by another doubly charged cation, were obtained by the interaction of  $\text{ACO}_3$  (chemically pure and analytical grade) and  $\text{XO}_3$  by the reaction  $\text{ACO}_3 + \text{XO}_3 = \text{AXO}_4 + \text{CO}_2$ . The synthesis conditions were as follows: in case of Ca, Pb – 500–650 °C, Sr – 500–750 °C, Cd – 450–500 °C for 50–60 h; tungstates: Ca, Sr – 600–900 °C, Cd – 500–650 °C, Pb – 500–750 °C for 70–80 h. The single-phase of the synthesized materials was monitored by powder X-ray diffraction analysis. The obtained compounds were identified by comparison with the ICDD PDF-2 database [20].

Powder X-ray diffraction analysis (XRD) was performed using a Bruker D8 ADVANCE diffractometer ( $\lambda\text{CuK}\alpha$ , secondary monochromator, scanning step 0.02076°). Unit cell parameters of polycrystalline samples  $\text{Li}_3\text{Ba}_2\text{R}_3(\text{XO}_4)_8$  ( $X = \text{Mo, W}$ ) was calculated by the selection of an isostructural compound. Unit cell parameters were refined by the least squares method using the ICDD software package for preparation of the experimental standards. The Smith–Snyder  $F_{30}$  criterion was used as a validation criterion for X-ray patterns indexing [21].

Differential scanning calorimetry studies were carried out using NETZSCH STA 449C synchronous thermal analyser,  $V_{\text{heat(cool)}} = 10^\circ/\text{min}$ .

For the ion-conducting properties investigation the ceramic discs  $\text{Li}_3\text{Ba}_2\text{Bi}_3(\text{XO}_4)_8$  ( $X = \text{Mo, W}$ ) were prepared by pressing the powder at 1 kbar and annealing at 680 ( $X = \text{Mo}$ ) or 730 °C ( $X = \text{W}$ ) for 4 hours. The density of the obtained tablets was 90–95 % of the theoretical values. The

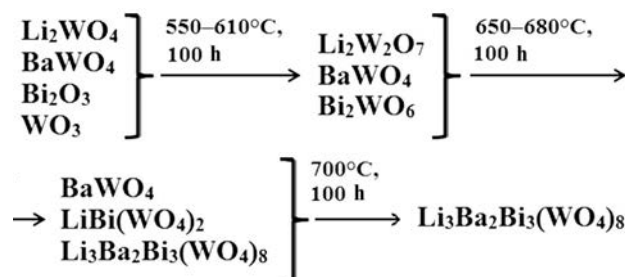
disks were in diameter of 10 mm and thickness of 1.8 mm. In order to prepare electrodes, the surfaces of the disks were coated with colloidal platinum, followed by annealing at 660 ( $X = \text{Mo}$ ) or 710 °C ( $X = \text{W}$ ) for 1 hour. The electrical conductivity measurements of the samples were tested using an impedance meter “Z-1500J” at selected frequencies from 1 Hz to 1 MHz in the temperature range of 200–650 °C ( $X = \text{Mo}$ ) and 300–700 °C ( $X = \text{W}$ ) with heating and cooling rates of 2 deg./min.

### 3. Results and discussion

In the single-phase polycrystalline state, the triple molybdate  $\text{Li}_3\text{Ba}_2\text{Bi}_3(\text{MoO}_4)_8$  synthesized by annealing of stoichiometric mixtures of  $\text{Li}_2\text{MoO}_4$ ,  $\text{BaMoO}_4$ , and  $\text{Bi}_2(\text{MoO}_4)_3$  at 450–550 °C for 150 h, analogous triple tungstate  $\text{Li}_3\text{Ba}_2\text{Bi}_3(\text{WO}_4)_8$  – 300 hour annealing of  $\text{Li}_2\text{WO}_4$ ,  $\text{BaWO}_4$ ,  $\text{Bi}_2\text{O}_3$  and  $\text{WO}_3$ , taken in a molar ratio of 3: 4: 3: 9, at 550–700 °C (intermediate homogenization was carried out every 15–20 h).

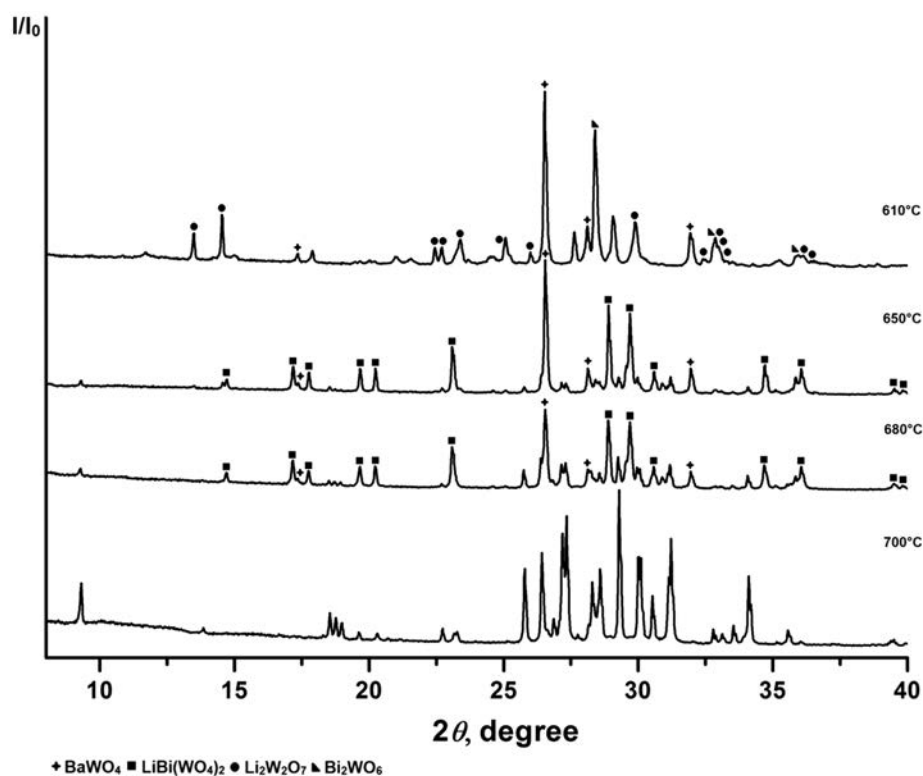
According to powder XRD data (Fig. 1), the sequence of chemical transformations occurring during the formation of  $\text{Li}_3\text{Ba}_2\text{Bi}_3(\text{WO}_4)_8$  from a

stoichiometric mixture of oxides and tertiary tungstates, can be illustrated by the scheme [22]:



The formation of  $\text{Li}_3\text{Ba}_2\text{Bi}_3(\text{MoO}_4)_8$  most likely also proceeds through the stage of formation of a double lithium-bismuth compound, but due to the close temperature ranges of the formation of intermediate and final products, the appearance of  $\text{LiBi}(\text{MoO}_4)_2$  in the reaction mixture was not recorded.

According to the differential scanning calorimetry (DSC) data, the obtained compounds melt incongruently at 756 ( $X = \text{Mo}$ ) and 786 °C ( $X = \text{W}$ ). In addition to  $\text{BaWO}_4$  and  $\text{LiBi}(\text{WO}_4)_2$  and  $\text{Bi}_2\text{WO}_6$  the presence of  $\text{BaMoO}_4$  and  $\text{LiBi}(\text{MoO}_4)_2$ , tungstate was revealed in the cooled melt of molybdate by XRD analysis.



**Fig 1.** Powder X-ray diffraction patterns of the reaction mixture  $\text{Li}_2\text{WO}_4 + 4\text{BaWO}_4 + 3\text{Bi}_2\text{O}_3 + 9\text{WO}_3$ , sequentially annealed at different temperatures

Powder XRD patterns of  $\text{Li}_3\text{Ba}_2\text{Bi}_3(\text{XO}_4)_8$  ( $X = \text{Mo}, \text{W}$ ) were indexed satisfactory under the assumption of isostructurality to lanthanide-containing analogues (in the case of molybdate  $F(30) = 217.1$  (0.0035; 39), tungstate  $-F(30) = 162.3$  (0.0047; 39)). The obtained crystallographic characteristics are shown in Table 1, the results of indexing of  $\text{Li}_3\text{Ba}_2\text{Bi}_3(\text{WO}_4)_8$  are shown in Table 2.

The possibility of realizing a similar structure in ternary bismuth molybdates and tungstates by replacing barium with another double-charged cation  $A^{2+}$  was investigated. However, attempts to synthesize  $\text{Li}_3\text{A}_2\text{Bi}_3(\text{XO}_4)_8$  ( $A = \text{Ca}, \text{Sr}, \text{Cd}, \text{Pb}$ ) were unsuccessful. The compositions  $\text{Li}_3\text{Ba}_{1.9}\text{A}_{0.1}\text{Bi}_3(\text{MoO}_4)_8$  were obtained by the partial substitution of barium with strontium, cadmium,

**Table 1.** Crystallographic characteristics of  $\text{Li}_3\text{Ba}_2\text{Bi}_3(\text{XO}_4)_8$  ( $X = \text{Mo}, \text{W}$ ), sp. gr.  $C2/c$ ,  $Z = 2$

Compound	Unit cell parameters				$V, \text{\AA}^3$
	$a, \text{\AA}$	$b, \text{\AA}$	$c, \text{\AA}$	$\beta, ^\circ$	
$\text{Li}_3\text{Ba}_2\text{Bi}_3(\text{MoO}_4)_8$	5.2798(1)	12.8976(4)	19.2272(5)	90.978(2)	1309.12
$\text{Li}_3\text{Ba}_2\text{Bi}_3(\text{WO}_4)_8$	5.2733(2)	12.9032(4)	19.2650(6)	91.512(3)	1310.38

**Table 2.** Indexing results of powder X-ray diffraction pattern for  $\text{Li}_3\text{Ba}_2\text{Bi}_3(\text{WO}_4)_8$

$2\theta_{\text{exp}}, ^\circ$	$I/I_0$	$d_{\text{exp}}, \text{\AA}$	$h$	$k$	$l$	$\Delta = 2\theta_{\text{exp}} - 2\theta_{\text{calc}}, ^\circ$	$2\theta_{\text{exp}}, ^\circ$	$I/I_0$	$d_{\text{exp}}, \text{\AA}$	$h$	$k$	$l$	$\Delta = 2\theta_{\text{exp}} - 2\theta_{\text{calc}}, ^\circ$
9.191	31	9.6140	0	0	2	-0.014	35.032	1	2.5593	-2	0	2	-0.002
13.723	3	6.4475	0	2	0	-0.009	35.293	1	2.5410	-1	3	5	-0.004
16.539	2	5.3555	0	2	2	-0.013	35.447	16	2.5303	0	2	7	-0.006
18.163	2	4.8802	1	1	0	+0.001	35.527	1	2.5248	2	0	2	-0.008
18.417	18	4.8134	0	0	4	-0.004	35.900	2	2.4994	1	3	5	-0.003
18.637	14	4.7571	-1	1	1	-0.004	36.810	1	2.4397	2	2	0	-0.005
18.857	11	4.7021	1	1	1	-0.004	37.084	1	2.4223	-1	1	7	+0.004
19.501	5	4.5482	0	2	3	-0.010	37.322	1	2.4074	0	0	8	+0.001
20.184	5	4.3958	-1	1	2	-0.002	38.601	1	2.3305	-1	3	6	-0.014
20.592	1	4.3097	1	1	2	-0.005	38.814	1	2.3182	-1	5	0	+0.007
22.601	10	3.9309	-1	1	3	-0.003	39.056	1L	2.3044	-1	5	1	+0.000
23.032	6	3.8583	0	2	4	-0.002	39.168	2	2.2981	1	5	1	+0.000
23.148	8	3.8392	1	1	3	-0.004	39.268	3	2.2924	1	3	6	-0.006
25.650	66	3.4701	-1	1	4	+0.002	39.382	5	2.2861	2	0	4	-0.012
26.298	57	3.3861	1	1	4	-0.001	39.819	2	2.2620	2	2	3	-0.010
26.723	16	3.3332	-1	3	0	0.005	39.945	2	2.2551	0	2	8	-0.005
26.943	9	3.3065	0	2	5	-0.005	41.030	1	2.1980	-2	2	4	-0.004
27.059	86	3.2926	-1	3	1	-0.004	41.228	1	2.1879	-1	5	3	-0.006
27.219	100	3.2736	1	3	1	-0.009	41.384	2	2.1800	-1	1	8	-0.003
27.639	8	3.2248	0	4	0	-0.009	41.554	1L	2.1714	1	5	3	-0.011
28.032	11	3.1804	0	4	1	-0.009	41.879	2	2.1553	2	2	4	+0.000
28.172	51	3.1650	-1	3	2	-0.006	41.975	2	2.1506	0	6	0	+0.002
28.464	45	3.1331	1	3	2	+0.000	42.245	1L	2.1375	0	6	1	+0.006
29.167	97	3.0592	-1	1	5	-0.007	42.946	2	2.1042	1	3	7	-0.005
29.880	63	2.9878	1	1	5	-0.003	43.041	1	2.0998	0	6	2	+0.021
29.982	28	2.9779	-1	3	3	-0.002	43.083	3	2.0979	-1	5	4	-0.002
30.402	26	2.9377	1	3	3	-0.001	43.158	1	2.0944	0	4	7	+0.024
31.001	47	2.8823	0	4	3	-0.001	43.378	2	2.0843	-2	2	5	-0.001
31.097	61	2.8736	0	2	6	-0.001	44.391	25	2.0390	0	6	3	-0.003
32.998	8	2.7123	-1	1	6	+0.000	44.584	23	2.0306	0	2	9	-0.008
33.411	14	2.6797	0	4	4	-0.003	44.740	2	2.0239	2	4	1	-0.033
33.781	5	2.6512	1	1	6	-0.012	45.180	12	2.0052	-2	4	2	+0.005
33.985	61	2.6357	2	0	0	+0.000	45.395	2	1.9962	-1	5	5	+0.001

## End of Table 2

$2\theta_{\text{exp}}, ^\circ$	$I/I_0$	$d_{\text{exp}}, \text{Å}$	$h$	$k$	$l$	$\Delta =$ $=2\theta_{\text{exp}} - 2\theta_{\text{calc}}, ^\circ$	$2\theta_{\text{exp}}, ^\circ$	$I/I_0$	$d_{\text{exp}}, \text{Å}$	$h$	$k$	$l$	$\Delta =$ $=2\theta_{\text{exp}} - 2\theta_{\text{calc}}, ^\circ$
45.581	15	1.9885	2	4	2	+0.001	56.460	8	1.6285	-2	2	9	-0.006
45.881	3	1.9762	1	5	5	+0.009	56.557	2	1.6259	-3	3	0	-0.029
46.136	21	1.9659	-2	2	6	+0.004	56.627	11	1.6241	3	1	4	+0.009
46.190	26	1.9637	0	6	4	+0.004	56.810	4	1.6193	-2	6	3	-0.006
46.363	25	1.9568	-2	4	3	+0.003	56.869	7	1.6177	3	3	1	+0.006
46.948	22	1.9338	2	4	3	+0.001	57.142	6	1.6106	-3	3	2	+0.009
47.077	2	1.9288	0	4	8	-0.014	57.309	4	1.6063	2	6	3	+0.000
47.147	9	1.9261	0	0	10	+0.006	57.464	8	1.6024	-3	1	5	+0.002
47.311	17	1.9198	2	2	6	-0.006	57.651	4	1.5976	3	3	2	+0.003
48.018	6	1.8931	-2	4	4	+0.001	57.965	5	1.5897	2	2	9	+0.002
48.116	4	1.8895	-1	5	6	+0.000	58.112	2	1.5860	-3	3	3	-0.001
48.447	3	1.8774	0	6	5	-0.008	58.229	7	1.5831	-2	6	4	+0.013
48.680	5	1.8689	1	5	6	+0.003	58.287	14	1.5817	-1	5	9	+0.011
48.771	7	1.8657	2	4	4	+0.004	58.557	2	1.5750	-2	0	10	+0.006
49.270	11	1.8479	-2	2	7	-0.003	58.659	4	1.5725	-2	4	8	-0.007
49.347	11	1.8452	0	2	10	-0.004	58.727	4	1.5709	3	1	5	-0.013
50.249	1	1.8142	-1	3	9	-0.006	58.893	13	1.5668	2	6	4	+0.011
50.481	9	1.8064	-1	1	10	-0.003	59.043	10	1.5632	1	5	9	+0.000
50.565	10	1.8036	2	2	7	-0.005	59.148	1	1.5607	-1	3	11	+0.002
51.066	1	1.7871	1	3	9	-0.001	59.302	1	1.5570	0	2	12	-0.016
51.198	25	1.7828	-1	5	7	-0.001	59.704	2	1.5475	-3	1	6	+0.001
51.391	11	1.7765	1	1	10	-0.003	59.972	1	1.5412	2	4	8	-0.006
51.829	24	1.7625	1	5	7	+0.000	60.070	3	1.5389	0	4	11	0.008
52.069	2	1.7550	2	0	8	+0.012	60.210	3	1.5357	-1	1	12	-0.001
52.558	22	1.7398	1	7	0	-0.007	60.459	7	1.5300	-2	2	10	+0.000
52.746	8	1.7340	-1	7	1	-0.008	60.887	1	1.5202	2	6	5	+0.006
52.826	7	1.7316	1	7	1	+0.000	61.040	1	1.5168	0	6	9	-0.003
53.373	4	1.7151	-1	7	2	+0.008	61.181	2	1.5136	1	1	12	+0.001
53.558	2	1.7096	1	7	2	-0.001	62.057	7	1.4943	2	2	10	+0.013
53.665	2	1.7065	2	4	6	-0.004	62.150	1	1.4923	-2	4	9	+0.005
54.601	1	1.6794	-1	3	10	-0.007	62.274	1	1.4897	-1	5	10	-0.005
54.727	1	1.6759	1	7	3	+0.005	62.368	5	1.4876	0	8	5	-0.004
55.063	2	1.6664	-2	6	0	+0.005	62.465	1	1.4856	3	3	5	+0.000
55.270	7	1.6607	-1	1	11	-0.007	63.061	1	1.4729	1	5	10	+0.004
55.526	1	1.6536	0	4	10	0.002	63.220	1L	1.4696	2	6	6	+0.035
55.627	8	1.6509	-3	1	4	-0.012	63.908	2	1.4555	-1	3	12	+0.000
55.832	3	1.6453	-2	6	2	-0.045	64.135	1	1.4508	-3	5	1	+0.008
56.021	2	1.6402	-1	7	4	-0.030	64.475	1L	1.4440	0	2	13	+0.009
56.133	1	1.6372	2	6	2	-0.005	64.608	8	1.4414	0	8	6	+0.010
56.208	5	1.6352	1	1	11	-0.004	64.832	6	1.4369	0	4	12	+0.003

and lead in the single-phase state. The solubility limit in similar tungstates was less than 5%.

The ion-conducting properties of the obtained compounds were studied. It was established that  $\text{Li}_3\text{Ba}_2\text{Bi}_3(\text{XO}_4)_8$  undergo phase transformations at 441 ( $X = \text{Mo}$ ) and 527 °C ( $X = \text{W}$ ), which, based on the presence of temperature hysteresis in  $\lg(\sigma T) - (10^3/T)$  dependences in the heating –

cooling cycle can be interpreted as the first order diffuse phase transitions. After the transition, the conductivity  $\text{Li}_3\text{Ba}_2\text{Bi}_3(\text{MoO}_4)_8$  reached values of  $3.5 \cdot 10^{-3}$  S/cm (640 °C) at  $E_a = 1.0$  eV,  $\text{Li}_3\text{Ba}_2\text{Bi}_3(\text{WO}_4)_8$  –  $2.7 \cdot 10^{-4}$  S/cm (700 °C) at  $E_a = 0.8$  eV. Temperature dependence of electrical conductivity of  $\text{Li}_3\text{Ba}_2\text{Bi}_3(\text{MoO}_4)_8$  as an example is shown in Fig. 2. The obtained interdependence

of the active and reactive components of the electrical impedance for this compound (at temperatures before and after the phase transition), typical for ionic conductors with blocking electrodes is shown in Fig. 3.

#### 4. Conclusions

Thus, the first compounds of  $\text{Li}_3\text{Ba}_2\text{R}_3(\text{XO}_4)_8$  ( $X = \text{Mo}, \text{W}$ ) family were obtained with the structure of  $\text{BaNd}_2(\text{MoO}_4)_4$  (sp. gr.  $C2/c$ ,  $Z = 2$ ),

containing different from the rare earth elements a trivalent metal. The sequence of chemical transformations occurring during the synthesis of ternary tungstate of lithium, barium, bismuth from a stoichiometric mixture of tertiary tungstates and oxides was established. Crystallographic and thermal characteristics of  $\text{Li}_3\text{Ba}_2\text{Bi}_3(\text{XO}_4)_8$  ( $X = \text{Mo}, \text{W}$ ) were determined and their ion-conducting properties were studied. It was shown that triple molybdates and tungstates

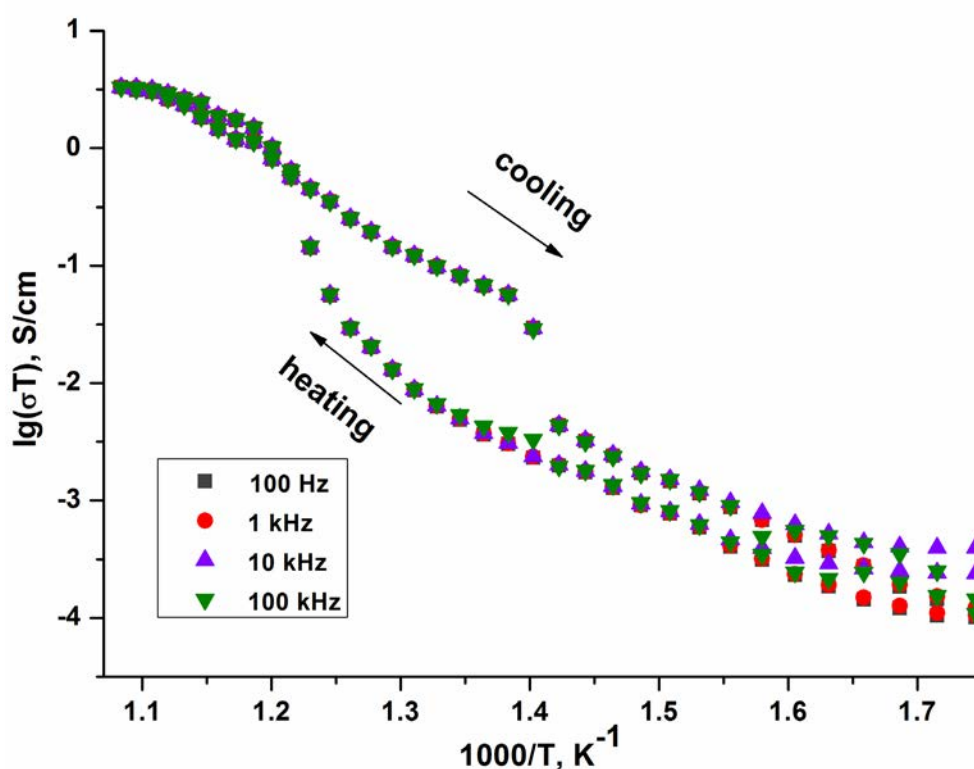


Fig. 2. The temperature dependence of the electrical conductivity for  $\text{Li}_3\text{Ba}_2\text{Bi}_3(\text{MoO}_4)_8$

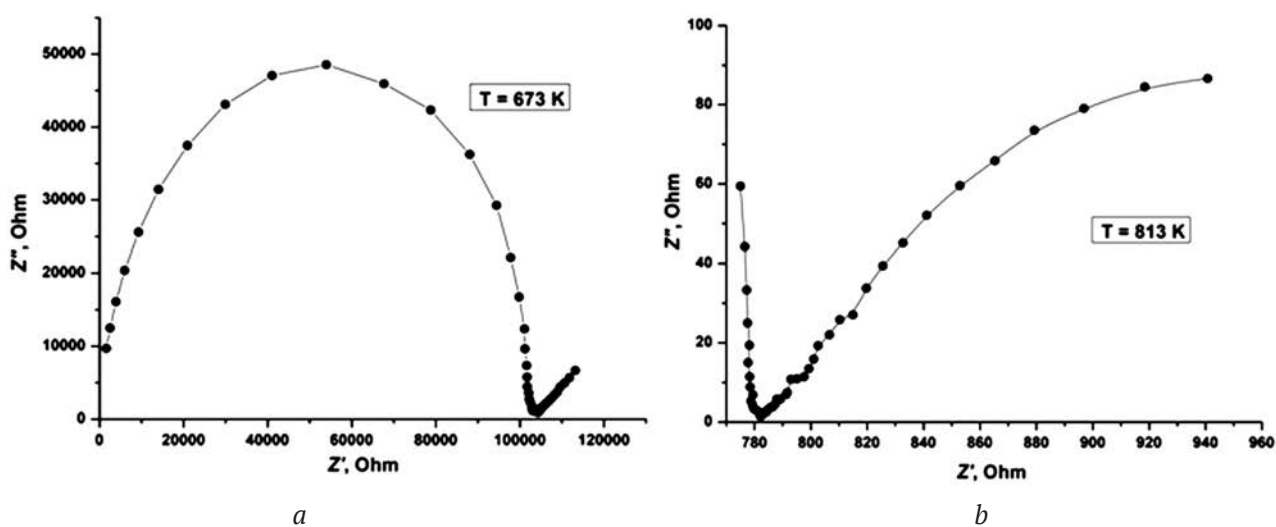


Fig. 3. Nyquist plot for  $\text{Li}_3\text{Ba}_2\text{Bi}_3(\text{MoO}_4)_8$  at 673 K (a) and 813 K (b)

$\text{Li}_3\text{A}_2\text{Bi}_3(\text{XO}_4)_8$  ( $\text{A} = \text{Ca}, \text{Sr}, \text{Cd}, \text{Pb}; \text{X} = \text{Mo}, \text{W}$ ) with the structure  $\text{BaNd}_2(\text{MoO}_4)_4$  are not formed.

### Conflict of interests

The authors declare that they have no known competing financial interests or personal relationships that could have influenced the work reported in this paper.

### References

1. Kozhevnikova N. M., Mokhosoev M. V. *Troinye molibdaty* [Ternary molybdates]. Ulan-Ude: Buryat State University Publ.; 2000. 298 c. (In Russ.)
2. Kozhevnikova N. M., Korsun V. P., Mokhosoev M. V., Alekseev F. P. Troinye molibdaty litiya, bariya i redkozemel'nykh elementov [Ternary molybdates of lithium, barium and rare earth elements]. *Russian Journal of Inorganic Chemistry*. 1990;35(4): 835–838. (In Russ.)
3. Khaikina E. G., Bazarova Zh. G., Solodovnikov S. F., Klevtsova R. F. Troinye molibdaty kak osnova novykh perspektivnykh slozhnooksidnykh materialov [Ternary molybdates as a basis for new promising complex oxide materials]. *Engineering Ecology*. 2011;1: 48–54. (In Russ.)
4. Kozhevnikova N. M., Kopylova O. A. Synthesis and electrophysical properties of ternary molybdates  $\text{Li}_3\text{Ba}_2\text{R}_3(\text{MoO}_4)_8$ ,  $\text{R} = \text{La} - \text{Lu}$ . *Russian Journal of Applied Chemistry*. 2011;84(3): 384–387. <https://doi.org/10.1134/S1070427211030086>
5. Kozhevnikova N. M. Synthesis and luminescence properties of a  $\text{Li}_3\text{Ba}_2\text{La}_3(\text{MoO}_4)_8:\text{Er}^{3+}$  phosphor with a scheelite-like structure. *Inorganic Materials*. 2019;55(6): 607–611. <https://doi.org/10.1134/S0020168519060098>
6. Kozhevnikova N. M., Batueva S. Yu. Synthesis and study of the luminescent properties of the phosphor  $\text{Li}_3\text{Ba}_2\text{Y}_3(\text{MoO}_4)_8:\text{Tb}^{3+}$  layered scheelite-like structure. *Inorganic Materials*. 2019;55(11): 1162–1166. <https://doi.org/10.1134/S0020168519110074>
7. Kozhevnikova N. M., Batueva S. Yu. Erbium-doped upconversion phosphor in the  $\text{Li}_2\text{MoO}_4 - \text{BaMoO}_4 - \text{Y}_2(\text{MoO}_4)_3$  system. *Inorganic Materials*. 2020;56(3): 286–291. <https://doi.org/10.1134/S0020168520030085>
8. Hu J., Gong X., Huang J., Chen Y., Lin Y., Luo Z., Huang Y. Near ultraviolet excited  $\text{Eu}^{3+}$  doped  $\text{Li}_3\text{Ba}_2\text{La}_3(\text{WO}_4)_8$  red phosphors for white light emitting diodes. *Optical Materials Express*. 2016;6(1): 181–190. <https://doi.org/10.1364/OME.6.000181>
9. Li H., Zhang L., Wang G. Growth, structure and spectroscopic characterization of a new laser crystals  $\text{Nd}^{3+}:\text{Li}_3\text{Ba}_2\text{Gd}_3(\text{WO}_4)_8$ . *Journal of Alloys and Compounds*. 2009;478: 484–488. <https://doi.org/10.1016/j.jallcom.2008.11.079>
10. Xiao B., Lin Z., Zhang L., Huang Y., Wang G. Growth, thermal and spectral properties of  $\text{Er}^{3+}$ -doped and  $\text{Er}^{3+}/\text{Yb}^{3+}$ -codoped  $\text{Li}_3\text{Ba}_2\text{La}_3(\text{WO}_4)_8$  crystals. *PLoS ONE*. 2012;7(7): e40631. <https://doi.org/10.1371/journal.pone.0040631>
11. Pan Y., Chen Y., Lin Y., Gong X., Huang J., Luo Z., Huang Y. Structure, spectral properties and laser performance of  $\text{Tm}^{3+}$ -doped  $\text{Li}_3\text{Ba}_2\text{La}_3(\text{WO}_4)_8$  crystal. *CrystEngComm*. 2012;14: 3930. <https://doi.org/10.1039/C2CE25190F>
12. Li H., Lin Z., Zhang L., Huang Y., Wang G. Spectroscopic characteristics of  $\text{Yb}^{3+}$ -doped  $\text{Li}_3\text{Ba}_2\text{Y}_3(\text{WO}_4)_8$  crystal. *Journal of Luminescence*. 2012;132(6): 1507–1510. <https://doi.org/10.1016/j.jlumin.2012.01.050>
13. Hu J., Gong X., Huang J., Chen Y., Lin Y., Luo Z., Huang Y. Near ultraviolet excited  $\text{Eu}^{3+}$  doped  $\text{Li}_3\text{Ba}_2\text{La}_3(\text{WO}_4)_8$  red phosphors for white light emitting diodes. *Optical Materials Express*. 2016;6(1): 181. <https://doi.org/10.1364/OME.6.000181>
14. Zeng X.-L., Zhang J.-Y., Chen D.-G., Huang F. Crystal structure and spectroscopic properties of a new ternary tungstate  $\text{Li}_3\text{Ba}_2\text{Ho}_3(\text{WO}_4)_8$ . *Chinese Journal of Structural Chemistry*. 2013;1: 33–38. Available at: [http://caod.oriprobe.com/articles/32299408/Crystal\\_Structure\\_and\\_Spectroscopic\\_Properties\\_of\\_a\\_New\\_Ternary\\_Tungst.htm](http://caod.oriprobe.com/articles/32299408/Crystal_Structure_and_Spectroscopic_Properties_of_a_New_Ternary_Tungst.htm)
15. Guo W. L., Jiao Y. T., Wang P. S., Liu Q., Liu S., Hou F. Energy transfer and spectroscopic characterization of new green emitting  $\text{Li}_3\text{Ba}_2\text{Gd}_3(\text{WO}_4)_8:\text{Tb}^{3+}$  phosphor. *Solid State Phenomena*. 2018;281: 686–691. <https://doi.org/10.4028/www.scientific.net/ssp.281.686>
16. Wei B., Liu Z., Xie C., Yang S., Tang W., Gu A., Wong W.-T., Wong K.-L. Fast synthesis of red  $\text{Li}_3\text{BaSrLn}_3(\text{WO}_4)_8:\text{Eu}^{3+}$  phosphors for white LEDs under near-UV excitation by a microwave-assisted solid state reaction method and photoluminescence studies. *Journal of Materials Chemistry C*. 2015;3(47): 12322. <https://doi.org/10.1039/c5tc03165f>
17. Singh K., Vaidyanathan S. Synthesis and optical properties of new red emitting phosphor  $\text{Li}_3\text{BaSrGd}_{3-x}\text{Eu}_x(\text{MO}_4)_8$  for white LEDs. *Chemistry Select*. 2017;1(17): 5448–5462. <https://doi.org/10.1002/slct.201601183>
18. Li H., Wang G., Zhang L., Huang Y., Wang G. Growth and structure of  $\text{Nd}^{3+}$ -doped  $\text{Li}_3\text{Ba}_2\text{Y}_3(\text{WO}_4)_8$  crystal with a disorder structure. *CrystEngComm*. 2010;12(4): 1307–1310. <https://doi.org/10.1039/B914641E>
19. Diagrammy sostoyaniya sistem tugoplavkikh oksidov: Spravochnik. Vyp. 5. Dvoynye sistemy. Ch. 2 [Diagrams of the state of systems of refractory oxides: Handbook. Issue 5. Binary systems. Part 2]. Leningrad: Nauka; 1986. 359 p. (In Russ.)
20. ICDD PDF-2 Data Base, Cards ## 00-053-0670, 00-029-0193, 01-070-1396, 01-079-2006, 01-085-0588, 01-085-1267, 01-085-0586, 00-007-0209, 00-



044-1486, 00-041-1431, 00-008-0490, 00-014-0676, 00-019-0708

21. Smith G. S., Snyder R. L.  $F_N$ : A criterion for rating powder diffraction patterns and evaluating the reliability of powder-pattern indexing. *Journal of Applied Crystallography*. 1979;12(1): 60–65. <https://doi.org/10.1107/s002188987901178x>

22. ICDD PDF-2 Data Base, Cards ## 00-051-1725, 01-070-0869, 00-039-0256

### Information about the authors

*Tatiana S. Spiridonova*, Leading Engineer, Laboratory of Oxide Systems, Baikal Institute of Nature Management, Siberian Branch of the Russian Academy of Sciences (BINM SB RAS), Ulan-Ude, Russian Federation; e-mail: [spiridonova-25@mail.ru](mailto:spiridonova-25@mail.ru). ORCID iD: <https://orcid.org/0000-0001-7498-5103>.

*Aleksandra A. Savina*, PhD in Chemistry, Researcher, Laboratory of Oxide Systems, Baikal Institute of Nature Management, Siberian Branch of the Russian Academy of Sciences (BINM SB RAS), Ulan-Ude and Skolkovo Institute of Science and Technology, Moscow, Russian Federation; e-mail: [a.savina@skoltech.ru](mailto:a.savina@skoltech.ru). ORCID iD: <https://orcid.org/0000-0002-7108-8535>.

*Yulia M. Kadyrova*, PhD in Chemistry, Researcher, Laboratory of Oxide Systems, Baikal Institute of Nature Management, Siberian Branch of the Russian Academy of Sciences (BINM SB RAS) and Senior Lecturer of the Department of General and Analytical Chemistry, Faculty of Chemistry, Dorji Banzarov Buryat State University (BSU), Ulan-Ude, Russian Federation; e-mail: [ylychem@yandex.ru](mailto:ylychem@yandex.ru). ORCID iD: <https://orcid.org/0000-0002-0106-8096>.

*Elena P. Belykh*, Master's student, Faculty of Chemistry, Dorji Banzarov Buryat State University (BSU), Ulan-Ude, Russian Federation; e-mail: [elena.belych1996@yandex.ru](mailto:elena.belych1996@yandex.ru)

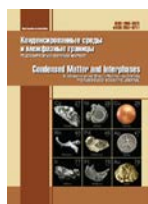
*Elena G. Khaikina*, DSc in Chemistry, Head of Laboratory Oxide Systems, Baikal Institute of Nature Management, Siberian Branch of the Russian Academy of Sciences (BINM SB RAS) and Professor of the Department of Inorganic and Organic Chemistry, Faculty of Chemistry, Dorji Banzarov Buryat State University (BSU), Ulan-Ude, Russian Federation; e-mail: [egkha@mail.ru](mailto:egkha@mail.ru). ORCID iD: <https://orcid.org/0000-0003-2482-9297>.

All authors have read and approved the final manuscript.

*Received 24 December 2020; Approved after reviewing 15 January 2021; Accepted 15 March 2021; Published online 25 March 2021.*

*Translated by Valentina Mittova*

*Edited and proofread by Simon Cox*



# Condensed Matter and Interphases

Kondensirovannye Sredy i Mezhfaznye Granitsy  
<https://journals.vsu.ru/kcmf/>

## Original articles

Original article

<https://doi.org/10.17308/kcmf.2021.23/3307>

## Vapour-liquid phase equilibria and thermodynamic properties of solutions of the ethylbenzene and n-alkylbenzenes binary systems

Yu. K. Suntsov✉, N. S. Suntsova

Voronezh State University,  
1 Universitetskaya pl., Voronezh 394018, Russian Federation

### Abstract

The methods of theoretical description of the patterns of changes in thermodynamic properties depending on the composition and structure of solution components are a priority direction in the development of the theory of solutions. This article is devoted to the establishment of relationships between the thermodynamic properties, composition of solutions, and the structure of their components. The study of the thermodynamic properties of binary solutions formed by a common solvent (ethylbenzene) and substances of the homologous series of n-alkylbenzenes contributes to the establishment of the aforementioned relationships. In the production of ethylbenzene and its homologues, solutions based on n-alkylbenzenes are quite common. Alkylbenzenes are widely used in various fields of science and chemical technology as solvents, extractants, and plasticisers.

Using the ebulliometric method, we measured the boiling points of solutions of four binary systems formed by ethylbenzene and n-alkylbenzenes under various pressure values. Compositions of equilibrium vapour phases of the binary systems were calculated using the obtained isotherms of saturated vapour pressure of the solutions. Using the Runge-Kutta method, the composition of the vapour phases of the solutions of the systems was calculated by the numerical integration of the Duhem–Margules equation on a computer. The obtained data on the vapour-liquid equilibrium became the basis for calculating the thermodynamic functions of the systems' solutions. The Gibbs and Helmholtz energy values, the enthalpies of vaporisation and mixing, the internal energy, and entropy of solutions were calculated. The thermodynamic properties of the solutions were calculated using a comparison of the values based on two standards: an ideal solution and an ideal gas.

It was found that the values of the Helmholtz energy linearly depend on the molar mass of the substance (the number of  $-\text{CH}_2-$  groups in a molecule) in the homologous series of n-alkylbenzenes. An increase in the Helmholtz energy values for n-alkylbenzenes in the homologous series is associated with a linear increase in the molar volume of liquid substances and an exponential decrease in the saturated vapour pressure of substances. For binary solutions of constant molar concentrations formed by ethylbenzene and n-alkylbenzenes, the Helmholtz energy linearly depends on the molar mass (number of  $-\text{CH}_2-$  groups in the molecule) of n-alkylbenzene in the homologous series. We obtained an equation that makes it possible to predict the thermodynamic properties of solutions of binary systems with high accuracy. The equation accelerates the process of studying vapour-liquid phase equilibria and thermodynamic properties of solutions of binary systems by 300 times. The determined patterns confirm the hypothesis of the additive contribution of functional groups to the thermodynamic properties of solutions. This hypothesis underlies the statistical theory of group models of solutions. The thermodynamic patterns determined by this study can also be used to solve a wide range of technological issues in the chemical industry.

**Keywords:** Solutions of binary systems, Vapour-liquid phase equilibria, Gibbs and Helmholtz energies, Enthalpies of vaporisation and mixing, Internal energy and entropy of solutions

**For citation:** Suntsov Yu. K., Suntsova N. S. Vapour-liquid phase equilibria and thermodynamic properties of solutions of the ethylbenzene and n-alkylbenzenes binary systems. *Kondensirovannye sredy i mezhfaznye granitsy = Condensed Matter and Interphases*. 2021;23(1): 81–92. <https://doi.org/10.17308/kcmf.2021.23/3307>

**Для цитирования:** Сунцов Ю. К., Сунцова Н. С. Фазовые равновесия жидкость-пар и термодинамические свойства растворов бинарных систем этилбензол- n-алкилбензолы. *Конденсированные среды и межфазные границы*. 2021;23(1): 81–92. <https://doi.org/10.17308/kcmf.2021.23/3307>

✉ Yuri K. Suntsov, e-mail: [jsyntsov@mail.ru](mailto:jsyntsov@mail.ru)

© Suntsov Yu. K., Suntsova N. S., 2021



The content is available under Creative Commons Attribution 4.0 License.

## 1. Introduction

To determine the relation between thermodynamic properties, molar characteristics, and the concentration of the components of solutions, the data on the properties of binary systems formed by substances of homologous series are the most valuable [1]. The existing methods for calculating the properties of multicomponent systems are also based on the properties of their binary components [2]. In the production of ethylbenzene and its homologues, solutions formed by *n*-alkylbenzenes are quite common [3,4]. The literature data on the properties of these solutions are fragmentary, since they have been mainly studied for technological purposes. At various temperatures, we studied vapour-liquid phase equilibria and bulk properties of solutions of the binary systems formed by ethylbenzene (common solvent) and: benzene, toluene, *n*-propylbenzene, *n*-butylbenzene (the second components of the solutions). The article attempts to establish the relationship between the Helmholtz energy values and the composition and molar mass of the components of solutions of the ethylbenzene and *n*-alkylbenzenes systems. Such relationships were previously established for solutions of 160 binary systems formed by substances of organic compounds of various classes.

## 2. Experimental

Benzene and ethylbenzene of kh. ch. (chemically pure) grade, toluene of os. ch. (special purity) grade, and *n*-propylbenzene and *n*-butylbenzene from Merk of “for synthesis” grade were purified as recommended in [5] and distilled without the access of air on a laboratory rectification column. Residual moisture was determined by potentiometric titration using

the Fischer reagent [6]. The content of water in the reagents did not exceed 0.01%. The physical constants of the purified substances, provided in Table 1, satisfactorily coincided with the literature data [7, 8, 9]. The saturated vapour pressure (*P*) was measured at the boiling point of liquid (*T*) using the Swietoslowski ebulliometers. The constant pressure in the system was maintained by an isodromic regulator with a precision of up to  $\pm 6.6 \text{ N/m}^2$ . The saturated vapour pressure of the solutions was measured with a mercury manometer using a V-630 cathetometer (GOST 15150-69) with a precision of  $\pm 6.6 \text{ N/m}^2$ ; and atmospheric pressure was measured with a first-class mercury barometer with the same precision. The density of solutions was measured with the Ostwald pycnometers with a precision of  $\pm 0.1 \text{ kg/m}^3$  [10].

## 3. Results and discussion

The isotherms of saturated vapour pressure  $P = f(x)$  of the solutions constructed on the basis of experimental data  $P = f(T)$  served as the basis for calculating the compositions of equilibrium vapour phases of the systems. Earlier it was established that at low pressure values the vapour phase of solutions of the systems is regulated by the ideal gas laws with the accuracy presented in our experiment [11]. The compositions of the equilibrium vapour phases of solutions of the systems were calculated by numerical computer integration of the Duhem–Margules equation, which at  $T = \text{const}$  and under the condition of the ideal vapour phase takes the form [11]:

$$dy = y(1-y)dP / (y-x)P, \quad (1)$$

where *x*, *y* are the mole fractions of the high-boiling component in liquid and vapour forms; *P*

**Table 1.** Properties of purified substances

Substance	Experimental value			Literature value		
	$\rho_4^{20}$	<i>T</i> , K	$n_D^{20}$	$\rho_4^{20}$	<i>T</i> , K	$n_D^{20}$
benzene	0.8789	353.3	1.5008	0.8790	353.25	1.5011
ethylbenzene	0.8671	383.8	1.4965	0.8669	383.77	1.4969 1.4961
этилбензол	0.8672	409.4	1.4959	0.8671	409.3	1.4959
<i>n</i> -propylbenzene	0.8620	432.3	1.4916	0.8619	432.4	1.4920
<i>n</i> -butylbenzene	0.8613	456.4	1.4898	0.8609	456.4	1.4898

Designations:  $\rho_4^{20}$  - density, g/cm<sup>3</sup>, *T* – boiling point K under normal pressure,  $n_D$  – refractive index at *T* = 293 K.

is the saturated vapour pressure of a binary solution. Analysing the compositions of equilibrium vapour phases of solutions, we can see that solutions of the ethylbenzene and n-alkylbenzenes systems have negative deviations from the ideal state. The toluene concentration in the vapour phase of the systems increases with an increase in the molar mass of the second component of solution (Table 2). When rectifying solutions of the systems, the concentration of ethylbenzene in the vapour phase of the systems

is higher than the concentration of propyl- and butylbenzene, and less than the concentration of benzene and toluene molecules. An increase in temperature (pressure) increases the concentration of ethylbenzene in the vapour phase of solutions of the ethylbenzene-benzene and ethylbenzene – toluene systems. On the contrary, for ethylbenzene – propylbenzene and ethylbenzene – butylbenzene solutions, an increase in temperature decreases the concentration of ethylbenzene in the vapour phase, since

**Table 2.** Vapour-liquid phase equilibria and the thermodynamic properties of solutions of the ethylbenzene and n-alkylbenzene systems at  $T = 353$  K

Parameter	ethylbenzene – benzene											
	x	1.0000	0.9000	0.8000	0.7000	0.6000	0.5000	0.4000	0.3000	0.2000	0.1000	0.0000
y	1	0.6102	0.4064	0.2833	0.2011	0.1424	0.0986	0.0648	0.0381	0.0168	0	
P	16.75	24.52	32.65	40.88	49.20	57.62	66.14	74.75	83.46	92.27	101.00	
V	130.5	127.0	123.5	120.0	116.5	113.0	109.5	106.0	102.5	99.0	96.0	
$G^e$	0.00	-36.50	-47.70	-55.40	-60.20	-62.00	-60.70	-55.50	-45.30	-28.10	0.00	
$H^e$	0.000	-2.097	-2.912	-3.135	-3.038	-2.746	-2.329	-1.825	-1.259	-0.647	0.000	
$S^e$	0.00	-5.84	-8.11	-8.72	-8.43	-7.60	-6.42	-5.01	-3.44	-1.75	0.00	
H	39.53	36.11	34.47	33.41	32.68	32.14	31.72	31.40	31.13	30.91	30.72	
$U^r$	36.60	35.25	34.40	33.56	32.73	31.89	31.06	30.24	29.41	28.59	27.80	
$A^r$	18.21	17.80	17.37	16.93	16.50	16.06	15.62	15.19	14.75	14.30	13.85	
$S^r$	50.69	49.43	48.26	47.11	45.98	44.85	43.74	42.64	41.55	40.48	39.51	
	ethylbenzene – toluene											
y	1	0.7942	0.6305	0.4976	0.3878	0.2957	0.2175	0.1506	0.0929	0.0429	0	
P	16.66	18.83	21.07	23.32	25.60	27.90	30.24	32.58	34.96	37.36	39.69	
V	130.5	128.8	127.1	125.5	123.8	122.1	120.4	118.8	117.1	115.4	113.7	
$G^e$	0.00	-15.00	-20.40	-24.40	-27.00	-27.90	-27.00	-23.90	-18.20	-9.00	0.00	
$H^e$	0.000	-0.211	-0.581	-0.994	-1.365	-1.620	-1.699	-1.557	-1.176	-0.587	0.000	
$S^e$	0.00	-0.56	-1.59	-2.75	-3.79	-4.51	-4.74	-4.34	-3.28	-1.64	0.00	
H	39.53	38.95	38.22	37.44	36.71	36.08	35.64	35.42	35.43	35.66	35.88	
$U^r$	36.60	36.02	35.29	34.51	33.77	33.15	32.71	32.48	32.50	32.72	32.95	
$A^r$	18.21	18.03	17.82	17.60	17.39	17.18	16.96	16.75	16.53	16.30	16.09	
$S^r$	52.01	50.95	49.47	47.87	46.38	45.23	44.59	44.57	45.23	46.50	47.74	
	ethylbenzene – n-propylbenzene											
y	1.0000	0.9540	0.9003	0.8385	0.7673	0.6851	0.5898	0.4783	0.3468	0.1897	0.0000	
P	16.66	15.67	14.72	13.77	12.85	11.93	11.04	10.16	9.293	8.426	7.621	
V	130.5	132.3	134.1	135.8	137.6	139.4	141.1	142.9	144.6	146.4	148.2	
$G^e$	0.00	-35.30	-50.60	-59.30	-62.80	-62.20	-57.80	-50.30	-39.70	-26.40	0.00	
$H^e$	0.000	-0.703	-0.834	-0.887	-0.960	-1.033	-1.054	-0.972	-0.758	-0.411	0.000	
$S^e$	0.00	-1.89	-2.22	-2.34	-2.54	-2.75	-2.82	-2.61	-2.04	-1.09	0.00	
H	39.53	39.85	40.22	40.69	41.04	41.10	41.18	41.19	41.28	42.06	44.02	
$U^r$	36.60	36.92	37.29	37.76	38.11	38.17	38.25	38.26	38.34	39.13	41.08	
$A^r$	18.21	18.44	18.64	18.84	19.04	19.23	19.42	19.61	19.79	19.98	20.15	
$S^r$	52.04	52.32	52.79	53.56	54.17	54.11	53.34	52.38	52.26	54.22	59.26	

## End of Table 2

	ethylbenzene – n-butylbenzene										
<i>y</i>	1.0000	0.9830	0.9618	0.9355	0.9022	0.8591	0.8015	0.7207	0.5996	0.3984	0.0000
<i>P</i>	16.66	15.24	13.76	12.32	10.91	9.53	8.19	6.87	5.59	4.33	3.18
<i>V</i>	130.5	134.0	137.5	140.9	144.4	147.9	151.4	154.9	158.4	161.8	165.3
<i>G<sup>e</sup></i>	0.00	-57.10	-83.90	-97.00	-100.60	-96.70	-86.70	-71.50	-51.60	-27.60	0.00
<i>H<sup>e</sup></i>	0.000	-0.810	-1.259	-1.510	-1.609	-1.584	-1.451	-1.225	-0.917	-0.533	0.000
<i>S<sup>e</sup></i>	0.00	-2.13	-3.33	-4.00	-4.27	-4.21	-3.87	-3.27	-2.45	-1.43	0.00
<i>H</i>	39.53	39.05	39.41	39.97	40.69	41.53	42.48	43.52	44.64	45.84	47.18
<i>U<sup>r</sup></i>	36.60	36.95	37.23	37.59	38.07	38.73	39.61	40.77	42.28	44.22	46.68
<i>A<sup>r</sup></i>	18.21	18.69	19.13	19.57	19.99	20.41	20.83	21.24	21.65	22.06	22.40
<i>S<sup>r</sup></i>	52.05	51.71	51.23	51.03	51.19	51.87	53.19	55.30	58.42	62.74	68.74

Designations: *x* and *y* – mole fractions of ethylbenzene in liquid and vapour phases of the systems, respectively (*x* – refers to solutions of all systems); *P* – saturated vapour pressure of solutions (kPa); *V* – molar volume of solutions (cm<sup>3</sup>/mol); *G<sup>e</sup>* – excess Gibbs energy J·mol<sup>-1</sup>·K<sup>-1</sup>; *H<sup>e</sup>* – excess enthalpy of solutions (kJ·mol<sup>-1</sup>); *S<sup>e</sup>* – excess entropy of solutions (J·mol<sup>-1</sup>·K<sup>-1</sup>); *H* – enthalpy of vaporisation of solutions (kJ·mol<sup>-1</sup>); *U<sup>r</sup>* – internal energy (kJ·mol<sup>-1</sup>); *A<sup>r</sup>* – Helmholtz energy of solutions (kJ·mol<sup>-1</sup>); *S<sup>r</sup>* – entropy of solutions (J·mol<sup>-1</sup>·K<sup>-1</sup>)

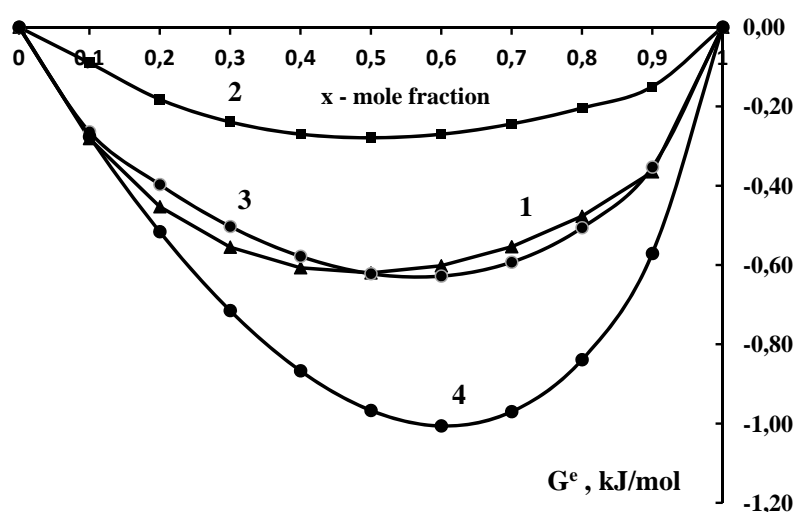
ethylbenzene has a lower enthalpy of vaporisation. The noted deviations in the vapour phase equilibrium of the systems are consistent with Konovalov's and Vrevesky's laws [12]. Based on the obtained *P*-*X*-*Y*-*T* data, using the known thermodynamic relations, we calculated the values of the activity coefficients ( $\gamma_i$ ) and the excess chemical potentials of the mixture components ( $\mu_i^e$ ), as well as the values of the excess Gibbs energy (*G<sup>e</sup>*) for solutions of the systems [1, 12]:

$$\gamma_i = Py_i / P_i^0 x_i, \quad (2)$$

$$\mu_i^e = RT \ln \gamma_i, \quad (3)$$

$$G^e = RT(x_1 \ln \gamma_1 + x_2 \ln \gamma_2), \quad (4)$$

where  $x_i$ ,  $y_i$  are the concentration of the *i*-component in the liquid and vapour phase of the solution; *P*, *P<sub>i</sub><sup>0</sup>* are, respectively, the saturated vapour pressure of the solution and pure *i*-component; *R* is the universal gas constant; *T*, K. The results of calculations show that for the components of solutions  $\gamma_i < 1$ ,  $\mu_i^e < 0$  for the entire concentration range. An increase in the molecular mass of the second component of solutions is associated with an alternation of negative deviations in the systems' properties. The absolute values of the excess Gibbs energy ( $G^e < 0$ ) decrease for the series of ethylbenzene-benzene, ethylbenzene-toluene solutions and again increase for the ethylbenzene and



**Fig. 1.** Dependence of the excess Gibbs energy (*G<sup>e</sup>*) on the composition of solutions of the systems at *T* = 353 K: 1 – ethylbenzene – benzene; 2 – ethylbenzene – ethylbenzene; 3 – ethylbenzene – n-propylbenzene; 4 – ethylbenzene – n-butylbenzene; *x* – ethylbenzene concentration

n-propylbenzene, ethylbenzene, and n-butylbenzene solutions (Fig. 1). The enthalpies of mixing (excess enthalpies) of solutions ( $H^e$ ) were calculated by equation (5), using experimental and literature data [7, 9, 13]:

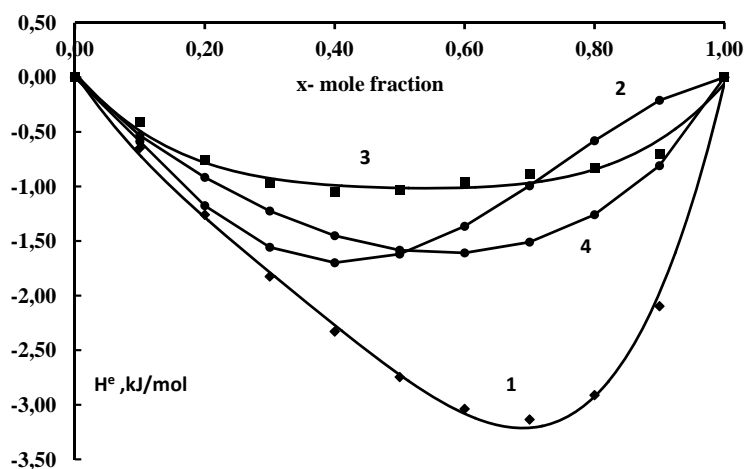
$$H^e = -RT^2 \left[ x_1 \left( \frac{\partial \ln \gamma_1}{\partial T} \right)_{x_2} + (1-x_1) \left( \frac{\partial \ln \gamma_2}{\partial T} \right)_{x_1} \right], \quad (5)$$

where  $\gamma_1, \gamma_2$  are the activity coefficients of ethylbenzene and n-alkylbenzene,  $x_1$  is the mole fraction of ethylbenzene in the mixture,  $R$  is the gas constant. The enthalpy of vaporisation of solutions of the systems ( $H_x$ ) was calculated using equation (6):

$$H_x = H_1^0 x_1 + H_2^0 (1-x_1) + H^e, \quad (6)$$

where  $H_1^0, H_2^0$  are the enthalpies of vaporisation of the pure components  $H^e$  is the excess enthalpy of the solution,  $x_1$  is the mole fraction of ethylbenzene in the mixture [13, 14]. When the components are mixed, in solutions of the systems, we can observe exothermic heat effects ( $H^e < 0$ ). This value also alternates with an increase in the molar mass of the second component (Fig. 2). The values of the excess entropy of solutions of the systems ( $S^e$ ) were calculated using the Gibbs equation. By analysing the obtained data, we determined that the concentration relation of the excess entropy  $S^e = f(x)$  of solutions symbatically imitates the isotherm  $H^e = f(x)$  (Table 2). This can be explained by the affinity of the mechanisms for structuring solutions of the systems characterised by correlation distribution functions [15, 16]. In the Gibbs equation, the predominance of the en-

thalpy component over its entropy component causes negative deviations in the properties ( $G^e < 0$ ) of solutions of the systems (Table 2). We did not manage to formulate an equation representing the relation between the values of the Gibbs energy, enthalpy, and entropy of solutions (calculated using the standard of an ideal solution) and the molar mass and composition of the components of solutions. Calculating the properties of solutions based on the properties of ideal solutions makes it difficult to assess the intermolecular interaction (IMI) in solutions. It should be noted that in pure liquids IMI sometimes has a more complex nature than in solutions [15, 16]. The choice of the standard state proposed by Lewis makes the assessment of IMI in solutions insensitive. For example, for an individual liquid in equilibrium with vapour, the Gibbs energy change is:  $\Delta G = G_{\text{vapour}} - G_{\text{liq}} = 0$ . Back in 1935, Rakovskii wrote that "the path of the Lewis' school is practically useful, but it began to dominate researchers, obscuring the theoretical side of thermodynamics from them" [17]. A number of researchers (Bell and Gatty, Hirschfelder, Curtiss and Bird, Nikolskii, Rowlinson) noted the insufficiency of the formal description of the thermodynamic properties of solutions, for example, [18, 19, 20]. The studies of these and some other scientists contain interesting attempts to assess the contribution of the intermolecular interactions to changes in the thermodynamic functions of solutions. The possibility of developing a general approach to assessing the contribution of the IMI



**Fig. 2.** Dependence of the excess enthalpy ( $H^e$ ) on the composition of solutions of the systems at  $T = 353$  K: 1 – ethylbenzene – benzene; 2 – ethylbenzene – ethylbenzene; 3 – ethylbenzene – n-propylbenzene; 4 – ethylbenzene – n-butylbenzene;  $x$  – ethylbenzene concentration

to thermodynamic functions based on these ideas was considered by Rudakov and the author of this study in works [13, 21–24]. It is known that the laws of thermodynamics do not contain the concepts of interaction. These concepts come from other areas. Using statistical methods, equations of state, mechanical analogies, we can get an idea of the interaction between molecules and assess its influence at thermodynamic parameters. Usually, the energy of intermolecular interaction is defined as the work of molecular separation over an infinite distance. However, the issue may be solved another way. Molecules may be isolated from interacting with each other by introducing an external energy field while maintaining the distance between them. If the energies of the “isolated” and “separated” molecules are equal, then the same work is required to block the intermolecular interaction in both cases. In a thermodynamic system, the calculation results also depend on the manner the process is carried out: whether intermolecular interaction is blocked by expanding the system to a volume of  $V \rightarrow \infty$ , or at  $V = \text{const}$ . The number of ways to carry out the process increases indefinitely if we take into account the intermediate cases (between  $V \rightarrow \infty$  and  $V = \text{const}$ ), as well as the cases of different heat exchange with the environment. It is not enough to say that a standard system without intermolecular interaction is an ideal gas; it is necessary to determine its state accurately. First of all, it is necessary to exclude work done against any forces, except for intermolecular interaction, which leads to the condition  $V = \text{const}$ . Then we have two options: 1) adiabatic option,  $S = \text{const}$ ; 2) isothermal option ( $T = \text{const}$ ) – when the system’s entropy changes due to intermolecular interaction, not temperature. These considerations explain the need to carry out the process under the condition  $V, T = \text{const}$ . We assumed two provisions: the first defines the standard state of the system; the second defines the contributions of intermolecular interaction to the change in the thermodynamic functions of a liquid system.

1. The standard state of a system without intermolecular interaction at any degree of compression is an ideal gas at temperature ( $T$ ), volume ( $V$ ), and with the composition of a real liquid.

2. The contributions of intermolecular interactions to the change in the thermodynamic

function are determined as the difference between the values of this function for standard and real liquid systems:

$$F^r = F^* - F, \quad (7)$$

where  $F^r$  is the contribution of intermolecular interaction to the change in the thermodynamic function,  $F$  – in the real state;  $F^*$  – in the state of an ideal gas, is considered to be the standard state for the system. By deduction of  $F^* - F$ , we obtain positive values of  $F^r$ . It should be noted that when intermolecular interaction in a liquid is blocked, the sign of  $F^r$  changes.

Let’s consider a binary liquid solution at temperature ( $T$ ), in equilibrium with a saturated vapour at pressure ( $P$ ). The molar Helmholtz energy of a binary solution ( $A$ ) is defined as follows:

$$A = x_1\mu_1 + x_2\mu_2 - PV, \quad (8)$$

where  $x_1$  and  $x_2$  are mole fractions;  $\mu_1$  and  $\mu_2$  are the chemical potentials of the solution components  $P$ ,  $V$  are the saturated vapour pressure and the molar volume of the solution. For the chemical potential of the solution component, we have:

$$\mu_i = \mu_i^0 + RT \ln \bar{p}_i, \quad (9)$$

where  $\mu_i^0$  is a function that depends only on the temperature;  $\bar{p}_i$  is the partial pressure of the  $i$ -component in the solution. Since we do not know the absolute values of the Helmholtz energy, we take as the standard state of the system a mixture of ideal gases of the same concentration as a liquid binary solution, at the same temperature ( $T$ ), and with the same molar volume ( $V$ ). The pressure in this standard state is defined as  $P^* = RT/V$ , when the molar Helmholtz energy is defined as ( $A^*$ ):

$$A^* = x_1\mu_1^* + x_2\mu_2^* - RT, \quad (10)$$

where  $\mu_1^*$ ;  $\mu_2^*$  are the chemical potentials of 1 and 2 components in the standard state of the mixture;  $R$  is the universal gas constant. For the chemical potential of a component in the standard state of an ideal gas, we have:

$$\mu_i^* = \mu_i^0 + RT \ln(x_i P^*). \quad (11)$$

As  $P^* = RT/V$ , equation (11) rearranges to the following:

$$\mu_i^* = \mu_i^0 + RT \ln \frac{x_i RT}{V}. \quad (12)$$

We define the contribution of the intermolecular interaction to the change in the mole Helmholtz energy ( $A^r$ ) as a difference of its values in the standard and real states of the system:

$$A^r = A^* - A = x_1(\mu_1^* - \mu_1) + x_2(\mu_2^* - \mu_2) - RT + PV. \quad (13)$$

Substituting expressions for chemical potentials (9, 12) into equation (13) and dividing by  $RT$  (which makes the equation dimensionless), we obtain:

$$\frac{A^r}{RT} = x_1 \ln \frac{x_1 RT}{p_1 V} + x_2 \ln \frac{x_2 RT}{p_2 V} - 1 + \frac{PV}{RT}, \quad (14)$$

where  $p_1, p_2$  are the partial pressure values of 1 and 2 components of the solution. In the extreme cases for pure  $x_1 = 1$  ( $x_2 = 0$ ) and  $x_2 = 1$  ( $x_1 = 0$ ) components, we have:

$$\begin{aligned} \frac{A_1^r}{RT} &= \ln \frac{RT}{P_1 V_1} - 1 + \frac{P_1 V_1}{RT}, \\ \frac{A_2^r}{RT} &= \ln \frac{RT}{P_2 V_2} - 1 + \frac{P_2 V_2}{RT}, \end{aligned} \quad (15)$$

where  $P_1, P_2, V_1, V_2$  are the pressure and molar volume of 1 and 2 pure components at  $T$ , respectively.

We define the excess dimensionless molar Helmholtz energy as:

$$\frac{A^e}{RT} \equiv \frac{A^r}{RT} - x_1 \frac{A_1^r}{RT} - x_2 \frac{A_2^r}{RT}. \quad (16)$$

We take into account that activity coefficient of a component of solution is defined as  $\gamma_i$ . When combined with equations (14, 15), equation (16) rearranges as follows:

$$\begin{aligned} \frac{A^e}{RT} &= x_1 \ln \frac{1}{\gamma_1} + x_2 \ln \frac{1}{\gamma_2} + x_1 \ln \frac{V_1}{V} + \\ &+ x_2 \ln \frac{V_2}{V} + \frac{PV - x_1 P_1 V_1 - x_2 P_2 V_2}{RT}. \end{aligned} \quad (17)$$

Let's provide two relations of the excess Gibbs energy ( $G^e$ ) and molar volume ( $V^e$ ) for a binary solution:

$$G^e = RT(x_1 \ln \gamma_1 + x_2 \ln \gamma_2), \quad (18)$$

$$V^e = V - x_1 V_1 + x_2 V_2. \quad (19)$$

Taking into account relations (18, 19), equation (17) rearranges to the following:

$$\begin{aligned} \frac{A^e}{RT} &= \frac{G^e}{RT} - \ln(V^e + x_1 V_1 + x_2 V_2) + x_1 \ln V_1 + \\ &+ x_2 \ln V_2 + \frac{PV^e + x_1 V_1(P - P_1) + x_2 V_2(P - P_2)}{RT}. \end{aligned} \quad (20)$$

Equation (20) establishes the relation between the values of the excess Gibbs energy ( $G^e$  – calculated using the standard of an ideal solution) and the Helmholtz energy ( $A^e$  – calculated using the standard state of an ideal gas). Using the known thermodynamic relations for internal energy ( $U^r$ ) and entropy ( $S^r$ ), we have [1, 12]:

$$S^r = - \left( \frac{\partial A^r}{\partial T} \right)_{v,x}, \quad (21)$$

$$U^r = -T^2 \left( \frac{\partial (A^r / T)}{\partial T} \right)_{v,x}. \quad (22)$$

After differentiation and transformations, we got the following for a binary solution:

$$S^r = \frac{H}{T} - R \left( x_1 \ln \frac{x_1 RT}{p_1 V} + x_2 \ln \frac{x_2 RT}{p_2 V} \right), \quad (23)$$

$$U^r = H - RT + PV, \quad (24)$$

where  $p_1, p_2$  are the partial pressure values of 1 and 2 components of the solution;  $H, V, P$  are the molar enthalpy of vaporisation, molar volume, and saturated vapour pressure of the solution with  $x_i$  mole fractions in it. The values of the functions are interrelated by the Gibbs-Helmholtz equation:  $A^r = U^r - TS^r$ .

The correlation analysis determined that the values of  $A^r$  for n-alkylbenzenes linearly depend on the molar mass of the substance in the homologous series:

$$A^r = 151.5M + 2065, R = 0.9993, \quad (25)$$

where  $M$  is the molar mass of n-alkylbenzene.  $R$  is the correlation coefficient. Equation (25) describes the Helmholtz energy  $A^r$  of n-alkylbenzenes at  $T = 353.15$  K with a precision of  $\pm 50$  J/mol. We can explain the linear dependence of the Helmholtz energy values on the molecular mass of n-alkylbenzene in the homologous series by the “similarity” of the molecular-statistical structure of liquid n-alkylbenzenes, characterised by the correlation distribution functions [16]. If such “similarity of structures” exists, then an increase in the size of molecules of n-alkyl benzenes



should lead to a decrease in the density of the liquid, which is consistent with an increase in the molar volume ( $V$ ) of  $n$ -alkylbenzenes (Table 2). An increase in the Helmholtz energy values  $A^r$  [J/mol] complicates the transition of molecules from the liquid to vapour phase of systems and decreases exponentially the saturated vapour pressure of  $n$ -alkylbenzenes ( $P$ , N/m<sup>2</sup>):

$$A^r = -2468.4 \ln P + 42255, R = 0.9998. \quad (26)$$

The analysis showed that the molar volumes of  $n$ -alkylbenzenes ( $V$ , m<sup>3</sup>/mol) linearly depend on the values of  $A^r$  [J/m] of  $n$ -alkylbenzenes in the homologous series:

$$A^r = 121.8 \cdot 10^6 V + 2229, R = 0.9992. \quad (27).$$

Equations (25–27) can be used to predict the properties of substances in the homologous series of  $n$ -alkylbenzenes. Using equations (14, 23, 24), we calculated the values of  $A^r, U^r, S^r$  of solutions of the systems (Table 2). The internal energy values  $U^r$ , characterising the entire scope of energy spent to block the intermolecular interaction in solutions, raise with the increase in the molecular mass of  $n$ -alkylbenzene in the homologous series of  $n$ -alkylbenzenes. This can be explained by the increase in the role of the molecules of the second component in the intermolecular interaction in solutions of the systems (Fig. 3). The values of the solution entropy  $S^r$ , calculated using the Helmholtz equation, also raise when the molecular mass of  $n$ -alkylbenzene increases

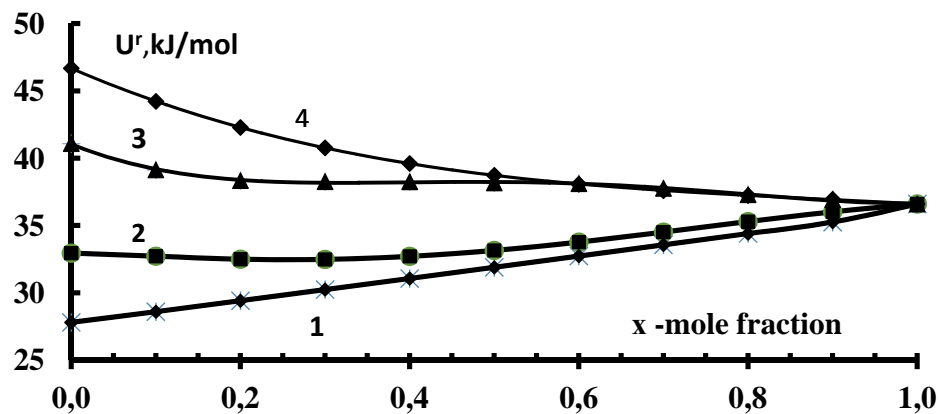


Fig. 3. Dependence of the internal energy of solutions ( $U^r$ ) on the composition of the systems at  $T = 353$  K: 1 – ethylbenzene - benzene; 2 – ethylbenzene - ethylbenzene; 3 – ethylbenzene -  $n$ -propylbenzene; 4 – ethylbenzene -  $n$ -butylbenzene;  $x$  – ethylbenzene concentration

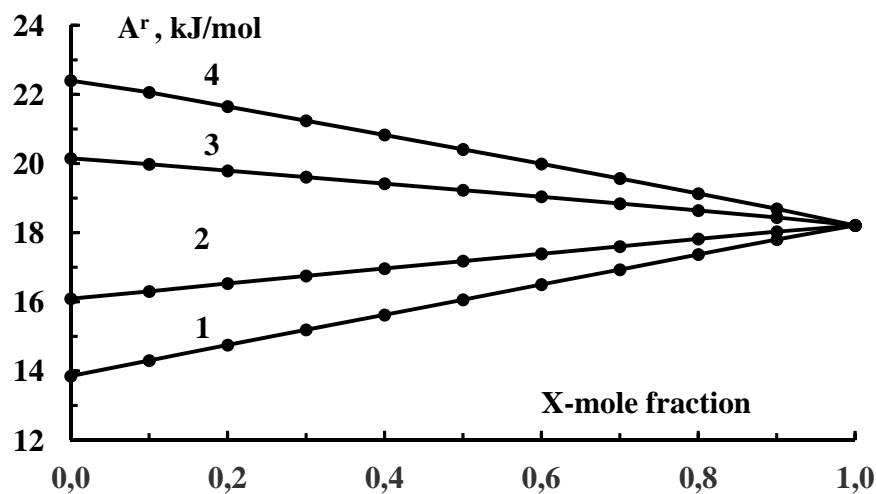


Fig. 4. Dependence of the Helmholtz energy ( $A^r$ ) on the composition of the systems at  $T = 353$  K: 1 – ethylbenzene - benzene; 2 – ethylbenzene - ethylbenzene; 3 – ethylbenzene -  $n$ -propylbenzene; 4 – ethylbenzene -  $n$ -butylbenzene;  $x$  – ethylbenzene concentration

(Table 2). Note that solutions of ethylbenzene and n-alkylbenzene systems demonstrate the sybatic pattern of the isotherms  $U^r = f(X)$  and  $S^r = f(X)$  [21–26]. It is consistent with the previously studied solutions of systems: benzene – n-alkylbenzenes, toluene – n-alkylbenzenes, n-butylbenzene – n-alkylbenzenes, ethanol – n-alkylethanoates, ethanol – n-alkylpropanoates, ethanol – n-alkylbutanoates, n-propanol – n-alkylethanoates, n-propanol, n-butanol, and substances of the homologous series of aliphatic ketones; isopropanol, isobutanol and substances of the homologous series of aliphatic ketones. The values of the Helmholtz energy ( $A^r$ ) for solutions of the systems also increase with an increase in the molecular mass of n-alkylbenzene (Fig. 4). An increase in the values of the Helmholtz energy characterising the intermolecular interactions, decreases the saturated vapour pressure of solutions of the binary systems (Table 2). An analysis of the obtained data showed that for solutions with constant molar concentration ( $x_1 = \text{const}$ ), the Helmholtz energy ( $A^r$ ) linearly depends on the molecular mass ( $M$ ) of n-alkylbenzene:  $A^r = k_i M + b_i$  (Fig. 5). The values of the coefficients  $k_i$  and  $b_i$  of the isotherms  $A^r = k_i M + b_i$  in turn, are linearly dependent on the composition of the systems. The established patterns allowed us to propose the following equation:

$$A^r = (-0.1500x + 0.1513)M + 16.06x + 2.070, \quad (28)$$

where:  $x$  is the mole fraction of ethylbenzene (common solvent) in a binary solution;  $M$  is the

molar mass of n-alkylbenzene. Equation (28) describes the Helmholtz energy ( $A^r$ , kJ/mol) of solutions of the systems at  $T = 353$  K with a precision of  $\pm 50$  J/mol. The established regularity of the change in the Helmholtz energy for solutions of systems of constant molar composition (in the case of pure components, the condition is  $x = 0$ ) can be explained by the “affinity” of the molecular-statistical structure of such solutions [16].

Above, we considered thermodynamic functions that characterise the intermolecular interaction of all molecules in a solution simultaneously. Let’s consider a function that characterises the interaction of one molecule with the rest of the molecules. At  $T, P = \text{const}$ , the following derivative is the partial molar Helmholtz energy:

$$\bar{A}_i^r = \left( \frac{\partial A^r}{\partial x_i} \right)_{T,P}. \quad (29)$$

Taking into account the Gibbs equation:

$$x_1 RT d \ln \bar{p}_1 + x_2 RT d \ln \bar{p}_2 - V dP = 0, \quad (30)$$

where  $\bar{p}_1, \bar{p}_2$  are the partial pressure values of 1 and 2 components in a solution with  $x_1$  mole fractions of 1 component. After transformations, for a binary solution with  $x_1$  mole fractions we have:

$$\bar{A}_i^r = RT \ln \frac{x_i RT}{\bar{p}_i V} - RT \frac{\bar{V}_i}{V} + P \bar{V}_i, \quad (31)$$

where  $\bar{V}_i, \bar{p}_i$  are the partial molar volume and partial pressure, respectfully, of  $i$ -th component

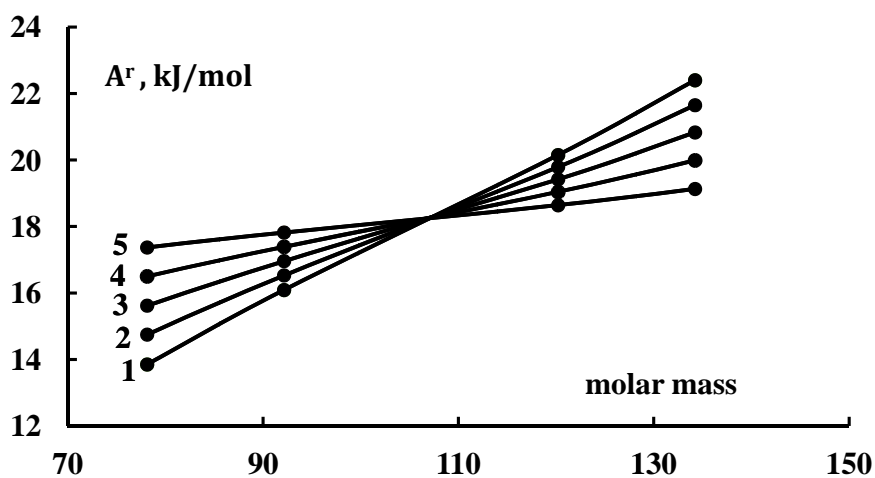
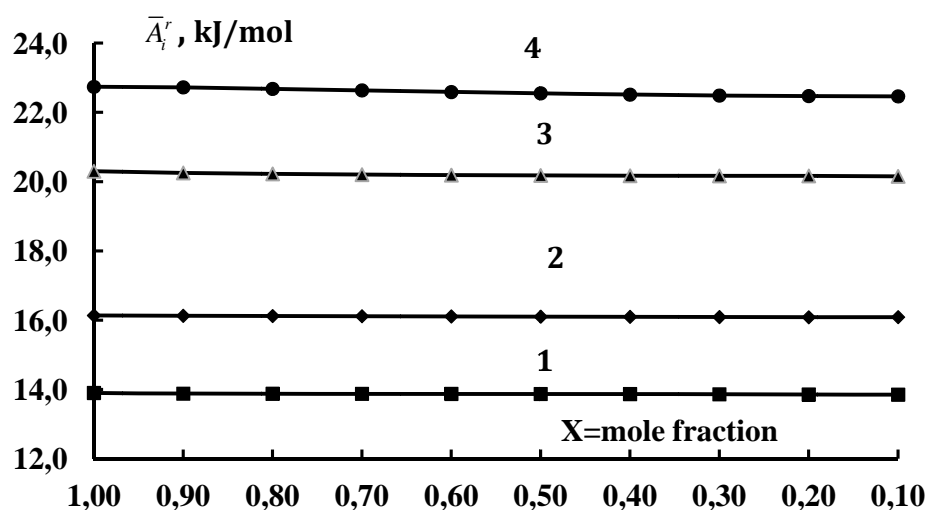


Fig. 5. Dependence of the Helmholtz energy ( $A^r$ ) on the molar mass of n-alkylbenzene the in solutions with a constant molar concentration of the ethylbenzene and n-alkylbenzene systems at  $T = 353$  K: 1 –  $x = 0$ ; 2 –  $x = 0.2$ ; 3 –  $x = 0.4$ ; 4 –  $x = 0.6$ ; 5 –  $x = 0.8$ , which are mole fractions of ethylbenzene



**Fig. 6.** Dependence of values of the partial Helmholtz energy ( $\bar{A}_i^r$ ) of the second component of solution on the composition of the ethylbenzene and n-alkylbenzene systems at  $T = 353$  K: 1 – ethylbenzene - benzene; 2 – ethylbenzene - toluene; 3 – ethylbenzene - n-propylbenzene; 4 – ethylbenzene - n-butylbenzene;  $x$  – ethylbenzene concentration

in a solution with  $x_i$  mole fractions;  $V, P$  are the molar volume and saturated vapour pressure of the solution. Note that at  $x_i = 1$ , equation (31) coincides with the equation for a pure component (15). Using equation (31), we calculated the values of partial molar Helmholtz energy  $\bar{A}_i^r$ . It appeared that the change in the  $\bar{A}_i^r$  value for the molecules of the common solvent (ethylbenzene) was insignificant, and the value of  $\bar{A}_i^r$  for n-alkylbenzene discretely increases with an increase in its molecular mass (the number of  $-\text{CH}_2-$  groups) in the homologous series (Fig. 6). This regularity confirms the validity of the hypothesis underlying the statistical models of solutions, known as “group” models [1, 12]. At  $P, T = \text{const}$ , for the excess partial Helmholtz energy of the  $i$ -th component in a solution consisting of  $x_i$  mass fractions, we obtain:

$$\begin{aligned} \bar{A}_i^e &= A_i^r - \bar{A}_i^r = \\ &= RT \ln \gamma_i - RT \left( \ln \frac{V_i^0}{V} - \frac{\bar{V}_i}{V} + 1 \right) + P_i^0 V_i^0 - P \bar{V}_i, \end{aligned} \quad (32)$$

where  $\gamma_i, V_i^0, P_i^0$  are the activity coefficient, molar volume, and saturated vapour pressure, respectively, of pure  $i$  component;  $V, \bar{V}_i$  are the molar volume of the solution and partial molar volume of the  $i$ -th component in the solution consisting of  $x_i$  mole fractions. There is significant difference between the values of  $\bar{A}_i^e$  and  $RT \ln \gamma_i$  (the values of  $RT \ln \gamma_i$  are often used to assess

the intermolecular interaction in solutions). This difference is associated with a change in the volumes of solutions when mixing components. It is taken into account by the last three terms of equation (32). From the data presented in Table 2, it can be seen that the role of volumetric effects increases with an increase in the molecule size of the solution components. It should be noted that equation (32) can be used to calculate the values of the activity coefficients ( $\gamma_i$ ) of the solution components, often used in chemical technologies.

Then, using the known thermodynamic relations, we can calculate the values of chemical potentials, Gibbs energy, and other thermodynamic functions. It should be noted that equation (28) was earlier obtained for solutions of 160 binary systems, formed by various solvents and substances of various homologous series (for instance, studies [10, 13, 14, 21–26]). The form of equation (28) is the same for a wide temperature range for solutions of all studied binary systems. To derive equation (28) we need the  $P, X, Y, T$  – values and the data on the molar volume ( $V$ ) of pure components (*reference data*) and only two solutions of the same molar composition. The accuracy of calculating the Helmholtz energy for solutions of binary systems according to equation (28) depends only on the accuracy of these experimental data. We believe that the established pattern is of a general nature

and can be used to predict the thermodynamic properties of solutions of binary systems formed by a common solvent and representatives of homologous series of organic substances.

#### 4. Conclusions

1. The values of the Helmholtz energy ( $A'$ ) linearly depend on the molar mass of the substance (the number of  $-\text{CH}_2-$  groups in a molecule) in the homologous series of n-alkylbenzenes.

2. An increase in the Helmholtz energy values ( $A'$ ) for substances in the homologous series of n-alkylbenzenes is associated with a linear increase in the molar volumes of liquid substances and an exponential decrease in the saturated vapour pressure of substances.

3. The Helmholtz energy ( $A'$ ) for binary solutions with constant molar concentration formed by ethylbenzene and substances of the homologous series of n-alkylbenzenes linearly depends on the molar mass of n-alkylbenzene (the number of  $-\text{CH}_2-$  groups) in the homologous series. Equation (28) obtained on the basis of this pattern describes the Helmholtz energy for solutions of the systems with deviations of  $\pm 50$  J/mol from its values calculated from experimental data. The determined pattern confirms the validity of the hypothesis about the additive contribution of functional groups to the thermodynamic properties of solutions, which underlies the statistical models of solutions, known as “group” models.

4. The determined pattern (equation 28) makes it possible to predict the thermodynamic properties of solutions of unexamined binary systems using the properties of pure components and only two solutions with the same molar concentration. It accelerates the process of studying vapour-liquid phase equilibria and thermodynamic properties of binary systems approximately by 340 times. The accuracy of predicting the thermodynamic properties of solutions using equation (28) depends on the accuracy of the experimental data on the properties of pure components and their two solutions.

#### Conflict of interests

The authors declare that they have no known competing financial interests or personal

relationships that could have influenced the work reported in this paper.

#### References

1. Walas S. M. *Phase equilibria in chemical engineering*. Boston: Butterworth-Heinemann; 1985. 581 p.
2. Suntsov Yu. K., Kharchenko G. Yu., Alferova S. I. Liquid–vapor phase equilibria in ternary systems formed by n-alcohols and n-alkyl ethanoates. *Russian Journal of Physical Chemistry A*. 2019;93(3): 594–597. <https://doi.org/10.1134/s0036024419030208>
3. Petlyuk F. B., Serafimov L. A. *Mnogokomponentnaya rektifikatsiya, teoriya i raschet* [Multicomponent rectification, theory and calculation]. Moscow: Khimiya Publ.; 1983. 304 p. (In Russ.)
4. Batuyeva I. Yu., Gayle A. A., Pokonova Yu. V., et al. *Khimiya nefi* [Oil chemistry] Leningrad: Khimiya Publ.; 1984. 360 p. (In Russ.)
5. Becker H, Berger W., et al. *Organikum*. Berlin: VEB Deutscher Verlag der Wissenschaften; 1976. 253 p.
6. Sharlo G. *Metody analiticheskoy khimii*. [Methods of analytical chemistry]. Moscow: Khimiya Publ.; 1965. 667 p. (In Russ.)
7. *TCI American organic chemical 88/89 catalog*. Portland: American Tokyo Kasei; 1988. Available at: <https://webbook.nist.gov/chemistry/form-ser/>
8. *Spravochnik khimika tom 2* [Chemist's Handbook vol. 2] B. P. Nikol'skii (ed.). Moscow: Khimiya Publ.; 1971. 1169 p. (In Russ.)
9. Haynes W. M. *CRC handbook of chemistry and physics* [Electronic resource]. Available at: <https://chemdb.net/ru/reference/A2xZLJnbJe/>
10. Suntsov Yu. K. *Zakonomernosti izmeneniya termodinamicheskikh svoystv binarnykh rastvorov n-alkilpropanoatov* [Regularities of changes in the thermodynamic properties of binary solutions of n-alkyl propanoates]. *Proceedings of Voronezh State University. Series: Chemistry. Biology. Pharmacy*. 2009;1: 42–47. Available at: <http://www.vestnik.vsu.ru/pdf/chembio/2009/01/2009-01-07.pdf> (In Russ., abstract in Eng.)
11. Perelygin V. M., Suntsov Yu. K. *Mashinnyy raschet fazovykh ravnovesiy zhidkost' – par po obshchemu davleniyu para binarnykh system* [Machine calculation of vapour-liquid phase equilibria based on the total vapour pressure of binary systems]. *Izdatel'stvo Vuzov SSSR. Pishchevaya tekhnologiya*. 1974;2: 133–140. (In Russ.)
12. Morachevskii A. G., Smirnova N. A., Piotrovskaya E. M., et al. *Termodinamika ravnovesiya zhidkost' – par*. [Thermodynamics of vapour-liquid equilibrium.] Leningrad: Khimiya Publ.; 1989. 342 p. (In Russ.)
13. Suntsov Yu. K. Liquid-vapor phase equilibria and thermodynamic properties of binary solutions of

n-alkyl benzenes. *Russian Journal of Physical Chemistry* A. 2008;82(4): 530–534. <https://doi.org/10.1007/s11504-008-4004-4>

14. Suntsov Yu. K., Semonov A. A. *Vzaimosvyaz' svoystv chistykh komponentov s fiziko-khimicheskimi i termodinamicheskimi svoystvami binarnykh rastvorov, obrazovannykh n-alkilarenami*. [Relationship between the properties of pure components and the physicochemical and thermodynamic properties of binary solutions formed by n-alkylarenes]. *Kondensirovannye sredy i mezhfaznye granitsy = Condensed Matter and Interphases*. 2004;6(3): 283–288. (In Russ., abstract in Eng.)

15. Belousov O. P., Panov M. Yu. *Termodinamika vodnykh rastvorov neelektrolitov* [Thermodynamics of aqueous solutions of nonelectrolytes]. Leningrad: Khimiya Publ.; 1983. 264 p. (In Russ.)

16. Skryshevskiy A. F. *Strukturnyy analiz zhidkostey* [Structural analysis of liquids]. Moscow: Vysshaya Shkola Publ.; 1971. 254 p. (In Russ.)

17. Rakovskiy A. V. *Predisloviye k knige: I. D. Van-der-Vaal's, F. Konstamm. Kurs termostatiki* [Preface to the book: I. D. Van der Waals, F. Konstamm. Thermostatics course]. Moscow: 1936. 452 p. (In Russ.)

18. Hirschfelder J. O., Curtiss Ch. F., Bird R. B. *Molecular theory of gases and liquids*. New York: Wiley; London: Chapman and Hall; 1954. 1219 p. Available at: <https://science.sciencemag.org/content/120/3131/1097.1>

19. Rowlinson J. B. *Liquids and liquid mixtures*. London; 1959. 360 p.

20. Nikol'skii B. P. *Znachenie ucheniya o rastvorakh dlya razvitiya teorii ionnogo obmena* [The importance of the theory of solutions for the development of the theory of ion exchange]. *Vestn. Leningr. un-ta. Fizika. Khimiya* [Bulletin of Leningrad State University]. 1960;22(4): 11–24. (In Russ.)

21. Rudakov E. S. *Molekulyarnaya, kvantovaya i evolyutsionnaya termodinamika* [Molecular, Quantum and Evolutionary Thermodynamics]. Donetsk: Nat. acad. Sciences of Ukraine. Inst Fiz. -Organ. Chemistry and Coal Chemistry them. L. M. Litvinenko, Ministry of Education of Ukraine; 1998. 139 p. (In Russ.)

22. Suntsov Yu. Legitimacies change of properties of binary systems on an example of solutions formed by aliphatic alcohol and complex ethers of organic acids. In: *Thermodynamics-2003. Proc. 18th Int. Conf., Apr. 9–11, 2003*. England, Cambridge: University of Cambridge; 2003. 99 p.

23. Suntsov Yu. K. *Zakonomernosti izmeneniya svoystv binarnykh sistem na primere rastvorov, obrazovannykh n-spirtami i slozhnymi efirmi*

*organicheskikh kislot* [Regularities of changes in the properties of binary systems by the example of solutions formed by n-alcohols and esters of organic acids]. Thesis of Doc. Chem. Sci. Moscow: 2004. 697 p. Available at: <https://www.dissercat.com/content/zakonomernosti-izmeneniya-termodinamicheskikh-svoystv-binarnykh-sistem-obrazovannykh-n-spirt> (In Russ.)

24. Suntsov Yu. K. New method of predicting the thermodynamic properties of solutions. *Journal of Chemistry and Chemical Engineering*. 2014;8(3): 306–314. <https://doi.org/10.17265/1934-7375/2014.03.013>

25. Kharchenko G. Yu. *Fazovyye ravnovesiya i termodinamicheskiye svoystva rastvorov, obrazovannykh n-alifaticeskimi spirtami i slozhnymi efirmi uksusnoy kisloty* [Phase equilibria and thermodynamic properties of solutions formed by n-aliphatic alcohols and acetic acid esters]. Thesis of Cand. Chem. Sci. St. Petersburg: 2004. 236 p. Available at: <https://www.dissercat.com/content/fazovyye-ravnovesiya-i-termodinamicheskiye-svoystva-rastvorov-obrazovannykh-n-alifaticeskimi> (In Russ.)

26. Vlasov M. V. *Fazovyye ravnovesiya i termodinamicheskiye svoystva binarnykh sistem, obrazovannykh spirtami i alifaticeskimi ketonami* [Phase equilibria and thermodynamic properties of binary systems formed by alcohols and aliphatic ketones]. Thesis of Cand. Chem. Sci. Voronezh: 2013. 238 p. Access mode: <https://www.dissercat.com/content/fazovyye-ravnovesiya-i-termodinamicheskiye-svoystva-binarnykh-sistem-obrazovannykh-spirtami-i> (In Russ.)

## Information about the authors

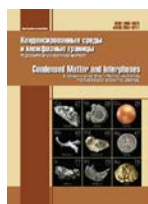
*Yuri K. Suntsov*, DSc in Chemistry, Professor at the Department of Physical Chemistry, Voronezh State University, Voronezh, Russian Federation; e-mail: [jsyntsov@mail.ru](mailto:jsyntsov@mail.ru). ORCID iD: <https://orcid.org/0000-0001-6408-8919>.

*Nina S. Suntsova*, engineer at the Department of Physical Chemistry, Voronezh State University, Voronezh, Russian Federation; e-mail: [suntsova.nina@bk.ru](mailto:suntsova.nina@bk.ru). ORCID iD: <https://orcid.org/0000-0002-1421-4830>.

All authors have read and approved the final manuscript.

*Received 3 February 2021; Approved after reviewing 15 February 2021; Accepted 15 March 2021; Published online 25 March 2021.*

*Translated by Anastasiia Ananeva  
Edited and proofread by Simon Cox*



# Condensed Matter and Interphases

Kondensirovannye Sredy i Mezhfaznye Granitsy  
<https://journals.vsu.ru/kcmf/>

## Original articles

Original article

<https://doi.org/10.17308/kcmf.2021.23/3309>

## Synthesis of bismuth ferrite nanopowder doped with erbium ions

E. V. Tomina<sup>1,2✉</sup>, A. A. Pavlenko<sup>2</sup>, N. A. Kurkin<sup>2</sup>

<sup>1</sup>Voronezh State University of Forestry and Technologies named after G. F. Morozov,  
8 Timiryazeva ul., Voronezh 394087, Russian Federation

<sup>2</sup>Voronezh State University,  
1 Universitetskaya pl., Voronezh 394018, Russian Federation

### Abstract

The potential for the practical application of bismuth ferrite (BFO) in information storage, microelectronic, and spintronic devices and in medical sensors of various purpose is limited by the presence of a spin cycloid. Its destruction, including destruction due to doping with rare earth elements and the transfer of BFO to a nanoscale state, contributes to the occurrence of ferromagnetism and the manifestation of the magnetoelectric effect. The study was aimed at the synthesis of bismuth ferrite nanopowder doped with erbium ions.

By spray pyrolysis at a temperature of 760 °C, we synthesised BFO samples with a nominal degree of doping with erbium ions from 0.05 to 0.20. The data of X-ray diffraction analysis show that there is a small amount of  $\text{Bi}_{25}\text{FeO}_{39}$  and  $\text{Bi}_2\text{Fe}_4\text{O}_9$  in the doped samples. The shift of the BFO reflections on diffraction patterns towards larger  $2\theta$  angles is representative of the incorporation of erbium ions into the crystal lattice of  $\text{BiFeO}_3$ . The morphological characteristics of the samples were determined using transmission electron microscopy. According to the data of electron probe X-Ray microanalysis, the real composition of the doped  $\text{Er}_x\text{Bi}_{1-x}\text{FeO}_3$  samples is very close to the nominal.

The particles of  $\text{Er}_x\text{Bi}_{1-x}\text{FeO}_3$  powders synthesised by spray pyrolysis have a nearly spherical shape, the particle-size distribution is in the range of 5–300 nm, the predominant number of particles have a size in the range of 50–200 nm, and the agglomeration is weak. The decrease in the crystal lattice parameters and the unit cell volume of  $\text{Er}_x\text{Bi}_{1-x}\text{FeO}_3$  and an increase in the degree of doping with erbium ions confirm the incorporation of  $\text{Er}^{3+}$  into the BFO crystal lattice to the bismuth position.

**Keywords:** Nanopowders, Bismuth ferrite, Multiferroics, Doping

**Acknowledgements and financial support:** the research results were partially obtained using the equipment of Shared Scientific Equipment Centre of Voronezh State University. URL: <http://ckp.vsu.ru>.

**For citation:** Tomina E. V., Pavlenko A. A., Kurkin N. A. Synthesis of bismuth ferrite nanopowder doped with erbium ions. *Kondensirovannye sredy i mezhfaznye granitsy = Condensed Matter and Interphases*. 2021;23(1): 93–100. <https://doi.org/10.17308/kcmf.2021.23/3309>

**Для цитирования:** Томина Е. В., Павленко А. А., Куркин Н. А. Синтез нанопорошка феррита висмута, допированного ионами эрбия. *Конденсированные среды и межфазные границы*. 2021;23(1): 93–100. <https://doi.org/10.17308/kcmf.2021.23/3309>

✉ Elena V. Tomina, e-mail: [tomina-e-v@yandex.ru](mailto:tomina-e-v@yandex.ru)

© Tomina E. V., Pavlenko A. A., Kurkin N. A., 2021



The content is available under Creative Commons Attribution 4.0 License.

## 1. Introduction

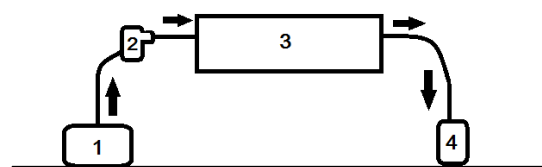
Among multiferroic materials, bismuth ferrite  $\text{BiFeO}_3$  is particularly interesting. The symmetry of the BFO crystal allows the presence of the linear magnetoelectric effect and weak ferromagnetism at room temperature [1–5]. However, bismuth ferrite in bulk state is characterised by a spin cycloid in its magnetic structure, with the period of 62 nm. It completely eliminates the weak ferromagnetism of BFO and prevents the appearance of the linear magnetoelectric effect. The inhomogeneity of the magnetoelectric interaction leads to the induction of spatial spin modulation of spontaneous electric polarisation. In the first approximation, the degree of rhombohedral distortion of the cell, the  $c/a$  ratio, can be a criterion for the degree of polarisation. To destroy the spin cycloid, it is necessary to decrease the  $c/a$  ratio, thereby reducing the degree of polarisation, which results in a change in the spin structure [6–11]. The synthesis of BFO by the solid-phase method is a rather challenging task, since the  $\text{Bi}_2\text{O}_3$ – $\text{Fe}_2\text{O}_3$  system is characterised by the formation of 3 intermediate phases:  $\text{Bi}_{25}\text{FeO}_{39}$ ,  $\text{BiFeO}_3$ , and  $\text{Bi}_2\text{Fe}_4\text{O}_9$ ; single-phase  $\text{BiFeO}_3$  exists in a very narrow range of compositions, temperature, and pressure [12–16]. A decrease in the impurity content in BFO requires long-term heat treatment, which is accompanied by an increase in the particle size of the target product. Unlike the solid-phase method, the synthesis of nanopowders by spray pyrolysis of aerosols has such advantages as sufficiently high productivity, purity of the target product, the ability to control morphology, and low energy consumption. Therefore, the study was aimed at the synthesis of  $\text{BiFeO}_3$  by spray pyrolysis with different degrees of doping with  $\text{Er}^{3+}$  ions.

## 2. Experimental

In this work, crystalline hydrates of  $\text{Fe}(\text{NO}_3)_3 \cdot 9\text{H}_2\text{O}$  (p.a. TU 6-09-02-553-96),  $\text{Bi}(\text{NO}_3)_3 \cdot 5\text{H}_2\text{O}$  (p.a. CAS 10035-06-0),  $\text{Er}_2(\text{SeO}_4)_3 \cdot 8\text{H}_2\text{O}$  (pur. TU 1083-63), tartaric acid  $\text{C}_4\text{H}_6\text{O}_6$  (GOST 5817-77), and nitric acid  $\text{HNO}_3$  (GOST 4461-77) were used as precursors. The samples were synthesised by the spray pyrolysis method similar to the procedure described in [17]. During the synthesis of erbium-doped bismuth ferrite, the concentration values of bismuth and erbium ions were calculated using the stoichiometric ratio:  $\text{Er}^{3+} : \text{Bi}^{3+} : \text{Fe}^{3+} = x : (1-x) : 1$ ,

where  $x = 0.05, 0.10, 0.15, 0.20$  is the nominal doping degree.

In accordance with this ratio, crystalline hydrates of erbium selenate, iron nitrate, and bismuth nitrate were dissolved in nitric acid. Tartaric acid  $\text{C}_4\text{H}_6\text{O}_6$ , taken at the rate of 3 moles of acid per 2 moles of metal ions, was dissolved in distilled water and added to a solution of metal nitrates. To carry out the synthesis, a laboratory spray pyrolysis unit was assembled (Fig. 1). The prepared solution was placed in a dispersant, where it was transformed into an aerosol with a particle size of 0.8 to 2.0  $\mu\text{m}$  and was transferred by an air flow into the reaction chamber of an MTP-2M furnace, the hottest part of which was heated to 760 °C. The temperature was controlled by an OVEN TRM1-Shch1.U.R thermostat with an error of  $\pm 1$  °C. The flow rate was 9 l/h. Aerosol particles were in the reaction zone for about 0.6 s. Influenced by the high temperature, the aerosol pyrolytically decomposed with the formation of the target product. The particles were collected by passing the gas through a glass of distilled water, then they were filtered off, and dried in air.



**Fig. 1.** The layout of the spray pyrolysis unit: 1 – compressor, 2 – dispersant, 3 – MTP-2M furnace, 4 – a glass of distilled water to collect the nanopowder

The phase composition of the synthesised powders  $\text{BiFeO}_3$ ,  $\text{BiFeO}_3:\text{Er}^{3+}(5\%)$ , and  $\text{BiFeO}_3:\text{Er}^{3+}(10\%)$  was determined by X-ray diffraction analysis (XRD), using a RIGAKU SmartLab III X-ray diffractometer with a Co anode ( $\lambda = 1.79030$  nm). The measurement was performed with a step of 0.010. To study the phase composition of  $\text{BiFeO}_3:\text{Er}^{3+}(15\%)$  and  $\text{BiFeO}_3:\text{Er}^{3+}(20\%)$  by XRD, we used an Empyrean B.V. X-ray diffractometer with a Cu anode ( $\lambda = 1.54060$  nm). The scanning was performed within a  $2\theta$  angle range of 10 to 80° with a step of 0.0200. The size of the coherent scattering regions (CSR) based on the XRD data of the synthesised bismuth ferrite samples was calculated using the Scherrer formula [18]:

$$D_{hkl} = \frac{k\lambda}{\beta_{hkl} \times \cos\theta},$$

where:  $D_{hkl}$  – average particle size, Å,  $k$  – correction factor (for cubic and orthorhombic structure  $k=0.9$ ),  $\lambda$  – X-ray tube wavelength,  $\theta$  – the position of the peak maximum, deg.,  $\beta_{hkl}$  – intrinsic physical broadening of the diffraction maximum, rad.

The quantitative elemental composition of the synthesised samples was determined by electron probe X-Ray microanalysis (EPXMA, scanning electron microscope JEOL-6510LV with a Bruker energy dispersive microanalysis system).

The size and morphology of BFO powder particles were determined using the results of transmission electron microscopy (TEM, Carl Zeiss Libra-120 transmission electron microscope).

For a semi-quantitative assessment of the content of impurity phases in the synthesised BFO nanopowders, we conducted a semi-quantitative analysis of the diffraction patterns by the corundum number method using the

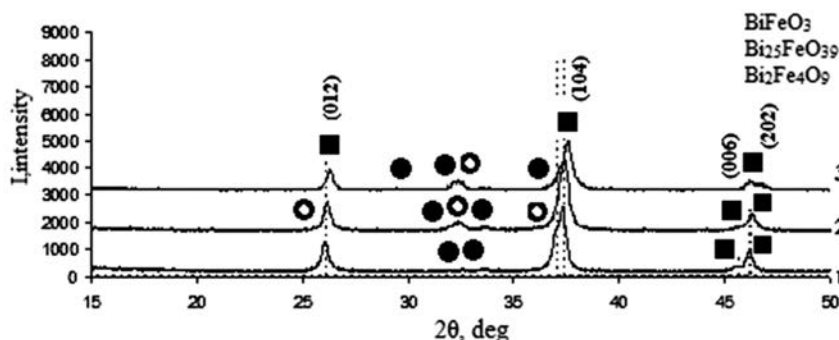
formula:

$$\omega_k = \frac{\frac{I_k^{\max}}{RIR_k}}{\sum_i \frac{I_i^{\max}}{RIR_i}},$$

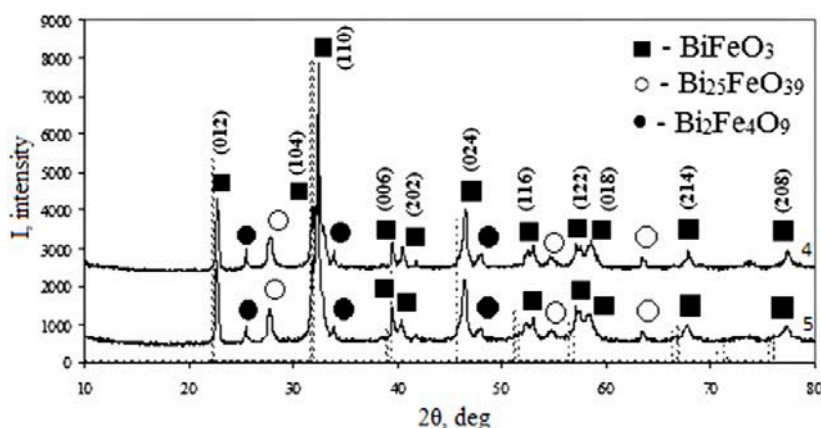
where:  $\omega_k$  – mass fraction of phase  $k$ ,  $I_k^{\max}$  – intensity of the largest reflection of phase  $k$ ,  $RIR_k$  – corundum number of phase  $k$ ,  $I_i^{\max}$  – intensity values of the largest reflections of  $i$ -phases,  $RIR_i$  – corundum number of  $i$ - phases.

### 3. Results and discussion

The data of X-ray phase analysis (Figs. 2 and 3) shows that the synthesised samples are mainly bismuth orthoferrite  $\text{BiFeO}_3$  (card number 73-0548) [19]. However, there are single reflections of the  $\text{Bi}_{25}\text{FeO}_{39}$  and  $\text{Bi}_2\text{Fe}_4\text{O}_9$  phases (card numbers 46-0416, 72-1832). A semi-quantitative assessment of the content of impurity phases in the synthesised samples by the corundum number method demonstrates a tendency for the increase in the amount of  $\text{Bi}_{25}\text{FeO}_{39}$  and  $\text{Bi}_2\text{Fe}_4\text{O}_9$  with an increase



**Fig. 2.** X-ray diffraction patterns of the samples of  $\text{BiFeO}_3$  (1),  $\text{BiFeO}_3:\text{Er}^{3+}$  (5 %) (2), and  $\text{BiFeO}_3:\text{Er}^{3+}$  (10 %) (3). The reflections of the  $\text{BiFeO}_3$  reference sample are indicated by the dotted line (card number 73-0548)



**Fig. 3.** X-ray diffraction pattern of the  $\text{BiFeO}_3:\text{Er}^{3+}$  (15%) (4) sample and X-ray diffraction pattern of the  $\text{BiFeO}_3:\text{Er}^{3+}$  (20 %) (5) sample. The reflections of the  $\text{BiFeO}_3$  reference sample are indicated by the dotted line (card number 73-0548)



in the degree of doping of BFO with  $\text{Er}^{3+}$  ions (Table 1), which may be associated with an increase in distortions of the crystal lattice of bismuth ferrite.

When the diffraction patterns recorded using the same diffractometer are superposed (Fig. 2 and Fig. 3, respectively), we can see a shift of the reflections of erbium-doped BFO samples toward larger  $2\theta$  angles compared to the undoped  $\text{BiFeO}_3$  sample. It indicates a distortion of the crystal lattice caused by the incorporation of an ion with a smaller ionic radius to the position of an ion with a larger ionic radius [20]. Since the  $\text{Er}^{3+}$  ion radius is 0.089 nm, and the  $\text{Bi}^{3+}$  and  $\text{Fe}^{3+}$  ion radii are 0.120 nm and 0.064 nm, respectively [21], it can be assumed that erbium is incorporated into the ferrite lattice to the position of bismuth. This is confirmed by a decrease in the parameters of the crystal lattice and the unit cell volume in relation to an increase in the degree of doping of bismuth ferrite with erbium ions (Table 2).

The energy dispersive spectra of the synthesised  $\text{Er}_x\text{Bi}_{1-x}\text{FeO}_3$  samples record not only the signals of Bi, Fe, and O, but also Er (Fig. 4), which also confirms that erbium ions incorporate into the BFO lattice. With an increase in the degree of doping of bismuth ferrite, the intensity of erbium signals in the synthesised samples expectedly increases. Nevertheless, the real composition of the synthesised samples of  $\text{BiFeO}_3:\text{Er}^{3+}$  (5 %),  $\text{BiFeO}_3:\text{Er}^{3+}$  (10 %), and  $\text{BiFeO}_3:\text{Er}^{3+}$  (15 %) is slightly different from the nominal (Table 3), which is explained by the presence of a certain amount of  $\text{Bi}_{25}\text{FeO}_{39}$  and  $\text{Bi}_2\text{Fe}_4\text{O}_9$  impurity phases in doped BFO nanopowders.

The size assessment CSR based on the XRF data is provided in Table 4. The average CSR of  $\text{Er}_x\text{Bi}_{1-x}\text{FeO}_3$  sample particles is within the range of 19 to 27 nm, it slightly raises with an increase in the nominal degree of BFO doping with  $\text{Er}^{3+}$  ions from 0.05 to 0.20.

**Table 1.** The composition of the synthesised samples, calculated by the method of corundum numbers

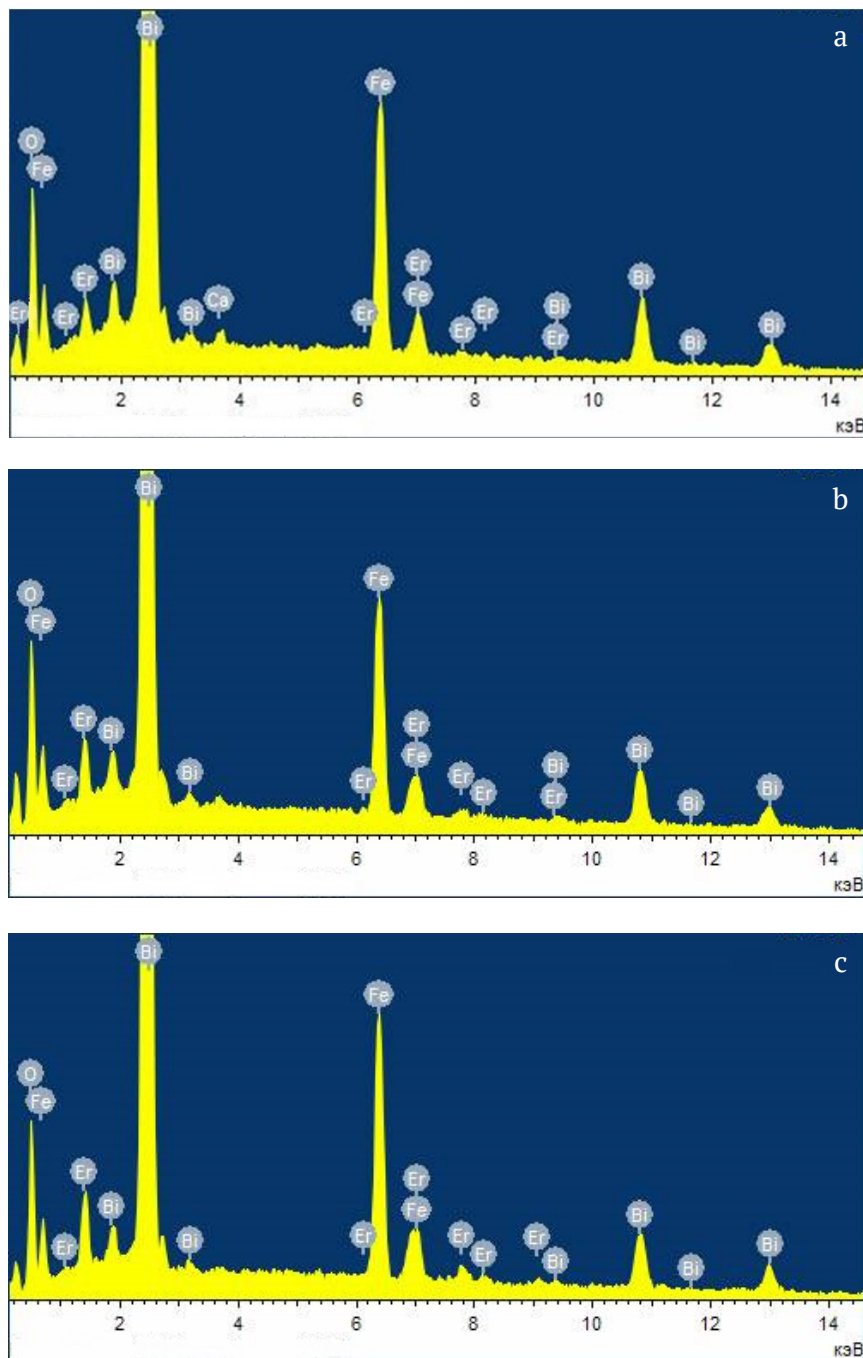
Phase, wt. %	Samples				
	$\text{BiFeO}_3$	$\text{BiFeO}_3:\text{Er}^{3+}$ (5 %)	$\text{BiFeO}_3:\text{Er}^{3+}$ (10 %)	$\text{BiFeO}_3:\text{Er}^{3+}$ (15 %)	$\text{BiFeO}_3:\text{Er}^{3+}$ (20 %)
$\text{BiFeO}_3$	95.7 %	84.3 %	72.6 %	75.4 %	72.1 %
$\text{Bi}_{25}\text{FeO}_{39}$	0.0 %	12.0 %	19.1 %	15.7 %	16.4 %
$\text{Bi}_2\text{Fe}_4\text{O}_9$	4.3 %	3.7 %	8.3 %	8.9 %	11.5 %

**Table 2** The lattice parameters and unit cell volume of  $\text{BiFeO}_3$  samples:  $\text{BiFeO}_3:\text{Er}^{3+}$  (5 %),  $\text{BiFeO}_3:\text{Er}^{3+}$  (10 %),  $\text{BiFeO}_3:\text{Er}^{3+}$  (15 %), and  $\text{BiFeO}_3:\text{Er}^{3+}$  (20 %), synthesised by spray pyrolysis (calculated for hexagonal packing)

Lattice parameters	Reference sample, $\text{BiFeO}_3$ Card 73-0548	$\text{BiFeO}_3$	$\text{BiFeO}_3:\text{Er}^{3+}$ (5 %)	$\text{BiFeO}_3:\text{Er}^{3+}$ (10 %)	$\text{BiFeO}_3:\text{Er}^{3+}$ (15 %)	$\text{BiFeO}_3:\text{Er}^{3+}$ (20 %)
$a$ , Å	5.58	5.58	5.56	5.55	5.46	5.44
$c$ , Å	13.90	13.85	13.82	13.71	13.67	13.66
$V$ , Å <sup>3</sup>	374.81	373.41	370.68	369.09	352.71	350.75

**Table 3.** Results of the electron probe X-Ray microanalysis for the samples of  $\text{BiFeO}_3:\text{Er}^{3+}$  (5 %),  $\text{BiFeO}_3:\text{Er}^{3+}$  (10 %), and  $\text{BiFeO}_3:\text{Er}^{3+}$  (15%)

Nominal composition of samples (N)		$\text{Er}_{0.05}\text{Bi}_{0.95}\text{FeO}_3$	$\text{Er}_{0.10}\text{Bi}_{0.90}\text{FeO}_3$	$\text{Er}_{0.15}\text{Bi}_{0.85}\text{FeO}_3$	
Elemental composition, at. %	Er	H	1.00	2.00	3.00
		P	1.17	2.24	3.32
	Bi	H	19.00	18.00	17.00
		P	18.07	18.00	15.72
	Fe	H	20.00	20.00	20.00
		P	20.09	19.76	20.96
	O	H	60.00	60.00	60.00
		P	59.83	60.00	60.00
Real composition of samples (R)		$\text{Er}_{0.05}\text{Bi}_{0.90}\text{FeO}_{2.98}$	$\text{Er}_{0.11}\text{Bi}_{0.91}\text{FeO}_3$	$\text{Er}_{0.16}\text{Bi}_{0.75}\text{FeO}_{2.86}$	



**Fig. 4.** The energy dispersive spectra of the samples: a)  $\text{BiFeO}_3:\text{Er}^{3+}$  (5 %); b)  $\text{BiFeO}_3:\text{Er}^{3+}$  (10 %), c)  $\text{BiFeO}_3:\text{Er}^{3+}$  (15 %), synthesised by spray pyrolysis

**Table 4.** CSR values of particles of the  $\text{Er}_x\text{Bi}_{1-x}\text{FeO}_3$  samples synthesised by spray pyrolysis

CSR diameter of particles, nm	$\text{BiFeO}_3$	$\text{Er}_{0.05}\text{Bi}_{0.95}\text{FeO}_3$	$\text{Er}_{0.10}\text{Bi}_{0.90}\text{FeO}_3$	$\text{Er}_{0.15}\text{Bi}_{0.85}\text{FeO}_3$	$\text{Er}_{0.20}\text{Bi}_{0.80}\text{FeO}_3$
$D_1$	$22 \pm 2$	$22 \pm 2$	$22 \pm 2$	$26 \pm 3$	$30 \pm 3$
$D_2$	$14 \pm 1$	$16 \pm 2$	$16 \pm 2$	$21 \pm 2$	$26 \pm 3$
$D_3$	$18 \pm 2$	$18 \pm 2$	$23 \pm 2$	$23 \pm 2$	$26 \pm 3$
$D_{\text{cp}}$	$18 \pm 2$	$19 \pm 2$	$20 \pm 2$	$23 \pm 2$	$27 \pm 3$

According to the TEM data (Fig. 5), the  $\text{Er}_{0.05}\text{Bi}_{0.95}\text{FeO}_3$  particles have a nearly spherical shape, the particle size does not exceed 300 nm, and the predominant fraction of the particles is in the range of 51–100 nm. For a sample with a higher degree of doping with  $\text{Er}_{0.15}\text{Bi}_{0.85}\text{FeO}_3$ , a weakly pronounced agglomeration is observed (Fig. 6). Although the particle size still does not exceed 300 nm, most of the particles have a size in the range of 101–200 nm.

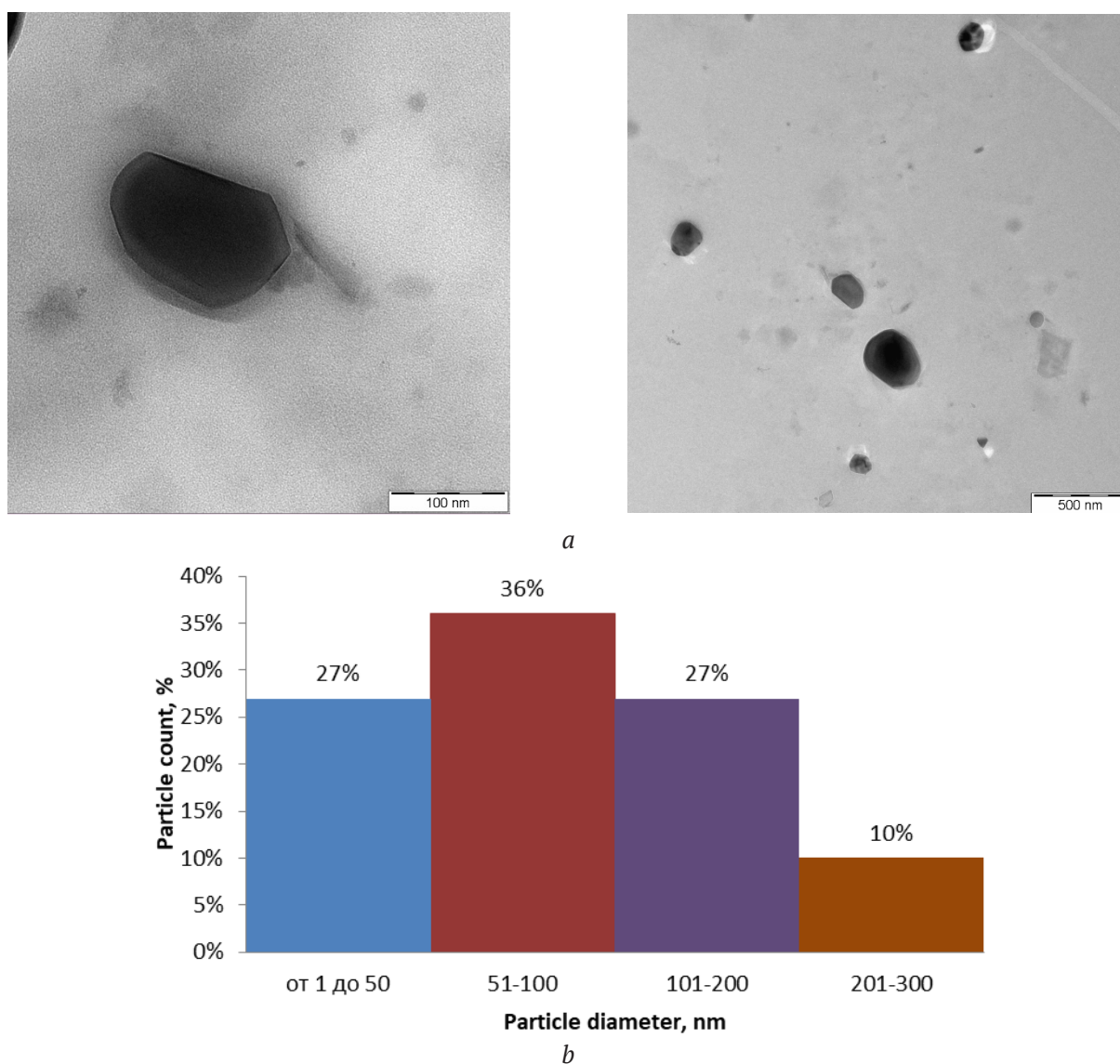
#### 4. Conclusions

We determined that spray pyrolysis makes it possible to synthesise bismuth ferrite nanopowders with various degrees of doping with erbium, which are characterised by

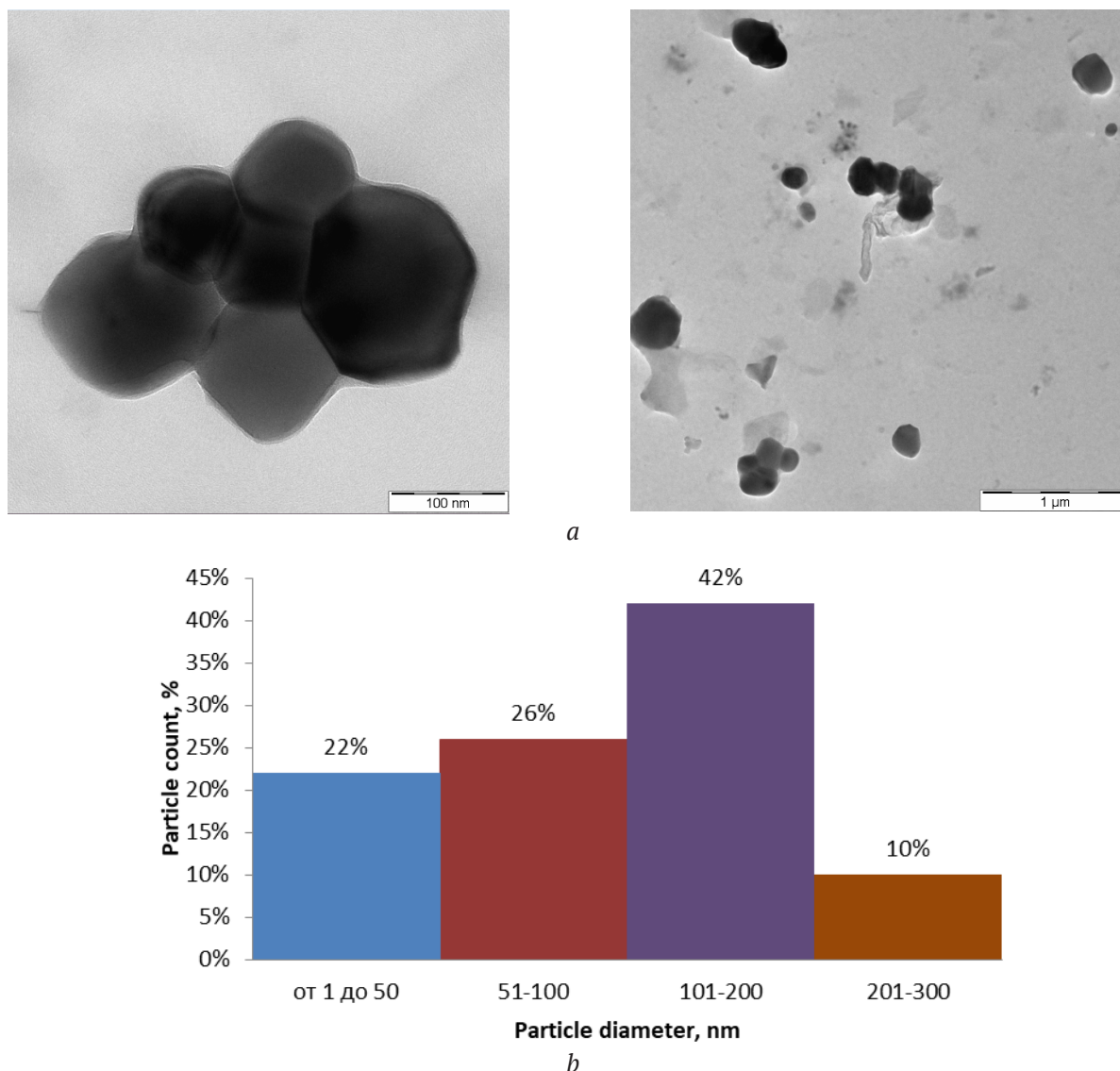
pronounced crystallinity, a low degree of agglomeration, a nearly spherical shape, and a predominant particle size within the range of 50–200 nm. The shift of the reflections of bismuth ferrite towards larger values of  $2\theta$  angles, observed in the diffraction patterns, a decrease in the lattice parameters and the unit cell volume of  $\text{Er}_x\text{Bi}_{1-x}\text{FeO}_3$  samples, as well as an increase in the degree of doping with erbium ions indicate the incorporation of erbium ions into the crystal lattice of ferrite at the bismuth position.

#### Conflict of interests

The authors declare that they have no known competing financial interests or personal



**Fig. 5.** TEM images (a) of the  $\text{Er}_{0.05}\text{Bi}_{0.95}\text{FeO}_3$  sample synthesised by spray pyrolysis, in the gelatinous layer, and the histogram of its particle-size distribution (b)



**Fig. 6.** TEM images (a) of the  $\text{Er}_{0.15}\text{Bi}_{0.85}\text{FeO}_3$  sample synthesised by spray pyrolysis, in the gelatinous layer, and the histogram of its particle-size distribution (b)

relationships that could have influenced the work reported in this paper.

## References

1. Dai Z., Fujita Y., Akishige Y. Dielectric properties and heating effect of multiferroic  $\text{BiFeO}_3$  suspension. *Materials Letters*. 2011;63(13): 2036–2039. <https://doi.org/10.1016/j.matlet.2011.04.029>
2. Lin Z., Cai W., Jiang W., Fu Ch., Li Ch., Song Y. *Ceramics International*. 2013;39(8): 8729–8736. <https://doi.org/10.1016/j.ceramint.2013.04.058>
3. Selbach S. M., Tybell T., Einarsrud M. *Chemistry of materials*. 2007;19(26): 6478–6484. <https://doi.org/10.1021/cm071827w>
4. Shirokov V. B., Golovko Yu. I., Mukhortov V. M. *Technical physics*. 2014;59(1): 102–106. <https://doi.org/10.1134/s1063784214010174>
5. Karthikeyan K., Thirumoorthi A. *Nanosystems: Physics, Chemistry, Mathematics*. 2018;9: 631–640. <https://doi.org/10.17586/2220-8054-2018-9-5-631-640>
6. Fiebig M. Revival of the magnetoelectric effect. *Journal of Physics D: Applied Physics*. 2005;38(8): R123–R152. <https://doi.org/10.1088/0022-3727/38/8/r01>
7. Eerenstein W., Mathur N. D., Scott J. F. Multiferroic and magnetoelectric materials. *Nature*. 2006;442(7104): 759–765. <https://doi.org/10.1038/nature05023>
8. Cheong S.-W., Mostvov M. Multiferroics: a magnetic twist for ferroelectricity. *Nature Materials*. 2007;6(1): 13–20. <https://doi.org/10.1038/nmat1804>
9. Ramesh R., Spaldin N. A. Multiferroics: progress and prospects in thin films. *Nature Materials*. 2007;6(1): 21–29. <https://doi.org/10.1038/nmat1805>

10. Tokura Y. Multiferroics—toward strong coupling between magnetization and polarization in a solid. *Journal of Magnetism and Magnetic Materials*... 2007;310(2): 1145–1150. <https://doi.org/10.1016/j.jmmm.2006.11.198>
11. Catalan G., Scott J. F. Physics and applications of bismuth ferrite. *Advanced Materials*. 2009;21(24): 2463–2485. <https://doi.org/10.1002/adma.200802849>
12. Morozov M. I., Lomanova N. A., Gusarov V. V. Specific features of BiFeO<sub>3</sub> formation in a mixture of bismuth(III) and iron(III) oxides. *Russian Journal of General Chemistry*. 2003;73(11): 1676–1680. <https://doi.org/10.1023/b:rugc.0000018640.30953.70>
13. Liu T., Xu Y., Zhao J. Low-temperature synthesis of BiFeO<sub>3</sub> via PVA sol-gel route. *Journal of the American Ceramic Society*. 2010;93(11): 3637–3641. <https://doi.org/10.1111/j.1551-2916.2010.03945.x>
14. Feroze A., Idrees M., Kim D. K., Nadeem M., Siddiqi S. A., Shaukat S. F., Atif M., Siddique M. Low temperature synthesis and properties of BiFeO<sub>3</sub>. *Journal of Electronic Materials*. 2017;46(7): 4582–4589. <https://doi.org/10.1007/s11664-017-5463-3>
15. Egorysheva A. V., Kuvshinova T. B., Volodin V. D., Ellert O. G., Efimov N. N., Skorikov V. M., Baranchikov A. E., Novotortsev V. M. Synthesis of high-purity nanocrystalline BiFeO<sub>3</sub>. *Inorganic materials*. 2013;49(3): 310–314. <https://doi.org/10.1134/s0020168513030035>
16. Selbach S. M., Tybell T., Einarsrud M. A., Grande T. Phase transitions, electrical conductivity and chemical stability of BiFeO<sub>3</sub> at high temperatures. *Journal of Solid State Chemistry*. 2010;183(5): 1205–1208. <https://doi.org/10.1016/j.jssc.2010.03.014>
17. Tomina E. V., Lastochkin D. A., Maltsev S. A. The synthesis of nanophosphors YP<sub>x</sub>V<sub>1-x</sub>O<sub>4</sub> by spray pyrolysis and microwave methods. *Kondensirovannye sredy i mezhfaznye granitsy = Condensed Matter and Interphases*. 2020;22(4): 496–503. <https://doi.org/10.17308/kcmf.2020.22/3120>
18. Brandon D., Kaplan U. *Microstructure of materials. Research and control methods*. John Wiley & Sons Ltd; 1999.
19. JCPDS PCPDFWIN: A Windows Retrieval / Display program for Accessing the ICDD PDF-2 Data base, International Centre for Diffraction Data, 1997.
20. Bhat I., Husain S., Khan W., Patil S. I. Effect of Zn doping on structural, magnetic and dielectric properties of LaFeO<sub>3</sub> synthesized through sol-gel auto-combustion process. *Materials Research Bulletin*. 2013;48(11): 4506–4512. <https://doi.org/10.1016/j.materresbull.2013.07.028>
21. Tret'yakov Yu. D. [et al.]. *Neorganicheskaya khimiya. Khimiya elementov: uchebnik dlya stud. vuzov, obuch. po napravleniyu 510500 "Khimiya" i spetsial'nosti 011000 "Khimiya": v 2 t.* [Inorganic chemistry. Chemistry of elements: a textbook for students. universities, studying under programme 510500 "Chemistry" and for speciality 011000 "Chemistry": in 2 vol.] Moscow: Akademkniga Publ.; 2007. V. 1. 538 p.; V. 2. 670 p. (In Russ.)

#### Information about the authors

*Elena V. Tomina*, DSc in Chemistry, Head of the Department of Chemistry, Voronezh State University of Forestry and Technologies, Voronezh, Russian Federation; e-mail: [tomina-e-v@yandex.ru](mailto:tomina-e-v@yandex.ru). ORCID iD: <https://orcid.org/0000-0002-5222-0756>.

*Anna A. Pavlenko*, a 1st year master's student, Voronezh State University, Voronezh, Russian Federation; e-mail: [anna.pavlienko.1999@mail.ru](mailto:anna.pavlienko.1999@mail.ru) ORCID iD: <https://orcid.org/0000-0003-4899-609X>

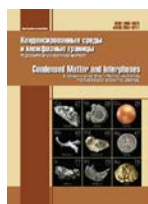
*Nikolay A. Kurkin*, a 2nd year master's student, Voronezh State University, Voronezh, Russian Federation; e-mail: [kurkin.nik@yandex.ru](mailto:kurkin.nik@yandex.ru). ORCID iD: <https://orcid.org/0000-0002-0468-8207>

All authors read and approved the final manuscript.

Received 17 January 2021; Approved after reviewing 15 February 2021; Accepted 15 March 2021; Published online 25 March 2021.

Translated by Anastasiia Ananeva

Edited and proofread by Simon Cox



# Condensed Matter and Interphases

Kondensirovannye Sredy i Mezhfaznye Granitsy  
<https://journals.vsu.ru/kcmf/>

## Original articles

Original article

<https://doi.org/10.17308/kcmf.2021.23/3310>

## Growth and physical properties of $\text{CaSrBaF}_6$ single crystals

S. N. Ushakov<sup>1,2</sup>, M. A. Uslamina<sup>1</sup>, A. A. Pynenkov<sup>1</sup>, V. P. Mishkin<sup>1</sup>, K. N. Nishchev<sup>1</sup>,  
S. V. Kuznetsov<sup>2</sup>, E. V. Chernova<sup>2</sup>, P. P. Fedorov<sup>2</sup>✉

<sup>1</sup>Ogarev Mordovia State University,  
68 Bolshevistskaya str., Saransk 430005, Republic of Mordovia, Russian Federation

<sup>2</sup>Prokhorov General Physics Institute of the Russian Academy of Sciences,  
38 Vavilov str., Moscow 119991, Russian Federation

### Abstract

Using the Bridgman-Stockbarger method, crystals of triple fluoride  $\text{CaF}_2$ - $\text{SrF}_2$ - $\text{BaF}_2$  were grown in a composition range similar to that of  $\text{CaSrBaF}_6$ . The crystals were 10–12 mm in diameter and 50–60 mm in length. The  $\text{CaSrBaF}_6$  crystal is a new optical material which is transparent in the mid-IR, visible and UV ranges. The uneven distribution of the components along the length of the crystal did not exceed 10 %. The edge of the absorption band in the IR range was 14.3  $\mu\text{m}$ , and the optical absorption at the wavelength of 200 nm did not exceed 18 % (less than 0.2  $\text{cm}^{-1}$ ). The refraction indices were 1.4527, 1.4488, and 1.4458 for the wavelengths of 633, 969, and 1539 nm respectively. The crystal melts in the temperature range of 1150–1210 °C. The  $\text{CaSrBaF}_6$  composition is an appropriate matrix for doping with rare-earth ions in order to obtain functional single-crystal and ceramic materials of the visible and IR ranges.

**Keywords:** Calcium fluoride, Strontium fluoride, Barium fluoride, Fluorite, Solid solution, Isomorphism, High entropy alloys

**Acknowledgements:** the study was performed using the equipment provided by the Centre for Collective Use “Materialovedeniye” of Ogarev Mordovia State University.

**For citation:** Ushakov S. N., Uslamina M. A., Pynenkov A. A., Mishkin V. P., Nishchev K. N., Kuznetsov S. V., Chernova E. V., Fedorov P. P. Growth and physical properties of  $\text{CaSrBaF}_6$  single crystals. *Kondensirovannye sredy i mezhfaznye granitsy = Condensed Matter and Interphases*. 2021;23(1): 101–107. <https://doi.org/10.17308/kcmf.2021.23/3310>

**Для цитирования:** Ушаков С. Н., Усламина М. А., Пыненко А. А., Мишкин В. П., Нищев К. Н., Кузнецов С. В., Чернова Е. В., Федоров П. П. Выращивание и физические свойства монокристаллов  $\text{CaSrBaF}_6$ . *Конденсированные среды и межфазные границы*. 2021;23(1): 101–107. <https://doi.org/10.17308/kcmf.2021.23/3310>

✉ Pavel P. Fedorov, e-mail: [ppfedorov@yandex.ru](mailto:ppfedorov@yandex.ru)

© Ushakov S. N., Uslamina M. A., Pynenkov A. A., Mishkin V. P., Nishchev K. N., Kuznetsov S. V., Chernova E. V., Fedorov P. P., 2021



The content is available under Creative Commons Attribution 4.0 License.

## 1. Introduction

Calcium, strontium, and barium fluorides crystallise in the fluorite structure with the following parameters of the crystal lattice: 5.463, 5.800, and 6.200 Å respectively. Single crystals of difluorides of alkaline earth elements are widely used as photonics materials [1–3] as well as matrices for doping with rare-earth ions [4–10]. They are characterised by wide transmission regions from vacuum ultraviolet to the mid-IR range. However, the use of pure fluorides can be limited when designing optical systems [11]. The use of solid solutions allows varying the physical properties and characteristics of matrices over a wide range. Continuous areas of solid solutions with the valleys on the melting curves are formed in the  $\text{CaF}_2$ – $\text{SrF}_2$  [12, 13] and  $\text{SrF}_2$ – $\text{BaF}_2$  systems [14, 15]. We grew and studied the corresponding series of single crystals  $\text{Ca}_{1-x}\text{Sr}_x\text{F}_2$  and  $\text{Sr}_{1-x}\text{Ba}_x\text{F}_2$  [16–22]. Isomorphism in the  $\text{CaF}_2$ – $\text{BaF}_2$  system is limited [18, 23, 24]. The corresponding binary solid solutions are of interest as optical materials for photonics. When isovalent solid solutions are formed, physical properties of the crystals significantly change (compared to the components), including the refractive index [16–18, 20], vibration spectra [25], and hardness [17, 20]. On the whole, mechanical characteristics of solid solutions improve, thermal conductivity decreases, and electrical conductivity increases. Spectral-luminescent characteristics and cluster structure of doping REE change in a non-monotonic way.

In recent years, multicomponent phases with several isostructural elements in their composition have been attracting greater interest. Such compositions containing 5 and more components were called high-entropy alloys (HEAs) [30, 31]. According to the third law of thermodynamics, these single-phase alloys cannot be stable at low temperatures, although only slow processes of atomic diffusion and phase relaxation in some cases help to reveal their kinetic stability and potential applications. Homogeneous materials with multicomponent compositions are usually found in glass [32]. Initially, this term had been used for metal alloys, but then HEA oxides were also found [33]. The synthesis of high-entropy fluoride ceramics  $\text{CeNdCaSrBaF}_{12}$  was reported [34].

The purpose of this work was to grow single crystals of the triple-component solid solution  $\text{Ca}_{1-x-y}\text{Sr}_x\text{Ba}_y\text{F}_2$  similar to the  $\text{CaSrBaF}_6$  composition and to study its properties. The corresponding composition can serve as a matrix for doping with rare-earth ions and obtaining a multicomponent functional material.

## 2. Experimental

We used shards of  $\text{CaF}_2$  (OST 3-6304-87) and  $\text{BaF}_2$  optical single crystals together with the remelted  $\text{SrF}_2$  powder (extra-pure grade) as the starting substances to grow  $\text{CaF}_2$ – $\text{SrF}_2$ – $\text{BaF}_2$  crystals. It is preferable to choose crystal reagents along with powder that was remelted under fluorinating atmosphere, as the reagents do not absorb moisture and can be stored for a long time. Each initial reagent was controlled by differential scanning calorimetry (DSC), X-ray diffraction analysis (XRD), and electron microscopy.

We grew the crystals of triple fluoride  $\text{CaF}_2$ – $\text{SrF}_2$ – $\text{BaF}_2$  in the composition range similar to  $\text{CaSrBaF}_6$  on an automated system NIKA-3 under conditions of induction heating of a six-cell graphite crucible placed inside the inductor. The temperature gradient was formed using graphite pipes and disks as screens that had radial sawcuts to exclude the heating with the induction current, which allowed obtaining the temperature gradient (according to the temperature of crucible wall) of about 30 °C/cm. The temperature was measured through the chamber windows using a manual IR pyrometer. As soon as the crucible was filled with the mixture, pumping was performed to the residual pressure of no more than  $5 \cdot 10^{-2}$  mbar. The  $\text{CF}_4$  gas that partially filled the chamber was used as a fluorinating agent. After that, it was smoothly heated (for 1.5–2 hours), and when the operational temperature was reached, the crucible was removed from the hot area to the cold area at 6 mm/hour. When the removal process was finished, the crucible was slowly cooled for 4–6 hours.

We performed a thermal analysis of the crystals on a Netzsch DSC 404 F1 differential scanning calorimeter. The measurements were made in platinum crucibles in a flowing argon atmosphere. Ground fragments of the seed boule cone were used as samples. We performed thermal analysis of all the crystals in the range of

temperatures of 20–1400 °C in the mode of two heating-cooling cycles.

The refractive index of the samples of the crystals was measured on a Metricon 2010 refractometer. The measurement method was based on the determination of the critical angle of incidence at which light starts going into the volume of the sample through the surface of the measuring prism (similar to an Abbe refractometer). This device allows performing measurements at three wavelengths: 633, 969, and 1539 nm. The measurements were performed on the crystal samples with the polished side surface in the region of 5–10 mm from the seed boule cone.

Spectrophotometers Shimadzu UV-2600 and Infralyum FT 02 were used to register optical transmission in the UV, visible, and IR ranges of the optical spectrum. The measurements were taken using a dual-beam method in the UV and visible range and using a single-beam method in the IR range. The measurements were performed on the samples with two polished side surface in the region of 5–10 mm from the seed boule cone.

The elemental composition of the crystals was studied on a Quanta 200i 3D FEI scanning electron microscope with the system of energy dispersive X-ray microanalysis which included an Apollo X energy dispersive silicon detector with a resolution of > 131 eV for an MnK line at 100000 imp/s. The peak-to-background ratio was no less than 10000/1. The concentration of the components of the crystals was measured in three regions along the crystal's length at the distances of 1 mm, 20 mm, and 40 mm from the seed boule cone. Three measurements were taken at different points of each region, and then the results were averaged.

### 3. Results and discussion

We grew a series of crystals that were 10–12 mm in diameter and 50–60 mm in length (Fig. 1). The crystals were optically transparent (Fig. 2). The uneven distribution of the components of the crystal along the length of the boule did not exceed 10 % for most of the crystals. The most uniform distribution was observed on the crystal of the  $\text{CaSrBaF}_6$  composition (33 mol %  $\text{CaF}_2$  – 33 mol %  $\text{SrF}_2$  – 33 mol %  $\text{BaF}_2$ ), Fig. 3.

The DSC curves for the sample of the crystal of the  $\text{CaSrBaF}_6$  composition for the first heating-

cooling cycle are presented in Fig. 4. The sample melts in the range of temperatures of 1150–1210 °C.

The results of the measurement of the refractive index are presented in Table 1. The maximum values of the refractive index are typical for the sample 31 mol %  $\text{CaF}_2$  – 31 mol %

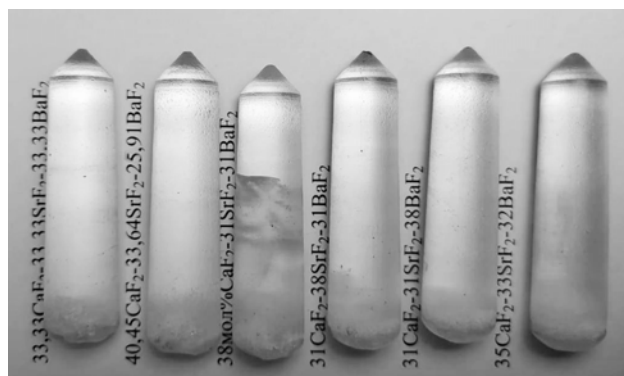


Fig. 1. Photo of untreated boules of triple fluoride  $\text{CaF}_2$ – $\text{SrF}_2$ – $\text{BaF}_2$  crystals in the composition range similar to  $\text{CaSrBaF}_6$

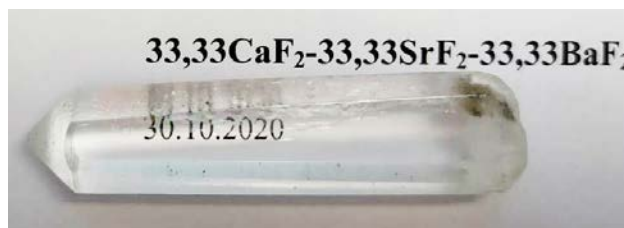


Fig. 2. Photo of a polished triple fluoride  $\text{CaSrBaF}_6$  crystal

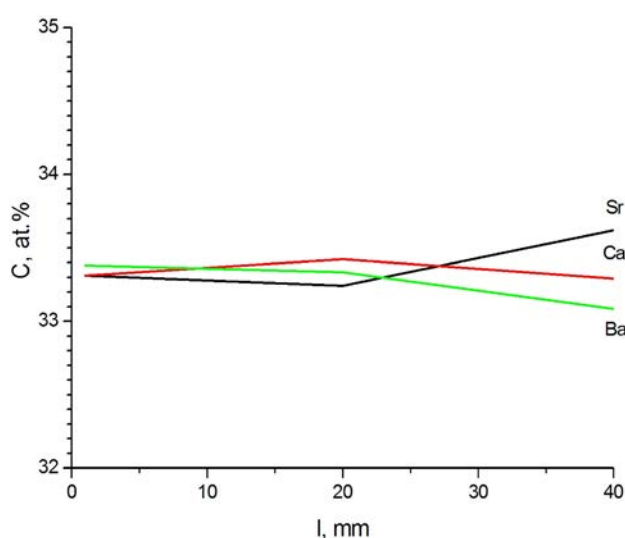
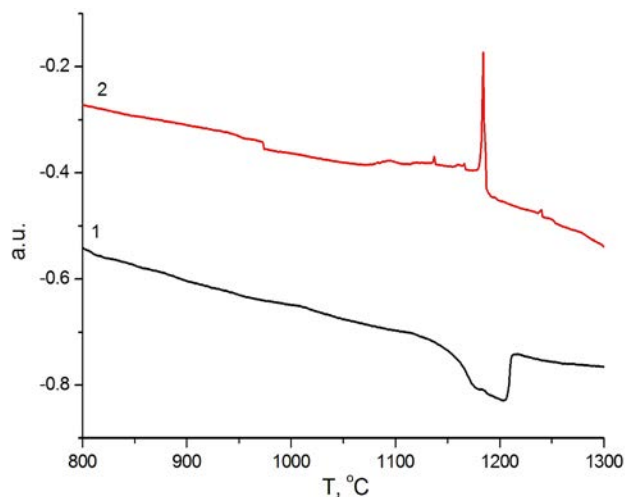


Fig. 3. Distribution of the components of a  $\text{CaSrBaF}_6$  crystal along the length of the boule for the 33 mol %  $\text{CaF}_2$  – 33 mol %  $\text{SrF}_2$  – 33 mol %  $\text{BaF}_2$  composition



**Table 1.** Values of the refractive index  $n$  at three wavelengths for crystals of triple fluorides in the composition range similar to  $\text{CaSrBaF}_6$ 

Compositions	$\lambda = 633 \text{ nm}$	$\lambda = 969 \text{ nm}$	$\lambda = 1539 \text{ nm}$
33 mol % $\text{CaF}_2$ – 33 mol % $\text{SrF}_2$ – 33 mol % $\text{BaF}_2$	1.4527	1.4488	1.4458
40.5 mol % $\text{CaF}_2$ – 33.6 mol % $\text{SrF}_2$ – 25.9 mol % $\text{BaF}_2$	1.4497	1.4458	1.4430
38 mol % $\text{CaF}_2$ – 31 mol % $\text{SrF}_2$ – 31 mol % $\text{BaF}_2$	1.4522	1.4483	1.4451
31 mol % $\text{CaF}_2$ – 38 mol % $\text{SrF}_2$ – 31 mol % $\text{BaF}_2$	1.4520	1.4472	1.4448
31 mol % $\text{CaF}_2$ – 31 mol % $\text{SrF}_2$ – 38 mol % $\text{BaF}_2$	1.4566	1.4526	1.4491
35 mol % $\text{CaF}_2$ – 33 mol % $\text{SrF}_2$ – 32 mol % $\text{BaF}_2$	1.4527	1.4486	1.4451

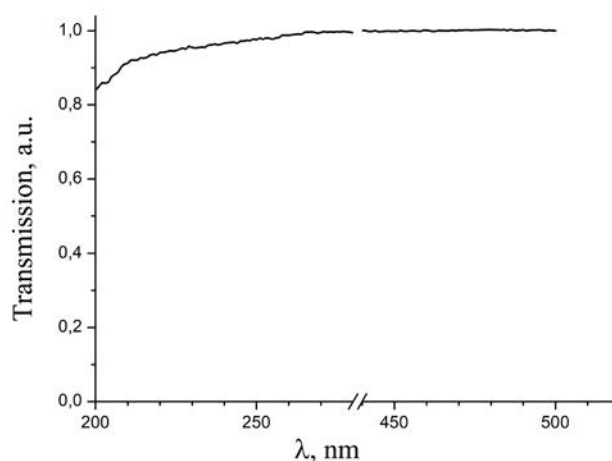
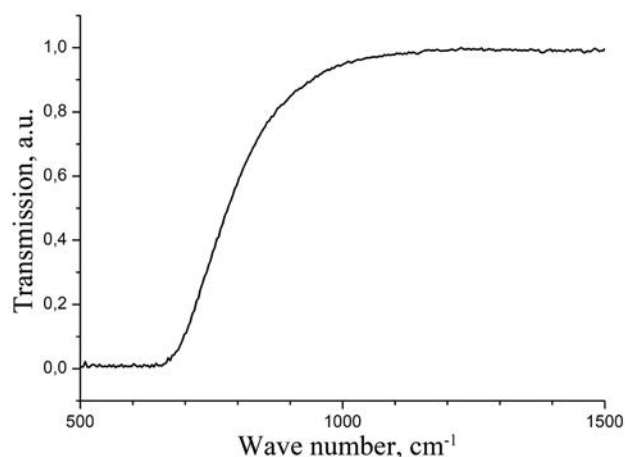
**Fig. 4.** Sections of the DSC curves of a crystal sample of the 33 mol %  $\text{CaF}_2$  – 33 mol %  $\text{SrF}_2$  – 33 mol %  $\text{BaF}_2$  composition, first cycle: 1 – heating, 2 – cooling

$\text{SrF}_2$  – 38 mol %  $\text{BaF}_2$  while the minimum values are typical for the composition 40.5 mol %  $\text{CaF}_2$  – 33.6 mol %  $\text{SrF}_2$  – 25.9 mol %  $\text{BaF}_2$ .

The transmission spectra for the crystal of the  $\text{CaSrBaF}_6$  composition in the region of UV and IR absorption edges are presented in Fig. 5 and Fig. 6 respectively. The measured sample was 10 mm thick. The spectra are presented taking into account the Fresnel reflection from the surfaces of the sample. The edge of the UV absorption was beyond the operating area of the spectrophotometer, and the absorption at the wavelength of 200 nm did not exceed 18 % (less than  $0.2 \text{ cm}^{-1}$ ).

The border region of the IR absorption for the transmission degree of 0.1 begins from  $700 \text{ cm}^{-1}$  ( $14.3 \mu\text{m}$ ). 50 % transmission occurred at  $12.5 \mu\text{m}$ .

Therefore, the crystal of the  $\text{CaSrBaF}_6$  composition is a new optical material which is transparent in the mid-IR, visible, and UV ranges. A big difference between the temperatures of liquidus and solidus exceeding  $50 \text{ }^\circ\text{C}$  is indicative

**Fig. 5.** Transmission spectrum of a crystal sample of the 33 mol %  $\text{CaF}_2$  – 33 mol %  $\text{SrF}_2$  – 33 mol %  $\text{BaF}_2$  composition in the UV and visible range. The thickness of the sample is 10 mm**Fig. 6.** Transmission spectrum of a crystal sample of the 33 mol %  $\text{CaF}_2$  – 33 mol %  $\text{SrF}_2$  – 33 mol %  $\text{BaF}_2$  composition in the IR range. The thickness of the sample is 10 mm

of the incongruent nature of the melting of this composition. Consequently, the growth from the melt of  $\text{CaSrBaF}_6$  crystals of high optical quality which are suitable for laser applications can hardly be implemented due to the problems

with concentration overcooling, instability of the crystallisation front, and the formation of a cellular and dendritic substructure [35, 36]. However, this composition can be a suitable crystal matrix for obtaining upconversion luminophores [37] and can be used in the production technology for optical ceramics [38].

### Conflict of interests

The authors declare that they have no known competing financial interests or personal relationships that could have influenced the work reported in this paper.

### References

1. Yushkin N. P., Volkova N. V., Markova G. A. *Opticheskii flyuorit* [Optical fluorite]. Moscow: Nauka Publ.; 1983. 134 p. (In Russ.)
2. Zverev V. A., Krivopustova E. V., Tochilina T. V. *Opticheskie materialy. Chast' 2. Uchebnoe posobie dlya konstruktorov opticheskikh sistem i priborov* [Optical materials. Part 2. Tutorial for designers of optical systems and devices]. S.-Peterburg: ITMO Publ.; 2013. 248 p. (In Russ.)
3. Fedorov P. P., Osiko V. V. Crystal growth of fluorides. In: *Bulk Crystal Growth of Electronic, Optical and Optoelectronic Materials*. P. Capper (ed.). Wiley Series in Materials for Electronic and Optoelectronic Applications. John Wiley & Son. Ltd.; 2005. pp. 339–356. <https://doi.org/10.1002/9780470012086.ch11>
4. Kaminskii A.A. Laser crystals. Their physics and properties. In: *Springer Series in Optical Sciences*. Berlin: Springer; 1990. <https://doi.org/10.1007/978-3-540-70749-3>
5. Siebold M., Bock S., Schramm U., Xu B., Doualan J. L., Camy P., Moncorge R. Yb:CaF<sub>2</sub> - a new old laser crystal. *Applied Physics B*. 2009;97: 327–338. <https://doi.org/10.1007/s00340-009-3701-y>
6. Druon F., Ricaud S., Papadopoulos D. N., Pellegrina A., Camy P., Doualan J. L., Moncorge R., Courjaud A., Mottay E., Georges P. On Yb:CaF<sub>2</sub> and Yb:SrF<sub>2</sub>: review of spectroscopic and thermal properties and their impact on femtosecond and high power laser performance. *Optical Materials Express*. 2011;1(3): 489–502. <https://doi.org/10.1364/ome.1.000489>
7. Basiev T. T., Orlovskii Yu. V., Polyachenkova M. V., Fedorov P. P., Kuznetsov S. V., Konyushkin V. A., Osiko V. V., Alimov O. K., Dergachev A. Yu. Continuously tunable cw lasing near 2.75 μm in diode-pumped Er<sup>3+</sup>:SrF<sub>2</sub> and Er<sup>3+</sup>:CaF<sub>2</sub> crystals. *Quantum Electronics*. 2006;36(7): 591–594. <https://doi.org/10.1070/qe2006v036n07abeh013178>
8. Alimov O. K., Basiev T. T., Doroshenko M. E., Fedorov P. P., Konyushkin V. A., Nakladov A. N., Osiko V. V. Investigation of Nd<sup>3+</sup> ions spectroscopic and laser properties in SrF<sub>2</sub> fluoride single crystal. *Optical Materials*. 2012;34(5): 799–802. <https://doi.org/10.1016/j.optmat.2011.11.010>
9. Brites C. D. S., Kuznetsov S. V., Konyushkin V. A., Nakladov A. N., Fedorov P. P., Carlos L. D. Simultaneous measurement of the emission quantum yield and local temperature: the illustrative example of SrF<sub>2</sub>:Yb<sup>3+</sup>/Er<sup>3+</sup> single crystals. *European Journal of Inorganic Chemistry*. 2020;2020(17): 1555–1561. <https://doi.org/10.1002/ejic.202000113>
10. Saleta Reiga D., Grauel B., Konyushkin V. A., Nakladov A. N., Fedorov P. P., Busko D., Howard I. A., Richards B. S., Resch-Genger U., Kuznetsov S. V., Turshatov A., Würtha C. Upconversion properties of SrF<sub>2</sub>:Yb<sup>3+</sup>, Er<sup>3+</sup> single crystals. *Journal of Materials Chemistry C*. 2020;8(12): 4093–4101. <https://doi.org/10.1039/c9tc06591a>
11. Barnett J., Levine Z., Shirley E. Intrinsic birefringence in calcium fluoride and barium fluoride. *Physical Review B*. 2001;64(24): 241102. <https://doi.org/10.1103/physrevb.64.241102>
12. Klimm D., Rabe M., Bertram R., Uecker R., Parthier L. Phase diagram analysis and crystal growth of solid solutions Ca<sub>1-x</sub>Sr<sub>x</sub>F<sub>2</sub>. *Journal of Crystal Growth*. 2008;310(1): 152–155. <https://doi.org/10.1016/j.jcrysgro.2007.09.031>
13. Stasjuk V. A., Buchinskaya I. I., Ust'yanceva N. A., Fedorov P. P., Arbenina V. V. Liquidus and solidus of fluoride solid solutions in the CaF<sub>2</sub>-SrF<sub>2</sub>-LaF<sub>3</sub> system. *Russian Journal of Inorganic Chemistry*. 1998;43(8): 1266–1269. Available at: <https://www.elibrary.ru/item.asp?id=13300529> (In Russ.)
14. Nafziger R. H. High-temperature phase relations in the system BaF<sub>2</sub>-SrF<sub>2</sub>. *Journal of the American Ceramic Society*. 1971;54(9): 467. <https://doi.org/10.1111/j.1151-2916.1971.tb12388.x>
15. Fedorov P. P., Ivanovskaya N. A., Stasyuk V. A., Buchinskaya I. I., Sobolev B. P. Phase equilibria in the SrF<sub>2</sub>-BaF<sub>2</sub>-LaF<sub>3</sub> system. *Doklady Physical Chemistry*. 1999;366(4-6): 168–170. (In Russ.)
16. Chernevskaya E. G. Smeshannye dvukh-komponentnye monokristally tipa fluoristy kal'tsifloristy strontsii i ikh opticheskie svoistva [Mixed two-component monocrystals of the calcium fluoride-strontium fluoride type and their optical properties]. *Optiko-mekhanicheskaya promyshlennost'*. 1960;5: 28–32. (In Russ.)
17. Chernevskaya E. G. Tverdost' smeshannykh monokristallov tipa CaF<sub>2</sub>. [The hardness of mixed single crystals of the CaF<sub>2</sub> type]. *Optiko-mekhanicheskaya promyshlennost'*. 1966;7: 51–52. (In Russ.)
18. Chernevskaya E. G., Anan'eva G. V. O strukture smeshannykh kristallov na osnove CaF<sub>2</sub>, SrF<sub>2</sub>, BaF<sub>2</sub> [About the structure of mixed crystals based on CaF<sub>2</sub>, SrF<sub>2</sub>, BaF<sub>2</sub>]. *Physics of the Solid State*. 1966;8(1): 216–219. (In Russ.)

19. Pastor R. C., Pastor A. C. Solid solutions of metal halides under a reactive atmosphere. *Materials Research Bulletin*. 1976;11(8): 1043–1050. [https://doi.org/10.1016/0025-5408\(76\)90183-5](https://doi.org/10.1016/0025-5408(76)90183-5)
20. Karimov D. N., Komar'kova O. N., Sorokin N. I., Sobolev B. P., Bezhanov V. A., Chernov S. P., Popov P. A. Growth of congruently melting  $\text{Ca}_{0.59}\text{Sr}_{0.41}\text{F}_2$  crystals and study of their properties. *Crystallography Reports*. 2010;55(3): 518–524. <https://doi.org/10.1134/s1063774510030247>
21. Popov P. A., Moiseev N. V., Karimov D. N., Sorokin N. I., Sulyanova E. A., Sobolev B. P., Konyushkin V. A., Fedorov P. P. Thermophysical characteristics of  $\text{Ca}_{1-x}\text{Sr}_x\text{F}_2$  solid-solution crystals ( $0 \leq x \leq 1$ ). *Crystallography Reports*. 2015;60(1): 116–122. <https://doi.org/10.1134/s1063774515010186>
22. Popov P. A., Krugovykh A. A., Konyushkin V. A., Nakladov A. N., Kuznetsov S. V., Fedorov P. P. Thermal conductivity of single crystals of  $\text{SrF}_2 - \text{BaF}_2$  solid solution. *Inorganic Materials*. 2021;57(6): <https://10.31857/S0002337X21060087>
23. Fedorov P. P., Buchinskaya I. I., Ivanovskaya N. A., Konovalova V. V., Lavrishchev S. V., Sobolev B. P.  $\text{CaF}_2 - \text{BaF}_2$  phase diagram. *Doklady Physical Chemistry*. 2005;401(2): 53–55. <https://doi.org/10.1007/s10634-005-0024-5>
24. Wrubel G. P., Hubbard B. E., Agladze N. I., Sievers A. G., Fedorov P. P., Klimenchenko D. I., Ryskin A. I., Campbell G. A. Glasslike two-level systems in minimally disordered mixed crystals. *Physical Review Letters*. 2006;96(23): 235503. <https://doi.org/10.1103/physrevlett.96.235503>
25. Chang R. K., Lacina B., Pershan P. S. Raman scattering from mixed crystals  $\text{Ca}_x\text{Sr}_{1-x}\text{F}_2$  and  $\text{Sr}_x\text{Ba}_{1-x}\text{F}_2$ . *Physical Review Letters*. 1966;17(14): 755–778. <https://doi.org/10.1103/physrevlett.17.755>
26. Basiev T. T., Vasil'ev S. V., Doroshenko M. E., Konyushkin V. A., Kouznetsov S. V., Osiko V. V., Fedorov P. P. Efficient lasing in diode-pumping  $\text{Yb}^{3+}:\text{CaF}_2 - \text{SrF}_2$  solid solution single crystals. *Quantum Electronics*. 2007;37(10): 934–937. <https://doi.org/10.1070/QE2007v037n10ABEH013662>
27. Lyapin A. A., Ermakov A. S., Kuznetsov S. V., Gushchin S. V., Ryabochkina P. A., Konyushkin V. A., Nakladov A. N., Fedorov P. P. Upconversion luminescence of  $\text{CaF}_2 - \text{SrF}_2 - \text{ErF}_3$  single crystals upon 1.5  $\mu\text{m}$  laser excitation. *Journal of Physics: Conference Series (SPbOPEN 2019)*. 2019;1410: 012086 (4 pp). <https://doi.org/10.1088/1742-6596/1410/1/012086>
28. Kuznetsov S. V., Konyushkin V. A., Nakladov A. N., Chernova E. V., Popov P. A., Pynenkov A. A., Nishchev K. N., Fedorov P. P. Thermophysical Properties of Single Crystals of  $\text{CaF}_2 - \text{SrF}_2 - \text{RF}_3$  ( $R = \text{Ho}, \text{Pr}$ ) Fluorite Solid Solutions. *Inorganic Materials*. 2020;56(9): 975–981. <https://10.1134/S0020168520090113>
29. Ushakov S. N., Fedorov P. P., Kuznetsov S. V., Osiko V. V., Usamina M. A., Nishchev K. N. Study of  $\text{Yb}^{3+}$  optical centers in fluoride solid solution crystals  $\text{CaF}_2 - \text{SrF}_2 - \text{YbF}_3$ . *Optics and Spectroscopy*. 2020;128(5): 600–604. <https://doi.org/10.1134/S0030400X20050185>
30. Zhang W., Liaw P. K., Zhang Y. Science and technology in high-entropy alloys. *Science China Materials*. 2018;61(1): 2–21. <https://doi.org/10.1007/s40843-017-9195-8>
31. Miracle D. B., Senkov O. N. A critical review of high entropy alloys and related concepts. *Acta Materialia*. 2017;122: 448–511. <https://doi.org/10.1016/j.actamat.2016.08.081>
32. Fedorov P. P. Glass formation criteria for fluoride system. *Inorganic Materials*. 1997;33(12): 1197–1205. Available at: <https://www.elibrary.ru/item.asp?id=13251524>.
33. Rost C. M., Sacht E., Borman T., Moballegh A., Dickey E. C., Hou D., Jones J. L., Curtarolo S., Maria J.-P. Entropy-stabilized oxides. *Nature Communications*. 2016;6(1): 8485. <https://doi.org/10.1038/ncomms9485>
34. Chen X., Wu Y. High-entropy transparent fluoride laser ceramics. *Journal of the American Ceramic Society*. 2019;103(2): 750–756. <https://doi.org/10.1111/jace.16842>
35. Kuznetsov S. V., Fedorov P. P. Morphological stability of solid-liquid interface during melt crystallization of solid solutions  $\text{M}_{1-x}\text{R}_x\text{F}_{2+x}$ . *Inorganic Materials*. 2008;44(13): 1434–1458. (Supplement). <https://doi.org/10.1134/S0020168508130037>
36. Fedorov P. P., Buchinskaya I. I. Spatial inhomogeneity in crystalline materials and saddle-type congruent melting points in ternary system. *Russian Chemical Reviews*. 2012;81(1): 1–20. <https://doi.org/10.1070/RC2012v081n01ABEH004207>
37. Alexandrov A. A., Mayakova M. N., Voronov V. V., Pominova D. V., Kuznetsov S. V., Baranchikov A. E., Ivanov V. K., Fedorov P. P. Synthesis upconversion luminophores based on calcium fluoride. *Kondensirovannye sredy i mezhfaznye granitsy = Condensed Matter and Interphases*. 2020;22(1): 3–10. <https://doi.org/10.17308/kcmf.2020.22/2524>
38. Kuznetsov S. V., Aleksandrov A. A., Fedorov P. P. Fluoride optical nanoceramics. *Inorganic Materials*. 2021;57(6). <https://10.31857/S0002337X21060075>

### Information about the authors

Sergey N. Ushakov, PhD in Physics and Mathematics, Senior Researcher, Department of Nanotechnologies at the Research Centre for Laser Materials and Technologies, Prokhorov General Physics Institute of the Russian Academy of Science, Moscow; Senior Researcher, Laboratory of Optical Materials Technology, Institute of Physics and Chemistry, Ogarev Mordovia State University, Saransk, Republic of Mordovia, Russian Federation; e-mail: ushserg63@

mail.ru. ORCID iD: <http://orcid.org/0000-0002-6420-6791>.

*Maria A. Uslamina*, PhD in Chemistry, Department of Nanotechnologies at the Research Centre for Laser Materials and Technologies, Prokhorov General Physics Institute of the Russian Academy of Science, Moscow; Senior Researcher, Laboratory of Optical Materials Technology, Institute of Physics and Chemistry, Ogarev Mordovia State University, Saransk, Republic of Mordovia, Russian Federation; e-mail: [uslaminam@mail.ru](mailto:uslaminam@mail.ru). ORCID iD: <https://orcid.org/0000-0003-0219-2643>.

*Aleksandr A. Pynenkov*, Engineer of Scientific and Educational Centre “High-purity Materials and Elements of Fibre Optics and Laser Technology”, Institute of Physics and Chemistry, Ogarev Mordovia State University, Saransk, Republic of Mordovia, Russian Federation; e-mail: [alekspyn@yandex.ru](mailto:alekspyn@yandex.ru). ORCID iD: <http://orcid.org/0000-0001-7546-7172>.

*Vladimir P. Mishkin*, Leading Engineer of the Laboratories of Electron Microscopy and Small-Angle X-ray Diffractometry of the Institute of Physics and Chemistry, Ogarev Mordovia State University, Saransk, Republic of Mordovia, Russian Federation; e-mail: [Vladimirm1978@mail.ru](mailto:Vladimirm1978@mail.ru). ORCID iD: <https://orcid.org/0000-0001-7514-1906>.

*Konstantin N. Nishchev*, PhD in Physics and Mathematics, Associate Professor, Head of the

Department of General Physics, Institute of Physics and Chemistry, Ogarev Mordovia State University, Saransk, Republic of Mordovia, Russian Federation; e-mail: [nishchev@inbox.ru](mailto:nishchev@inbox.ru). ORCID iD: [0000-0001-7905-3700](https://orcid.org/0000-0001-7905-3700)<https://orcid.org/>.

*Sergey V. Kuznetsov*, PhD in Chemistry, Leading Researcher of the Laboratory of Technology of Nanomaterials for Photonics, Department of Nanotechnologies at the Research Centre for Laser Materials and Technologies, Prokhorov General Physics Institute of the Russian Academy of Science, Moscow, Russian Federation; e-mail: [kouznetsovsv@gmail.com](mailto:kouznetsovsv@gmail.com). ORCID iD: <https://orcid.org/0000-0002-7669-1106>.

*Elena V. Chernova*, Researcher of the Prokhorov General Physics Institute of the Russian Academy of Science, Moscow, Russian Federation; e-mail [e-chernova@yandex.ru](mailto:e-chernova@yandex.ru). ORCID iD: <https://orcid.org/0000-0001-7401-5019>.

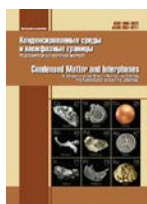
*Pavel P. Fedorov*, DSc in Chemistry, Full Professor, Chief Researcher, Department of Nanotechnologies at the Research Centre for Laser Materials and Technologies, Prokhorov General Physics Institute of the Russian Academy of Science Moscow, Russian Federation; e-mail: [ppfedorov@yandex.ru](mailto:ppfedorov@yandex.ru). ORCID iD: <https://orcid.org/0000-0002-2918-3926>.

All authors have read and approved the final manuscript.

*Received 22 January 2021; Approved after reviewing 15 February 2021; Accepted 15 March 2021; Published online 25 March 2021*

*Translated by Marina Strepetova*

*Edited and proofread by Simon Cox*



# Condensed Matter and Interphases

Kondensirovannyye Sredy i Mezhfaznye Granitsy  
<https://journals.vsu.ru/kcmf/>

## Original articles

Original article

<https://doi.org/10.17308/kcmf.2021.23/3312>

## Synthesis and experimental study of liquid dispersions of magnetic fluorescent polystyrene microspheres

P. V. Shalaev<sup>1,2,3</sup> ✉, E. V. Bondina<sup>2,3</sup>, N. N. Sankova<sup>4,5</sup>, E. V. Parkhomchuk<sup>4,5</sup>, S. A. Dolgushin<sup>1,3</sup>

<sup>1</sup>N. F. Gamaleya Federal Research Center for Epidemiology & Microbiology,  
18 Gamaleya st., Moscow 123098, Russian Federation

<sup>2</sup>National Research University of Electronic Technology,  
Bld. 1, Shokin Square, Zelenograd, Moscow 124498, Russian Federation

<sup>3</sup>Aivok LLC,  
proezd 4922, bld. 4, Zelenograd, Moscow 124498, Russian Federation

<sup>4</sup>Novosibirsk State University,  
1 Pirogova str., Novosibirsk 630090, Russian Federation

<sup>5</sup>Boreskov Institute of Catalysis Siberian Branch of the Russian Academy of Sciences,  
5 Lavrentiev Ave. (Prospekt Akademika Lavrentieva 5), Novosibirsk 630090, Russian Federation

### Abstract

Multiplex microsphere-based immunofluorescence assay is a reliable, accurate, and highly sensitive method for the detection of various biomolecules. However, for the moment, the wide application of the method in clinical practice is prevented by the high cost of reagents for analysis - magnetic spectrally encoded microspheres. Therefore, an urgent task is the development of new methods for the synthesis of microspheres with the required properties. The aim of this study was the creation of new magnetic fluorescent microspheres suitable for use in multiplex immunoassay.

Samples of magnetic fluorescent polystyrene microspheres were synthesized by dispersion polymerization and two-stage swelling methods. Experimental studies of geometric parameters, fluorescence, magnetic properties of the synthesized microspheres have been carried out.

The results of the studies have shown that microspheres synthesized by dispersion polymerization are promising for the use in immunofluorescence analysis. The obtained results can be used for the development of new diagnostic multiplex test systems based on spectrally encoded microspheres.

**Keywords:** Immunofluorescence assay, Planar immunoassay, Microspheres, Fluorescence, Dispersion polymerization, Two-stage swelling

**Acknowledgements:** the research was carried out with the support of the Ministry of Science and Higher Education of the Russian Federation (agreement No. 075-03-2020-216 of December 27, 2019). The authors are grateful to PhD in Chemistry V. S. Semeykina (Boreskov Institute of Catalysis Siberian Branch of the Russian Academy of Sciences) for help in carrying out the stage of swelling of sample No. 2 and its subsequent polymerization.

**For citation:** Shalaev P. V., Bondina E. V., Sankova N. N., Parkhomchuk E. V., Dolgushin S. A. Synthesis and experimental study of liquid dispersions of magnetic fluorescent polystyrene microspheres. *Kondensirovannyye sredy i mezhfaznye granitsy = Condensed Matter and Interphases*. 2021;23(1): 108–121. <https://doi.org/10.17308/kcmf.2021.23/3312>

**Для цитирования:** Шалаев П. В., Бондина Е. В., Санькова Н. Н., Пархомчук Е. В., Долгушин С. А. Синтез и экспериментальное исследование жидких дисперсий магнитных флуоресцентных полистирольных микросфер. *Конденсированные среды и межфазные границы*. 2021;23(1): 108–121. <https://doi.org/10.17308/kcmf.2021.23/3312>

✉ Shalaev Pavel V., e-mail: shalaev.pv@gmail.com

© Shalaev P. V., Bondina E. V., Sankova N. N., Parkhomchuk E. V., Dolgushin S. A., 2021



The content is available under Creative Commons Attribution 4.0 License.

## 1. Introduction

Now, fluorescent microspheres are widely used in various methods of immunoassay. Immunofluorescence analysis based on microspheres has a number of important advantages, such as the ability to simultaneously detect several analytes in one sample (multiplicity), a small sample volume required for analysis, as well as high accuracy and sensitivity at a high analysis speed.

Multiplex microsphere-based analysis methods are widely used in scientific research, medicine, biology, and immunology. These methods are used for the detection of nucleic acids [1], the detection of carcinogens and toxins in food [2, 3], the detection of organophosphate pesticides, causing environmental pollution [4], for the diagnosing of tumour markers [5, 6] and various infections [7], for the detection of coronavirus infection COVID-19 [8].

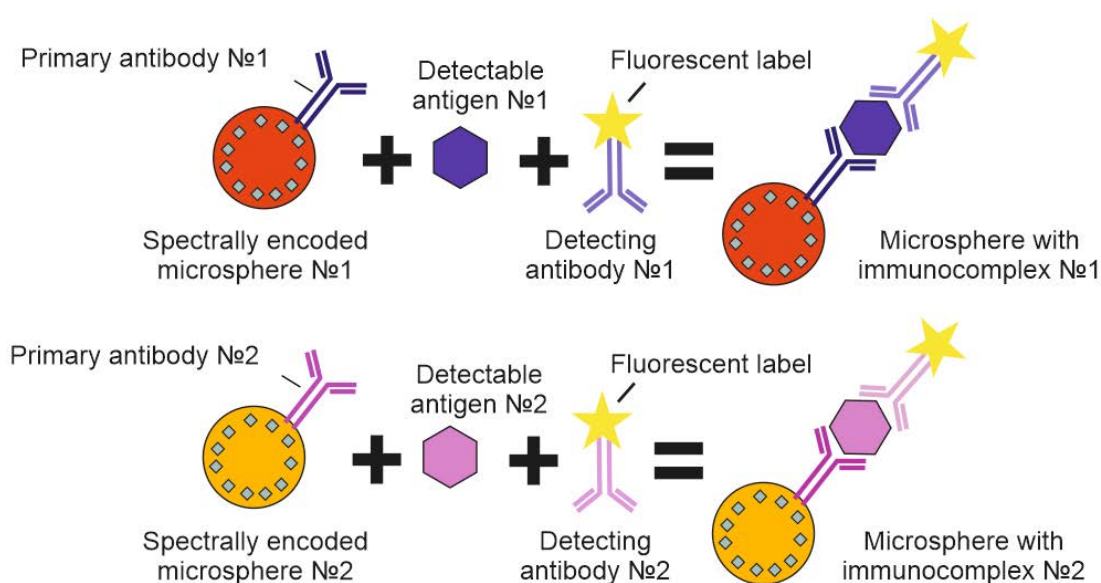
Multiplexity in modern analysis methods is usually achieved through the use of spectrally-encoded microspheres [9]. Spectral coding of microspheres is used for the creation of different types of microspheres to which the analysed analytes will correspond, and is carried out by staining the microspheres with various fluorescent dyes in different concentrations. Thus, for example, the use of a combination of three dyes in different concentrations allows encoding up to 500 types of microspheres [10].

Most methods of multiplex immunoassay are based on a specific antigen-antibody reaction. Immunocomplexes are formed on the surface of optically encoded polymeric microspheres. For example, the so-called “sandwich” method involves the formation of immunocomplexes “primary antibody - detectable antigen - detecting antibody – fluorescent label” on the surface of microspheres (Fig. 1).

The reading of fluorescence signals for identification of microspheres and detection of a fluorescent label during a multiplex immunoassay can be performed by different methods.

A widely used approach is based on flow cytometry, in which particles are analysed in the flow one by one [11]. In the flow cell, the particles are irradiated with laser radiation, the signals of light scattering and fluorescence from each particle are recorded using detectors based on photomultiplier tubes (PMT) or avalanche photodiodes (APD).

Over recent years, flow cytometry has been replaced by a new method - planar immunoassay based on fluorescent magnetic microspheres [12]. In this method, particles are immobilized in one plane using a magnet, after which fluorescence is excited using LED and recorded using a CCD (charge-coupled device) or a CMOS (complementary metal-oxide-semiconductor) camera using the necessary light filters (Fig. 2).



**Fig. 1.** Formation of immunocomplexes on the surface of microspheres in the multiplex immunoassay method

Analysis of the obtained images in different fluorescence channels allows identifying the spectrally encoded microspheres. After identification of the microspheres, the signal from the fluorescent label is recorded in the same way using an appropriate filter. In this case, the presence or absence of fluorescence from a certain type of microsphere indicates the presence or absence of the corresponding analyte in the sample. In addition, the value of the fluorescence intensity can be used to estimate the concentration of the analyte in the sample, since the fluorescence intensity depends on the amount of the analyte bound to the microsphere [13].

Instruments based on the method of planar immunoassay are more affordable, compact and reliable in comparison with analysers based on flow cytometry [14].

Multiplex analysis based on magnetic spectrally encoded microspheres is a reliable, accurate, and highly sensitive method [15]. However, currently, the wide application of the method in clinical practice is prevented by the high cost of reagents for analysis - magnetic spectrally encoded microspheres, due primarily to the closed technology.

The aim of this study was the creation of new magnetic fluorescent microspheres suitable for use in multiplex immunoassay.

Magnetic fluorescent polystyrene microspheres samples were synthesized by the methods of dispersive polymerization and two-stage swelling within the framework of this study. Experimental studies of geometric parameters, fluorescence, magnetic properties were performed

in order to assess the possibility and prospects of using the synthesized microspheres in multiplex immunofluorescence analysis.

## 2. Experimental

### 2.1. Reagents

The following reagents were used for the synthesis of microspheres: styrene, Pur., Russia (purified by vacuum distillation with preliminary removal of the inhibitor with an aqueous solution of NaOH); methyl methacrylate containing 10–110 ppm of 4-methoxyphenol as inhibitor (99%, ACROS Organics); divinylbenzene (80% mixture of isomers, Aldrich), 2-ethoxyethanol, P.A., Russia; tetrahydrofuran, Pur., China; ethanol, 95%; toluene, P.A., “Reakhim”; Pluronic F-127, Sigma, BioReagent, CCM = 950–1000 ppm; azobisisobutyronitrile (AIBN), C.P., Russia; sodium lauryl sulphate, P.A., “Reakhim”; acetone, P.A., Russia; polyvinylpyrrolidone (mol. weight - 40,000 g/mol) “Sigma-Aldrich”; magnetic fluid in kerosene was provided by Nanocomposite LLC, average particle radius is 9 nm, particles were stabilized with oleic acid; deionized water, 13–15 MOhm cm.

### 2.2. Synthesis of microspheres

The synthesis of polymer particles is based on the method of dispersion polymerization (sample No.1) [16–18] and the method of two-stage swelling (sample No.2) [19, 20]. The main requirement for polymer particles is based on the use of “hard” solvents (for example, toluene, tetrahydrofuran) at the stage of introducing magnetic particles and staining with fluorescent dyes. Thus, the particles must have a high

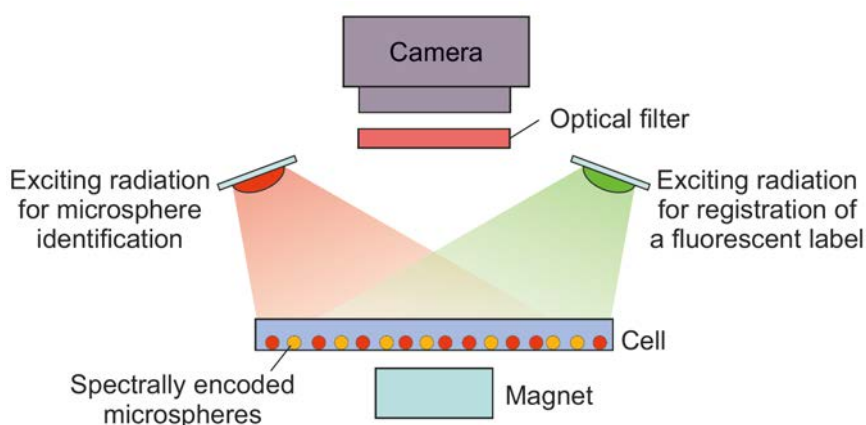


Fig. 2. Planar immunoassay based on fluorescent magnetic microspheres

crosslinking density in order to avoid dissolution and excessive swelling.

### 2.2.1. Synthesis of sample No.1 by dispersion polymerization method

The synthesis was carried out in a temperature-controlled reactor at a temperature of 74 °C, equipped with a rotary stirrer, a reflux condenser, a funnel for supplying reagents, and a capillary for nitrogen blow. The stirrer speed was 150 rpm. Ethanol was used as the reaction medium. The following reagents were mixed separately on a magnetic stirrer: 15 ml of styrene and 0.41 g of AIBN. 0.85 ml of divinylbenzene-80 in 10 ml of 2-ethoxyethanol was introduced 10 min after the initiation. The SEM of the obtained particles is shown in Fig. 3a.

### 2.2.2. Synthesis of sample No.2 by two-stage swelling method

First, 1 g of the initial polymer particles, preliminarily obtained by dispersion polymerization (Fig.4a), with a molecular weight of about 10,000 Da was dispersed in 50 ml of an aqueous solution of sodium lauryl sulphate (0.25 wt. %) using an ultrasonic bath for 30 min. Then an emulsion containing 10 ml of acetone in 50 ml of 0.25 wt. % sodium lauryl sulphate solution was added to the solution, and the mixture was left stirring for 12 hours at a temperature of 25 °C for the first stage of swelling.

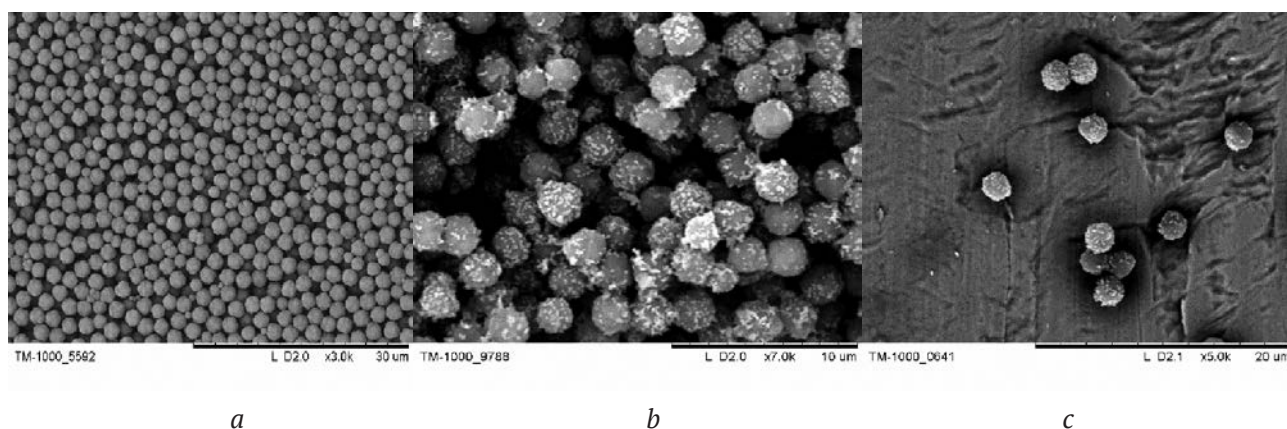
At the next stage, a monomer emulsion, consisting of 1 ml of styrene, 1 ml of methyl methacrylate, 2 ml of a crosslinking agent (divinylbenzene-80) with a dissolved initiator (AIBN, 1–2 wt. % of the monomers) in 50 ml

0.25 wt. % sodium lauryl sulphate solution was added to the resulting mixture, and left for the second stage of swelling for 8–12 hours.

For the polymerization, 50 ml of 1 wt. % solution of the stabilizer polyvinylpyrrolidone-40 was added, the temperature of the mixture was raised to 70 °C and held for 10 hours. The resulting suspension was washed with water (3 times) and ethyl alcohol (3 times) for the removal of unreacted monomer and small side particles. The SEM of particles after two-stage swelling is shown in Fig. 4a.

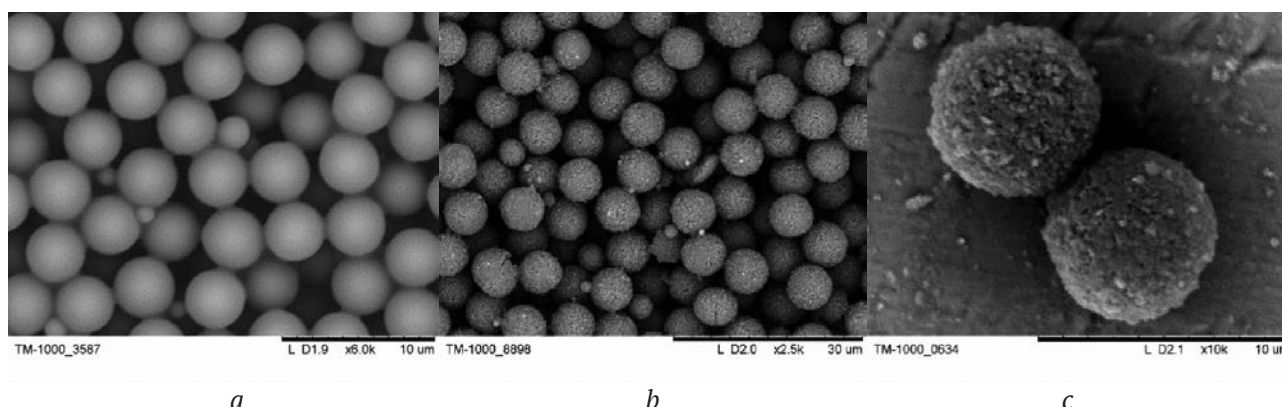
### 2.3. Method of introducing magnetic particles into polymer microspheres

Polymer particles were centrifuged in ethanol three times for 20 min at 907 g for sample No.1, and at 403 g for sample No.2, on a ThermoFisher Heraeus Labofuge 200 centrifuge, after which they were transferred into butanol-1 and butanol three more times with the same centrifugation parameters. Then, a magnetic fluid in toluene was added drop wise under the action of ultrasound on a 5 ml vessel in a VGT-1613QTD ultrasound bath with a volume of 1.3 L with an operating frequency of ultrasonic vibrations of 40 kHz. The particles were sonicated for at least two hours, after which they were separated by centrifugation three times for 20 min at 45 g from the magnetic particles that were not attached to the spheres. The particles were repeatedly washed with ethanol and water, separating them with permanent magnets (Nd–Fe–B) with pull off forces of 2.35, 8.62, 20.65 kg, while separating the middle fraction of particles. For the subsequent staining of the particles, they



**Fig. 3.** SEM images of: a) original sample No.1 obtained by dispersion polymerization; b) sample No.1 after application of magnetic particles; c) sample No.1 after application of the dye and magnetic particles





**Fig. 4.** SEM images of: a) original sample No.2; b) sample No.2 after two-stage swelling; c) sample No.2 after application of the dye and magnetic particles

were transferred into deionized water containing 0.5 wt. % Pluronic F-127.

#### 2.4. The introduction of dyes into polymer microspheres

Cyanine fluorescent dyes Cy5 and Cy5.5 (Fig. 5) were introduced into particles by the diffusion method [21]. The dyes were dissolved in a tetrahydrofuran medium and added drop wise to a known amount of polymer magnetic particles dispersed in deionized water containing 0.5 wt. % Pluronic F-127. The dyes were left to diffuse into polymer spheres at 40 °C for 6 hours with constant stirring on a UT-4331S shaker. The spheres were separated with a magnet and washed with water several times, after which they were transferred to deionized water.

#### 2.5. Research methods

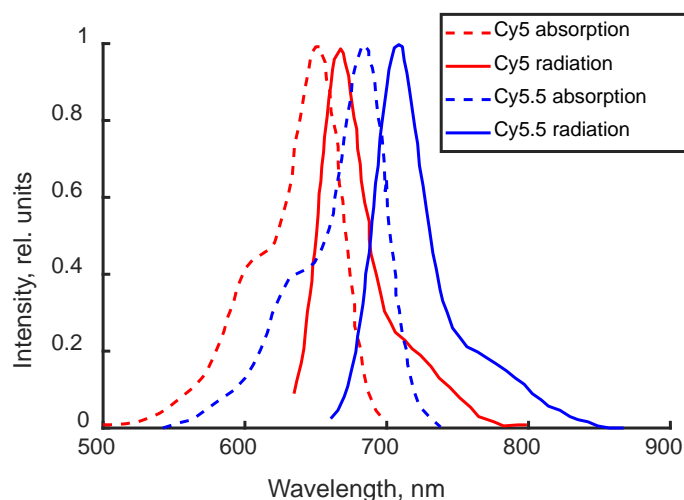
The study of the geometric parameters of the samples was carried out by of optical and electron

microscopy methods, as well as by the dynamic light scattering (DLS) method.

Scanning electron microscopy (SEM) images were obtained using a TM-1000 microscope (Hitachi, Japan).

The optical microscope LOMO BIOLAM M-1 (LOMO, Russia) was used in the optical microscopy experiments. ImageJ software (NIH, USA) was used for image processing and automatic analysis. The geometric parameters of at least 500 particles of each sample were measured for obtaining statistically reliable results in the course of automatic image analysis.

In the dynamic light scattering method, the investigated liquid dispersion of particles is irradiated by a laser and the scattered laser radiation is recorded. Since the particles are in continuous Brownian motion, local inhomogeneities of the refractive index appear,



**Fig. 5.** Absorption and fluorescence spectra of Cy5 and Cy5.5 dyes

which, when light passes through the medium, lead to fluctuations in the intensity of the scattered light. The diffusion coefficient is measured based on the analysis of the time autocorrelation function (ACF) of the scattered light intensity. The hydrodynamic radius of the particles is then calculated using the Stokes-Einstein formula.

The DLS method was used to study synthesized samples for the presence of large particle aggregates in them. According to the theory of light scattering for small particles with radius  $R$ , with a refractive index  $n_1$  in a liquid with a refractive index  $n_2$  scattered radiation intensity  $I$  is equal to:

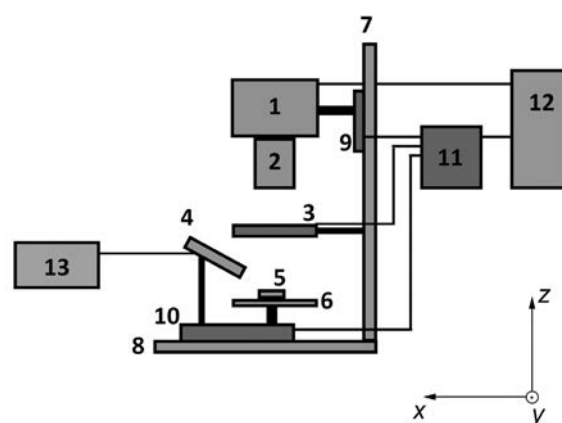
$$I = \frac{16\pi^4 R^6}{r^2 \lambda^4} \left( \frac{n^2 - 1}{n^2 + 2} \right)^2 \Psi I_0, \quad (1)$$

where  $r$  is the distance from the scattering region to the observation point,  $\lambda$  is the wavelength of the incident light beam,  $n$  – relative refractive index ( $n_2/n_1$ ),  $\psi$  is the angle between the direction of polarization of the incident wave and the direction of scattering,  $I_0$  – the intensity of the incident radiation,  $I$  – the intensity of the scattered radiation. From formula (1) it can be seen that the intensity of the scattered light is determined by the radius of the particle raised to the sixth power. Thus, when analysing a mixture of particles of different sizes by the DLS method, the intensity of the scattered light from larger particles will be significantly higher. In this regard, the method allows registering even small concentrations of large particles in a sample of a liquid dispersion.

The DLS measurements were carried out using a Photocor Complex particle size analyser (Photocor Ltd, Russia). A laser with a wavelength of 657 nm was used for the measurements. The measurements were carried out at a temperature of 23 °C. When calculating the hydrodynamic radius of particles, the viscosity of water at a given temperature – (0.9 cP) and the refractive index of the medium (1.332) were used. The ACF was measured for a scattering angle of 30°; the ACF accumulation time was 30 seconds. For each sample at least 10 measurements were carried out.

The experimental setup was developed for obtaining fluorescent images of spectrally

encoded microspheres, the scheme of the setup is shown in Fig. 6. A sample of the suspension of microspheres was placed in the optical cell on an object stage and illuminated with a laser. CPS635F laser with a wavelength of 635 nm (Thorlabs Inc., USA) was used to excite the fluorescence of cyanine dyes. For the registration of the fluorescence, bandpass filters 661/20 nm and 700/13 nm BrightLine (Semrock, USA) for Cy5 and Cy5.5, respectively, were used.



**Fig. 6.** Scheme of the experimental setup for fluorescence imaging of microspheres: 1 – camera, 2 – microscope lens, 3 – motorized filter wheel, 4 – laser, 5 – cell with a sample, 6 – object stage, 7, 8 – vertical and horizontal guides, 9 – linear translator for moving the camera along the axis  $z$ , 10 – linear translator for moving the sample along the axes  $x$ ,  $y$ ,  $z$ , 11 – linear translator controller, 12 – PC, 13 – laser power controller

A highly sensitive Kingfisher 6MP CCD camera (Raptor Photonics, UK) and a 20x microscope objective were used to obtain fluorescent images of microspheres. The analysis of the obtained images was carried out using the ImageJ program.

Samples were also analysed in a QuattroPlex analyser (Aivok LLC, Russia) for the assessment of the magnetic properties of particles. The device is designed for multiplex immunofluorescence analysis based on magnetic spectrally encoded microspheres. During the analysis, the microspheres are immobilized in the flow cell using a magnet, after which fluorescence images are obtained in different fluorescence channels. Conclusions about the magnetic properties of the particles can be drawn based on the obtained images.

### 3. Results and discussion

Despite the significant laboriousness of two-stage swelling, the method has become one of the main methods for obtaining particles with a size of more than two microns [22–24]. The corresponding theoretical basis of the method was actively developed due to problems with the quality of the product obtained by an alternative method - dispersion polymerization. For the use of the particles in multiplex immunofluorescence analysis, they must withstand “hard” solvents (e.g., toluene, tetrahydrofuran, etc.), which are used in the diffusion staining method and the method of introducing magnetite nanoparticles. Particles meeting these requirements can theoretically be obtained by the method of dispersion polymerization: the polymerization is carried out in the presence of a large proportion of the cross-linking agent in relation to the basic monomer. However, a significant disadvantage of the dispersion polymerization method in the presence of a significant amount of a crosslinking agent is uncontrolled aggregation of particles and a high value of the polydispersity coefficient of the resulting particles [25]. Over recent years, it was proposed to add a crosslinking agent after the end of the nucleation of the primary particles in order to solve the above problems in the dispersion polymerization method. However, the task of determining the optimal moment of adding the crosslinking agent is not trivial due to the wide range of conditions under which synthesis is usually carried out for obtaining the desired particle size and degree of polydispersity. Moreover, it remains unclear how the time of addition of the crosslinking agent will affect the crosslinking density in the resulting particle [26]. Therefore, a comparison of the properties of particles obtained by these two methods was made for the selection of particles with the desired properties: the degree of monodispersity, the proportion of impurities of irregular shape, magnetic properties, and the variation of fluorescence brightness.

#### 3.1. Particle size

Micrographs were obtained using optical microscopy for both microsphere samples. As a result of automatic image analysis, information was obtained on the average particle size, which

was  $2.2 \pm 0.7 \mu\text{m}$  for sample No.1 and  $6.5 \pm 0.4 \mu\text{m}$  for sample No.2.

The optimal particle size for use in a microsphere-based immunofluorescence assay is determined by instrumental and biochemical factors. Thus, the possibility of using particles of small diameter (less than  $0.5 \mu\text{m}$ ) is limited by the complexity of their detection, as well as by the low degree of adsorption of the analyte associated with the small surface area of the microspheres. These factors significantly reduce the sensitivity of the analysis. At the same time, the large surface area of the microspheres (with a diameter of more than  $9 \mu\text{m}$ ) can cause uneven distribution of the analyte during the analysis and the high consumption of expensive reagents (first of all – antibodies). For example, magnetic polystyrene microspheres prepared by spray suspension polymerization have a narrow size distribution, but a large average diameter of about  $10 \mu\text{m}$  [27].

Therefore, microspheres with sizes of  $2.2$  and  $6.5 \mu\text{m}$  are suitable for use in immunofluorescence assays.

#### 3.2. Particle shape

The particle shape different from spherical complicates the analysis of images in the process of immunofluorescence analysis and negatively affects its accuracy [28].

For a quantitative assessment of this parameter based on the obtained micrographs of the samples, the coefficient of roundness of particles was measured  $k_c$ :

$$k_c = 4\pi \frac{A}{P^2}, \quad (2)$$

where  $A$  is the area of the particle, and  $P$  is the length of its outer border in the image. Thus, the value  $k_c = 1$  corresponds to a perfect circle, and the values  $k_c$  approaching 0 correspond to a more elongated particle shape.

The measured values of the coefficient of roundness were  $0.90 \pm 0.02$  for sample No.1 and  $0.92 \pm 0.02$  for sample No.2. Thus, for both synthesized samples, the difference between the particle shape and spherical shape is insignificant and will not negatively affect the analysis results.

#### 3.3. The degree of monodispersity

Monodispersity of particles is also an important parameter. First, a high degree of monodispersity

is necessary for accurate identification of microspheres, since the fluorescence intensity of an individual microsphere depends on its size. This is especially important when microspheres are encoded with different concentrations of a fluorescent dye.

Second, the accuracy of determining the analyte concentration will depend on the degree of monodispersity, since the kinetics of the reaction on the surface of the microsphere and the fluorescence intensity of the label depend on the surface area of the particle [29].

The results of the study by optical microscopy indicate a rather high degree of monodispersity for both samples. The coefficient of variation was 7.4% for sample No.1 and 6.2% for sample No.2.

For comparison, the study [30] described microspheres synthesized by dispersion polymerization in an alcoholic medium, the coefficient of variation of the sizes of which ranged from 14.2 to 21.7%, depending on the amount of the stabilizer.

#### 3.4. The presence of impurities and particle aggregates

The presence of particle aggregates can have a negative effect on the results of immunofluorescence analysis, since such particles during the analysis will either provide a false signal of fluorescence or will not be taken into account in the analysis, depending on the parameters of the optical system and the parameters of image processing of the device [31].

The obtained micrographs of the synthesized samples contained individual particles of irregular shape. The relative concentration of impurities  $c_{imp}$  was measured according to optical microscopy data:

$$c_{imp} = \frac{N_{imp}}{N} \times 100 \%$$

where  $N_{imp}$  is the amount of impurities,  $N$  is the total number of particles. Impurities included particles recognized in images with the coefficient of roundness less than 0.8 or with the diameter different from the average by more than 30%.

The measured values  $c_{imp}$  were 4.1% for sample No.1 and 8.4% for sample No.2. In this case, a significant part of the impurities were large particle aggregates. Since it is difficult to distinguish particle aggregates from particles closely located in microphotographs according to optical microscopy data, synthesized samples of liquid dispersions of microparticles were studied by the DLS method. The DLS method allows registering even small concentrations of large particles in a sample of a liquid dispersion.

As a result, it was found that the composition of the liquid dispersion of microspheres of sample No.2 contains particles of large sizes, while sample No.1 practically does not contain large aggregates of particles (Fig. 7).

Sample No.2 was sonicated in an ultrasonic bath with a frequency of 22 kHz and a power

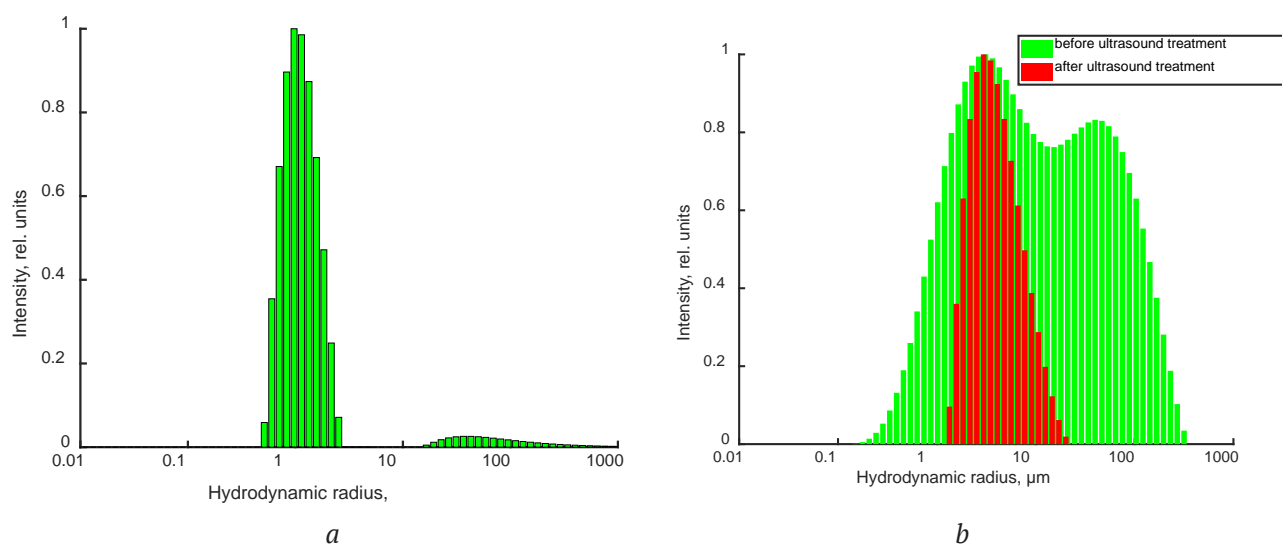


Fig. 7. The distribution of the scattered light intensity by particle size for samples No.1 (a) and No.2 (b)

of 75 W for 5 minutes. As a result of repeated measurements, it was found that there were no large aggregates in the dispersion (Fig. 7b). Thus, it can be concluded that the particles in sample No.2 are more prone to aggregation in comparison with sample No.1.

However, surfactants and stabilizers can be used for the prevention of the aggregation, moreover, particles used in immunofluorescence analysis have a shell of carboxyl groups, preventing particle aggregation [32, 33].

Thus, the revealed tendency to aggregation of particles in sample No. 2 should be taken into account in further study with microspheres. However, it is not a factor preventing the use of microspheres in immunoassay methods.

### 3.5. Magnetic properties

For the use of microspheres in planar immunoassay, they must have sufficient magnetic properties, for example, due to the high content of magnetite [34]. This condition is due to the need to immobilize the microspheres in the cell using a magnet for analysis [35].

In this study, the presence of magnetic properties in samples of synthesized microspheres was assessed visually using an optical microscope. A neodymium magnet was brought to the cell with microspheres in liquid dispersion. After that, the microspheres of both samples were aligned along the lines of magnetic induction, which indicates that the microspheres have magnetic properties.

The efficiency of immobilization of microspheres in a cell using a magnet was evaluated by analysing samples in a QuattroPlex device for multiplex immunofluorescence assay. During the analysis, the microspheres were immobilized in a flow cell using a magnet, after which fluorescence images were obtained in different fluorescence channels.

As a result of the study, it was found that the magnetic properties of the microspheres of both samples allow, firstly, to collect microspheres from the entire volume of the cell in one plane using a magnet, and secondly to keep them motionless for the time required to obtain fluorescent images in several channels (about 1 minute), preventing the displacement of microspheres under action of gravity, which is also important, since the

displacement of microspheres in images obtained in different channels does not allow to take them into account when analysing images during multiplex immunoassay.

### 3.6. Fluorescence

Microspheres of each type were stained with Cy5 and Cy5.5 fluorescent dyes separately and with both dyes at different concentrations.

We studied such fluorescence parameters of synthesized microspheres as fluorescence intensity (brightness of microspheres in the image) and uniformity of dye distribution.

The brightness of the microspheres in the image was compared with the brightness of the reference particles. It should be noted that the reference particles contained other fluorescent dyes and the corresponding filters were used to obtain images. Otherwise, the experimental conditions were identical. The purpose of this experiment was to find out whether it is possible to obtain fluorescent images of samples of synthesized microspheres with a comparable exposure time in the camera, and also to draw conclusions about the required concentration of the dye.

Luminex microspheres with the highest and lowest dye concentration (regions 12 and 78) were used as reference.

The resulting 16-bit images contained a distribution of  $2^{16}$  brightness gradations. The camera exposure was selected in a way, that the microspheres with the lowest dye concentration were distinguishable (that their brightness value in the image was twice the average brightness value for background noise), provided that the microspheres with the highest concentration of dye were not light-striking the image (i.e. their brightness value in the image did not exceed 65535 a.u.).

The images were analysed using the ImageJ software. Individual particles were identified by the intensity threshold in the image. Then the average intensity in the image of each detected particle was measured. In order to avoid false recognition of two aggregated particles as one, particles with a roundness value less than 0.8 were ignored. The roundness value was calculated using the formula (2).

As a result, for the synthesized samples, the selected exposure value in both fluorescence

channels (corresponding to Cy5 and Cy5.5) was 5 seconds for sample No.1 and 20 seconds for sample No.2, with a exposure time of 3.5 seconds for reference microspheres. Thus, we can conclude that for sample No.1 the selected dye concentrations were close to optimal, and for sample No.2 the concentration of the dye should be increased in order to reduce the analysis time.

The uniformity of the distribution of the dye for individual microspheres of the same sample is an important parameter, since it determines the spread of the brightness of the microspheres in the image. Due to the fact that the dynamic range of the camera is limited, the maximum possible number of distinguishable types of microspheres and, consequently, the multiplexing of the analysis depend on the spread in the brightness of one type of microspheres.

Based on the analysis of the obtained images, the values of the coefficient of variation of the fluorescence intensity were calculated, which characterize the variation of the brightness of microspheres of the same type (Table 1). In [36], a method for the synthesis of particles with a high degree of homogeneity and a fluorescence variation coefficient of 3.7%; was described,

however, such particles had a large size (from 10  $\mu\text{m}$ ) and were not magnetic. Therefore, Luminex magnetic fluorescent microspheres were chosen as reference particles for comparison. The analysis was carried out on 5 fluorescence images for each sample of microspheres in both fluorescence channels.

It can be seen that microspheres of sample No.2 were characterized by a greater variation of brightness in both fluorescence channels. Thus, sample No.1 had the most uniform distribution of the fluorescent dye, which made it more promising for use in immunofluorescence analysis.

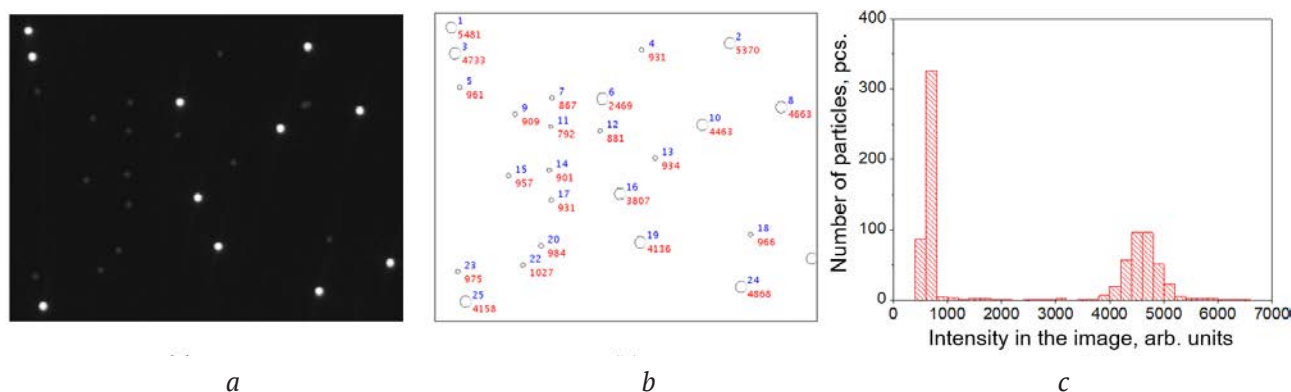
Fluorescence images for a mixture of two types of microspheres of sample No.1, differing in the concentration of one dye were also obtained. As a result, it was shown that it is possible to identify microspheres with different dye concentration by brightness in the image (Fig. 8).

Fluorescent images of two types of microspheres of sample No.1, containing both fluorescent dyes at different concentrations were also obtained.

As a result of the analysis of the obtained images, it was shown that the coefficient of variation of the fluorescence intensity in the

**Table 1.** Coefficient of variation of the fluorescence intensity of microspheres

Sample	Coefficient of variation of the fluorescence intensity, %	
	Cy5 / Dye 1	Cy5.5 / Dye 2
Sample No.1	8.8 $\pm$ 0.2	9.4 $\pm$ 0.3
Sample No.2	16.1 $\pm$ 0.6	19.6 $\pm$ 0.8
Reference microspheres	7.4 $\pm$ 0.2	7.9 $\pm$ 0.2



**Fig. 8.** a) Fragment of the obtained fluorescent image of a mixture of microspheres of sample No.1 with high and low concentration of the dye Cy5; b) analysis of the same fragment of the image: the upper number is the number of the particle detected in the image; the lower number is the average fluorescence intensity of the detected particle; c) the distribution of microspheres with different fluorescence intensities in the resulting image

image for both types of fluorescent dyes and for both samples of microspheres with different concentrations of dyes was also less than 10% (Fig. 9).

The low coefficient of variation of the fluorescence intensity allows encoding a large number of microsphere types, at least 36 regions, by introducing different concentrations of a fluorescent dye. This number is sufficient for the vast majority of applications of the multiplex immunofluorescence analysis.

#### 4. Conclusions

As a result of the studies, it was found that the microspheres in both samples have optimal sizes for the use in immunofluorescence analysis and a high degree of monodispersity, do not contain a statistically significant amount of irregular impurities. The magnetic properties of the microspheres of both samples make it possible to quickly and reliably immobilize the microspheres in one plane of the measuring cell using a magnet. At the same time, the microspheres synthesized by the two-stage swelling method are characterized by a larger spread in the fluorescence brightness. Therefore, from the point of view of the uniformity of the distribution of the fluorescent dye, the use of microspheres synthesized by dispersion

polymerization seems to be more promising for use in immunofluorescence analysis.

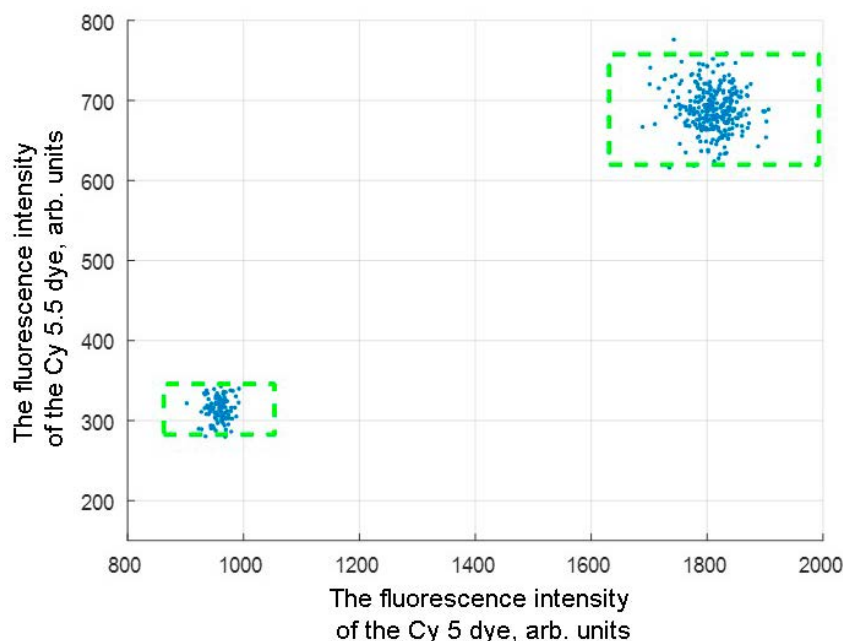
The possibility of identifying microspheres with different dyes and different concentration of dyes in the image was shown. The low coefficient of variation of the fluorescence intensity makes it possible to use a large number of types of spectrally encoded microspheres in immunofluorescence analysis, and, therefore, to identify a large number of pathogens simultaneously. The obtained results can be used to develop new diagnostic multiplex test systems based on spectrally encoded microspheres.

#### Conflict of interests

The authors declare that they have no known competing financial interests or personal relationships that could have influenced the work reported in this paper.

#### References

1. Gu Z., Zhao, S., Xu G., Chen C., Wang Y., Gu H., Xu H. Solid-phase PCR based on thermostable, encoded magnetic microspheres for simple, highly sensitive and multiplexed nucleic acid detection. *Sensors and Actuators B: Chemical*. 2019;298: 126953. <https://doi.org/10.1016/j.snb.2019.126953>
2. Su R., Tang X., Feng L., Yao G. L., Chen J. Development of quantitative magnetic beads-based flow



**Fig. 9.** The result of the analysis of the obtained fluorescent images of two types of microspheres with dyes Cy5 and Cy5.5 for the sample No.1. Dotted rectangles correspond to 10% deviation from the mean

cytometry fluorescence immunoassay for aflatoxin B1. *Microchemical Journal*. 2020;155: 104715. <https://doi.org/10.1016/j.microc.2020.104715>

3. Klisara N., Peters J., Haasnoot W., Nielen M. W., Palaniappan A., Liedberg B. Functional fluorescence assay of botulinum neurotoxin A in complex matrices using magnetic beads. *Sensors and Actuators B: Chemical*: 2019;281: 912–919. <https://doi.org/10.1016/j.snb.2018.10.100>

4. Jin M., Luo J., Dou X., Yang M., Fan Z. A sensitive cytometric bead array for chlorpyrifos using magnetic microspheres. *Microchemical Journal*. 2020;156: 104847. <https://doi.org/10.1016/j.microc.2020.104847>

5. Ding L., Chen X., He L., Yu F., Yu S., Wang J., Qu L. Fluorometric immunoassay for the simultaneous determination of the tumor markers carcinoembryonic antigen and cytokeratin 19 fragment using two kinds of CdSe/ZnS quantum dot nanobeads and magnetic beads. *Microchimica Acta*. 2020;187(3): 1–8. <https://link.springer.com/article/10.1007/s00604-019-3914-7>

6. Wei X., Bian F., Cai X., Wang Y., Cai L., Yang J., Zhao Y. Multiplexed detection strategy for bladder cancer microRNAs based on photonic crystal barcodes. *Analytical Chemistry*. 2020;92(8): 6121–6127. Available at: <https://pubs.acs.org/doi/10.1021/acs.analchem.0c00630>

7. Priest J. W., Moss D. M. Measuring cryptosporidium serologic responses by multiplex bead assay. In: Mead J., Arrowood M. (eds). *Cryptosporidium. Methods in Molecular Biology*, vol. 2052. New York, NY: Humana; 2020. 61–85 p. [https://doi.org/10.1007/978-1-4939-9748-0\\_5](https://doi.org/10.1007/978-1-4939-9748-0_5)

8. Chen J. H.-K., Yip C. C.-Y., Chan J. F.-W., Poon R. W. S., To K. K.-W., Chan K. H., Yuen K. Y. Clinical performance of the luminex NxTAG CoV extended panel for SARS-CoV-2 detection in nasopharyngeal specimens of COVID-19 patients in Hong Kong. *Journal of Clinical Microbiology*. 2020;58(8): e00936-20. <https://doi.org/10.1128/jcm.00936-20>

9. Wilson R., Spiller D. G., Prior I. A., Veltkamp K. J., Hutchinson A. A simple method for preparing spectrally encoded magnetic beads for multiplexed detection. *ACS Nano*. 2007;1(5): 487–493. <https://pubs.acs.org/doi/abs/10.1021/nn700289m>

10. Graham H., Chandler D. J., Dunbar S. A. The genesis and evolution of bead-based multiplexing. *Methods*. 2019;158: 2–11. <https://doi.org/10.1016/j.ymeth.2019.01.007>

11. Ligler F. S., Kim J. S. *The Microflow Cytometer*. Boca Raton: Pan Stanford Publ.; 2010. 394 p. <https://doi.org/10.1201/9780429109157>

12. Dunbar S. A. Bead-based suspension arrays for the detection and identification of respiratory viruses. In: Tang Y. W., Stratton C. (eds) *Advanced techniques in diagnostic microbiology*. Boston, MA; Springer: 2013.

813–833 pp. [https://doi.org/10.1007/978-1-4614-3970-7\\_42](https://doi.org/10.1007/978-1-4614-3970-7_42)

13. Mountjoy K. G. ELISA versus LUMINEX assay for measuring mouse metabolic hormones and cytokines: sharing the lessons I have learned. *Journal of Immunoassay and Immunochemistry*. 2020: 1–20. <https://doi.org/10.1080/15321819.2020.1838924>

14. Ligler F. S., Erickson J. S., Golden J. P., Kim J. S., Nasir M., Howell P. J., Thangawng A. L., Hilliard L., Anderson G. P. Microflow cytometer. In: *Proc. SPIE 7167, Frontiers in Pathogen Detection: From Nanosensors to Systems, 71670N, 19 February 2009*. <https://doi.org/10.1117/12.807671>

15. Germeraad E. A., Achterberg R.P., Venema S., Post J., de Leeuw O., Koch G., van der Wal F.J., Beersens N. The development of a multiplex serological assay for avian influenza based on Luminex technology. *Methods*. 2019;158: 54–60. <https://doi.org/10.1016/j.ymeth.2019.01.012>

16. Choi J., Kwak, S. Y., Kang S., Lee S. S., Park M., Lim S., Hong S. I. Synthesis of highly crosslinked monodisperse polymer particles: effect of reaction parameters on the size and size distribution. *Journal of Polymer Science Part A: Polymer Chemistry*. 2002;40(23): 4368–4377. <https://doi.org/10.1002/pola.10514>

17. Barrett K. E. *Dispersion polymerization in organic media*. New York: John Wiley & Sons, Inc.; 1975. 338 p.

18. Lok K. P., Ober C. K. Particle size control in dispersion polymerization of polystyrene. *Canadian Journal of Chemistry*. 1985;63(1): 209–216. <https://doi.org/10.1139/v85-033>

19. Ugelstad J., Mork P. C., Kaggerud K. H., Ellingsen T., Berge A. Swelling of oligomer-polymer particles. New methods of preparation. *Advances in Colloid and Interface Science*. 1980;13(1-2): 101–140. [https://doi.org/10.1016/0001-8686\(80\)87003-5](https://doi.org/10.1016/0001-8686(80)87003-5)

20. Ugelstad J., Mfutakamba H. R., Mørk P. C., Ellingsen T., Berge A., Schmid R., Nustad K. Preparation and application of monodisperse polymer particles. *Journal of Polymer Science: Polymer Symposia*. 1985;72(1): 225–240. <https://doi.org/10.1002/polc.5070720125>

21. Lee J. H., Gomez I. J., Sitterle V. B., Meredith J. C. Dye-labeled polystyrene latex microspheres prepared via a combined swelling-diffusion technique. *Journal of Colloid and Interface Science*. 2011;363(1): 137–144. <https://doi.org/10.1016/j.jcis.2011.07.047>

22. Ugelstad J.; Kaggerud K. H.; Hansen F. K.; Berge A. Absorption of low molecular weight compounds in aqueous dispersions of polymer-oligomer particles. A two step swelling process of polymer particles giving an enormous increase in absorption capacity. *Die Makromolekulare Chemie*. 1979;180(3):



737–744. <https://doi.org/10.1002/macp.1979.021800317>

23. Okubo M., Shiozaki M., Tsujihiro M., Tsukuda Y. Preparation of micron-size monodisperse polymer particles by seeded polymerization utilizing the dynamic monomer swelling method. *Colloid and Polymer Science*. 1991;269(3): 222–226. <https://doi.org/10.1007/bf00665495>

24. Bedre J., Chandler D., Mize B. *Method and system for manufacture and use of macroporous beads in a multiplex assay*. Patent US9745438B2. 2009. Режим доступа: <https://patents.google.com/patent/US9745438B2>

25. Song J.S., Winnik M.A. Cross-linked, monodisperse, micron-sized polystyrene particles by two-stage dispersion polymerization. *Macromolecules*. 2005;38(20): 8300–8307. DOI: <https://doi.org/10.1021/ma050992z>

26. Gao H., Matyjaszewski K. Synthesis of functional polymers with controlled architecture by CRP of monomers in the presence of cross-linkers: From stars to gels. *Progress in Polymer Science*. 2009;34(4): 317–350. <https://doi.org/10.1016/j.progpolymsci.2009.01.001>

27. Yang C., Guan Y., Xing J., Liu J.; Shan G., An Z., Liu H. Preparation of magnetic polystyrene microspheres with a narrow size distribution. *AIChE Journal*. 2005;51(7): 2011–2015. <https://doi.org/10.1002/aic.10467>

28. Šálek P., Horák D. Hypercrosslinked polystyrene microspheres by suspension and dispersion polymerization. *e-Polymers*. 2011;11(1). <https://doi.org/10.1515/epoly.2011.11.1.688>

29. Kawaguchi H. Functional polymer microspheres. *Progress in Polymer Science*. 2000;25(8): 1171–1210. [https://doi.org/10.1016/S0079-6700\(00\)00024-1](https://doi.org/10.1016/S0079-6700(00)00024-1)

30. Hong J., Lee J., Rhym Y. M., Kim D. H., Shim S. E. Polyelectrolyte-assisted synthesis of polystyrene microspheres by dispersion polymerization and the subsequent formation of silica shell. *Journal of Colloid and Interface Science*. 2010;344(2): 410–416. <https://doi.org/10.1016/j.jcis.2010.01.001>

31. Liu N., Li Y., Liang W., Liu Y. Fluorescence-encoded polystyrene microspheres for the application of suspension array technology. *Materials for Biomedical Engineering*. 2019: 221–267. <https://doi.org/10.1016/b978-0-12-818433-2.00007-8>

32. Tobias C., Climent E., Gawlitza K., Rurack K. Polystyrene microparticles with convergently grown mesoporous silica shells as a promising tool for multiplexed bioanalytical assays. *ACS Applied Materials & Interfaces*. 2020;13(1): 207–218. <https://doi.org/10.1021/acsmi.0c17940>

33. Serkhacheva N. S., Gainanova A. A., Kuz'micheva G. M., Podbelskiy V. V., Sadovskaya N. V., Zybinskiy A. M., Domoroshchina E. N., Dorokhov A. V.,

Chernyshev V. V., Prokopov N. I., Gerval'd A. Yu. Composites based on polystyrene microspheres with nano-scaled titanium dioxide. *International Journal of Polymer Analysis and Characterization*. 2015;20(8): 743–753. <https://doi.org/10.1080/1023666x.2015.1081190>

34. Liu G., Guan Y., Ge Y., Xie L. Preparation of monodisperse magnetic polystyrene microspheres and its surface chemical modification. *Journal of Applied Polymer Science*. 2011;120(6): 3278–3283. <https://doi.org/10.1002/app.33495>

35. Pushparaj P. N. Multiple analyte profiling (xMAP) technology coupled with functional bioinformatics strategies: potential applications in protein biomarker profiling in autoimmune inflammatory diseases. In: Shaik N., Hakeem K., Banaganapalli B., Elango R. (eds). *Essentials of Bioinformatics, Volume II*. Springer, Cham.; 2019. 151–165 pp. [https://doi.org/10.1007/978-3-030-18375-2\\_9](https://doi.org/10.1007/978-3-030-18375-2_9)

36. Fulwyler M. J., Perrings J. D., Cram L. S. Production of uniform microspheres. *Review of Scientific Instruments*. 1973;44(2): 204–206. <https://doi.org/10.1063/1.1686082>

## Information about the authors

*Pavel V. Shalaev*, Engineer, National Research Center for Epidemiology and Microbiology named after Honorary Academician N.F. Gamaleya of the Ministry of Health of the Russian Federation, Moscow; Postgraduate Student, National Research University of Electronic Technology - MIET, Zelenograd, Moscow; Leading Development Engineer, Aivok LLC, Zelenograd, Moscow, Russian Federation; e-mail: [shalaev.pv@gmail.com](mailto:shalaev.pv@gmail.com). ORCID iD: <https://orcid.org/0000-0003-0552-9715>.

*Ekaterina V. Bondina*, Master Student, National Research University of Electronic Technology - MIET, Zelenograd, Moscow, Russian Federation; engineer, Aivok LLC, Zelenograd, Moscow, Russian Federation; e-mail: [e\\_bondina97@mail.ru](mailto:e_bondina97@mail.ru). ORCID iD: <https://orcid.org/0000-0002-1986-7961>.

*Natalya N. Sankova*, Postgraduate Student, Novosibirsk State University, Novosibirsk; Researcher Associate, Boreskov Institute of Catalysis of the Siberian Branch of the Russian Academy of Sciences, Novosibirsk, Russian Federation; e-mail: [natali\\_9999@bk.ru](mailto:natali_9999@bk.ru). ORCID iD: <https://orcid.org/0000-0002-1913-5293>.

*Ekaterina V. Parkhomchuk*, PhD in Chemistry, Senior Researcher, Novosibirsk State University, Novosibirsk; Senior Researcher, Boreskov Institute of Catalysis of the Siberian Branch of the Russian Academy of Sciences, Novosibirsk, Russian Federation; e-mail: [ekaterina@catalysis.ru](mailto:ekaterina@catalysis.ru). ORCID iD: <https://orcid.org/0000-0003-2200-884X>.

*Sergey A. Dolgushin*, PhD in Physics and Mathematics, Senior Researcher, National Research Center for Epidemiology and Microbiology named after Honorary Academician N.F. Gamaleya of the Ministry of Health of the Russian Federation, Moscow; Director, Aivok LLC, Zelenograd, Moscow, Russian Federation;

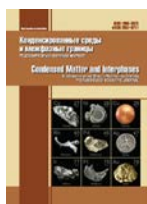
e-mail: [dolgushin.sergey@gmail.com](mailto:dolgushin.sergey@gmail.com). ORCID iD: <https://orcid.org/0000-0002-6965-6409>.

All authors have read and approved the final manuscript.

*Received 2 December 2020; Approved after reviewing 20 January 2021; Accepted 15 February 2021; Published online 25 March 2021*

*Translated by Valentina Mittova*

*Edited and proofread by Simon Cox*



## Original articles

Original article

<https://doi.org/10.17308/kcmf.2021.23/3313>

## Synthesis, structure and superconducting properties of laminated thin film composites of $\text{YBa}_2\text{Cu}_3\text{O}_{7-\delta}/\text{Y}_2\text{O}_3$ as components of 2G HTS wires

A. E. Shchukin<sup>1</sup>✉, A. R. Kaul<sup>1</sup>, A. L. Vasiliev<sup>2,3</sup>, I. A. Rudnev<sup>4</sup><sup>1</sup>Chemistry Department, Lomonosov Moscow State University, GSP-1, Leninskie Gory, Moscow 119991, Russian Federation<sup>2</sup>National Research Center “Kurchatov Institute”, 1 Akademika Kurchatova pl., Moscow 123182, Russian Federation<sup>3</sup>Shubnikov Institute of Crystallography Russian Academy of Sciences 59 Leninsky pr., Moscow 119333, Russian Federation<sup>4</sup>National Research Nuclear University “Moscow Engineering Physics Institute”, 31 Kashirskoe shosse, Moscow 115409, Russian Federation**Abstract**

2G HTS wires are capable of transferring huge amounts of electrical energy without loss. An increase in the current-carrying capacity in these materials is possible due to an increase in the thickness of the superconducting layer; however, there is a problem with the appearance of impurity orientations and other defects with increasing thickness. We have proposed a solution of this problem by increasing the thickness of the superconducting layer by the MOCVD method using interlayers of yttrium oxide.

The aim of this study was the production of thick composite films with yttrium oxide interlayers and high critical current density. In addition, we want to show the effectiveness of the approach of introducing yttrium oxide interlayers for the reduction of the number of parasitic orientations and defects with an increase in HTS film thickness.

The deposition of  $\text{YBa}_2\text{Cu}_3\text{O}_{7-\delta}$  and  $\text{Y}_2\text{O}_3$  films was carried out layer by layer using reel-to-reel MOCVD equipment. A 12 mm wire of the following architecture was used as a substrate: 200 nm  $\text{CeO}_2(\text{Gd}_2\text{O}_3)/30-50$  nm  $\text{LaMnO}_3/5-7$  nm IBAD-MgO/50 nm  $\text{LaMnO}_3/50$  nm  $\text{Al}_2\text{O}_3/60$   $\mu\text{m}$  Hastelloy 276. The resulting films were annealed in oxygen for obtaining the orthorhombic YBCO phase.

$\text{YBa}_2\text{Cu}_3\text{O}_{7-\delta}/\text{Y}_2\text{O}_3$  composites were obtained. In these composites, obtained using the MOCVD method, the amount of side ( $c_{\parallel}$ ) orientation of the HTS layer was reduced and high values of the critical current density, exceeding 1 MA/cm at a thickness of  $> 2$   $\mu\text{m}$  remained. The efficiency of the approach of introducing yttrium oxide interlayers for the increase in the current characteristics with increasing film thickness was shown. It was found that further thickening of films with interlayers is prevented by the formation of nanopores, reducing the critical current density.

**Keywords:** YBCO, MOCVD, Heterostructures, Buffer layers,  $\text{Y}_2\text{O}_3$ , HTS, Superconductor

**Acknowledgements:** the study was carried out within the framework of the RFMEFI 58214X0005 project with the support of the Ministry of Education and Science within the framework of event 1.4 “Applied research aimed at solving complex scientific and technological problems.”

**For citation:** Shchukin A. E., Kaul A. R., Vasiliev A. L., Rudnev I. A. Synthesis, structure and superconducting properties of laminated thin film composites  $\text{YBa}_2\text{Cu}_3\text{O}_{7-\delta}/\text{Y}_2\text{O}_3$  as the components of 2G HTS wires. *Kondensirovannyye sredy i mezhfaznye granitsy = Condensed Matter and Interphases*. 2021;23(1): 122–139. <https://doi.org/10.17308/kcmf.2021.23/3313>

✉ Shchukin Alexander E., email: [aleksandr.shukin@mail.ru](mailto:aleksandr.shukin@mail.ru)

© Shchukin A. E., Kaul A. R., Vasiliev A. L., Rudnev I. A., 2021



The content is available under Creative Commons Attribution 4.0 License.

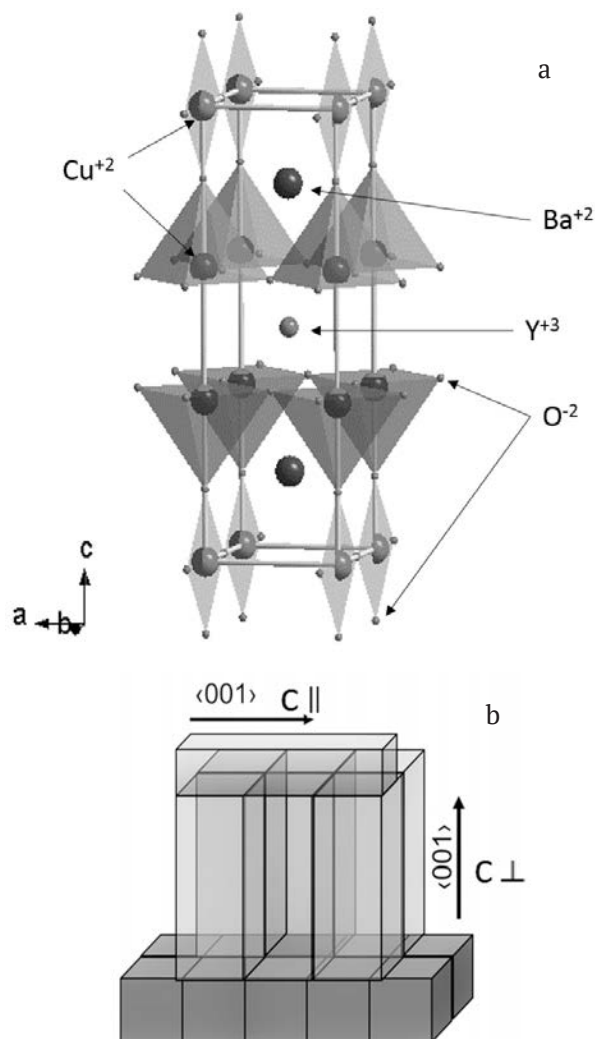
**Для цитирования:** Шукин А. Е., Кауль А. Р., Васильев А. Л., Руднев И. А. Синтез, структура и сверхпроводящие свойства тонкопленочных слоистых композитов  $\text{YBa}_2\text{Cu}_3\text{O}_{7-\delta}/\text{Y}_2\text{O}_3$  как компонентов ВТСП-лент второго поколения. *Конденсированные среды и межфазные границы*. 2021;23(1): 122–139. <https://doi.org/10.17308/kcmf.2021.23/3313>

## 1. Introduction

The last 15 years in the field of applied superconductivity have been marked by the development of technology for the production of long wires, in which the current-carrying layer is a thin film of high-temperature superconductor  $\text{RBa}_2\text{Cu}_3\text{O}_{7-x}$  (RBCO, R = REE, Y) grown epitaxially on oxide buffer layers covering the base metal wire. Such materials, called 2G HTS wires (2G coated conductors), have already proven their effectiveness in the electric power industry for the transmission of electricity through superconducting cables, for production of motors, generators, current limiters, transformers and other electrical equipment with record power and weight and size characteristics [1, 2]. The development of magnets for accelerators and fusion reactors, 10 MW wind turbines, superconducting energy storage devices, levitation bearings, high-resolution medical tomographs and many other fundamentally new devices for various fields of technology, from the extractive industries to aerospace industry is performed using 2G HTS wires [3–7]. The efficiency of superconducting materials directly depends on the critical current density characterizing them ( $j_c$ ). The high  $j_c$  values, inherent to RBCO heteroepitaxial thin films, occur for two reasons: 1) their structure approaches a two-dimensional mosaic monocrystal with a small misorientation of neighbouring grains, which reduces the likelihood of the appearance of the so-called “weak links” characteristic for polycrystalline HTS ceramics and strongly limiting  $j_c$ ; 2) their structure contains a large number of nonequilibrium defects – misfit dislocations, packing defects, antistructural defects formed during film growth, and preventing magnetic vortex creep. However, along with the listed “useful” defects in RBCO films, morphological defects reducing the  $j_c$  value are often formed. First of all, such defects include crystallites with the orientation of the  $\text{CuO}_2$  planes perpendicular to the substrate plane. It is known [8, 9] that the crystal structure of the  $\text{RBa}_2\text{Cu}_3\text{O}_{7-\delta}$  orthorhombic phases (Fig. 1a) is highly anisotropic, and the superconducting

current in them propagates along the  $\text{CuO}_2$ , therefore, the achievement of the maximum  $j_c$  values requires RBCO film growth in the  $\langle 001 \rangle$  direction, e.g. along the  $c$  axis, perpendicular to the substrate plane ( $c_\perp$  in Fig. 1b). The growth of RBCO films with other axial orientations ( $a$  and  $b$  oriented growth, hereinafter not distinguished by us and denoted as  $c_\parallel$ ) not only significantly reduces the superconducting current [10], but also prevents a further increase in the thickness of the  $c_\perp$  oriented film.

In many studies devoted to the formation and properties of superconducting epitaxial  $c_\perp$  RBCO



**Fig. 1.** Structure  $\text{YBa}_2\text{Cu}_3\text{O}_{7-\delta}$  (a); Schematic picture of  $c_\perp$  grains heteroepitaxy and further  $c_\parallel$  RBCO grains growth (b)

films, the problem of obtaining high  $j_c$  values in the upper layers of films with a thickness of about  $1\ \mu\text{m}$  was revealed [11, 12]. With increasing thickness, the oriented crystallization of the layers changes from the predominant  $c_\perp$  to the preferential  $c_\parallel$  (Fig. 1b). This phenomenon does not allow an arbitrary increase in the value of the superconducting current by a proportional thickness increase of the RBCO layers. Discussing various physicochemical reasons for switching the growth direction, it is important to understand that the  $c_\perp$  orientation is thermodynamically preferable (corresponds to the minimum energy of the heteroepitaxial system), and the appearance of the  $c_\parallel$ -orientation is caused by kinetic reasons. The deposition of the HTS layer is carried out by various methods, but in all cases it is performed on a substrate heated to  $750\text{--}900\ \text{°C}$ . Increasing the thickness of the HTS layer leads to a decrease in the actual temperature of the growth surface and slows down the mass transfer in the surface layer. Under these conditions (as well as at an insufficiently high temperature of film deposition and/or an excessively high rate of their deposition), the  $c_\parallel$ -orientation becomes advantageous, since the fastest growth occurs along  $ab$ -planes, which is typical for all layered crystals. The complete match of the unit cell (UC) parameters at the interface  $c_\parallel/c_\perp$  (Fig. 1b) contributes to the nucleation of crystallites with a  $c_\parallel$ -orientation, i.e., crystallites oriented as  $c_\perp$ , prove to be an excellent substrate for the growth of  $c_\parallel$ -oriented crystallites. The critical nucleus of  $c_\parallel$ -oriented crystallites in this situation has a minimum size, and its formation is characterized by a minimum energy barrier [13].

According to the literature, for the suppression of grain growth in the  $c_\parallel$ -orientation it is recommended to change the deposition conditions of HTS layers as their thickness grows, namely: an increase in the deposition temperature, a decrease in oxygen pressure (which also increases the diffusion mobility in R-Ba-Cu-O systems) and/or a decrease in the deposition rate [14]. Another approach recommended in [13, 15], proposes the use of buffer layers with an increased mismatch of the UC parameters in HTS/buffer layer interface.

In this study, we proposed suppressing the growth of  $c_\parallel$ -crystallites by introducing intermediate  $\text{Y}_2\text{O}_3$  layers of nanometer-scale

thickness in YBCO matrix. Yttrium oxide forms heteroepitaxial boundaries with YBCO, since the difference between UC and YBCO parameters is small, its introduction should not prevent  $c_\perp$  YBCO epitaxial growth. It was previously noted [16] that in thin YBCO films containing an excess of  $\text{Y}_2\text{O}_3$ , the density of  $c_\parallel$ -crystallites decreases. These features allowed us to assume that laminated two-phase composites YBCO/ $\text{Y}_2\text{O}_3$  deposited to metal wires with biaxially textured buffer layers can be formed with a predominant  $c_\perp$  orientation of crystallites to a higher thickness than layers of stoichiometric composition ( $\text{YBa}_2\text{Cu}_3\text{O}_{7-8}$ ), and therefore, with equal thickness, they can have a higher critical current density.

The deposition of HTS layers was carried out on moving substrate wires used in the 2G HTS wire technology by metal-organic chemical vapour deposition (MOCVD). The peculiarity of this method is the transport of the film's metal components to the reactor in the form of vapours of metal-organic volatile compounds (precursors). In presence of oxygen these components decompose on a heated substrate with the formation of an oxide film. This method allows the formation of films, uniform in composition and thickness, on the substrates of complex shapes and large area, including the continuous sputtering of a film on a long metal wire in reel-to-reel mode. Today, MOCVD technology is one of the most popular in the production of 2G HTS wires, and wires obtained using this technology are not inferior in characteristics to wires formed by laser ablation [17].

This study presents the results of comparative studies of the texture, microstructure, and current-carrying properties of YBCO films and two-phase laminated YBCO/ $\text{Y}_2\text{O}_3$  composites of various thicknesses.

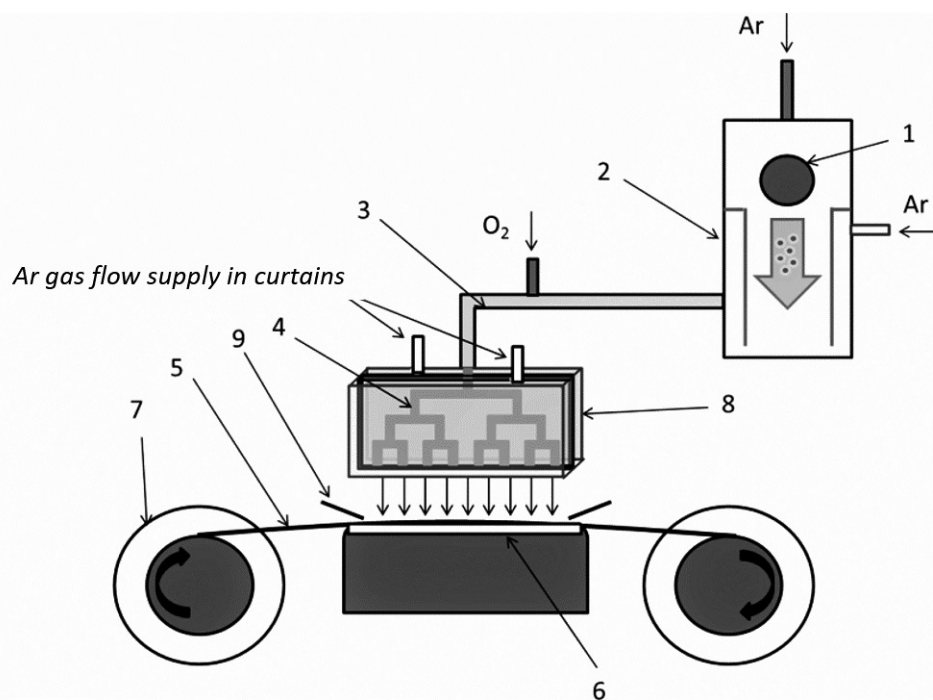
## 2. Experimental

The deposition of films was carried out using reel-to-reel MOCVD equipment (Fig. 2). Solid mixtures of complex compounds of yttrium, barium, and copper with dipivaloylmethane were used as precursors:  $\text{Y}(\text{thd})_3$ ,  $\text{Ba}(\text{thd})_2$  (tetraglyme),  $\text{Cu}(\text{thd})_2$ . Since the long-term exposure of the precursors at high temperatures leads to the gradual loss of their ability to sublimation, the sublimation was carried out by the flash

evaporation of micro-portions of the solid mixture of the listed precursors. For this, a tablet (1) obtained by pressing previously purified by sublimation (in the case of  $\text{Ba}(\text{thd})_2$  (tetraglyme) - recrystallization) and thoroughly mixed precursors, was placed in an automatic dispenser, which includes a device for microstepping the tablet and a knife moving reciprocally in the direction transverse to the axis of tablet movement. With the simultaneous movement of the tablet and the knife, very thin layers of the precursor mixture were cut off, which turned into a continuous stream of fine particles. Then these particles, entrained by the argon flow, entered the evaporator (2), heated to 335 °C, where they were instantly evaporated. From the evaporator, the flow of Ar and precursor vapours were directed along a metal tube heated to 320 °C (3) into the hot ( $T = 350$  °C) distributor unit (4), in which it was mixed with an oxygen flow and divided into 8 equal parts, uniformly distributed along the entire length of the deposition zone (5). On both sides of the precursor vapour outlet openings into the deposition zone, there were outlets for additional argon flow, which forms gas “curtains” (8), directing the precursor vapours onto the substrate wire which is heated to 820–850 °C. A

reel with the rewind ability (7), driven by a stepper motor, allowed setting the required rewind speed (up to 30 mm/s), and a braking asynchronous motor on the feed reel allowed to keep the wire tension necessary for reliable thermal contact of the wire with the heated “table”. When the precursors vapours with oxygen reached the heated substrate wire, oxidative thermolysis occurred with the formation of an oxide film on the substrate surface. The gas products of this reaction, together with the unreacted vapours of the precursors, were pumped out by a pump supplied with dust filter. The pressure of 3.5 mbar was maintained in the reactor by a control valve at the outlet of the reactor. All gas flows were controlled by gas flow regulators. For the deposition of the HTS film, an extensive preliminary study on the selection of the optimal gas flows and temperatures for each of the heating zones of the MOCVD unit was performed.

As substrates, metal wires made of the heat-resistant Hastelloy 276 alloy, covered with buffer layers with the following multilayer architecture: 200 nm  $\text{CeO}_2(\text{Gd}_2\text{O}_3)/30\text{--}50$  nm  $\text{LaMnO}_3/5\text{--}7$  nm  $\text{IBAD-MgO}/50$  nm  $\text{LaMnO}_3/50$  nm  $\text{Al}_2\text{O}_3/60$   $\mu\text{m}$  Hastelloy were used. The amorphous  $\text{Al}_2\text{O}_3$  layer prevented the oxidation of the metal wire and



**Fig. 2.** MOCVD equipment scheme: Precursor tablet (1), Evaporator (2), Transportation pipe (3), Distributor (4), Wire (5), “Table” (6) with heating, Reel with rewinding (7), “Curtains” (8), Windscreens (9), that restrict precursor deposition on unheated wire parts

the diffusion of its components into the HTS layer during its high-temperature deposition; the next  $\text{LaMnO}_3$  layer reduced the roughness of the growth surface and prevented the interaction of the  $\text{Al}_2\text{O}_3$  and  $\text{MgO}$  layers. The biaxial texture was created in  $\text{MgO}$  layer applied over  $\text{LaMnO}_3$  by ion beam assisted deposition (IBAD). The biaxial texture was transferred epitaxially to the deposited  $\text{LaMnO}_3$  layer and then to the final buffer layer of  $\text{CeO}_2(\text{Gd}_2\text{O}_3)$  solid solution, which has a slight mismatch between the UC and YBCO parameters, also contributing to a decrease in the number of  $c_{\parallel}$ -oriented crystallites in the film [18–21]. All used substrates were 12 mm wide; therefore, the absolute values of the critical current given below refer to this width of the superconducting layer.

It is known that the MOCVD process of multicomponent compounds is incongruent, since the precursors of different metals have differing values of volatility and thermal stability. Therefore, the deposition process of superconducting layers was preceded by the stage of optimization of the precursors ratio in the initial mixture of precursors. The elemental composition of the obtained films, their phase composition and the superconducting critical current were studied. Thus, the region of optimal composition of the films and the molar ratio of precursors 1(Y):1.18(Ba):1.56(Cu) were established for the optimal  $T$ - $p\text{O}_2$  deposition conditions.

When choosing these conditions, we were guided by the diagram described in [22], while taking into account the features of the MOCVD technology used (reel-to-reel unit, the use of a “table” as a heating element): the temperature of the heating element was 990 °C, the reel-to-reel speed was 2 mm/s, the precursor feed rate was 9.6 g/h. In all experiments, an oxygen partial pressure of 1.6 mbar was maintained; constancy of  $p\text{O}_2$  is extremely important, since this parameter has the greatest effect on the elemental ratio in the deposited films. For samples with intermediate  $\text{Y}_2\text{O}_3$  layers the deposition of the latter was carried out at a temperature of 800 °C, wire reeling speed was 10 mm/s and  $\text{Y}(\text{thd})_3$  precursor feed rate was 3.2 g/h.

During high-temperature film deposition, the YBCO phase was formed in the non-

superconducting tetragonal modification with the composition  $\text{YBa}_2\text{Cu}_3\text{O}_{6.5}$ . For the transfer of YBCO into the superconducting orthorhombic phase, the obtained samples were oxidized in an oven at 450 °C and atmospheric pressure with an additional supply of oxygen and subsequent slow cooling.

### *2.1. Study of the elemental and phase compositions of films, their morphology; method for the determination of $c_{\parallel}$ -oriented grains concentration*

Determination of the phase composition of the films was carried out using Rigaku D/MAX 2500 and Rigaku SmartLab diffractometers with a Ge (220)×2 monochromator with a primary beam using  $\text{Cu-K}_{\alpha}$  radiation ( $\lambda = 1.54046 \text{ \AA}$ ). Diffraction patterns were recorded with Bragg–Brentano geometry (Siemens, Rigaku D/MAX) or with a parallel beam (Rigaku SmartLab). Scanning was performed in the  $\theta$ - $2\theta$  scan mode with  $0.02^\circ$  steps. The surface morphology of the films was investigated using scanning electron microscopy (SEM) with JEOL and LEO Supra 50 VP (LEO, Germany) with a magnification up to 200000.

Cross-sectioned samples were prepared using a  $\text{Ga}^+$  focused ion beam (FIB)<sup>+</sup> and HeliosNanoLab™ 600i (FEI, USA) electron-ion microscope for investigation by transmission and scanning transmission electron microscopy (TEM and STEM, respectively). For the prevention of damage to the sample surface, a protective platinum layer with a thickness of about 1.5  $\mu\text{m}$  was deposited on the film surface before starting the standard procedure for preparing a cross section by the FIB method. Then the thin sample was cut out using focused ion beam with  $\text{Ga}^+$  energy  $E = 30 \text{ keV}$  and current  $I = 6.5 \text{ nA}$ . This sample was transferred using an Omniprobe 200 manipulator (Omniprobe, USA) directly in the microscope chamber and welded by the deposition of tungsten onto a special copper grid. During the last stage, the sample was successively thinned using FIB while changing the ion beam parameters to  $E = 2 \text{ keV}$ ,  $I = 28 \text{ pA}$ .

The studies were carried out using TITAN 80-300 TEM/STEM (FEI, USA) with an accelerating voltage of 300 kV, equipped with a spherical aberration corrector, high-angle annular dark-field detector (HAADF) (Fischione, USA), an

analyser of characteristic electron energy losses (GIF, Gatan, USA) and an energy-dispersive X-ray spectrometer (EDAX, USA).

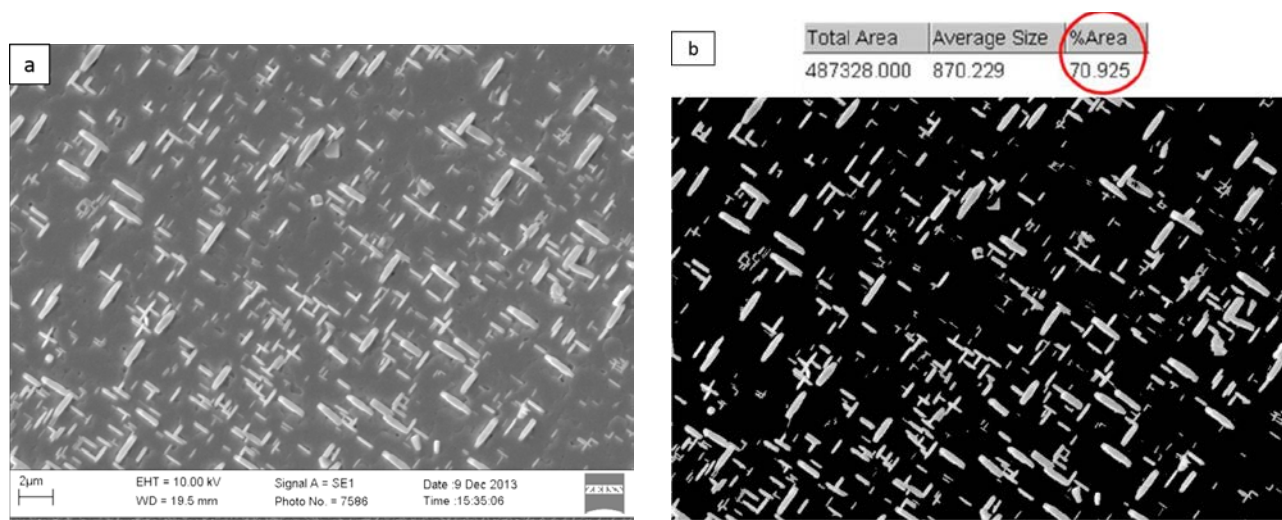
Since  $c_{\parallel}$ -oriented YBCO grains are formed predominantly in the upper part of the superconducting layer; the method of X-ray phase analysis turned out to be insufficiently informative for their quantitative determination and even can provide incorrect information about their content on the surface. Thus, it was important to develop a quantitative detection method of  $c_{\parallel}$ -grains on the surface of the YBCO film. For the determination of surface concentration of  $c_{\parallel}$ -oriented crystallites, the SEM data were processed using the ImageJ software, which allowed distinguishing zones with different brightness of grey after transforming the original image into an image with a combination of two contrasting colours (Fig. 3).

In Fig. 3a  $c_{\parallel}$ -oriented grains which on SEM images look like bright and light stripes can be clearly seen against the background of  $c_{\perp}$  matrix. Areas occupied by  $c_{\parallel}$ -oriented crystallites can be selected and determination of the fraction of the surface area occupied by these crystallites can be performed using the ImageJ program (Fig. 3b).

## 2.2. Critical current measurement by the “Superscan” method

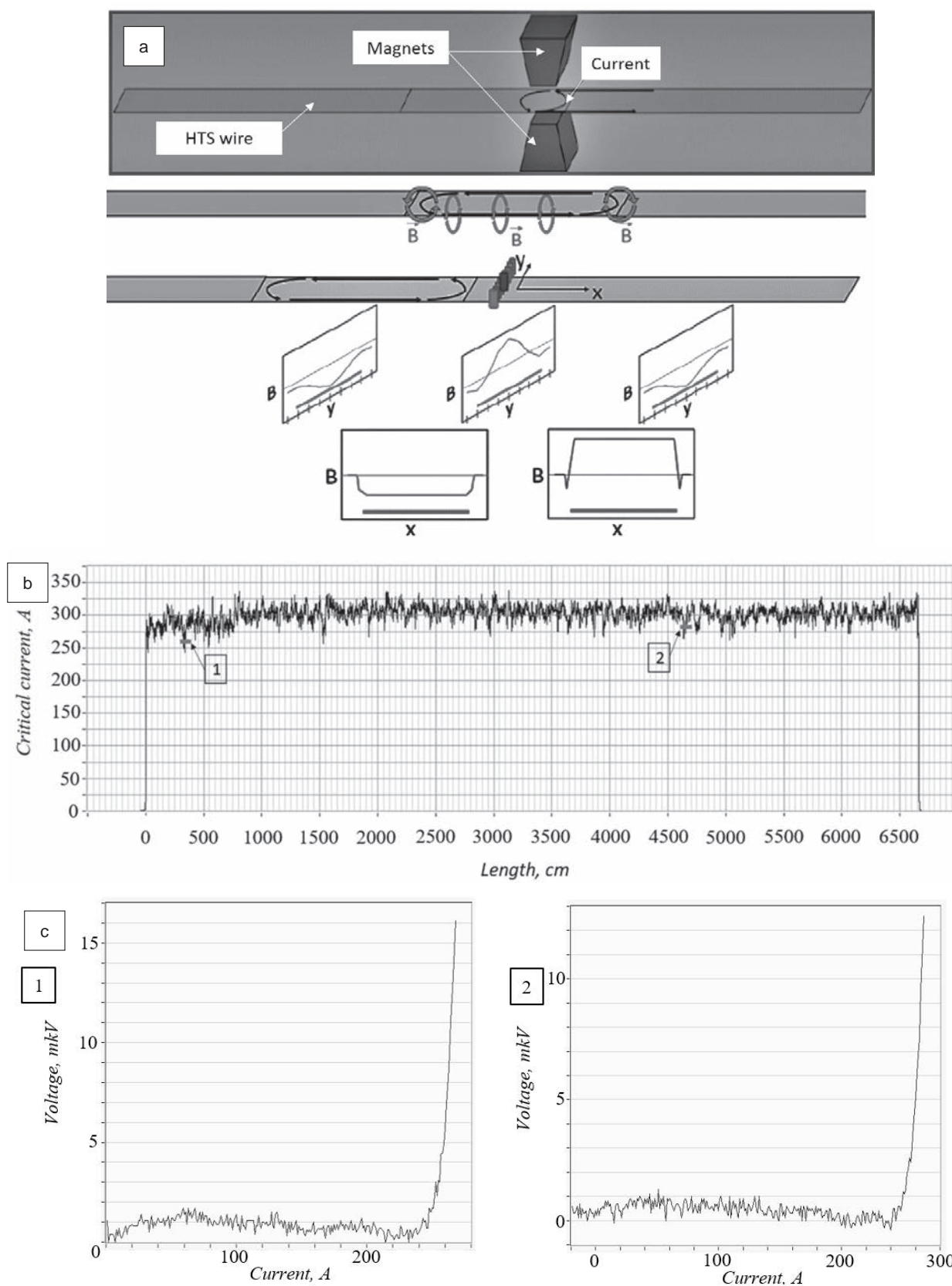
Two methods for the determination of critical current were used in the study: contactless

Superscan technique and four probe method for measuring current-voltage characteristics. The latter was also used for the calibration of the Superscan technique, which is described below. The Superscan method was implemented using a unit, the design and the measurement principle of which are shown in Fig. 4a. During the measurement of the critical current, the wire was rewound from reel to reel, passing through a Dewar vessel with liquid nitrogen, where it cooled and transferred into a superconducting state, passed between two poles of a permanent magnet (0.15 T) and then passed through a head with 9 Hall sensors covering the entire width of the wire. Since YBCO is a type II superconductor, the magnetic field penetrates into the superconducting layer and initiates an eddy current along the length of the wire. Hall sensors measured the value of magnetic induction corresponding to the current in the wire. The signals from the Hall sensors were recorded in a file containing all information about the distribution of current along the width and length of the wire, the file was analysed using a computer program. The final presentation of the results allowed determining the current distribution of the critical current along the width (transverse component) and the length of the wire (longitudinal component) (Fig. 4a). In most cases, the values of the critical current obtained in this way were in good agreement with the



**Fig. 3.** Calculations of  $c_{\parallel}$ -oriented grains using the ImageJ Software: SEM image (up view) of the YBCO film surface (a), SEM image processing with the same area:  $c_{\parallel}$ -oriented grains are white coloured,  $c_{\perp}$  grains are black (b)





**Fig. 4.** SuperSCAN method: Operating principle and obtained information (a), the comparison of SuperSCAN method measurements (b) with 4-point probe measurements of segments 300–400 cm (1) and 4600–4700 cm (2) (c)

results of direct measurements of the current-voltage characteristics obtained by the four probe method, as it can be seen from Fig.4(b and c). The data for 1 m long sample are shown; it proves the reliability of the Superscan technique.

### 3. Results and discussion

Numerous studies of the structure and properties of epitaxial films of RBaCuO superconductors indicated that  $j_c$  values of films strongly depend on the cationic R:Ba:Cu ratio with the best  $j_c$  values achieved not in single-phase films with a stoichiometric cation ratio of 1:2:3, but in those with a significant deviation from this composition. Since the  $\text{YBa}_2\text{Cu}_3\text{O}_{7-x}$  phase does not have a homogeneity range for cations, impurity phases appear with a deviation from the ratio of 1:2:3. The resulting phase ensembles containing the dominant epitaxial phase of  $\text{YBa}_2\text{Cu}_3\text{O}_{7-x}$  differ from equilibrium phase ensembles with the same ratio of elements in polycrystalline powder compositions or polycrystalline films. Thus, in the presence of an excess of barium and copper oxides in equilibrium polycrystalline samples, the  $\text{BaCuO}_2$  phase coexists with the  $\text{YBa}_2\text{Cu}_3\text{O}_{7-x}$  phase [23–25]. However, this impurity phase was not observed in epitaxial films of (001)  $\text{RBa}_2\text{Cu}_3\text{O}_7$  (R = Lu, Ho, Y, Gd, Nd). In this case, instead of it, (001)-oriented  $\text{Ba}_2\text{CuO}_3$  and  $\text{BaCu}_3\text{O}_4$  phases were formed, and the latter existed only until epitaxial contact with the  $\text{YBa}_2\text{Cu}_3\text{O}_{7-x}$ . A similar phenomenon was observed with an excess of yttrium: the non-superconducting  $\text{Y}_2\text{BaCuO}_5$  phase was thermodynamically stable in polycrystalline samples. However, in thin films with an excess of yttrium in the matrix of the  $\text{YBa}_2\text{Cu}_3\text{O}_{7-x}$  epitaxial film,  $\text{Y}_2\text{O}_3$  nanoinclusions with the size of 3–20 nm appeared [25]. These and similar phenomena were interpreted as a manifestation of epitaxial phase stabilization due to the low energy of epitaxial interfaces [26].

$\text{Ba}_2\text{CuO}_3$  and  $\text{BaCu}_3\text{O}_4$  phases formed with an excess of barium and copper had a negative effect on the superconducting properties of the epitaxial HTS film, while  $\text{Y}_2\text{O}_3$  nanoinclusions on the contrary improved them, being additional pinning centres for the magnetic vortices, increasing the stability of the critical current of the HTS film in strong magnetic fields. Moreover, the excess of  $\text{Y}_2\text{O}_3$  in the film shifted the phase ensemble

to the  $\text{YBCO}-\text{Y}_2\text{O}_3-\text{CuO}_x$  region with a lower melting point, which accelerated diffusion and suppressed the growth of  $a$ -oriented crystallites, and this, in turn, led to a significant increase in the critical current density [16]. The foregoing considerations explain why, during the deposition of YBCO films, we deliberately made an effort to obtain compositions with an excess of yttrium, composing the corresponding mixtures of volatile precursors and considering the incongruence of the MOCVD process. As a result of a large number of iterative experiments, we found the optimal ratio of precursors 1(Y):1.18(Ba):1.56(Cu), which provided the highest critical current under the chosen deposition conditions (at 77 K,  $H = 0$ ) for films of the same thickness.

In the XRD spectra of heteroepitaxial YBCO layers with an excess of yttrium (Fig. 5),  $\text{Y}_2\text{O}_3$  impurity in the form of dispersed particles oriented by the  $\langle 110 \rangle$  axis perpendicular to the  $ab$ -planes of the matrix of the  $\text{YBa}_2\text{Cu}_3\text{O}_{7-x}$  phase, as evidenced by a blurred reflex (440) was observed. In the context of the present study, the ratio between the (006) and (200) reflections of the  $\text{YBa}_2\text{Cu}_3\text{O}_{7-x}$  phase corresponding to  $c_{\perp}$  and  $c_{\parallel}$ -crystallites, respectively, was of interest. Cuttings of the XRD spectra, including these reflections for four film samples of different thicknesses are shown in Fig. 5. The volume content of the  $c_{\parallel}$ -phase (VC) can be determined through the area ratio of the (200) and (006) peaks, found by plotting curves, approximating each peak separately:  $\text{VC of } c_{\parallel}\text{-phase} = S_{\parallel} / (S_{\perp} + S_{\parallel})$ . VC values of  $c_{\parallel}$ -phases calculated from the spectra presented in Fig. 5 were 0%, 2.4%, 7.4%, and 63.7% for samples 1–4, respectively.

The above procedure for determining the surface content of the  $c_{\parallel}$ -phase according to SEM data allowed establishing the fraction of the film surface occupied by  $c_{\parallel}$ -crystallites for the same samples. Microphotographs of the surface of the films of samples 1–4 are shown in Fig. 6.

These results (Figs. 5 and 6), as well as a quantitative comparison of the XRD and SEM results for films of successively increasing thickness (Fig. 7) allowed us to conclude that  $c_{\parallel}$ -crystallites were located mainly on the surface of the films and, as the thickness of the film increased, gradually filled its surface completely. The dependence in Fig. 7 shows a clear non-

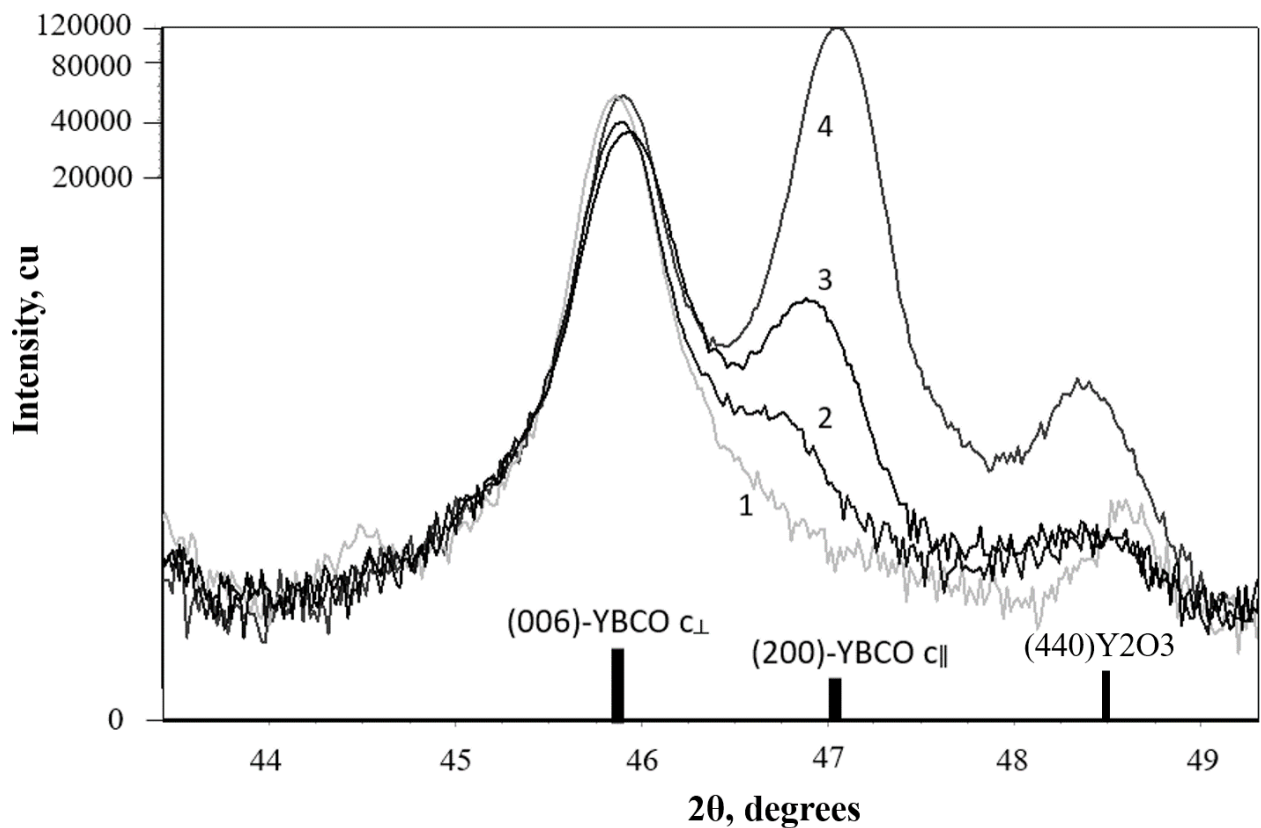


Fig. 5. XRD graphs for the samples 1–4 with different quantities of  $c_{\parallel}$ -oriented grains

linear course corresponding to our ideas about the development of growth of  $c_{\parallel}$ -crystallites in the following stages:

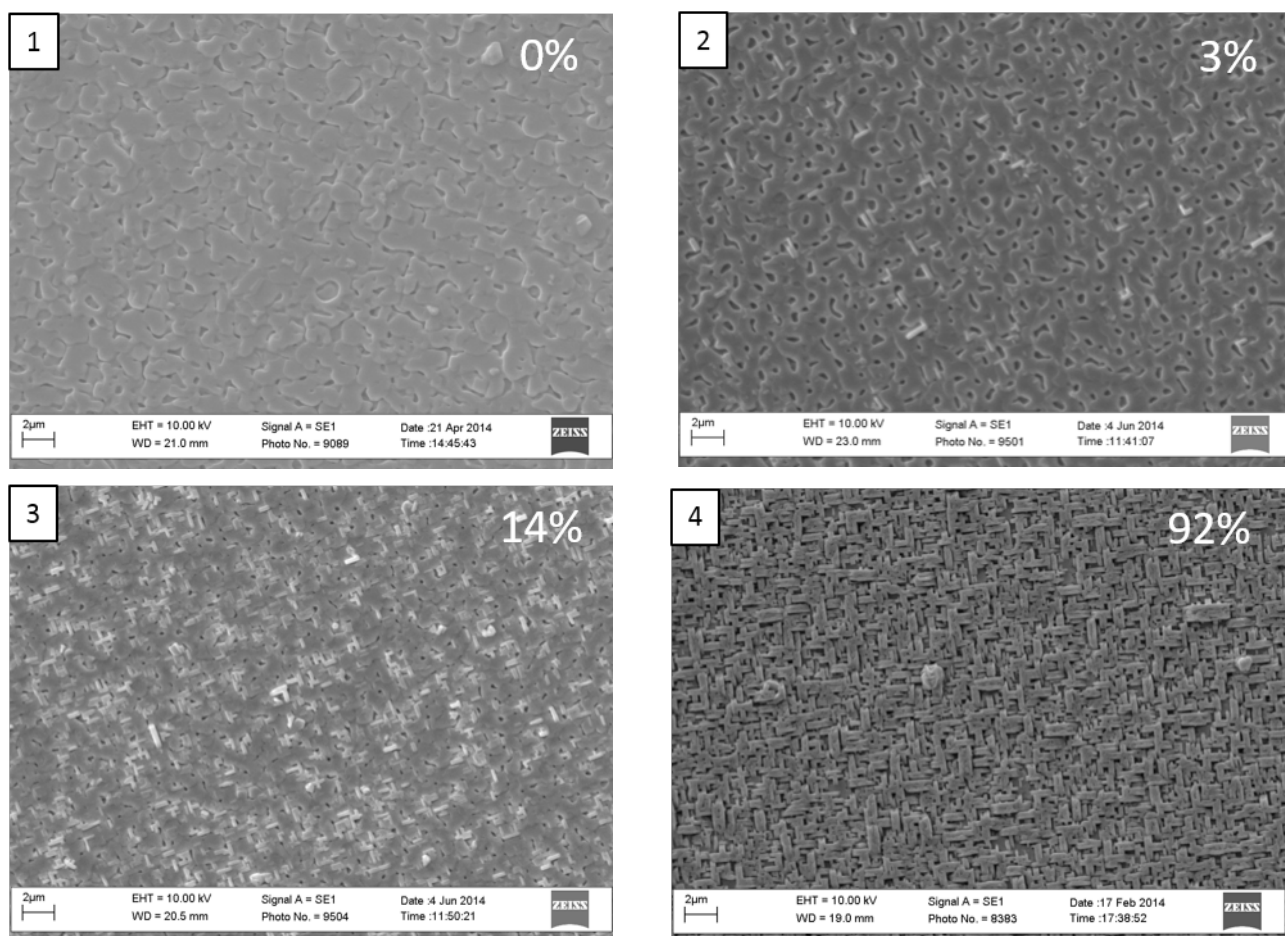
1. The formation of nuclei – at this stage, the competitive nucleation of crystallites of the  $\text{YBa}_2\text{Cu}_3\text{O}_{6.5}$  phase in  $c_{\perp}$  and  $c_{\parallel}$ -orientations and their initial growth occurred.

2. Extensive growth of nucleated crystallites of the  $c_{\parallel}$ -phases on the surface of the film, as well as the formation of new nuclei of this orientation. The development of the process at this stage is facilitated by three features: a) lamellar crystallites of the tetragonal phase grow faster along the base plane  $ab$ , than in the perpendicular direction (single crystals of  $\text{YBa}_2\text{Cu}_3\text{O}_{6.5}$  phase look as thin plates), b)  $c_{\parallel}$ -crystallites protrude above the growth surface and therefore were the first to meet the flow of the material feeding the film during the growth of the HTS layer from the gas phase, c)  $c_{\parallel}$ -oriented crystallites were easily formed on  $c_{\perp}$ -oriented crystallites, while the opposite was not observed.

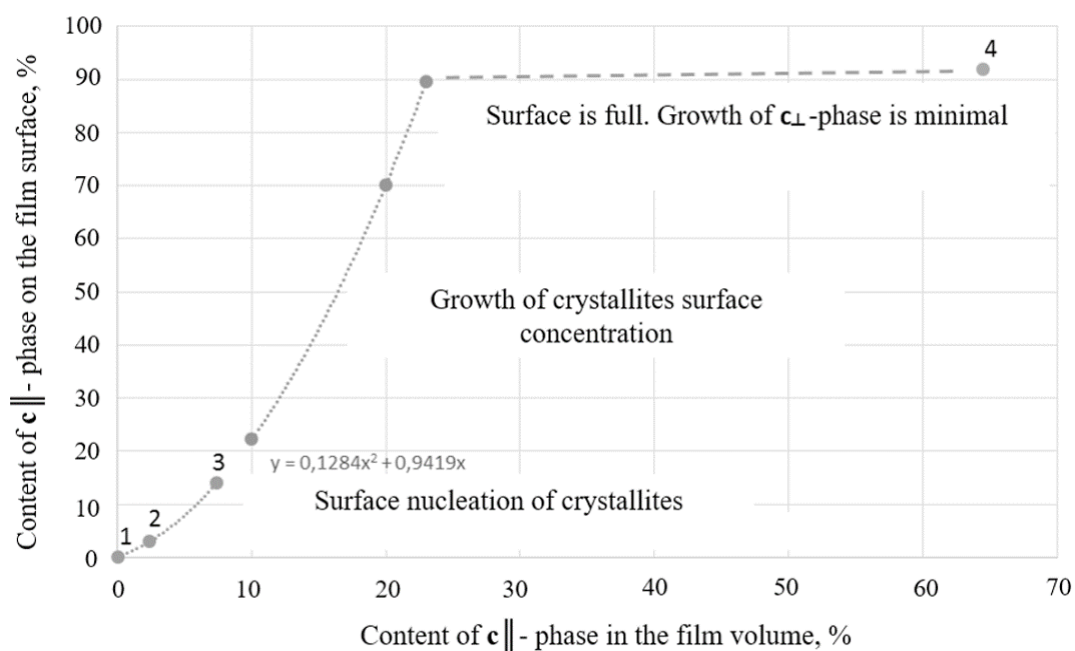
3. Full surface coverage with  $c_{\parallel}$ -crystallites, while there was practically no growth of  $c_{\perp}$  phases.

The combined action of the factors listed in the description of stage 2, as the film thickness increased, led to the growth of colonies of  $c_{\parallel}$ -oriented crystallites, which, as a result, covered the entire surface of the film, suppressing the growth of a conductive  $c_{\perp}$  oriented layer.

The results shown in Fig. 7, clearly demonstrated that surface analysis was the most important stage in the study of the growth of YBCO films (more indicative than XRD), since it allowed understanding whether there is a possibility of increasing the critical current with increasing film thickness. Thus, if, according to XRD data, the volume content of the  $c_{\parallel}$ -phase in the film was still not high and it was at the level of 20-30%, then the surface may already be so filled with this phase that further deposition of HTS layers became ineffective in terms of increasing the critical current. This is illustrated in Fig. 8, showing the results of measurements of critical currents ( $I_c$ ) and the microstructure of the surface of the HTS layer, which was grown in thickness ( $h$ ) in 6 consecutive cycles of the YBCO deposition. It can be seen that at a thickness ( $h$ )



**Fig. 6.** SEM images of 1-4 samples. The calculated content of  $c_{\parallel}$ -oriented grains on the film surface is indicated on the corresponding photo

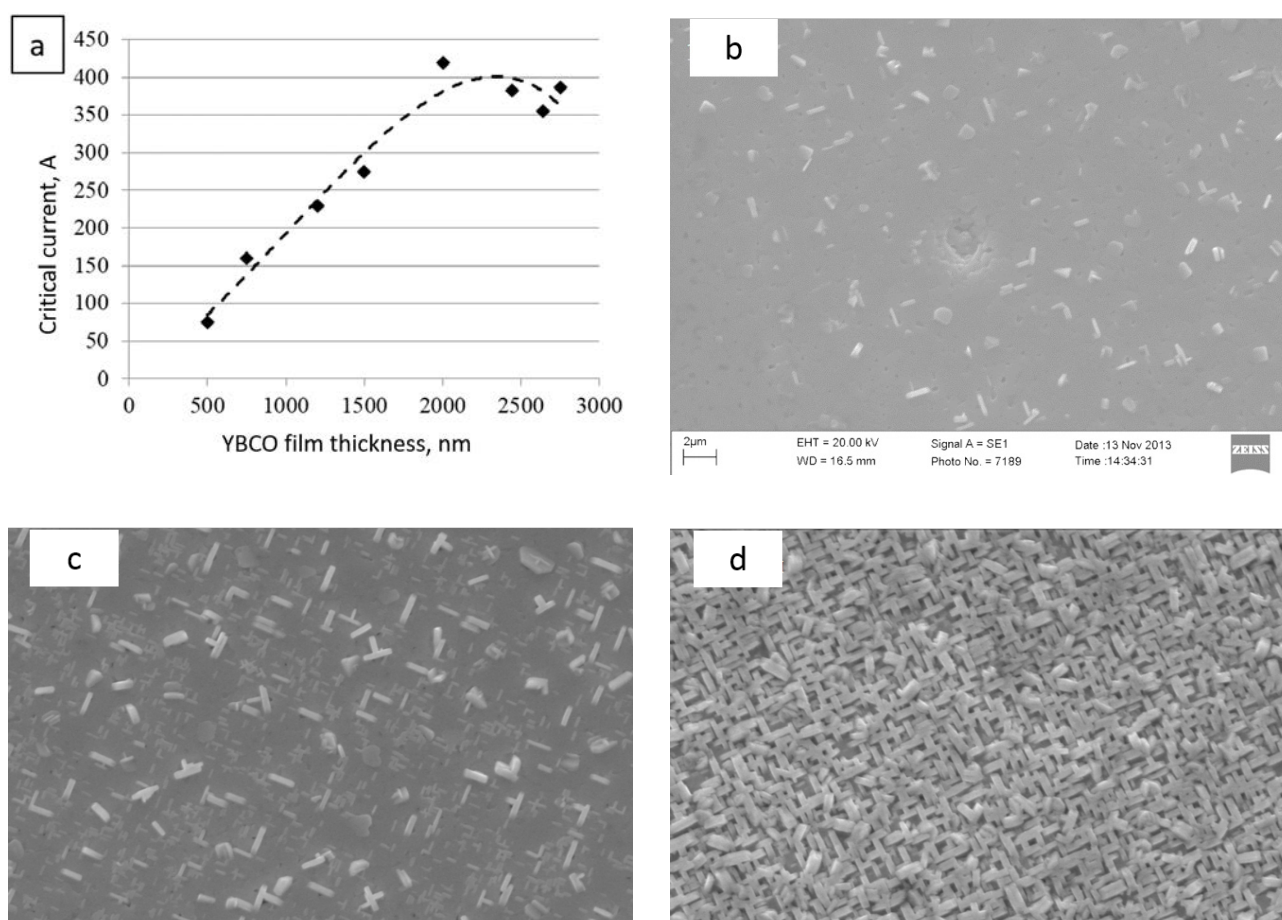


**Fig. 7.** The dependence between the volume content of the  $c_{\parallel}$ -oriented phase (from XRD data) and the surface content of crystallites with this orientation (from the SEM data) on the  $YBa_2Cu_3O_{7-\delta}$  film surface with increasing thickness (thickness increasing along the X-axis)

of about 1900 nm, the slope of the dependence  $I_c(h)$  changed sharply, and with further thickening of the HTS layer, its critical current increased insignificantly (Fig.8a), which was a direct consequence of the fact that at a thickness of 1900 nm the film surface was almost completely blocked with  $c_{\parallel}$ -oriented crystallites (Fig. 8d).

It was already noted above that the change in growth from a thermodynamically stable  $c_{\perp}$  orientation to a kinetically favourable  $c_{\parallel}$ -orientation was promoted by lowering the temperature of the film growth surface. In this context it is important to understand the reasons for this cooling. Assuming that the total thermal effect of decomposition and oxidation of volatile precursors of metal components of YBCO in the MOCVD process is low, it can be argued that the temperature of the growth surface reflects the ratio of the heat flux coming from the heater located under the substrate to

the radiant energy flux emitted by the heated wire surface. The dependence of the thermal conductivity of the YBCO film on its thickness in the direction perpendicular to the substrate is difficult to predict *a priori*, since it is influenced by many factors. The crystalline anisotropy of the superconducting phase causes the anisotropy of thermal conductivity: in the direction of the  $c$  axis (i.e. perpendicular to the substrate) the thermal conductivity was 4–10 times lower than along the substrate [27]. The uncertainty in the value of the anisotropy factor was associated with the dependence of the phonon thermal conductivity (it dominates at a high temperature of film deposition) on the crystallite size of the film, which depended on the method and conditions of film deposition, but increases with increasing film thickness. At the same time, the fraction of  $c_{\parallel}$ -crystallites increased, which, as well as the coarsening of grains, contributed



**Fig. 8.** a) The thickness dependence of critical current in YBCO films produced in 6 sequential MOCVD cycles; b–d – the YBCO film surface evolution with an increase in its thickness (thickness is shown on the images)

to an increase in thermal conductivity in the direction of the growth surface. At the same time, packing defects and plane defects accumulated in the film at the boundaries of the layers deposited during successive passes of the wire through the deposition zone. These defects were perpendicular to the direction of the heat flux through the substrate and, according to [27], reduced the thermal conductivity. However, the experiment in [27] found an increase in the thermal conductivity along the normal to the substrate with increasing film thickness suggested that the effect of the recrystallization factor dominated, reducing the grain boundary scattering of phonons.

Another factor that strongly influenced the temperature of the growth surface was the intensity of the light energy flux emitted by it. The emissivity of the surface, which is at the maximum for a black body, strongly increased with an increase in the roughness of the radiating surface [28, 29]. The roughness itself increased as the thickness of the HTS crystal layer increased. The overgrowth of  $c_{\parallel}$ -crystallites, rising above the average surface height, especially promoted an increase in roughness, an increase in emissivity, and a decrease in the temperature of the growth surface with constant heat supply from the heater.

An increase in the growth surface temperature by increasing the heater temperature, which seems to be the simplest solution counteracting the formation of  $c_{\parallel}$ -orientation is not an appropriate approach. In this approach, it was difficult to avoid the overheating of the underlying YBCO layers; the danger of their incongruent melting increased, since the deposition temperature was very close to the peritectic temperature. In addition, when the temperature rose above 1000 °C a noticeable degradation was observed in the substrate (oxidation of its reverse side, crystallization of the amorphous buffer  $\text{Al}_2\text{O}_3$ , the  $\text{Y}_2\text{O}_3$  layers, causing additional roughness of the growth surface). Finally, the need for repeated adjustment of the heater temperature when applying successive YBCO layers significantly complicated the process of obtaining HTS wires.

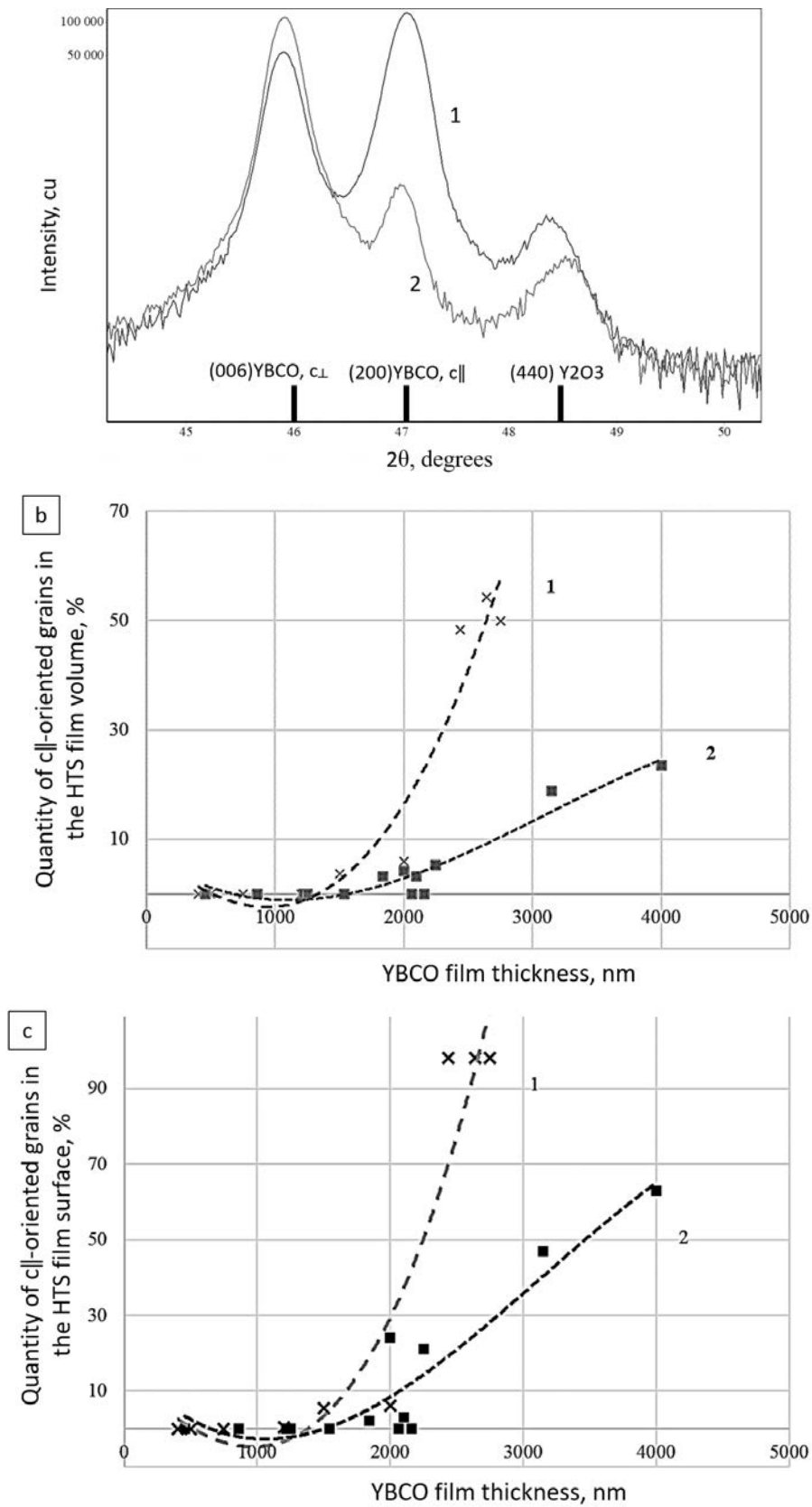
An alternative method of preventing the growth of  $c_{\parallel}$ -crystallites is based on the creation

of mechanical stresses in the growing YBCO film at the interface with the substrate or with an additionally introduced buffer layer. It was previously noted that on perovskite-like substrates with a minimum lattice mismatch with the  $a$ -parameter of YBCO, it was especially easy to switch  $c_{\perp}$  growth to  $c_{\parallel}$ -growth (with a smaller film thickness and at a higher growth temperature) [30, 15]. On the contrary, films on substrates with a large parameter mismatch at the interface with YBCO, for example, on MgO, demonstrated a stable  $c_{\perp}$  growth. These facts prompted some studies [13, 31], in which GdBCO/ $\text{Gd}_2\text{O}_3$ / $\text{SrTiO}_3$  and YBCO/ $\text{BaZrO}_3$ /MgO heterostructures, practically devoid of  $c_{\parallel}$ -crystallites due to buffer layers with a significant difference in parameters at the interface, were obtained.

In this study, we have applied the idea of introducing intermediate layers, causing stresses in the growing film and thus preventing the growth of  $c_{\parallel}$ -crystallites for the increase in the thickness of the HTS layer while maintaining the critical current density. Yttrium oxide was chosen for the intermediate layers for the following reasons: first, it can form epitaxial contacts with  $\text{YBa}_2\text{Cu}_3\text{O}_{7-x}$ , due to which, under high deposition temperatures, the chemical interaction typical of polycrystalline contacts of this system was absent [26]; second, the epitaxial nature of the contacts allowed preserving the sharp biaxial texture of the HTS layer, despite the introduction of a non-superconducting phase; third,  $\text{Y}_2\text{O}_3$  is a simple oxide, therefore, during its precipitation, impairment of the cationic stoichiometry did not occur.

It is obvious that the development of parasitic  $c_{\parallel}$ -crystallites must be controlled during the stage of nucleation; however, during subsequent stages of growth it will be unproductive. Therefore, the deposition of YBCO and  $\text{Y}_2\text{O}_3$  layers alternated starting from a thickness of ~ 100 nm. With the selected both movement speed of the substrate wire and the  $\text{Y}(\text{thd})_3$  precursor feeding rate, the thickness of deposited  $\text{Y}_2\text{O}_3$  interlayers should have been ~ 10 nm. An XRD of the obtained composite samples with 4 interlayers of  $\text{Y}_2\text{O}_3$  (Fig. 9a) showed a significant decrease in the number of  $c_{\parallel}$ -oriented crystallites in the films in comparison with YBCO films.

The same was evidenced by a comparison of the XRD data for films of YBCO and  $\text{Y}_2\text{O}_3$



**Fig. 9.** The graphs of YBCO samples without interlayers (1) and with  $Y_2O_3$  interlayers (2): XRD analysis of the samples with film thickness of 2000 nm (a); The comparison of  $c_{\parallel}$ -phase quantity on different film thicknesses: from XRD data (b), from SEM data (c)

composites obtained on a large set of samples in which the thickness of the HTS layers reached 4  $\mu\text{m}$  (Fig. 9b): the introduction of  $\text{Y}_2\text{O}_3$  interlayers can significantly reduce the proportion of  $c_{\parallel}$ -oriented crystallites in the film, and this effect was especially pronounced when the total thickness of the HTS layer exceeded 1500 nm. The alternation of YBCO and  $\text{Y}_2\text{O}_3$  layers created an obstacle to YBCO growth in the  $c_{\parallel}$ -orientation, since the parameters of the crystal lattice of  $\text{Y}_2\text{O}_3$  had a greater mismatch with it than the  $c$ -oriented YBCO film. The deposition of the upper layer of  $\text{Y}_2\text{O}_3$  with different UC parameters creates an additional stress at the interface with the next YBCO layer, which causes a predominant growth of  $c_{\perp}$ -oriented crystallites, despite the obvious decrease in the surface temperature with a successive increase in the film thickness

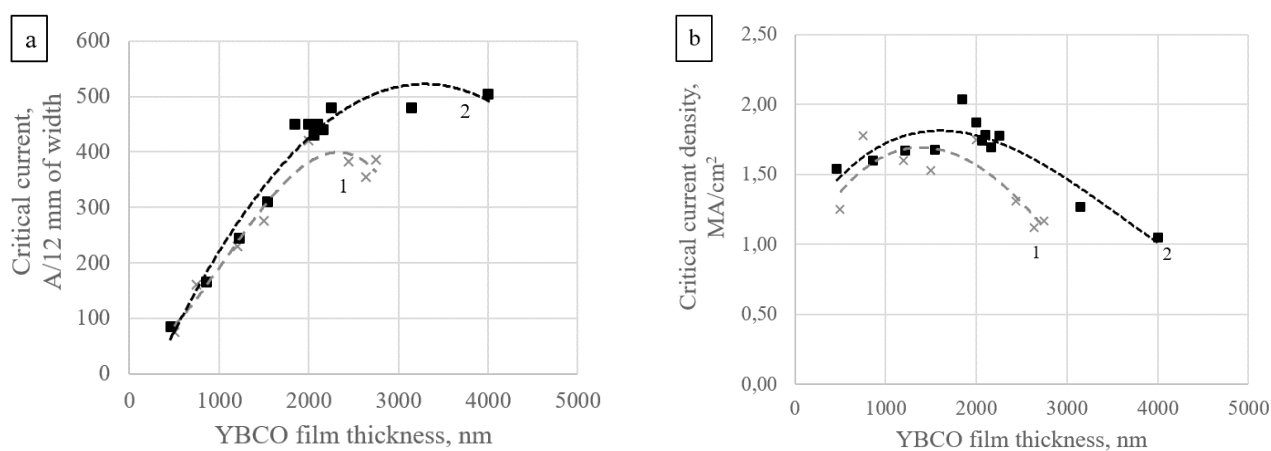
For the control of the surface condition and understanding of the possibility of further deposition of HTS- layers with a high current density, all samples were studied by SEM with the measurement of the fraction of  $c_{\parallel}$ -crystallites on the surface (Fig. 9c) using the ImageJ software package. For all samples, the critical currents were also measured using the Superscan method. The results of these measurements are shown in Fig. 10 (a, b).

It was found that with a thickness close to 2  $\mu\text{m}$ , with the absence of yttrium oxide interlayers,  $c_{\parallel}$ -oriented crystallites with a total film thickness of about 2400 nm occupied 98% of the surface, which was accompanied by the termination of the growth of the critical current with an increase in

the film thickness. In films with interlayers the pattern changed significantly: the formation of  $\text{Y}_2\text{O}_3$  layers noticeably decreased the density of  $c_{\parallel}$ -oriented crystallites; however, after a thickness of more than 2400 nm, the critical current in films with interlayers did not significantly increase (Fig.10a). Since, due to the presence of  $\text{Y}_2\text{O}_3$  interlayers such films were thicker than similar films without interlayers, after recalculation for the critical current density, the differences in the current-carrying capacity of films with and without interlayers were not so large. The maximum  $j_c$  2MA/cm<sup>2</sup> (77 K, SF) value was obtained for the composite film thickness of 1850 nm with six  $\text{Y}_2\text{O}_3$  interlayers (Fig.10b).

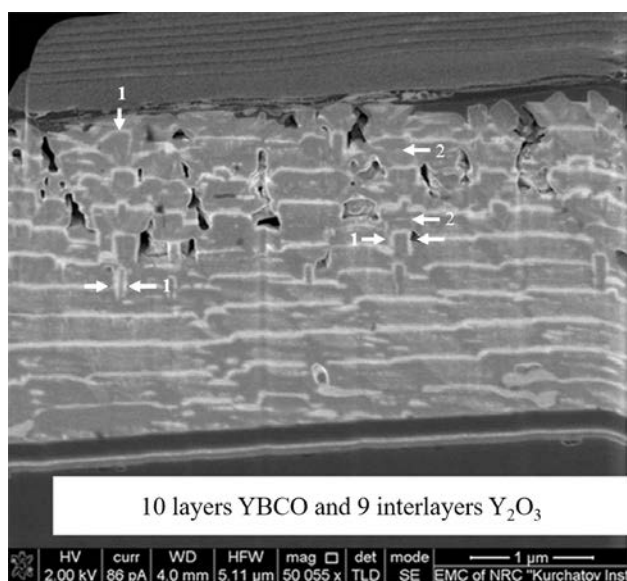
The main reason for the decrease in  $j_c$  with a further increase in the thickness of the composite superconducting layer, was revealed using a TEM of cross sectioned samples. The morphology of a sample formed by successive deposition of ten YBCO layers with nine  $\text{Y}_2\text{O}_3$  interlayers with a total thickness of the composite layer of 2.6  $\mu\text{m}$  is shown in Fig. 11.

The photo clearly shows the darker YBCO layers and the lighter  $\text{Y}_2\text{O}_3$  interlayers with a thickness close to 10 nm, located almost equidistantly, as was expected from the conditions of their deposition. Due to the colour contrast of matrix and interlayers  $c_{\parallel}$ -oriented YBCO crystallites can be distinguished easily: upon deposition the  $\text{Y}_2\text{O}_3$  interlayer covered  $c_{\parallel}$ -crystallites protruding above the growth surfaces, thus rectangular steps were formed, some of which are shown in Fig. 11 with arrows. The TEM data of the cross section



**Fig. 10.** The graphs of YBCO samples (1) and "YBCO +  $\text{Y}_2\text{O}_3$  interlayers" composites (2): Thickness dependencies of: a) critical current (A/12 mm of width, 77 K, SF); b) critical current density (77 K, SF)





**Fig. 11.** SEM image of a cross-section of 10 layers of a YBCO sample with 9  $Y_2O_3$  interlayers:  $Y_2O_3$  layer roughness caused by  $c_{\parallel}$ -crystallites (1); flat  $Y_2O_3$  particles parallel to the substrate plane (2)

(Fig. 11) were consistent with the SEM results of the surface of films of different thicknesses (Fig. 9c). Indeed, both methods revealed the formation of  $c_{\parallel}$ -crystallites in composite films in a noticeable concentration, starting with a thickness of  $\sim 1 \mu$ m.

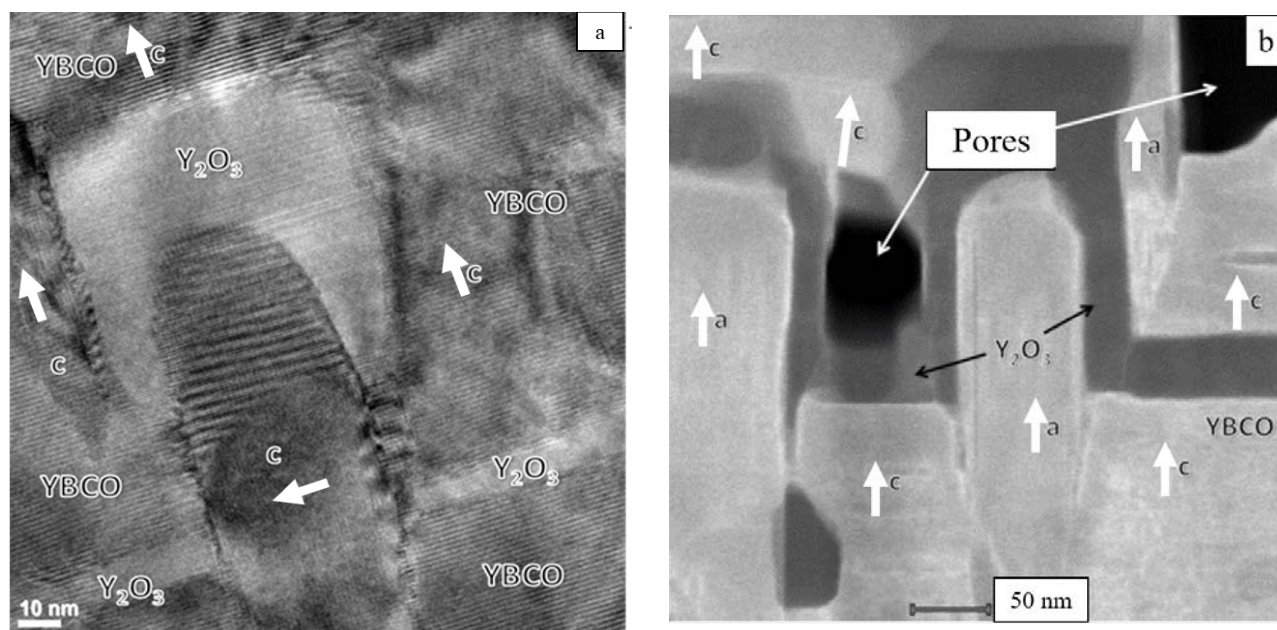
The good conformity of the interlayers ( $Y_2O_3$  layers with the uniform thickness covered faces of  $c_{\parallel}$  and  $c_{\perp}$ -crystallites), which was a consequence of the epitaxial nature of these contacts and low surface tension at the interface. The TEM results in Figs. 11 and 12 revealed an important feature of the morphology of composites, which confirmed the initial hypothesis of this study:  $Y_2O_3$  interlayers completely cover  $c_{\parallel}$ -oriented grains and block their further growth along the plane  $ab$ , during the deposition of the next YBCO layer on the  $Y_2O_3$  only  $c_{\perp}$ -oriented crystallites are nucleated. This was confirmed by Figs. 11 and 12, the orientation of the YBCO layers adjacent to  $c_{\parallel}$ -crystallite is shown on Fig. 12 by arrows indicating the crystallographic axes.

In the YBCO matrix, multiple inclusions of  $Y_2O_3$  nanoparticles predominantly in the form of flat flakes elongated along the plane of the substrate were clearly visible. These particles were formed as a result of the deliberately enriched composition of YBCO with the yttrium component in comparison with the stoichiometry

of 1:2:3 [16]; they must play the role of pinning centres increasing the stability of the critical current of a superconductor in a magnetic field.

Starting from a thickness of  $\sim 1.5 \mu$ m, nanosized pores started to form in the composite layer. They are clearly visible in Fig. 11 and enlarged in Fig. 12b. This phenomenon was noted in [11], but there is still no clear understanding of the reasons for their formation. The TEM results allowed proposing the following scenario for the formation of nanopores. For the gas phase epitaxial crystallization of films of multicomponent phases, in particular,  $YBa_2Cu_3O_{6.5}$  it is necessary that each of the components in the vapour reach the growth surface and be able to freely move along it due to the surface diffusion of atoms or ions.

Colonization of the growth surface with  $c_{\parallel}$ -oriented crystallites noticeably changes both the accessibility of this surface for particles in vapour and the conditions of surface diffusion. Between the walls of adjacent  $c_{\parallel}$ -crystallites “wells” with an aspect ratio of  $\geq 2$  formed (Fig. 12b), the conformal filling of which with a  $c_{\perp}$  YBCO layer becomes difficult. It is known from the fundamentals of gas dynamics and mass transfer that a diffusion layer forms above the film growth surface. This barrier must be overcome by particles from the gas phase in order to reach the surface. The thickness of this layer increases at the lowering of the gas flow rate and it is obvious that in “wells”, where the flow rate is low, the diffusion layer has the greatest thickness and provides the greatest resistance to the penetration of YBCO components into the growth surface. It should be noted that the inner surface of nanopores in the composites obtained by us was conformally coated with a  $Y_2O_3$ , and in the study [13], dense filling of spaces between neighbouring  $c_{\parallel}$ -crystallites of YBCO with copper oxide was noted on TEM-images, i.e., the delivery of the yttrium and copper components from the vapour completely ensures the filling of nanopores. It can be argued with great certainty that the lack of the barium component prevents the formation of the HTS phase between neighbouring  $c_{\parallel}$ -crystallites, which can be attributed to the high molecular weight of the particles supplying the barium component, although their true composition is unknown.



**Fig. 12.** TEM images of the areas with  $c_{\parallel}$ -oriented crystallites covered by  $Y_2O_3$  layer:  $c_{\perp}$ -oriented YBCO growth on  $c_{\parallel}$ -oriented crystallite is demonstrated (a); Pore formation near  $c_{\parallel}$  oriented crystallites (b)

$c_{\parallel}$ -crystallites rising above the surface significantly increased the roughness of the surface. This contributes to its cooling and sharply increases the path of surface diffusion which the adsorbed particles of the components must pass before they will occupy places with a local minimum of energy. As a result, the surface diffusion flux turned out to be insufficient for providing the conformal growth of the phase, primarily in the spaces between closely-spaced vertical  $c_{\parallel}$ -crystallites. Comparing the values of the atomic masses and radii of the cations composing the  $YBa_2Cu_3O_{6.5}$  phase, it can be argued that the least diffusion-mobile was the largest and “heaviest” cation,  $Ba^{2+}$ , therefore, the local deficiency of barium (arising from the difficulties of its delivery through the surface diffusion layer) cannot be compensated for by its lateral diffusion movement. Thus, it can be argued that superficial  $c_{\parallel}$ -crystallites complicated both successive stages of gas phase epitaxy of YBCO, which are the supply of nutrients to the growth surface and surface diffusion along it. As a result of the close location of neighbouring  $c_{\parallel}$  crystallites between them, places not filled with the crystallizing YBCO phase arose, i.e., nanopores lowering the critical current density of superconducting layers of large thickness.

## Conclusions

Heteroepitaxial layers of a high-temperature YBCO superconductor and laminated composites YBCO/ $Y_2O_3$ , components of 2G HTS wires, were obtained in deposition mode on a continuously moving wire substrate by the MOCVD method. It was shown that after reaching the YBCO thickness of  $\sim 1900$  nm, the preferred orientation of the growth of the  $YBa_2Cu_3O_{7-x}$  phase in the surface layer changes, as a result of which the surface is covered with  $c_{\parallel}$ -crystallites preventing the passage of the superconducting current in the direction along the substrate wire; this circumstance lowers the critical current density and does not allow an increase in the current-carrying capacity by increasing the thickness of the HTS layer. It was shown that the method of scanning electron microscopy is more informative than the XRD for the analysis of the orientation of surface crystallites. The method for reducing the concentration  $c_{\parallel}$ -oriented crystallites in laminated YBCO/ $Y_2O_3$  composites was proposed and experimentally tested. It was shown that thin ( $\sim 10$  nm) layers of  $Y_2O_3$  prevent the emergence and development of  $c_{\parallel}$ -oriented crystallites, they do not impair the highly oriented state of the HTS matrix, and they allow obtaining predominantly  $c_{\perp}$ -oriented YBCO layers with a thickness up to  $4 \mu\text{m}$ . Due to this, it was possible

to increase the critical current by 25–30% and obtain wires with a current-carrying capacity of 500 A (12 mm wide, 77 K, in the intrinsic magnetic field), while maintaining a high critical current density ( $j_c > 2$  MA/cm). Using the TEM method, it was shown that the main reason for the decrease in  $j_c$  with a further increase in the thickness of the composites is the formation of nanopores in the near-surface layer of the growing film. The reasons for the appearance of nanopores were analysed and it was concluded that they were formed due to the proximity of  $c_{\parallel}$ -oriented crystallites, causing an increase in the thickness of the diffusion near-surface boundary layer and inhibiting the surface diffusion flow. It was suggested that during the formation of nanopores, the difficulties with delivery to the surface from the vapour and difficulties in surface diffusion were characteristic primarily for the barium component of the HTS.

### Conflict of interests

The authors declare that they have no known competing financial interests or personal relationships that could have influenced the work reported in this paper.

### References

1. Fleshler S., Buczek D., Carter B., Ogata M. Scale-up of 2G wire manufacturing at American Superconductor Corporation. *Physica C*. 2009;469(15-20): 1316–1321. <https://doi.org/10.1016/j.physc.2009.05.234>
2. Nagaishi T., Shingai Y., Konishi M., Taneda T., Ota H., Honda G., Kato T., Ohmatsu K. Development of REBCO coated conductors on textured metallic substrates. *Physica C*. 2009;469(15-20): 1311–1315. <https://doi.org/10.1016/j.physc.2009.05.253>
3. Rosner C. H. Superconductivity: star technology for the 21st century. *IEEE Transactions on Applied Superconductivity*. 2001;11(1): 39–48. <https://doi.org/10.1109/77.919283>
4. Mansour R. R. Microwave superconductivity. *IEEE Transactions on Microwave Theory and Techniques*. 2002;50(3): 750–759. <https://doi.org/10.1109/22.989959>
5. Hayakawa H., Yoshikawa N., Yorozu S., Fujimaki A. Superconducting digital electronics. *Proceedings of the IEEE*. 2004;92(10): 1549–1563. <https://doi.org/10.1109/JPROC.2004.833658>
6. Wimbush S. C. Large scale applications of HTS in New Zealand. *Physics Procedia*. 2015;65: 221–224. <https://doi.org/10.1016/j.phpro.2015.05.125>
7. Zhu J., Zheng X., Qiu M., Zhang Z., Li J., Yuan W. Application simulation of a resistive type superconducting fault current limiter (SFCL) in a transmission and wind power system. *Energy Procedia*. 2015;75: 716–721. <https://doi.org/10.1016/j.egypro.2015.07.498>
8. Iwasaki H., Inaba S., Sugioka K., Nozaki Y., Kobayashi N. Superconducting anisotropy in the Y-based system substituted for the Y, Ba and Cu sites. *Physica C*. 1997;290: 113. [https://doi.org/10.1016/S0921-4534\(97\)00634-5](https://doi.org/10.1016/S0921-4534(97)00634-5)
9. Freyhardt H. C., Hellstrom E. E. High-temperature superconductors: A Review of  $\text{YBa}_2\text{Cu}_3\text{O}_{6+x}$  and  $(\text{Bi,Pb})_2\text{Sr}_2\text{Ca}_2\text{Cu}_3\text{O}_{10}$ . *Cryogenic Engineering*. New York: Springer; 2007. pp. 309–339. <https://doi.org/10.1007/0-387-46896-X>
10. Dimos D., Chaudhari P., Mannhart J. Superconducting transport properties of grain boundaries in  $\text{YBa}_2\text{Cu}_3\text{O}_7$  bicrystals. *Phys. Rev. B*. 1990;41: 4038–4049. <http://dx.doi.org/10.1103/PhysRevB.41.4038>
11. Goyal A. (ed.) *Second-Generation HTS Conductors*. Boston/Dordrecht/New York/London: Kluwer Academic Publ.; 2009. 432 p.
12. Zhang H., Yang J., Wang S., Wu Y., Lv Q., Li S. Film thickness dependence of microstructure and superconductive property of PLD prepared YBCO layers. *Physica C*. 2014;499: 54–56. <https://doi.org/10.1016/j.physc.2014.01.001>
13. Markelov A. V., Samoilenkov S. V., Akbashaev A. R., Vasiliev A. L., Kaul A. R. Control of orientation of  $\text{RBa}_2\text{Cu}_3\text{O}_7$  films on substrates with low lattice mismatch via seed layer formation. *IEEE Transactions on Applied Superconductivity*. 2011;21(3): 3066–3069. <https://doi.org/10.1109/TASC.2010.2102992>
14. Granozio F. M., Salluzzo M., Scotti di Uccio U., Maggio-Aprile I., Fischer O. Competition between a-axis and c-axis growth in superconducting  $\text{RBa}_2\text{Cu}_3\text{O}_{7-x}$  thin films. *Phys. Rev. B*. 2000;61(1): 756–765. <https://doi.org/10.1103/PhysRevB.61.756>
15. Jeschke R., Schneider G., Ulmer G. Linker influence of the substrate material on the growth direction of YBaCuO thin films. *Physica C*. 1995;243: 243–251. [https://doi.org/10.1016/0921-4534\(95\)00019-4](https://doi.org/10.1016/0921-4534(95)00019-4)
16. Moyzykh M., Boytsova O., Amelichev V., Samoilenkov S., Voloshin I., Kaul A., Lacroix B., Paumier F., Gaboriaud R. Effects of yttrium oxide inclusions on the orientation and superconducting properties of YBCO films. *Kondensirovannye sredy i mezhfaznye granitsy = Condensed Matter and Interphases*. 2013;15(2): 91–98. Available at: [http://www.kcmf.vsu.ru/resources/t\\_15\\_2\\_2013\\_001.pdf](http://www.kcmf.vsu.ru/resources/t_15_2_2013_001.pdf)
17. *2G HTS Wire Specification Overview*. Available at: <http://www.superpower-inc.com/system/files/>

SP\_2G+Wire+Spec+Sheet\_2014\_web\_v1\_0.pdf (accessed 29 October 2016).

18. Murakami M., Gotoh S., Fujimoto H., Yamaguchi K., Koshizuka N., Tanaka S. Flux pinning and critical currents in melt processed YBaCuO superconductors. *Superconductor Science and Technology*. 1991;4: S43–S50. <https://doi.org/10.1088/0953-2048/4/1S/005>

19. Zhao P., Ito A., Goto T. Rapid deposition of YBCO films by laser CVD and effect of lattice mismatch on their epitaxial growth and critical temperature. *Ceramics International*. 2013;39: 7491–7497. <https://doi.org/10.1016/j.ceramint.2013.02.098>

20. Zhao P., Ito A., Goto T., Tu R. High-speed growth of YBa<sub>2</sub>Cu<sub>3</sub>O<sub>7-δ</sub> film with high critical temperature on MgO single crystal substrate by laser chemical vapor deposition. *Superconductor Science and Technology*. 2010;23(12): 125010. <https://doi.org/10.1088/0953-2048/23/12/125010>

21. Zhao P., Ito A., Goto T., Tu R. Fast epitaxial growth of *a*-axis- and *c*-axis-oriented YBa<sub>2</sub>Cu<sub>3</sub>O<sub>7-δ</sub> films on (1 0 0) LaAlO<sub>3</sub> substrate by laser chemical vapor deposition. *Applied Surface Science*. 2010;257: 4317–4320. <https://doi.org/10.1016/j.apsusc.2010.12.047>

22. Hammond R. H., Bormann R. Correlation between the in situ growth conditions of YBCO thin films and the thermodynamic stability criteria. *Physica C*. 1989;162-164: 703–704. [https://doi.org/10.1016/0921-4534\(89\)91218-5](https://doi.org/10.1016/0921-4534(89)91218-5)

23. Voronin G. F., Degterov S. A. Solid State Equilibria in the Ba-Cu-O System. *J. Solid State Chem*. 1994;110(1): 50–57. (and references therein). <https://doi.org/10.1006/jssc.1994.1134>

24. Lindemer T. B., Specht E. D. The BaO-Cu-CuO system. Solid-liquid equilibria and thermodynamics of BaCuO<sub>2</sub> and BaCu<sub>2</sub>O<sub>2</sub>. *Physica C*. 1995;255(1-2): 81–94. (and references therein). [https://doi.org/10.1016/0921-4534\(95\)00460-2](https://doi.org/10.1016/0921-4534(95)00460-2)

25. Samoylenkov S. V., Gorbenko O. Yu, Graboy I. E., Kaul A. R., Zandbergen H. W., Connolly E. Secondary phases in (001)RBa<sub>2</sub>Cu<sub>3</sub>O<sub>7-δ</sub> epitaxial thin films. *Chemistry of Materials*. 1999;11(9): 2417–2428. <https://doi.org/10.1021/cm991016v>

26. Kaul A. R., Gorbenko O. Yu., Kamenev A. A. The role of heteroepitaxy in the development of new thin-film oxide-based functional materials. *Russian Chemical Reviews*. 2004;73(9): 932–953. <https://doi.org/10.1070/RC2004v073n09ABEH000919>

27. Murakami Y., Goto H., Taguchi Y., Nagasaka Y. Measurement of out-of-plane thermal conductivity of epitaxial YBa<sub>2</sub>Cu<sub>3</sub>O<sub>7-δ</sub> thin films in the temperature range from 10 K to 300 K by photothermal reflectance. *International Journal of Thermophysics*. 2017;38(10): 160. <https://doi.org/10.1007/s10765-017-2294-7>

28. Agababov S. G., Vliyanie sherohovatosti poverhnosti tverdogo tela na ego radiatsionnie

svoistva I metody ih eksperimentalnogo opredeleniya [Influence of the surface roughness of a solid on its radiation properties and methods of their experimental determination]. *Teplofizika visokih temperatur*. 1968;6(1): 78–88. (In Russ.)

29. Sayapina V. I., Svet D. Ya., Popova O. R., Vliyanie sherohovatosti poverhnosti na izluchatelnyu sposobnost metallov [Influence of surface roughness on the emissivity of metals]. *Teplofizika visokih temperatur*. 1972;10(3): 528–535. (In Russ.)

30. Mukaida M., Miyazawa S. Nature of preferred orientation of YBa<sub>2</sub>Cu<sub>3</sub>O<sub>x</sub> thin films. *Japanese Journal of Applied Physics*. 1993;32(10): 4521–4528. <https://doi.org/10.1143/jjap.32.4521>

31. Markelov A. V. *The influence of buffer layers on the oriented growth of RBa<sub>2</sub>Cu<sub>3</sub>O<sub>7-δ</sub> (R – rare earth element) films and their superconducting characteristics*. Thesis of Cand. in Chem. Moscow: MSU (Lomonosov University); 2011. 108 p.

### Information about the authors

Alexander E. Shchukin, PhD student, Chemistry Department, Lomonosov Moscow State University, Moscow, Russian Federation; e-mail: aleksandr.shukin@mail.ru. ORCID iD: <https://orcid.org/0000-0002-3502-2950>.

Andrey R. Kaul, DSc in Chemistry, Professor, Chemistry Department, Lomonosov Moscow State University, Moscow, Russian Federation; e-mail: arkaul@mail.ru. ORCID iD: <https://orcid.org/0000-0002-3582-3467>.

Alexander L. Vasiliev, PhD in Physics and Mathematics, Associate Professor, Leading Researcher of the Resource Center for Probe and Electron Microscopy of the National Research Center “Kurchatov Institute”, Head of the Laboratory of Electron Microscopy of Federal Research Center “Crystallography and photonics” of the Shubnikov Institute of Crystallography of Russian Academy of Science, Moscow, Russian Federation; e-mail: a.vasiliev56@gmail.com. ORCID iD: <https://orcid.org/0000-0001-7884-4180>.

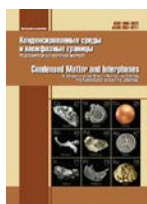
Igor A. Rudnev, DSc in Physics and Mathematics, Professor, Institute of Laser and Plasma Technologies, National Research Nuclear University “Moscow Engineering Physics Institute”, Moscow, Russian Federation; e-mail: iarudnev@mephi.ru. ORCID iD: <https://orcid.org/0000-0002-5438-2548>.

All authors have read and approved the final manuscript.

Received 2 January 2021; Approved after reviewing 15 February 2021; Accepted 15 March 2021; Published online 25 March 2021

Translated by Valentina Mittova

Edited and proofread by Simon Cox



## Guide for Authors – 2021

Manuscripts should be submitted as single **Microsoft Word 2003** files.

**Preferred font** 12 pt Times New Roman (please, do not use any other fonts, except for Symbol), 1.5 spaced lines, 1.25 cm first-line indent. Decimal values (e.g. 0.1; 0.9; 2.3) should be written using a decimal point.

Review/Original article/Short communication  
<https://doi.org/10.17308/kcmf.2021.23/0000>

## Modelling of interdiffusion and phase formation in thin-film two-layer systems of polycrystalline oxides of titanium and cobalt

*(All proper nouns should be capitalized; titles and subtitles should be left-aligned)*

N. N. Afonin<sup>\*1</sup>, V.A. Logacheva<sup>2</sup>

<sup>1</sup>Voronezh State Pedagogical University,  
86 ul. Lenina, Voronezh 394043, Russian Federation  
*(Official name and address of the organisation)*

<sup>2</sup>Voronezh State University,  
1 Universitetskaya pl., Voronezh 394018, Russian Federation

### Abstract

The abstract should be 200–250 words and include the following sections.

**Purpose:** States the problem considered in the article, its importance, and the purpose of the research.

**Experimental:** Provides information about the objects being studied and the methods used.

**Conclusions:** Provides a brief description of the principal results, major conclusions, and their scientific and practical relevance.

**Keywords:** Please, provide 5–10 keywords for the principal concepts, results, and terms used in the article.

**Acknowledgements:** Please, list the organisations that provided the funding for the research.

**Example:** the work was carried out within the framework of project No... supported by the Russian Science Foundation. The authors are grateful to PhD in Chemistry V. S. Semeykina (Siberian Branch of the Russian Academy of Sciences) for help ...

**For citation:** Afonin N. N., Logacheva V. A. Modelling of interdiffusion and phase formation in the thin-film two-layer system of polycrystalline oxides of titanium and cobalt. *Kondensirovannyye sredy i mezhfaznyye granitsy = Condensed Matter and Interphases*. 2021;23(1): 000–000. <https://doi.org/10.17308/kcmf.2021.23/0000>

<sup>\*</sup>Nikolay N. Afonin, [nafonin@vspu.ac](mailto:nafonin@vspu.ac)

© Afonin N. N., Logacheva V. A., 2021

## Article structure

The main text of the manuscript should have the following structure.

### 1. Introduction

*The introduction* (1–2 pages) states the problem under consideration, its relevance, and the most important tasks that need to be resolved. Describe the scientific problems which have not yet been solved and which you sought to solve in your research. The introduction should contain a short critical review of previously published works in this field and their comparative analysis. It is recommended that the analysis is based on 20–30 studies. **The purpose** of the article is indicated by the problem statement.

The Vancouver reference style is used in the journal: bibliographic references in the text of the article are indicated by numbers in square brackets; in the references section, the references are numbered in the order they are mentioned in the text.

#### *Example of references in-text citations:*

Single crystals of difluorides of alkaline earth elements are widely used as photonics materials [1–3] as well as matrices for doping with rare-earth ions [4, 10].

References should primarily be made to original articles published in scientific journals indexed by global citation databases. It is advisable to use 20–30 sources with at least 15 being published over the past 3 years. References should indicate the names of all authors, the title of the article, the name of the journal, year of publication, volume (issue), number, pages, and DOI (Digital Object Identifier <https://search.crossref.org/>). If a DOI is lacking, a link to the online source of the article must be indicated. References to dissertation abstracts are acceptable if the texts are available online. It is vital that our readers can find any of the articles or other sources listed in the reference section as fast as possible. Links to unpublished literature sources or sources not available online are unacceptable.

### 2. Experimental

*The experimental section* (2–3 pages) provides the details of the experiment, the methods, and the equipment used. The object of the study and the stages of the experiment are described in detail and the choice of research methods is explained.

### 3. Results and discussion

*Results and discussion* (6–8 pages) should be brief, but detailed enough for the readers to assess the conclusions made. It should also explain the choice of the data being analysed. Measurement units on graphs and diagrams should be separated with a comma. **Formulae should be typed using Microsoft Office Equation 3 or Math Type** and aligned on the left side. Latin letters should be in italics. Do not use italics for Greek letters, numbers, chemical symbols, and similarity criteria.

All subheadings should be in italics.

#### *Example:*

1.1. X-ray diffraction analysis

*Example of figure captions in the text of the article:* Fig. 1, curve 1, Fig. 2b.

A complete list of figures should be provided at the end of the paper after the information about the authors.

**Figures and tables should not be included in the text of the article.** They should be placed on a separate page. Figures should also be **submitted as separate** \*.tif, \*.jpg, \*.cdr, or \*.ai. files. **All figures should have a minimum resolution of 300 dpi.** Name each figure file with the name of the first author and the number of the figure.

#### 4. Conclusions

*Conclusions* (1 paragraph) should briefly state the main conclusions of the research. Do not repeat the text of the article. The obtained results are to be considered with respect to the purpose of the research. This section includes the conclusions, a summary of the results, and recommendations. It states the practical value of the research and outlines further research problems in the corresponding field.

#### Contribution of the authors

At the end of the Conclusions the authors should include notes that explain the actual contribution of each co-author to the work.

##### Example 1:

Nikolay N. Afonin – Scientific management, Research concept, Methodology development, Writing – original draft, Final conclusions.

Vera A. Logachova – Investigation, Writing – review & editing.

##### Example 2:

The authors contributed equally to this article.

#### Conflict of interests

The authors declare that they have no known competing financial interests or personal relationships that could have influenced the work reported in this paper.

#### References

*(The references are to be formatted according to the Vancouver Style. The reference list should only include articles published in peer-reviewed journals)*

##### Examples:

#### Articles in scientific journals

1. Luo Y., Zhao J. Plasmon-exciton interaction in colloiddally fabricated metal nanoparticle-quantum emitter nanostructures. *Nano Research*. 2019;12(9): 2164–2171. <https://doi.org/10.1007/s12274-019-2390-z>

2. Alexandrov A. A., Mayakova M. N., Voronov V. V., Pominova D. V., Kuznetsov S. V., Baranchikov A. E., Ivanov V. K., Fedorov P. P. Synthesis upconversion luminophores based on calcium fluoride. *Kondensirovannye sredy i mezhfaznye granitsy = Condensed Matter and Interphases*. 2020;22(1): 3–10. <https://doi.org/10.17308/kcmf.2020.22/2524>

3. Ryabtsev S. V., Shaposhnik A. V., Samoylov A. M., Sinelnikov A. A., Soldatenko S. A., Kushchev S. B., Ievlev V. M. Thin films of palladium oxide for gas sensors. *Doklady Physical Chemistry*. 2016;470(2): 158–161. <https://doi.org/10.1134/s0012501616100055>

#### Books: print

4. Kofstad P. *Nonstoichiometry, diffusion, and electrical conductivity in binary metal oxides*. Wiley-Interscience; 1972. 382 p.

5. Fedorov P. P., Osiko V. V. Crystal growth of fluorides. In: *Bulk Crystal Growth of Electronic, Optical and Optoelectronic Materials*. P. Capper (ed.). Wiley Series in Materials for Electronic and Optoelectronic Applications. John Wiley & Son. Ltd.; 2005. pp. 339–356. <https://doi.org/10.1002/9780470012086.ch11>

#### References to online sources

6. NIST Standard Reference Database 71. *NIST Electron Inelastic-Mean-Free-Path Database: Version 1.2*. Available at: [www.nist.gov/srd/nist-standard-reference-database-71](http://www.nist.gov/srd/nist-standard-reference-database-71)

#### Conference proceedings: individual papers

7. Afonin N. N., Logacheva V. A., Khoviv A. M. Synthesis and properties of functional nanocrystalline thin-film systems based on complex iron and titanium oxides. In: *Amorphous and microcrystalline semiconductors: Proc. 9th Int. Conf., 7–10 July 2014*. St. Petersburg: Polytechnic University Publ.; 2014. p. 356–357. (In Russ.)

### Information about the authors

This section should include the full last and first name(s) of the author(s), their academic degree, academic title, affiliation, position, city, country, e-mail, and ORCID (register for an ORCID here <https://orcid.org/register>).

#### Example:

*Nikolay N. Afonin*, DSc in Chemistry, Research Fellow, Professor at the Department of *Science and Technology Studies*, Voronezh State Pedagogical University, Voronezh, Russian Federation; e-mail: nafonin@vspu.ac.ru. ORCID iD: <https://orcid.org/0000-0002-9163-744X>.

*Vera A. Logachova*, PhD in Chemistry, Research Fellow at the Department of General and Inorganic Chemistry, Voronezh State University, Voronezh, Russian Federation; e-mail: kcmf@main.vsu.ru. ORCID iD: <https://orcid.org/0000-0002-2296-8069>.

*Valery V. Voronov*, PhD in Physics and Mathematics, Head of the Laboratory, Prokhorov General Physics Institute of the Russian Academy of Science, Moscow, Russian Federation; e-mail: voronov@lst.gpi.ru. ORCID iD: <https://orcid.org/0000-0001-5029-8560>.

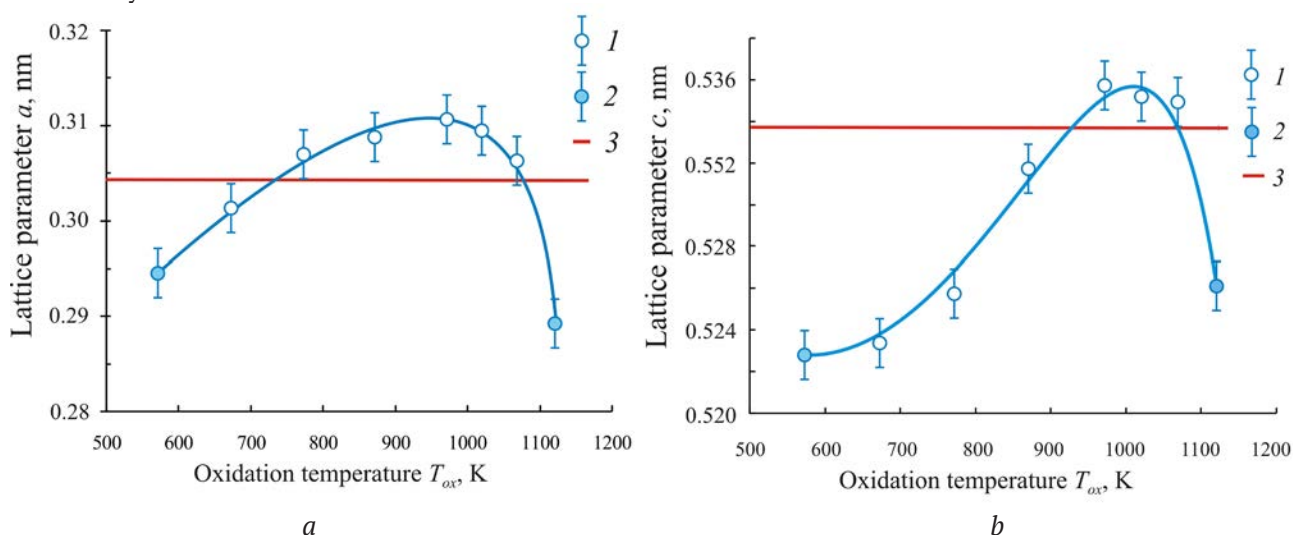
*Received 30 January 2021; Approved after reviewing 15 February 2021; Accepted 15 March 2021; Published online 25 March 2021.*

A complete list of figures should be provided at the end of the paper after the information about the authors.

#### Example:

**Fig. 1.** Dependences of the parameters  $a$  and  $c$  of the tetragonal lattice of nanocrystalline PdO films on the oxidation temperature  $T_{ox}$ : 1 – single-phase PdO films, 2 – heterophase PdO + Pd films; 3 – data of the ASTM standard [22, 23]

**Table 1.** The values of relative electronegativity (ENE) of some chemical elements [30] and the proportion of the ionic component of the chemical bond in binary compounds of the AB composition formed by these elements



**Fig. 1.** Dependences of the parameters  $a$  and  $c$  of the tetragonal lattice of nanocrystalline PdO films on the oxidation temperature  $T_{ox}$ : 1 – single-phase PdO films; 2 – heterophase PdO + Pd films; 3 – data of the ASTM standard [22, 23]



**Table 1.** Values of the ionic radii of palladium Pd<sup>2+</sup> and oxygen O<sup>2-</sup> [30–32]

Ion	Coordination number CN	Coordination polyhedron	Values of ionic radii $R_{ion}$ , nm
Pd <sup>2+</sup>	4	Square (rectangular)	0.078 [30]; 0.086 [31]; 0.078 [32]
O <sup>2-</sup>	4	Tetragonal tetrahedron	0.132 [30]; 0.140 [31]; 0.124* [31]; 0.132 [32]

\*The values of ionic radius were obtained on the basis of quantum mechanical calculations.

### ACCOMPANYING DOCUMENTS

*(The following documents should be submitted as PDF files)*

1. Covering letter (with authorisation for open access publication)
2. License agreement (signed by all authors) <https://journals.vsu.ru/kcmf/Licensingcontract>

### EDITING AND PROOFREADING

When the layout is ready it is sent back to the authors for proofreading. The article should be sent back to the publisher within a maximum of three days. The authors may only correct printing mistakes and introduce minor changes to the text or tables.